Simulation of seismic wave fields in inhomogeneous half-plane by non-conventional BEM

Dissertation
zur Erlegung des akademischen Grades
Doktor–Ingenieur
an der Mathematisch-Naturwissenschaftlichen
Fakultät der Christian-Albrechts-Universität zu
Kiel

vorgelegt von

Ioanna-Kleoniki M. Fontara

Kiel 2015

Gutachter:

1. Prof. Dr.-Ing. habil. Frank Wuttke
   Kiel University
2. Prof. Dr. George D. Manolis
   Aristotle University of Thessaloniki
3. Prof. Dr.-Ing. habil. Stavros Savidis
   Technical University of Berlin

Tag der mündlichen Prüfung: 22.07.2015
Zum Druck genehmigt: 29.09.2015

Der Dekan

Eidesstattliche Erklärung

Hiermit erkläre ich, dass ich die vorliegende Arbeit nach Inhalt und Form–abgesehen von der Beratung durch meinen Betreuer–selbständig verfasst und keine weiteren Quellen und Hilfsmittel als die im Quellenverzeichnis angegeben verwendet habe. Diese Arbeit hat weder ganz, noch in Teilen, bereits an anderer Stelle einer Promotionskommission zur Erlangung des Doktorgrades vorgelegen.
Ich erkläre, dass die vorliegende Arbeit gemäss den Grundsätzen zur Sicherung guter wissenschaftlicher Praxis der Deutschen Forschungsgemeinschaft erstellt wurde.

Kiel, 22.07.2015
Ioanna-Kleoniki Fontara

Vorwort des Herausgebers

Die vorliegende Promotionsschrift von Frau Dr.-Ing. Ioanna-Kleoniki Fontara ist dem Forschungs- und Arbeitsgebiet Bodendynamik und des Erdbebeningenieurwesens zuzuordnen. Die untersuchten Fragestellungen ergaben sich aus den bisherigen jahrelangen Forschungsarbeiten an der Professur auf diesem Gebiet. Die Arbeit beinhaltet originär weiterentwickelte Lösungen und Methoden zur unkonventionellen Randelementmethodik sowie neue Ansätze zur Simulation einer Wellenausbreitung. Die erzielten Lösungen beziehen ihre Aktualität aus den beständigen Bestrebungen, die Ausbreitung von laufenden Wellenfeldern präziser, unter den gegebenen Randbedingungen im Untergrund abzubilden und den numerischen Aufwand zu reduzieren. Für viele Fragestellungen im Bereich der Naturkatastrophenforschung, dem Erdbebeningenieurwesen, der Strukturidentifikation oder auch der Baudynamik ist die effektive Simulation von Wellenfeldern eine Grundvoraussetzung, um Untersuchungen und Entwicklungen zu tätigen. Speziell die Randelementmethoden bieten sich für die Analyse von propagierenden Wellenfelder an. Allerdings ist die numerische Realisierung von komplexeren Untergrundverhältnissen bislang nicht effektiv und erfordert noch hohe Rechenkapazitäten. Das führt zu numerischen Problemen insbesondere, wenn großskalige inhomogene Gebiete abgebildet werden müssen. Mit der Entwicklung von unkonventionellen Randelementmethoden, welche eine kontinuierliche Änderung der Bodeneigenschaften, in der Regel der Dichten und Steifigkeiten, über die Tiefe beinhalten, kann der Modellierungsaufwand stark reduziert werden und zugleich typische Bodenprofile für die Simulation abgebildet werden. Numerisch vergleichende Studien zu Bodenschichtung mit zunehmender Steifigkeit über die Tiefe, haben die Übereinstimmung und Anwendbarkeit zu konventionellen Schichtmodellierungen bei einer ausreichend hohen Anzahl von modellierten Schichten nachgewiesen. Mit der Erweiterung der Green'schen Funktionen hinsichtlich einer seismischen Punktquelle können propagierende Wellenfelder im Erdbebeningenieurwesen oder der Bodendynamik realitätsnah und unter Berücksichtigung einer geometrischen Wellendämpfung, auftretender Interferenz- und Überlagerungseffekten analysiert werden. Die Arbeit schließt die vorgenannten Entwicklungen in einem numerischen Programmsystem ein, so dass die erarbeiteten Lösungen an unterschiedlichen Fallstudien validiert werden konnten.

Kiel, im Juli 2015 Frank Wuttke

Preface by the author

The present Ph.D. thesis has been conducted during my work as research assistant in Bauhaus University in Weimar and in Christian Albrechts University in Kiel. There are many people who contributed either directly or indirectly to the present work and to whom I would like to extend my deepest acknowledgments.

First and foremost I would like to thank my advisor Professor Frank Wuttke. I appreciate all his contributions of ideas and funding to make my Ph.D. experience productive and stimulating. Besides my advisor I would like to acknowledge honorary to the other two members of the committee, Professor George Manolis and Professor Stavros Savidis. Moreover, I would like to cordially thank Professor George Manolis, Professor Petia Dineva and Professor Tsviatko Rangelov for guiding my research and helping me to develop my background in Boundary Element Methodology. Their scientific and moral contribution to the present work was substantial. Also I am grateful to Professor Asimina Athanatopoulou for enlightening me the first glance of research and keep supporting me till now.

I would like also to thank my colleagues in Christian Albrechts University in Kiel, Bauhaus University in Weimar and Aristotle University in Thessaloniki. Especially I would like to mention: Kostantinos Kostinakis, Magda Titirla, Maria Noack and Peter Appel.

Last but not least, I acknowledge the support of Michail the last months of writing my thesis. Also I would like to thank my family for all their love and encouragement. I am fully grateful to my parents Michail and Eirini and my brother Athanasios for their dedicated love and support in all my pursuits. Closing this acknowledgment note, I would like to refer to the following Greek gnome that Alexander the Great said to his tutor Aristotle:

$$Ει\varsigma \quad μεν \quad τον \quad πατὲρα \quad μου \quad οφειὶλω \quad το \quad ζην$$
$$ει\varsigma \quad δεν \quad τον \quad διδὰσκαλὸ \quad μου \quad το \quad ευ \quad ζην$$

(*I am indebted to my father for living, but to my teacher for living well*)

Ioanna-Kleoniki M. Fontara

Abstract

The estimation of seismic motion in regions with natural or induced seismicity is increasingly becoming important nowadays. Seismic motion is influenced by the dynamic characteristics of the seismic source, the wave propagation path, the surface topography, the soil layering, plus the mechanical properties of the surrounding geological materials. From an engineering point of view, local site conditions generate large amplifications as well as spatial variations in the seismic motions, which are important for the analysis and design of large infrastructure such as dams, bridges, industrial plants and pipelines. To date, no seismic design code has succeeded to fully address the case of local site conditions due to the sheer complexity of the problem. As a result one of the major objectives in earthquake engineering is to develop mechanical models and accompanied numerical tools able to estimate the seismic field in complex geological media. Among the numerical methods the BEM is recognized as a valuable technique to solve wave propagation problems due to many advantages in comparison with other domain techniques.

The major contribution of the present thesis is the development of non-conventional BEM numerical schemes and accompanied research software for wave propagation in continuously or discrete inhomogeneous geological media with heterogeneities such as homogeneous or graded layers, cavities, tunnels and valleys. In the BEM formulation is efficiently inserted a library of fundamental solutions and Green's functions that account for different types of material gradient; in contrast to the conventional BEM formulations which employ fundamental solutions for homogeneous media. Hence, the main advantages and novelty of the proposed method are as follows: (a) direct modeling of the inhomogeneity through the use of a library of special class of functions; as a result different models of the geological media are investigated; (b) the ability to account for all three components of the problem (source - wave path inhomogeneity - surface topography) in one step; (c) due to the usage of the Green's function and special class of fundamental solutions, the solution accuracy increases and the computational time and memory is reduced.

A successful validation with existing solutions as well as a series of parametric studies considering different geological configurations and seismic scenarios is given for SH–wave propagation. All results reveal the potential of the developed models to study wave propagation in complex geological profiles with high accuracy

and minimal modeling effort. Considering the investigated problem of SH–wave propagation, it is evidently demonstrated the sensitivity of the seismic signal to the existence and type of the material gradient, to the type and properties of the seismic source and to the lateral inhomogeneity due to the free-surface and/or sub-surface relief peculiarities such as layering, tunnels, cavities, valleys. Seismic signals in time domain are generated at the surface of complex geological profiles using inverse Fourier transformation able to describe efficiently and with high accuracy all three components of the Earth system; seismic source, wave path and local geological region of interest.

Applications of the developed numerical tools in material modeling and earthquake engineering are conducted. For the former application, wave propagation phenomena are reproduced in a continuous matrix with position dependent-material properties and containing any number and configuration of cavities for pure elastic and poroelastic geological media. Stress and displacement field is presented. For the latter application, the influence of site effects on ground motions and subsequent structural damage of aboveground constructions is investigated considering 2D analysis of the soil profile. Bridge and building models are examined under site dependent ground motions computed at the surface of complex geological profiles that account for canyon topography, soil layering and material gradient.

Zusammenfassung

Die Einschätzung der seismischen Bewegungen in Regionen mit natürlicher oder induzierter Seismik ist ein in der heutigen Zeit zunehmend wichtiger und aktueller Punkt. Die seismischen Bewegungen des Bodens werden beeinflusst durch die dynamischen Eigenschaften der Quelle, den Wellenpfad, die lokalen oberflächennahen Standortbesonderheiten, die Schichtungsstruktur und die mechanischen Eigenschaften des Bodens. Lokale Standortbedingungen können grosse Verstärkungen sowie ausgeprägte räumliche Variationen in den seismischen Bewegungen erzeugen, die für die Analyse und das Design grosser Infrastrukturprojekte, wie Dämme, Brücken, Industrieanlagen und Rohrleitungen wichtig sind. Aufgrund der immensen Komplexität dieses Problems ist es bisher keiner Erdbebennorm möglich, den Fall der lokalen Standortbedingungen vollständig anzusprechen. Somit ist eines der wichtigsten Ziele der Erdbebenforschung, mechanische Modelle und numerische Tools zu entwickeln, die in der Lage sind, die seismischen Bewegungen in komplexen geologischen Medien berechnen zu können. Unter den numerischen Methoden ist die Randelemente-Methode (BEM) als eine wesentliche Methode zur Analyse von Wellenausbreitungsproblemen anerkannt. Sie besitzt im Vergleich zu anderen Domain-Techniken eine Reihe von Vorteilen.

Der wichtigste Beitrag der vorliegenden Promotionsschrift ist die Entwicklung einer nicht-konventionellen Randelemente (BEM) Methode und die Entwicklung einer Forschungs-Software zur Wellenausbreitung in kontinuierlichen oder diskreten inhomogenen geologischen Medien mit Heterogenitäten (z.B. homogen oder gradierten Schichten, Hohlräume, Tunnel und Täler). Diese BEM Implementierung beinhalt eine Bibliothek von Fundamentallösungen und Green'schen-Funktionen, welche verschiedene Arten von internen Materialsteifigkeitsgradienten bzw.–heterogenitäten darstellen können. Die folgenden Punkte sind die wichtigsten Vorteile und Neuheiten der genutzten Methoden: (a) direkte Modellierung der Inhomogenität durch die Verwendung einer Bibliothek von spezifischen Funktionen; wodurch unterschiedliche Modelle der geologischen Struktur analysiert worden; (b) die Möglichkeit, alle drei Komponenten des Problems (Quelle - Wellenpfad Inhomogenität - oberflächlichen Standortbesonderheiten) in einem Schritt darzustellen; (c) wegen der Nutzung der Green'schen–Funktion und einer Sonderklasse von Fundamentallösungen, wodurch die Lösungsgenauigkeit erhöht und Rechenzeit und der erforderliche Speicherplatz reduziert wurde.

Eine erfolgreiche Validierung anhand vorhandener analytischer Lösungen sowie eine Vielzahl von Parameterstudien unter Berücksichtigung unterschiedlicher geologischer Konfigurationen und seismischer Szenarien für SH–Wellenausbreitung wurden durchgeführt. Alle Ergebnisse zeigen dass, die entwickelten Modelle zur Untersuchung der Wellenausbreitung unter komplexen geologischen Bedingungen ein hohes Potential zur erfolgreichen und genauer Problemlösung beim minimalen Modellierungsaufwand besitzen. In Anbetracht des untersuchten Problems der SH-Wellenausbreitung wurde nachgewiesen, dass die Empfindlichkeit des seismischen Signals auf (1) das Vorhandensein und die Art der Materialänderung, (2) der Art und der Eigenschaften der seismischen Quelle und (3) den seitlichen Inhomogenität aufgrund der Freifläche und / oder Sub-Oberflächenrelief wie z.B. Schichtung, Tunnel, Höhlen, Tälern vorhanden ist. Ausgehend davon wurden seismische Zeitbereichs-Signale an der Oberfläche der komplexen geologischen Profile berechnet, welche effizient und mit hoher Genauigkeit das Bewegungsmuster bzw.–einfluss der seismischen Quelle, Wellenpfad und der lokalen geologischen Region signifikant abbilden.

Abschliessend erfolgten Betrachtungen zur Anwendung der entwickelten numerischen Methoden in den Gebieten der Materialmodellierung und dem Erdbeben-Ingenieurwesen. Für die erste Anwendung wurden die Wellenausbreitungsphänomene in einem kontinuierlichen Material/Raum mit positionsabhängigen Materialeigenschaften und mit einer beliebigen Anzahl bzw. Konfiguration der Hohlräume in rein elastischen oder poro-elastischen geologischen Medien abgebildet. Dabei erfolgte die Berechnung des Spannungs- und Verschiebungsfeld innerhalb des Kontinuums. In der letzten Anwendung erfolgte die Analyse eines Einflusses der lokalen Standortbedingungen auf die Bodenbewegungen und sich anschliessende potentiellen Strukturschäden der oberirdischen Baustrukturen. Als Strukturmodelle wurden Brücken und Gebäude analysiert, wobei relevante Bodenbewegungen an der Oberfläche entsprechender geologischer Modelle berechnet wurden. Die dazu genutzte Modellierung des geologischen Raums berücksichtigt Materialänderungen über die Tiefe, Bodenschichtung und Oberflächentopographien.

Contents

List of Figures

List of Tables

Abbreviations

CPU	**C**entral **P**rocessing **U**nit
BIEM	**B**oundary **I**ntegral **E**quation **M**ethod
BEM	**B**oundary **E**lement **M**ethod
FEM	**F**inite **E**lement **M**ethod
FDM	**F**inite **D**ifference **M**ethod
WNIM	**W**ave **N**umber **I**ntegration **M**ethod
R/T	**R**eflection **T**ransmission matrices
BVP	**B**oundary **V**alue **P**roblem
IBVP	**I**nitial **B**oundary **V**alue **P**roblem
BE	**B**oundary **E**lement
CPV	**C**auchy **P**rinciple **V**alue
FFT	**F**ast **F**ourier **T**ransform
IFFT	**I**nverse **F**ast **F**ourier **T**ransform
FGM	**F**unctionally **G**raded **M**aterial
SCF	**S**tress **C**oncetration **F**actor
SSI	**S**oil **S**tructure **I**nteraction
RC	**R**einforced **C**oncrete
MIDR	**M**aximum **I**nterstorey **D**rift **R**atio
OSDI	**O**verall **S**tructural **D**amage **I**ndex

Chapter 1

Introduction

1.1 Motivation

It is well known that geological formations have different kinds of irregularities and produce distortions in the incoming wave by processes such as bending, scattering and focusing [2]. Such distortions are generally called site effects. The expression "local amplification", widely used in earthquake engineering, and the rough synonym "seismic site effects", actually denote a set of different physical phenomena arising from the propagation of seismic waves in near-surface geological formations or in geometrically irregular configurations at the earth surface such as canyons, ridges, hilltops. The key factors involved in this phenomenon are: (a) seismic source characteristics, (b) wave propagation path, defined by source-to-site distance and (c) subsurface geology, see Fig.1.1. Site effects are responsible for large

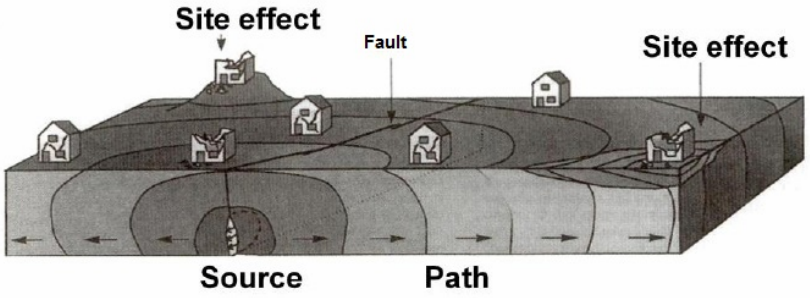

FIGURE 1.1: Key parameters responsible for site effects [1]

amplifications as well as spatial variations in the seismic motions which in most cases lead to important structural damage. As a result, one of the major objectives in earthquake engineering is to quantify the amplification of seismic waves due to complex geological profiles in order to mitigate the seismic hazard [3]. It

is important to note that to date no seismic design code has succeeded to fully address the case of local site effects due to the sheer complexity of the problem.

However, many researchers have investigated the problem of wave propagation phenomena in geological deposits. The developed methods of analysis can be briefly classified as: (a) Analytical, (b) Semi-Analytical, (c) Approximate, (d) Numerical and (e) Hybrid. Methods referring to the first three classifications are mainly restricted to media with simple geometry. Analytical solutions for wave motion in alluvial basins of regular shape are derived in [4, 5]. Semi-analytical solutions for wave diffraction by geological irregularities of arbitrary shape are presented in [6–8]. Approximate methods are generally based on the ray theory [9, 10], mode matching methods [11, 12], integral representation theorems [13], matrix methods [14], reflectivity methods and generalized R/T coefficient methods [15–18]. Numerical methods are mostly employed for analyzing complex heterogeneous media, but require much computational effort in terms of CPU time and memory. Namely, they are based on the following techniques: (i)FEM [19], (ii)FDM [20, 21] and (iii)BIEM [22, 23]. Finally, hybrid methods have appeared in recent years and their basic structure combines numerical methods to model interior domains containing all the inhomogeneities, with semi-analytical or approximate representations for the exterior regular domain [24–28].

1.2 Essential use of BEM as numerical tool

Among the numerical methods the BEM is recognized as a valuable technique to solve wave propagation problems in complex geological domains, due to many advantages in comparison with other domain techniques, eg. FEM and FDM. In general, the advantages of the BEM for applications in seismic mechanics are: (i) the ability to deal with infinite or semi-infinite media with high accuracy and minimal modeling effort due to implicit satisfaction of the Sommerfeld radiation condition associated with unbounded domains; (ii) reduction of the problem dimensionality because only surfaces need to be discretized in contrast to domain methods; (iii) high solution accuracy since quadrature techniques are directly applied to the boundary integral equations, which in turn are an exact mathematical statement of the problem under consideration; (iv) high accuracy in computation of field variables at internal points because they are expressed in terms of boundary values without recourse to domain discretization.

Nevertheless, BEM technique has also some limitations considering the investigated here problems, namely: (i) a fundamental solution of the governing equation of motion is required, which is not always available or it is not in a simple mathematical form, (ii) great computational effort is needed due to integrals with singular kernels and (iii) in most cases is recommended for linear problems.

Considering the case of direct BEM numerical models describing seismic wave propagation in elastic isotropic inhomogeneous geological media only few studies can be briefly identified. Leung et al. (1991) [29] investigated the vibration isolation of structures from ground transmitted waves by trenches in continuously inhomogeneous soil using BEM based on Green's function of Kausel-Peek-Hull for a thin layered half space. The shear modulus of the soil can vary exponentially or linearly with the depth. Hisada (1992) [30] developed a new BEM based on Green's function for layered half-plane. Next Fujiwara and Takenaka (1994) [31] developed a direct BEM based on Green's function computed by the summation of normal modes to calculate wave field in a thin sedimentary basin exhibiting lateral inhomogeneity. Also Ge (2010)[32] presented a BEM using approximate analytical Green's function for inhomogeneous half-plane with varying velocity.

As mentioned above the problem of wave propagation in inhomogeneous half-plane can be also treated by hybrid techniques. Since the investigated problem can be decomposed in three main parts see Fig.1.2 - seismic source, inhomogeneous wave path from the source to the region of interest plus its lateral inhomogeneity, two or more methods can be coupled in order to produce total wave field at the free-surface. The idea was realized in Panza et al. (2009) [33], where modal summation method and BEM are used in two-step hybrid approach, or Wuttke et al. (2011) [27] where is proposed a combined usage of wave number integration method (WNIM) and BEM. The main disadvantage of the hybrid approach based on a two-step procedure is that the backscattering phenomena are not taken into consideration. Extensive state-of-the-art review is given in Chapter 2 regarding the problem of wave propagation in continuously inhomogeneous geological media via BEM.

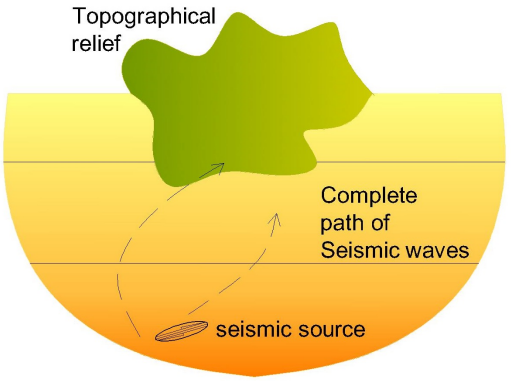

FIGURE 1.2: The three main components of the seismic motion

In conclusion, there is a lack of numerical models based on BEM to investigate seismic wave propagation problems in inhomogeneous geological media taking into account in one step the three main components of the problem; (i) seismic source

characteristics, (ii) inhomogeneous wave path from the source to the region of interest and (iii) the finite laterally inhomogeneous soil stratum.

1.3 Scope and outline

BEM is an ideal method for wave propagation problems in large geological domains with infinite or semi-infinite regions. The conventional BEM for 2D wave propagation employs the fundamental solution of elastodynamics for homogeneous media. For inhomogeneous geological media, several researchers have used appropriate fundamental solutions or Green's functions in the BEM formulation in order to express material inhomogeneity in the computational model by a continuous or discrete manner. In the latter case the following studies can be addressed [16, 17, 29, 34, 35] in which BEM employs existing Green's function for stratified half-plane with complex mathematical form that prevents the easy implementation in the BEM formulation and increases the CPU time and memory. In the former case the inhomogeneity is expressed by smooth functions of the material properties with respect to the depth. BEM for continuously inhomogeneous media with constant velocity are addressed in [36, 37] and with velocity variation in [32, 38, 39]. However, all the above mentioned studies consider no heterogeneities and if they do so are restricted to simple geometry like a single crack, a semi-circle alluvial valley. On the other hand, two step hybrid methods [24–28] are developed which are able to consider both inhomogeneity and heterogeneity in the geological model, but they fail to account for the backscattering phenomena.

The objective of the present thesis is to develop a non-conventional BEM for wave propagation problems in inhomogeneous geological media with heterogeneities (like canyons, cavities, layers, etc) using a library of fundamental solutions and Green's functions. The main advantages and novelty of the proposed method are as follows: (a) direct modeling of inhomogeneity through the use of closed form Green's functions and Fundamental solutions for specific cases of study; as a result different mechanical models of the geological media are investigated; (b) the ability to account for all three components of the problem (source - wave path inhomogeneity - subsurface geology) in one step; (c) due to the usage of the Green's function and special class Fundamental solutions, the solution accuracy increases and the CPU time and memory is reduced in comparison with the conventional BEM. Complete software package is developed using Matlab covering a range of wave propagation problems in inhomogeneous geological media.

Briefly the work is structured as follows:

- **Chapter 2**: Extensive state-of-the-art review is given regarding wave propagation problems in continuously inhomogeneous geological media and the

accompanied numerical tools developed to-date under out-plane and in-plane strain state. The following categories are defined based on the characteristics of the geological media and the mechanical models used to describe them: (a) continuously inhomogeneous soil media with constant velocity, (ii) continuously inhomogeneous soil media with variable velocity and (ii) discrete inhomogeneous soil media. Additionally the presence of heterogeneities like cracks, cavities and inclusions in the inhomogeneous background is addressed.

- **Chapter 3**: BEM technique is developed and presented which is based on closed form Green's function (Rangelov and Manolis [40]) for quadratically inhomogeneous in depth half-plane of quadratic type and constant velocity. Detailed description is given of the problem's mathematical statement, formulation of the BEM and the corresponding numerical implementation and validation. Time harmonic and transient SH-wave propagation in continuously inhomogeneous half-plane with free-surface relief and buried unlined tunnels is investigated. The following key parameters of the seismic wave field via the developed BEM model are examined: (a) type and characteristics of the seismic source, (b) existence and type of the material gradient and (c) the lateral inhomogeneity due to the free-surface and/or sub-surface relief peculiarities. Seismograms due to complex geological profiles are recovered and site dependent response spectra are produced.

- **Chapter 4**: BEM technique is developed and presented which is based on fundamental solution (Manolis and Shaw [41, 42]) for geological media with variable wave velocity profile. The problem's mathematical statement, formulation of the BEM and the corresponding numerical implementation and verification is presented. Time harmonic and transient SH-wave propagation in continuously inhomogeneous geological medium that possesses variable velocity profile, in addition to the presence of either parallel or nonparallel graded layers, of surface relief, and of cavities and tunnels is investigated via BEM. A series of parametric studies are conducted and numerical results are generated in form of synthetic seismic signals for several number of geological deposits. An insight investigation is presented on the seismic wave field dependence on the material gradient and the wave velocity variation in the medium, on the presence of layers, canyons and cavities, and on the frequency content of the incoming signal.

- **Chapter 5**: An application of the new-developed BEM numerical models (see as defined in the previous chapters) in the context of material modeling is presented, investigating wave propagation in functionally graded pure elastic or poroelastic materials consisting of multiple cavities. Kinematic and stress fields are demonstrated due to wave interaction phenomena between cavities and free surface. Additionally wave diffraction phenomena due to the inhomogeneous structure of the material matrix are taken into consideration. A number of cases involving graded half-plane containing any number

of cavities of various shapes and geometry are solved in the frequency domain. The potential of the developed BEM techniques to deal with dynamic problems in functionally graded materials with cavities is demonstrated.

- **Chapter 6**: The effect of local site conditions on the nonlinear response of conventional mid-rise buildings and reinforced concrete bridges is investigated using the developed BEM methodologies described above. Ground motion records are recovered at the surface of complex geological profiles that consider canyon topography, layering and material gradient effect. Next, nonlinear time history analyses are conducted and the seismic response of the structures is evaluated under site dependent ground motions and spring coefficients that account for (a) local site conditions, (b) spatial variability and (c) Soil-Structure-Interaction using a 2D analysis of the subsoil configuration via the new developed BEM.
- **Chapter 7**: Conclusions and Outlook

1.4 Introduction to BEM formulation

The present section demonstrates step by step the description of the BEM technique in order to introduce the fundamental ideas underlying the formulation of the boundary element method used as a main computational tool. First, the derivation of the Boundary Integral Equation (BIE) is presented and then a short description of the numerical solution of the BIE is given based on discretization and collocation procedure. Note here referring to the terminology that between the term BIEM and BEM there is no difference. Usually the term BIEM is used when we speak about formulation of a given BVP via integral equations along the boundary of the domain under investigation. The term BEM is used when the numerical algorithm is based on discretization and collocation techniques.

1.4.1 Boundary integral equation

Consider the general elastodynamic initial boundary-value problem in Ω domain, Fig.1.3. The governing equations of the problem are the followings:

Constitutive equations (Hook's law):

$$\sigma_{ij}(x,t) = C_{ijkl} s_{ij}(x,t); \quad i,j = 1,2,3 \quad x \in \Omega \tag{1.1}$$

where $x = (x_1, x_2, x_3)$ is the position vector in a Cartesian coordinate system $Ox_1x_2x_3$, t is the time, σ_{ij} and s_{ij} denote the stress and strain tensors of the elastic continuum, C_{ijkl} is the forth order stiffness tensor, which is presented for isotropic material by Lame's constant λ and μ as $C_{ijkl} = \lambda\delta_{ij}\delta_{kl} + \mu(\delta_{ik}\delta_{jl} + \delta_{il}\delta_{jk})$, δ_{ij} is the Kronecker symbol.

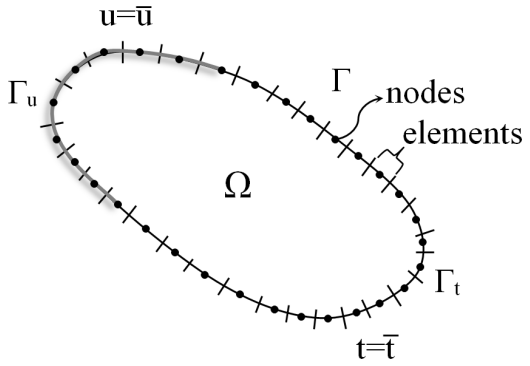

FIGURE 1.3: Initial boundary value problem

Kinematics relations under assumption of small displacements:

$$s_{ij}(x,t) = \frac{1}{2}[u_{i,j}(x,t) + u_{j,i}(x,t)]; \quad i,j = 1,2,3 \quad x \in \Omega \tag{1.2}$$

Equation of motion:

$$\sigma_{ij,j} + \varrho f_i = \varrho \ddot{u}_i \quad x \in \Omega \tag{1.3}$$

where ϱ is the mass density, f_i is the body force, u_i are displacement components, a comma after a quantity designates partial differentiation of the quantity with respect to spatial variables, while superscript dots stand for temporal derivatives of the quantity. Also, the conventional summation rule over double indices is implied.
Boundary conditions along $\Gamma = \Gamma_u \cup \Gamma_t$, where Γ_u, Γ_t are the surfaces where displacements and tractions are prescribed respectively:

$$u_i(x,t) = \tilde{u_i}(x,t) \quad x \in \Gamma_u \quad and \quad t_i(x,t) = \tilde{t_i}(x,t) \quad x \in \Gamma_t \tag{1.4}$$

where tractions are defined as $t_i = \sigma_{ij} n_j$, $i,j = 1,2,3$ and n_j is the outward pointing unit normal vector to the surface under consideration.

Initial conditions: zero initial conditions at the beginning of the motion are assumed:

$$u_i(x,t) = \dot{u_i}(x,t) = 0 \quad for \quad t = 0 \quad x \in \Omega \tag{1.5}$$

Finally, we search for time-dependent solution in terms of displacements that satisfies the equation of motion Eqn.(1.3) in the domain Ω, boundary conditions, Eqn. (1.4), along the domain's surface Γ and initial conditions expressed in Eqn. (1.5).

The above formulated initial boundary value problem can be described by integral equations along the boundary Γ of the considered domain Ω via Betti-Rayleigh

reciprocal theorem which at the assumption of zero initial conditions can be stated as [23, 43]:

$$\int_{\Gamma}[\sigma_{ij}^{(1)} * u_i^{(2)} - \sigma_{ij}^{(2)} * u_i^{(1)}]n_j d\Gamma = \varrho \int_V [f_i^{(2)} * u_i^{(1)} - f_i^{(1)} * u_i^{(2)}]dV \tag{1.6}$$

where $\{u_i^{(1)}; \sigma_{ij}^{(1)}\}$ and $\{u_i^{(2)}; \sigma_{ij}^{(2)}\}$ represent two independent elastodynamic states of the state solid and "*" denotes the Riemann convolution which is defined as:

$$g(x,t) * h(x,t) = \int_0^t g(x, t-\tau)h(x,\tau)d\tau \tag{1.7}$$

Considering the following steps (1) and (2):
(1) The state $\{u_i^{(2)}; \sigma_{ij}^{(2)}\}$ as the fundamental solution $\{U_{ij}^*; \sigma_{ijk}^*\}$ due to an impulsive body force at point $x = y$ defined by $f_2 = \delta(t-\tau)\delta(x-y)$, where the fundamental solution satisfies the following partial differential equation:

$$\sigma_{ijk,j}^* - \varrho \ddot{U}_{ik}^* = -\delta(t-\tau)\delta(x-y)\delta_{ik} \tag{1.8}$$

where $\delta(.)$ is the Dirac delta function and $\sigma_{ijk}^* = C_{ijmn}\frac{\partial U_{mk}^*}{\partial y_n} = -C_{ijmn}\frac{\partial U_{mk}^*}{\partial x_n}$
(2) The state $\{u_i^{(1)}; \sigma_{ij}^{(1)}\}$ as the unknown actual mechanical state $\{u_i; \sigma_{ij}\}$
and substituting them in the reciprocity theorem Eqn(1.6) the following representation formulae, Eqn.(1.9), is obtained having in mind the properties of the Dirac delta function:

$$u_j(x,t) = \int_{\Gamma} U_{ij}^*(x,y,t) * t_j(y,t)dy - \int_{\Gamma} P_{ij}^*(x,y,t) * u_j(y,t)dy; \quad x \in \Omega; \quad x \notin \Gamma \tag{1.9}$$

where: $P_{ij}^* = \sigma_{ijk}^* n_k$ and x and y are the position vectors of the observation and source point respectively.

After application of a direct limit process $x \to \Gamma$ to integral Eqn.(1.9) the following boundary integral equation is obtained:

$$c_{ij}u_j(x,t) = \int_{\Gamma} U_{ij}^*(x,y,t) * t_j(y,t)dy - \int_{\Gamma} P_{ij}^*(x,y,t) * u_j(y,t)dy; \quad x \in \Gamma \tag{1.10}$$

where the free term is defined by $c_{ij}(x) = \delta_{ij}$ when $x \in \Gamma$ and $c_{ij}(x) = 0$ when $x \notin \Gamma$. In case $x \in \Gamma$ the boundary integrals include a singularity, which can be taken out by a limiting process. From this process one may compute the value of $c_{ij}(x)$ which depends on the geometry of the boundary at point x. The singular integrals can be interpreted in the sense of Cauchy Principal Value (CPV).

Finally the Initial Boundary Value Problem (IBVP) defined by the equation of motion Eqn.(1.3) in the domain Ω, boundary conditions Eqn.(1.4) along the

domain's surface $\Gamma = \Gamma_u \cup \Gamma_t$ and initial conditions Eqn.(1.5) is reformulated by the boundary integral equation Eqn.(1.10) along the boundary Γ of the domain Ω and accompanied boundary and initial conditions defined by Eqn.(1.4) and Eqn.(1.5) respectively.

The final aim of the IBVP is to find solution at any point inside the domain Ω and satisfying boundary and initial conditions. The following procedure is followed when the formulation via boundary integral equations is used: (1) the BIE is solved in respect to the unknowns along the boundary Γ; (2) once having all field variables along the domain's boundary Γ the solutions at any point inside the domain Ω can be found by the usage of well-known integral representation formulae, Eqn.(1.9). What follows is a short description of the numerical solution of the BIE based on discretization and collocation procedures.

1.4.2 Numerical solution of the boundary integral equation

Assume for simplicity that the body is two dimensional and its boundary is divided into N segments or elements. It is worth mentioning here that the number of discretization elements (boundary elements) should remain small if one is going to have a reasonable representation of the problem. For example for time-harmonic wave propagation problems the length of the element should be $l = \lambda/6$, where λ is the wave length. The points where the unknown values are considered are called "nodes" and in case of "constant" elements are taken to be in the middle of the elements, see Fig.1.3.

For the constant elements considered here the boundary is assumed to be divided into $N = N_u + N_t$ elements. The values of vector components of displacement u and traction t are assumed to be constant over each element and equal to the value at the mid-element node. Then, BIE (Eqn.1.11) can be discretized for a given collocation point "i" as follows:

$$\begin{array}{l} cu^i + \sum_{j=1}^{N_t} (\int_{\Gamma_j} P^*_{ij} d\Gamma) u^j - \sum_{j=1}^{N_u} (\int_{\Gamma_j} U^*_{ij} d\Gamma) t^j \quad = \\ \sum_{j=1}^{N_u} (\int_{\Gamma_j} P^*_{ij} d\Gamma) \tilde{u^j} + \sum_{j=1}^{N_t} (\int_{\Gamma_j} U^*_{ij} d\Gamma) \tilde{t^j} \end{array} \tag{1.11}$$

where U^*_{ij} and P^*_{ij} are fundamental solutions for displacements and tractions respectively at point j when a load or source is applied at point i, u^j and t^j are the displacement and traction boundary conditions at point j at the boundary Γ_j and c is a multiplier depending on the type of the element used for discretization. For constant boundary elements c=0.5. The u^j and t^j values can be taken out of the integrals as they are constants over each element. There are two types of integrals

to be carried out over the elements:

$$H^{ij} = \int_{\Gamma_j} P^*_{ij} d\Gamma \quad \text{and} \quad G^{ij} = \int_{\Gamma_j} U^*_{ij} d\Gamma \tag{1.12}$$

These integrals relate the "i" node where the fundamental solution is acting to any other "j" node. Because of this, their resulting values are sometimes called *influence coefficients*. Note here that boundary integral equation (Eqn.1.11) and the resulting influence coefficients apply for a concentrated charge at "i" and consequently the values of U^* and P^* are those corresponding to that particular position of charge. For any other x^i position new integral equation should be found. For a particular "i" node Eqn.(1.11) can be written:

$$cu^i + \sum_{j=1}^{N_t} H^{ij} u^j - \sum_{j=1}^{N_u} G^{ij} t^j = \sum_{j=1}^{N_u} H^{ij} \tilde{u^j} + \sum_{j=1}^{N_t} H^{ij} \tilde{t^j} \tag{1.13}$$

The point j can vary from 1 to $N = N_u + N_t$. If we assume that the position of "i" can also vary from 1 to N and the fundamental solution is applied at each node successively then we obtain a system of NxN equations resulting from applying Eqn.(1.13) to each boundary point in turn. This procedure is called collocation technique (Fig.1.4). This set of equations can be expressed in matrix form as:

$$\mathbf{HU} = \mathbf{GP} \tag{1.14}$$

where **H** and **G** are two NxN matrices and **U**, **P** are vectors of size N. Notice that N_u values of u and N_t values of t are known on Γ_u and Γ_t respectively (Γ_u+Γ_t=Γ), hence there are only N unknowns in the system of equations (Eqn(1.14)). To introduce these boundary conditions into Eqn.(1.14) one has to rearrange the system by moving columns of **G** and **H** from one side to the other. Once all unknowns are passed to the left-hand side one can write,

$$\mathbf{AX} = \mathbf{F} \tag{1.15}$$

where **X** is a vector of unknowns u's and t's boundary values. **F** is found by multiplying the corresponding columns by the known values of u's and t's. It is interesting to point out that the unknowns are now a mixture of the u and the t, rather than u only as in FEM. This is a consequence of the boundary element being a *mixed* formulation. Eqn.(1.15) can now be solved and all the boundary values are then known.

The kernels of the integrals which appear in the influence matrices can be computed after discretization of the domain and collocation of the points. Integrals in H^{ij} and G^{ij} for the case i≠j can be calculated using numerical integration formulas since no singularity exists. When the collocation point is the node of the integration element; i.e. $i = j$, the singularity of the fundamental solution

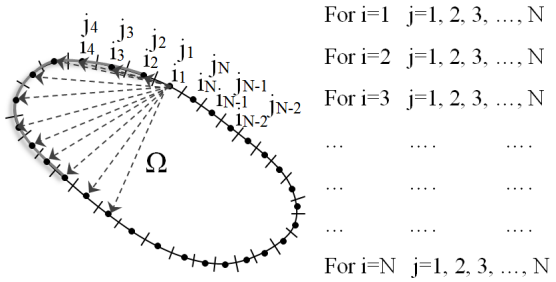

FIGURE 1.4: Collocation technique

demands special handling. However, strongly singular integrals arise only for H^{ij} and only if the collocation point i coincides with one of the element nodes.

Internal points

Once the boundary values are known it is possible to calculate any internal value of u or its derivative t by the following equation:

$$u^i = \sum_{j=1}^{N} G^{ij} t^j - \sum_{j=1}^{N} H^{ij} u^j \tag{1.16}$$

Notice that now the fundamental solution is considered to be acting on an internal point i and that all values of u and t at the boundary are already known. The coefficients **G** and **H** have to be calculated anew for each different internal point. No singularity exists on the integrals along the boundary elements when u or t are being calculated at internal points.

All the above mentioned description of the BEM technique can be summarized in a flowchart, see Fig.1.5 and can be programmed with the aid of any programming language without demanding very high computational capacity.

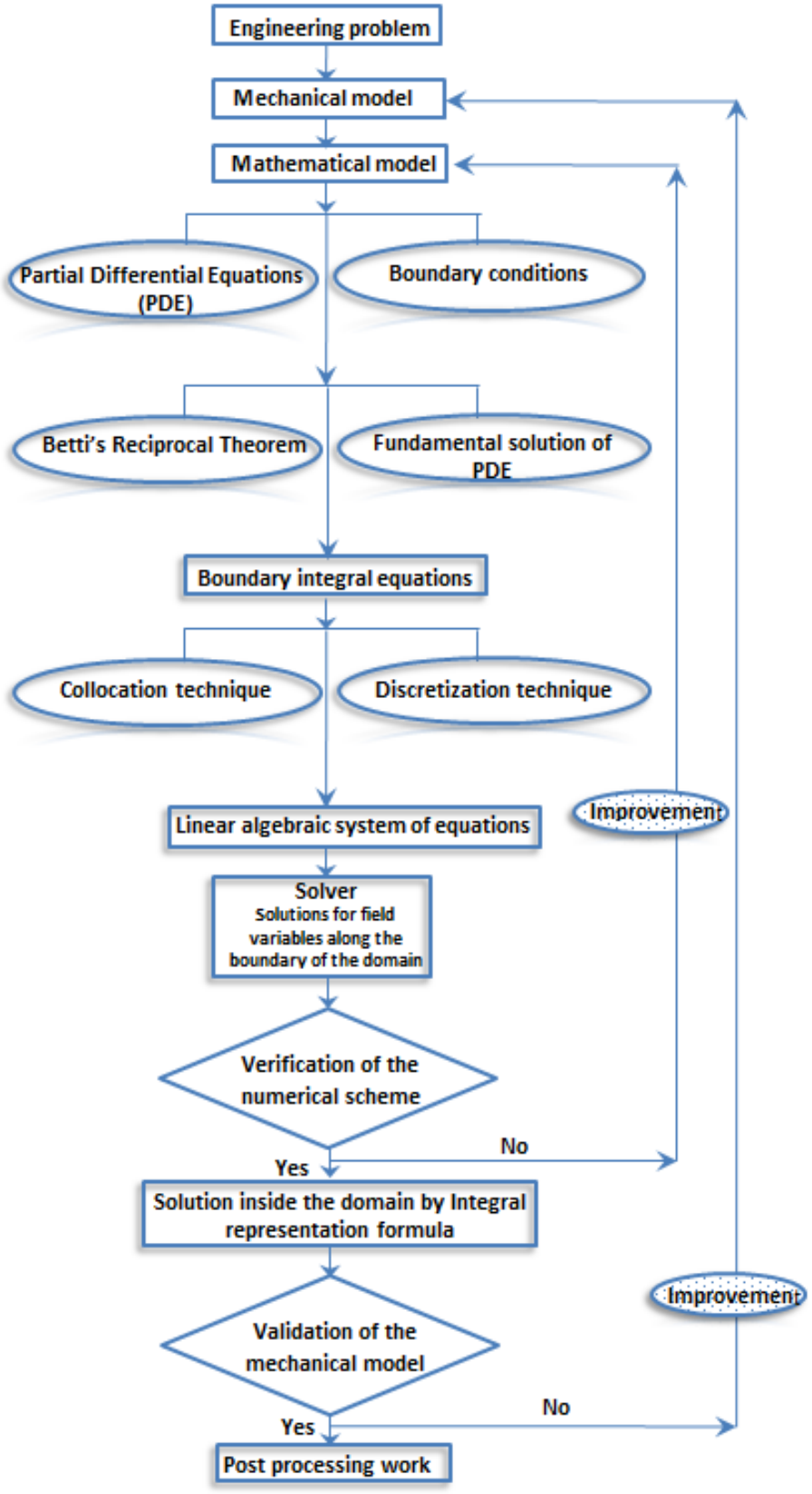

FIGURE 1.5: The BEM flowchart

Chapter 2

State-of-the-art: Wave propagation in inhomogeneous media via BEM

2.1 Introduction

The earth is strongly inhomogeneous (with varying material properties) and heterogeneous due to different types of inclusions, both in vertical and lateral direction. The Earth's varying surface geology as topography, faults, alluvial basins, cavities, tunnels, pipelines, foundations, etc., may produce significant spatial variations on seismic ground motions that can lead to large amplifications during earthquakes. Knowledge on local site effects has been historically improved due to the parallel advances in experimental and theoretical study of this phenomenon which demonstrates a remarkable complexity. The quantitative prediction of strong ground motion at a given site involves dealing with the source of seismic waves, their path to the site and the effects of local site conditions. The present thesis concerns the development of a numerical model for site effects based on BEM taking into consideration the specific characteristics of all three constituents: the seismic source, the wave path and the local site conditions, accounting for both soil inhomogeneity and heterogeneity. A way of shedding some light on the understanding of the site-response phenomena consists in developing of high-performance methods for the simulations of the seismic wave propagation in a complex media with position dependent material characteristics and with existence of different types of heterogeneities.

In general, four BEM formulations in elastodynamics are known: (a) **time-domain BEM** see [44–46] for 2D problems and [22, 47–52] for 3D problems. The

first direct time-domain BEM formulation was presented by Friedman and Shaw [53]; (b) **frequency or Laplace domain BIEM** that uses the fundamental solution in the Fourier or Laplace form, see [22, 23, 54]; (c) **dual reciprocity BEM** which is based on the fundamental solution of elastostatics, see [55–57]; (d) **time domain based on the Convolution quadrature method** proposed by Schanz and Antes [58, 59]. The last case does not require a time domain fundamental solution and avoids very sensitive forms of fundamental solutions, which may yield to not very stable results. The analysis is carried out with Laplace fundamental solution. This approximation is based on the operational quadrature method [60, 61], in which the convolution integrals are substituted by a quadrature formula, whose weights are computed using the Laplace transform of the fundamental solution and a linear multi step method. The final solution of the problem is obtained in the time domain.

For all the above mentioned BEM formulation a fundamental solution of the governing equation of motion is required. The notion of a fundamental solution gradually became clearer during the 19th and 20th century. At the beginning it was only that fundamental solutions can be applied - via the convolution of distributions - to the solution of linear partial differential equations with constant coefficients. The transient point-force solution of the elastodynamic equation for homogeneous isotropic media was found by Stokes [62]. This well-known solution, known as the elastodynamic fundamental solutions for homogeneous isotropic and unbound media, plays a fundamental role in elastodynamics.

The mechanical sense of the fundamental solution $g(x, t, y, \tau)$ is the response at observation point x at observation time t due to unit body force at source y at time τ. Note here the difference in the terms fundamental solution and Green's function. The term fundamental solution is used only for the solution of a differential equation with Dirac-function on the right-hand side and the term Green's function means the fundamental solution which additionally satisfies the corresponding boundary conditions. The Green's function, if exists, is unique. The fundamental solution is not unique and is determined up to a function which solves the differential equation with zero on the right-hand side. For more sophisticated region, specific Green's function can be used, less unknown boundary data appear in the representation integral, fewer elements and associated approximations would be needed with the discretization process, and accuracy would be higher. The Green's functions usually have not be known, except for relatively simple geometry (usually half-plane). This is perhaps the main reason why the most of the BEM papers are based on the fundamental solution, not on the Green's function. A detail review of the fundamental solutions and Green's functions in elastodynamics can be found in Kausel [63]. The most of the fundamental solutions are derived by the Fourier, Laplace or Radon transforms.

According to [64] when fundamental solution is used, the truncation of the infinite boundaries influences both the solutions along the boundaries and inside the domain. However, it is also shown that this truncation has smaller effect on the solutions along the boundaries and in opposite it has a big effect on the results inside the considered domain. When the BEM formulation employs a Green's function the CPU time increases in comparison with the case of a fundamental solution. The optimal way is to use in a hybrid way the BEM schemes based on both the fundamental solution and Green's function as follows: (a) use the BEM based on the fundamental solution and obtain solutions along boundaries, (b) use the BEM based on the Green's function when use the integral representation formulae in order to find solutions inside the domain.

In what follows an extended review is presented in the field of seismic wave propagation under assumption of out-of-plane and in-plane strain state via BEM in the following types of continua: (i) *continuously inhomogeneous soil media with constant velocity*, (ii) *continuously inhomogeneous soil media with variable velocity* (iii) *discrete inhomogeneous soil media with variable velocity* and (iii) *inhomogeneous soil media with heterogeneities*.

The state of the art concerns two-dimensional problems for plane (or plane strain elasticity) and out-of-plane (i.e., anti-plane strain) elastic wave propagation. 2D elastodynamic problems in respect to a Cartesian coordinate system $Ox_1x_2x_3$ are defined as follows: (a) plane strain state (in-plane P- and SV- wave motion) in a plane $x_3 = 0$, where the only non-zero field quantities are displacements u_1, u_2, stresses σ_{11}, σ_{12}, σ_{22} and tractions $t_i = \sigma_{ij}n_j$, $i, j = 1, 2$ all dependent on coordinates $x = (x_1, x_2)$, where n_j is the outward pointing unit normal vector to the surface; (b) out-of-plane shear state (out-plane SH-wave motion) in respect to the plane $x_3 = 0$, where the only nonzero quantities are displacement u_3, shear stresses σ_{13}, σ_{23} and traction $t_3 = \sigma_{3j}n_j$, j=1, 2, all dependent on coordinates $x = (x_1, x_2)$.

2.2 Out-of-plane wave motion

Mathematically speaking, BVPs for continuously inhomogeneous media are described by partial differential equations with variable coefficients. Variable wave velocity implies the derivation of fundamental solutions for differential operators of variable coefficients. General differential operators with variable coefficients do not necessarily have fundamental solutions [65]. In the following short review are presented the obtained in the literature results concerning the analytically derived fundamental solutions for materials with position dependent properties and the concrete BEM formulations and solutions based on these fundamental solutions. Three main categories of BEM results can be distinguished: (i) BEM formulations

based on Green's functions for stratified half-plane; (ii) BEM formulations based on Green's functions or fundamental solutions of equations of motion for media with material properties varying as continuous functions with respect to the depth in one and the same manner and in this case the phase velocity remains constant; (iii) BEM formulations based on Fundamental solutions of equations of motion for media with continuous variation of density and shear modulus, in a different way that leads to a velocity gradient.

2.2.1 Continuously inhomogeneous soil media with constant velocity

In this category the available in the literature frequency dependent fundamental solutions are for exponential and trigonometric variation of material properties in [66, 67]. Time-dependent fundamental solutions are also developed for the case of exponential and trigonometrical variation of both density and shear modulus in [67]. In Rangelov and Manolis [40] are derived two frequency-dependent Green's functions in the frequency domain for a half-plane with exponential and quadratic variation of density and stiffness. BEM formulations and solutions based on the fundamental solution for exponential and trigonometric variation of material properties are presented by Daros [37]. The above literature review is presented in Table 2.1.

	Type of model	**References**
Fundamental solution in time domain	exponential, trigonometric	Daros (2008)
Fundamental solution in frequency domain	exponential	Manolis et al. (2012)
	exponential, trigonometric	Daros (2008)
Green's function in frequency domain	exponential, quadratic	Rangelov and Manolis (2014)
BEM in frequency domain	exponential, trigonometric	Daros (2010) direct traction BEM based on f.s. from Daros (2008)

TABLE 2.1: Fundamental solutions, Green's functions for half-plane and BEM realizations for elastic continuously inhomogeneous continua with constant velocity profile under out-plane wave motion.

2.2.2 Continuously inhomogeneous soil media with variable velocity

In this category of inhomogeneous media where the velocity gradient is taken into account, available fundamental solutions can be found for the following limited cases of velocity profiles: (a) linear velocity profile with time-dependent fundamental solutions is considered in Watanabe [68], Watanabe and Payton [69], Daros [67, 70], Sanchez-Sesma et al. [71], frequency-dependent fundamental solutions are available in Watanabe and Payton [69], Daros [67, 70], Sanchez-Sesma et al. [71]; (b) power function velocity profile with time-dependent fundamental solutions are derived in Daros [67, 70] and Watanabe and Payton [69] and frequency dependent fundamental solution can be found in Watanabe and Payton [69], (c) variable velocity profile depending on shear modulus and density, varying in a different manner, with frequency dependent fundamental solution is considered in Manolis and Shaw [41, 42] and in Karakostas and Manolis [72]. Mechanical models for seismic wave propagation in continuously inhomogeneous media with position dependent phase velocity are solved via BEM in the following papers. Luzon et al. [38, 39] used indirect BEM based on the fundamental solution of Sanchez-Sesma et al. [71] to solve the anti-plane wave motion problem in frequency and in time domain for an inhomogeneous alluvial basin, resting on homogeneous half-plane, with linear velocity profile in arbitrary direction (Luzon et al. [38]) and in respect to the depth (Luzon et al. [39]). Ge [32] solved the same problem as in Luzon et al.[39] with the same fundamental solution, but by the direct BEM. A short summary of the existing studies in this group is presented in Table 2.2.

2.2.3 Discrete inhomogeneous soil media

In this model the material properties vary in a discrete way by considering the half-plane as horizontally stratified media, i.e. half-plane is presented by a stack of homogeneous layers with horizontal interfaces rested on seismic bed. In this group exist a lot of results among them are the frequency dependent Green's functions for stratified half-plane derived analytically in [16, 17, 34, 73–80]. The direct BEM formulation and solution in frequency and time domain based on the Green's function for a stratified half-plane is presented in [16, 17, 31, 34, 35].

2.2.4 Inhomogeneous media with heterogeneities

The presence of heterogeneities like cracks, cavities, inclusions, layers, topographic peculiarities, underground structures, etc. in the inhomogeneous background presents a new set of difficulties, since wave signals travel through heterogeneous geological structures causing reflection, refraction, diffraction and scattering phenomena. The difficulties arise not only due to the complexity of the mechanical

	Type of the velocity profile	References
Fundamental solution in time domain	linear	Watanabe (1982) Daros (2008)-anisotropic
	linear function of depth (Cartesian c.s.) power function of radial distance (Polar c.s.)	Watanabe and Payton (2004)
	power function and linear of one space variable	Daros (2013)-anisotropic
	linear	Sanchez-Sesma et al. (2001)
Fundamental solution in frequency domain	linear function of depth (Cartesian c.s.) power function of radial distance (Polar c.s.)	Watanabe and Payton (2004)
	linear	Daros (2008)-anisotropic Sanchez-Sesma et al. (2001) Luzon et al. (2009)
	linear in depth	Luzon et al. (2004) indirect BEM based on f.s. from Sanchez-Sesma et al. (2001)
	variable (depth dependent described by a special frequency dependent relation)	Manolis and Shaw (1996a, 1996b) Karakostas and Manolis (1997)
BEM in time domain	linear in arbitrary direction	Luzon et al. (2003) indirect BEM based on f.s. from Sanchez-Sesma et al. (2001)
BEM in frequency domain	linear in depth	Luzon et al. (2003) indirect BEM based on f.s. from Sanchez-Sesma et al. (2001)
	linear in arbitrary direction	Luzon et al. (2003)-indirect BEM Ge (2010)-direct BEM

TABLE 2.2: Fundamental solutions, Green's functions for half-plane and BEM realizations for elastic continuously inhomogeneous continua with velocity profile under out-plane wave motion.

model, but also due to the complexity of the mathematical model describing the discussed above phenomena via partial differential equations with variable coefficients. It exists only two examples in the literature which are restricted to heterogeneities with simple geometry; (i) in Daros [37] where direct BEM is applied in order to consider a single anti-plane crack in infinite exponentially inhomogeneous (phase velocity is constant) plane subjected to time-harmonic SH wave and (ii) in Luzon et al. [81] by indirect BEM and in Ge [32] by direct BEM based on the fundamental solution derived by Sanchez-Sesma et al. [71] in order to examine wave motion in a sedimentary alluvial valley with semi-circular shape, linear velocity profile and rested in a homogeneous half-plane.

2.3 In-plane wave motion

For the shake of completeness, in the present section a short review is presented in the field of seismic wave propagation under assumption of plane strain state (in-plane wave motion) in the following types of continua: (i) *continuously inhomogeneous soil media with constant velocity*, (ii) *continuously inhomogeneous soil media with variable velocity* (iii) *discrete inhomogeneous soil media* and (iv) *inhomogeneous soil media with heterogeneities*. The focus is on the following computational

tools developed for solution of the problems mentioned above: (i) BEM formulations based on Green's functions for stratified half-plane; (ii) BEM formulations based on Green's for variable material properties and constant phase velocity; (iii) BEM formulations based on fundamental solution for variable material properties and variable phase velocity.

2.3.1 Continuously inhomogeneous soil media with constant velocity

In this group where the material properties vary proportionally and the phase velocity remains constant, the available in the literature frequency dependent fundamental solutions are for the following types of material gradient: (a) fixed Poisson's ratio v=0.25 and quadratic variation in respect to the depth of the rest material properties, see Manolis et al. [82], Dineva et al. [83], Rangelov et al. [84]; (b) exponential variation of the material properties, see Rangelov et al. [84], Daros [85] and Dineva et al. [86]; (c) material gradient is of trigonometric type, see Rangelov et al. [84] and Daros [85]. BEM formulations and solutions based on the fundamental solutions or Green's functions discussed above one can find only in Dineva et al [36] where site effects due to exponentially and quadratically inhomogeneous wave path by direct BEM in frequency domain are studied. The above literature review is presented in Table 2.3.

	Type of the model	**References**
Fundamental solution in frequency domain	quadratic	Manolis et al. (2004) Dineva et al. (2006)
	quadratic, exponential, trigonometric	Rangelov et al. (2005) anisotropic
	exponential, trigonometric	Daros (2009) transversely isotropic
	exponential	Dineva et al. (2007)
BEM in frequency domain	quadratic, exponential	Dineva et al. (2008) direct BEM

TABLE 2.3: Fundamental solutions, Green's functions for half-plane and BEM realizations for elastic continuously inhomogeneous continua with constant velocity profile under in-plane wave motion.

2.3.2 Continuously inhomogeneous soil media with variable velocity

In this category where velocity gradient is considered, available fundamental solutions can be found for geological media with linear velocity profile, see Hook [87], Watanabe and Takeuchi [88] and Sanchez-Sesma [71], where fundamental solutions in time domain are derived, while fundamental solutions in frequency domain for the same case are available in Watanabe and Takeuchi [88], Sanchez-Sesma et al. [71] and Luzon et al. [81]. BEM scheme for this category is developed only in the paper of Luzon et al. [81] where indirect BEM based on the frequency dependent fundamental solution of Sanchez-Sesma et al. [71] is presented. For a short summary of the previous studies see Table 2.4.

	Type of the velocity profile	**References**
Fundamental solution in time domain	linear	Hook (1962) Watanabe and Takeuchi (2002)
	linear with depth v=constant	Sanchez-Sesma et al. (2001)
Fundamental solution in frequency domain	linear	Watanabe and Takeuchi (2002)
	linear with depth v=constant	Sanchez-Sesma et al. (2001) Luzon et al. (2009)
BEM in time domain	linear in arbitrary direction	Luzon et al. (2003) indirect BEM based on f.s. from Sanchez-Sesma et al. (2001)
BEM in frequency domain	linear	Luzon et al. (2009) indirect BEM

TABLE 2.4: Fundamental solutions, Green's functions for half-plane and BEM realizations for elastic continuously inhomogeneous continua with velocity profile under in-plane wave motion.

2.3.3 Discrete inhomogeneous soil media

In this model the inhomogeneity is expressed by a stack of flat homogeneous layers rested on seismic bed. For this type of inhomogeneity one can find analytically derived frequency dependent Green's functions in [16–18, 34, 73–80, 89]. BEM formulations based on the aforementioned Green's functions are presented in [16, 17, 29, 34, 35].

2.3.4 Inhomogeneous media with heterogeneities

The combination of an inhomogeneous background and the presence of different types of heterogeneities creates a more complex wave field since wave signals no longer travel undisturbed, but are subjected to continuous amplitude changes and

phase angle shifts. It exists only one example in the literature from Luzon et al. [81] for in-plane time-harmonic and transient wave motion in a sedimentary alluvial valley with semi-circular shape, linear velocity profile and rested in a homogeneous half-plane solved by indirect BEM based on fundamental solution derived in Sanchez-Sesma et al. [71].

2.4 Conclusions arising from the state of the art

The state of the art shows that there are few mechanical models available to construct numerical methods for evaluating the seismic response of continuously inhomogeneous geological region with a prescribed material gradient and additionally containing different types of heterogeneities such as non-parallel layers, cavities, inclusions, tunnels, free and subsurface relief of arbitrary geometry via BEM. Furthermore, models which have been already developed are restricted to either very simple geometry of the heterogeneities existing in the geological continuum or to the pure case of homogeneous media.

The main reason for this is the lack of fundamental solutions or Green's functions with relatively simple mathematical form that can be implemented easily in the existing BEM codes. In the most papers the inhomogeneity is presented in a discrete way by a stratified half-plane with homogeneous elastic isotropic flat layers. The existing Green's functions for a stratified half-plane are usually with complex mathematical form that prevents their easy implementation in the developed already for homogeneous case BEM codes.

The conclusions arising after evaluation of the state of the art in the research field under investigation motivate additionally the author to work for realization of the main idea formulated in the previous chapter. In particular, to develop an efficient package of knowledge consisting of mechanical models, computational techniques, verified research software and intensive simulations based on the BEM using a library of fundamental solutions and Green's functions for synthesis of seismic signals taking into account all three key parameters: seismic source, wave path and local site conditions.

Chapter 3

BEM for quadratically inhomogeneous geological media

The present chapter concerns the development and verification of a non-conventional BEM based on a closed form Green's function for continuously inhomogeneous in depth half-plane of quadratic type and constant velocity. The chapter is structured as follows: Statement of the problem; BEM formulation; Verification study; Parametric study and seismic signal synthesis. The proposed method can take into consideration the following key factors: (a) continuously inhomogeneous in depth half-plane; (b) lateral inhomogeneity in a local geological region due to relief peculiarities. Extensive numerical simulations are conducted which demonstrate the potential of the proposed tool to reveal the sensitivity of the seismic signal to the type and properties of the seismic source, to the existence and type of the material gradient and to the lateral inhomogeneity due to the free-surface and/or sub-surface relief peculiarities.

3.1 Statement of the problem

In a Cartesian coordinate system consider continuously inhomogeneous in depth half-space with free-surface relief in the form of a canyon V_{canyon} and sub-surface relief as a cavity V_{cavity} of arbitrary shape. The dynamic loads comprise either (a) an incident time-harmonic SH wave tracing an incident angle θ with respect to axis Ox_1 or (b) waves generated by an embedded seismic line source $F_3(x_0, t) = f_{03}g(t)\delta(x, x_0)$ with magnitude f_{03} and time function $g(t)$ located at $x_0(x_{01}, x_{02})$. The anti-plane deformation state is considered in the plane $x_3 = 0$, where is situated the half-plane $G = R^2_-/V$, here $R^2_- = \{x : x = (x_1, x_2), x_2 < 0\}$ and $V = V_{can} \cup V_{cav}$. Denote with S_{can} the boundary of the canyon, while S_2 is the part of the free surface line $x_2 = 0$ out of the canyon, so the boundary S is defined by $S = S_{can} \cup S_{cav} \cup S_2$, while the free surface boundary is $S_{free-surface} = S_{can} \cup S_2$.

The geometry of the problem is presented in Fig.3.1. Transient and time harmonic load with frequency ω is considered, where in the latter case $g(t) = e^{i\omega t}$. For the state of anti-plane wave motion, the only non-zero field quantities are displacement component u_3, stresses $\sigma_{i3} = \mu(x_2)u_{3,i}$ i=1,2 all depending on the coordinates (x_1, x_2) and on time t or frequency ω.

It is considered the case of small deformations and the material is elastic and isotropic. The conservation of linear momentum, i.e. the dynamic equilibrium equation is as follows:

$$\sigma_{i3,i}(x,\omega) = \begin{array}{c} \varrho(x_2)\dfrac{\partial u_3^2}{\partial t} - \psi F_3(x_{01}, x_{02}, t)\ for\, transient\, load \\ -\varrho(x_2)\omega^2 u_3(x,\omega) - \psi F_3(x_{01}, x_{02}, \omega)\ for\, time-harmonic\, load \end{array} \tag{3.1}$$

Where $\psi = 0$ when the seismic load is presented by the incident wave, $\psi = 1$ when the seismic load is wave radiating from an embedded seismic source, $\varrho(x_2)$, $\mu(x_2)$ are density and shear modulus, comma subscripts denote partial differentiation with respect to the spatial coordinates, while the summation convention over repeated indices is implied.

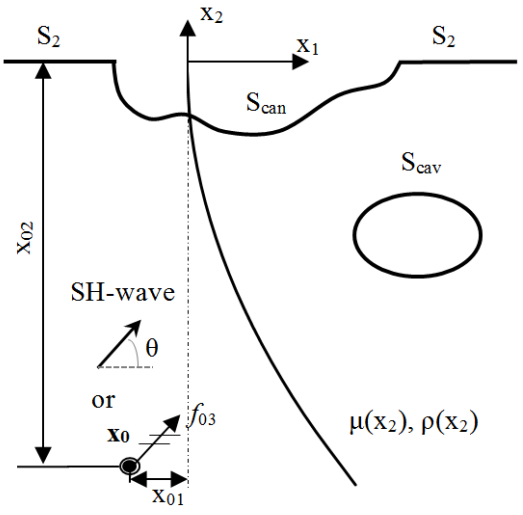

FIGURE 3.1: The problem geometry

The boundary value problem for the graded geological media is defined by the partial differential equation Eqn.(3.1) with variable coefficients depending on the depth and the following boundary conditions:

$$t_3(x) = 0\ for (x_1, x_2) \in S \tag{3.2}$$

where $t_3 = \sigma_{i3} n_i$ is the traction and $n(n_1, n_2)$ is the outward normal vector to the boundary S. Additionally the Sommerfeld radiation condition is satisfied at infinity.

The solution of the problem for transient waves is solved by the usage of the following well-known numerical procedure, see Chaillat et al. [90]: (a) Fast Fourier Transform (FFT) is applied to governing equations and the corresponding boundary-value problems in frequency domain are solved by BEM based on the frequency dependent fundamental solution/Green's function for discrete values of frequencies; (b) inverse Fast Fourier Transform (IFFT) is applied to the solutions in frequency domain and finally solutions in time-domain are determined.

Inhomogeneity

The geological profile is presented with material characteristics expressed by continuous and smooth functions of depth:

$$\begin{array}{ccc} \mu(x_2) = \mu_o h(x_2) & and & \varrho(x_2) = \varrho_o h(x_2) \\ h(x_2) = (bx_2 + 1)^2, & b \leq 0, h \leq 0 & \end{array} \tag{3.3}$$

here h(x) is the inhomogeneity function of a quadratic type and b is the inhomogeneity coefficient, i.e. the inhomogeneity magnitude. For the value $b = 0$, Eqn.(3.3) reflects the homogeneous case. According to this type of inhomogeneity the material properties vary proportionally and the phase velocity remains constant. Both parameters μ_o and ϱ_o represent the reference constant values taken at the traction free surface of the half-plane.

Free-field motion in quadratically inhom. in-depth half-plane

The free-field motion in the considered case is defined as the SH-wave propagation in elastic inhomogeneous in depth half-plane with flat free surface and without any type of heterogeneities. Analytical expression are derived in Rangelov and Dineva [91] and Manolis et al. [92] for the displacement at any observer point $x = (x_1, x_2)$ and traction on the segment ℓ with normal vector n, $x \in \ell$:

$$\begin{aligned} u_3^{ff}(x) &= U_{30}(bx_2+1)^{-1}\left[\tfrac{-b+ik\eta_2}{b+ik\eta_2} e^{ik(x_1\eta_1+x_2\eta_2)} + e^{ik(x_1\eta_1-x_2\eta_2)}\right] \\ t_3^{ff}(x) &= u_0\mu_0(bx_2+1)\left[\left(\frac{-b+ik\eta_2}{b+ik\eta_2} e^{ik(x_1\eta_1+x_2\eta_2)} + e^{ik(x_1\eta_1-x_2\eta_2)}\right) ik\eta_1 n_1\right. \\ &- b(bx_2+1)^{-1}\left(\frac{-b+ik\eta_2}{b+ik\eta_2} e^{ik(x_1\eta_1+x_2\eta_2)} + e^{ik(x_1\eta_1-x_2\eta_2)}\right)\eta_2 \\ &+ \left.\left(-\frac{-b+ik\eta_2}{b+ik\eta_2} e^{ik(x_1\eta_1+x_2\eta_2)} + e^{ik(x_1\eta_1-x_2\eta_2)}\right) ik\eta_2 n_2\right] \end{aligned} \tag{3.4}$$

where $\eta = (\eta_1, \eta_2) = (cos\theta, sin\theta)$ is the vector of the wave propagation direction, $k = \omega\sqrt{(\varrho_o/\mu_o)}$ is the wave number and U_{30} is the unit amplitude.

3.2 BEM formulation

The boundary-value problem defined by Eqns.(3.1), (3.2) is solved by BEM based on the integral representation formula and frequency dependent Green's function for inhomogeneous in depth half-plane, see Dominguez [23] and Manolis and Beskos [22]. Note, that because the problem is linear, the superposition principal is applied. In particular, the total wave field at any point in the half-plane is a superposition of the free-field motion (u_3^{ff}, t_3^{ff}) and scattered wave field (u_3^{sc}, t_3^{sc}), i.e. $u_3 = u_3^{ff} + u_3^{sc}$ and $t_3 = t_3^{ff} + t_3^{sc}$. Along the free surface the total traction is equal to zero, $t_3 = 0$ so $t_3^{sc} = -t_3^{ff}$

For the case of incident time-harmonic SH wave propagating under incident angle θ and with frequency ω, the scattered wave displacement along the boundary of both heterogeneities canyon and cavity $S = S_{can} + S_{cav}$ can be described by boundary integral Eqn(3.5). Once having solution of Eqn(3.5), the total wave field is obtained as sum of the scattered and free-field motion quantities. For the case of wave radiating from an embedded seismic source located at point x_0 in the inhomogeneous half-plane, the total wave displacement is expressed by Eqn.(3.6).

$$\begin{aligned} cu_3^{sc}(x,\omega) = &-\int_S t_3^{g^*}(x,\xi,\omega)u_3^{sc}(\xi,\omega)dS \\ &-\int_S g_3^*(x,\xi,\omega)t_3^{ff}(\xi,\omega)dS; \quad x\in S \end{aligned} \tag{3.5}$$

$$cu_3(x,\omega) = -\int_S t_3^{g^*}(x,\xi,\omega)u_3(\xi,\omega)dS + f_{03}g_3^*(x,x_0,\omega); \quad x\in S \tag{3.6}$$

where x and ξ are the vector-positions of the source and field points respectively, c is the jump term depending on the surface geometry at the collocation point, $g_3{}^*$ is the frequency-dependent Green's function for quadratically inhomogenous in depth half-plane and $t_3{}^{g*}$ is its corresponding traction. Once having displacement along the boundary S one can find displacement and traction at any point in the half-plane by the well-known representation formulae.

$$\begin{aligned} u_3^{sc}(x,\omega) = &-\int_S t_3^{g^*}(x,\xi,\omega)u_3^{sc}(\xi,\omega)dS \\ &-\int_S g_3^*(x,\xi,\omega)t_3^{ff}(\xi,\omega)dS, \quad x\notin S \end{aligned} \tag{3.7}$$

The aim of the examined here boundary-value problem is to compute the seismic signal along the free-or sub-surface relief and to know strain-stress state at any point inside the quadratically inhomogeneous half-plane.

The novelty of the described here BEM formulation is the ability to model continuously inhomogeneous half-plane with an advanced generation of Green's function which makes the numerical scheme high accurate and mesh reducing. The proposed approach demands only the modeling of the free- or sub- surface relief, avoiding discretization of the free surface where the Green's function satisfies the boundary condition. In opposite the conventional boundary element method based on the fundamental solution requires discretization along the sub- surface as well as the whole free surface.

3.2.1 Green's function for quadratically inhomogeneous half-plane

The presented here non-conventional BEM formulation is based on the closed form frequency-dependent Green's function for quadratically inhomogeneous in depth half-plane, which is analytically derived in Rangelov and Manolis [40]. The aim of this section is to shortly present the derivation steps of this function. The Green's function is defined as the solution of the equation of motion under a point time-harmonic load $(L^b(u_3(x))\equiv\sigma_{i3,i}(x) + \varrho(x)\omega^2 u_3(x) = 0)$ that satisfies the traction free boundary condition along the free-surface of the half-plane. Additionally it satisfies the Sommerfeld radiation condition at infinite. The Green's function is the solution of the following boundary value problem:

$$\begin{aligned} &L^b(g_3^*) = -\delta(x-\xi) \quad for \quad x,\xi \in R^2_- \\ &t_3^{g^*} \mid_{x_2=0} = 0 \end{aligned} \tag{3.8}$$

here $x(x_1, x_2)$ is the field point, $\xi(\xi_1, \xi_2)$ is the source point, $\delta(x, \xi)$ is Dirac's delta function. The derivative of the Green's function with respect to the field point x defines the corresponding traction $t_3^{g*}(x, \xi) = \mu(x) g_3^*(x, \xi)\eta_i(x)$. The following steps should be realized for the analytical derivation of the Green's function and the corresponding traction for quadratically inhomogeneous half-plane:

1. Using the following algebraic transformation: $g_3^*(x, \xi) = h^{-1/2}(x) G_3^*(x, \xi)$ the partial differential equation with variable coefficients in Eqn.(3.8) is transformed into the partial differential equation with constant coefficients in respect to G_3^*, making the problem easier from the mathematical point of view:

$$L^b(g_3^*) = h^{-1/2} L^1(G_3^*) \tag{3.9}$$

$$L^1(G_3^*) = -h^{-1/2}(\xi)\delta(x-\xi) = \mu_0 G^*_{3,ii} + \varrho_0\omega^2 \, for \, x\xi \in R^2_- \tag{3.10}$$

$$\mu_0(-0.5h^{-1/2}h_{,2}G_3^* + h^{-1/2}G_{3,2}^*) \mid_{x_2=0} = 0 \tag{3.11}$$

2. Ask for solution of the BVP defined by Eqns.(3.9-3.11) in the form $G_3^*(x,\xi) = U(x,\xi)+W(x,\xi)$, where $U(x,\xi) = \frac{ih^{-1/2}(\xi)}{4\mu_0}H_0^{(1)}(kr)$ is the solution of Eqn.(3.9). Function $W(x,\xi)$ is a general solution of $L^1(W) = 0$ in R_-^2 that satisfies boundary condition expressed by Eq.(3.11) and it has the following form:

$$W(x,\xi) = \int_{i\zeta-\infty}^{i\zeta+\infty} D\frac{1}{\gamma}e^{\gamma(x_2+\xi_2)}e^{i\eta(x_1-\xi_1)}d\eta \tag{3.12}$$

where $\gamma = \sqrt{\eta^2 - k^2}$, $k = k_1 + ik_2$, $k_1^2 = \frac{\varrho_0\omega^2}{\mu_0}$. The kernel $D = D(\eta, \xi_2, b)$ is determined from the boundary condition by the following expression:

$$D(\eta,\xi_2,b) = -\frac{h^{-1/2}(\xi)}{4\pi\mu_0}\frac{\gamma+b}{\gamma-b} \tag{3.13}$$

3. Finally, applying the inverse algebraic transformation and passing k_2 to the limit 0, i.e. ζ=0, the Green's function has the following final form:

$$\begin{aligned} g_3^*(x,\xi) &= h^{-1/2}(\xi)h^{-1/2}(x)\left[\frac{i}{4\mu_0}H_0^{(1)}(k.r)\right. \\ &+ \left.\frac{1}{4\pi\mu_0}\int_{-\infty}^{\infty}\frac{\gamma+b}{\gamma(\gamma-b)}e^{\gamma(x_2+\xi_2)}e^{i\eta(x_1-\xi_1)}d\eta\right] \end{aligned} \tag{3.14}$$

The corresponding traction Green's function and its derivatives are as follows:

$$t_3^{g*}(x,\xi) = \mu(x)g_{3,i}^*(x,\xi)\eta_i(x)$$

$$\begin{aligned} g_{3,1}^*(x,\xi) &= h^{-1/2}(\xi)h^{-1/2}(x)\left[\frac{k}{4\mu_0}H_1^{(1)}(k.r)\frac{\partial r}{\partial x_1}\right. \\ &+ \left.\frac{1}{4\pi\mu_0}\int_{-\infty}^{\infty}\frac{\gamma+b}{\gamma(\gamma-b)}(i\eta)e^{\gamma(x_2+\xi_2)}e^{i\eta(x_1-\xi_1)}d\eta\right] \end{aligned}$$

$$\begin{aligned} g_{3,2}^*(x,\xi) &= Z_1\left[\frac{1}{4\mu_0}\int_{-\infty}^{\infty}\frac{\gamma+b}{\gamma(\gamma-b)}e^{\gamma(x_2+\xi_2)}e^{i\eta(x_1-\xi_1)}d\eta\right. \\ &+ \left. Z_2\,\frac{k}{4\mu_0}H_1^{(1)}(k.r)\frac{\partial r}{\partial x_2} + \frac{1}{4\pi\mu_0}\int_{-\infty}^{\infty}\frac{\gamma+b}{(\gamma-b)}e^{\gamma(x_2+\xi_2)}e^{i\eta(x_1-\xi_1)}d\eta\right] \end{aligned}$$

$$Z_1 = h^{-1/2}(\xi)(\tfrac{-1}{2}h^{-3/2}(x)\tfrac{\partial h}{\partial x_2}$$

$$Z_2 = h^{-1/2}(\xi)h^{-1/2}(x) \tag{3.15}$$

where $h = (bx_2 + 1)^2$, b<0, $r = \sqrt{(x_1 - \xi_1)^2 + (x_2 - \xi_2)^2}$, $H_0^{(1)}(z)$ 1-st Hankel of 0 order.

For the homogeneous case, i.e. when $b = 0$ the well-known, (see [93]) half-plane Green's function is recovered:

$$g_3^*(x, \xi) = \frac{i}{4\mu_0}[H_0^{(1)}(k.r) + H_0^{(1)}(k.r\prime)] \tag{3.16}$$

where $r\prime = \sqrt{(x_1 - \xi_1)^2 + (x_2 + \xi_2)^2}$

As can be seen, the Green's function and it's derivatives give solutions for the strain-stress wave field in a quadratically inhomogeneous in respect to the depth half-plane subjected to time-harmonic load. The above expressions show that this wave field depends on the following parameters: frequency of the dynamic load, references material constants, material gradient and the distance between the source and the observation points.

3.3 Verification study

The numerical scheme for solution of the boundary-value problem solved by the BEM using Green's function for inhomogeneous half-plane is based on discretization and collocation technique, see [22, 23]. Good convergence in numerical solution is achieved when the well-known accuracy condition is satisfied: $\lambda \geq 10 l_{BE}$, where λ is the wavelength and l_{BE} is the length of the boundary element. In case of constant boundary elements the jump term in Eqn.(3.5) and Eqn.(3.6) is $c = 0.5$. Two types of integrals appear after discretization: (a) regular integrals when the field point and the source point do not coincide; for the computation of these integrals is employed Gauss integration scheme for single integrals and Quasi Monte Carlo Method for integration of double integrals; (b) singular integrals when the field point coincide with the source point; singular integrals are with weak integrable singularity of lnr type and with strong singularity of $1/r$ type and all they are Cauchy principal value integrals. The singular integrals are solved analytically in a small vicinity of the singular point and numerically in the rest of the integration interval. After discretization, collocation and satisfaction of the boundary conditions, a system of linear algebraic equations is obtained with respect to the unknown field quantities along the boundary S. The described numerical scheme is for solution in frequency domain. The solutions in time-domain are obtained by the usage of FFT and IFFT technique. A source code has been developed using Matlab software [94] and in order to verify its accuracy, several test examples are solved and the results are compared against available analytical and/or numerical results [95].

3.3.1 Verification: Incident time-harmonic wave

Considering the fact that there are no results in the literature for quadratically inhomogeneous half-plane with different types of free-surface relief, the verification of the proposed methodology is done by test examples for homogeneous case, using the codes developed for inhomogeneous material, but working with zero inhomogeneous coefficient, i.e. $b = 0$.

As first test example a homogeneous elastic isotropic half-plane with semi-circular canyon with radius $a = 15m$ under incident SH-wave is studied, see Fig.3.2. The reference material properties are $\mu_0 = 123{\cdot}10^7 Pa$ and $\varrho_0 = 1230kg/m^3$. Normalized frequency is defined as $\eta = 2\mathrm{a}/\lambda_0$, where $\lambda = (2\pi/\omega)\sqrt{(\mu_o/\varrho_0)}$. This benchmark example was solved in Trifunac [4] by analytical solutions and in Hirai [96] by a time-dependent BEM formulation. Also solutions are obtained by conventional BEM based on the fundamental solution for the full plane and by non-conventional BEM based on the Green's function for quadratically inhomogeneous (with inhomogeneous coefficient $b = 0$) half-plane for the normal incident wave. Fig.3.3 a,b,c plots the surface displacement amplitude $|u_3|$ versus normalized distance x_1/a for the semi-circular canyon at a fixed value of frequency $\eta = 0.25$, $\eta = 0.75$ and $\eta = 1.25$. The discretization mesh consists of 13 constant boundary elements along the canyon, when BIEM based on Green's function is applied and 24 quadratic boundary elements along $S = S_1 \cup S_{can}$ when fundamental solution is inserted in the BEM. For all practical purposes, the BEM results are indistinguishable from those obtained by Trifunac and Hirai. Also solution obtained by BEM numerical scheme based on Green's function for the half-plane and the fundamental solution for the full plane are almost identical.

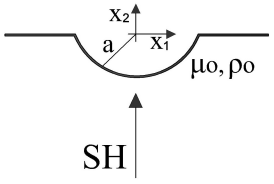

FIGURE 3.2: Geometry of test example 1: Homogeneous elastic isotropic half-plane with a semi-circular canyon with radius a under normal incident time-harmonic SH-wave

As second test example consider a homogeneous elastic isotropic half-plane with a triangle canyon under normal SH-wave, see Fig.3.4. Comparison of the results from the new developed method with solutions in Hirai [96], Sanchez-Sesma and Rosenblueth [97] which employ an analytical method based on Fredholm integral equation, and solutions obtained by the BEM based on fundamental solution for the full plane is presented in Fig.3.5 for $\eta = 0.25, 0.50, 1.00$ and $a = 15m$. The

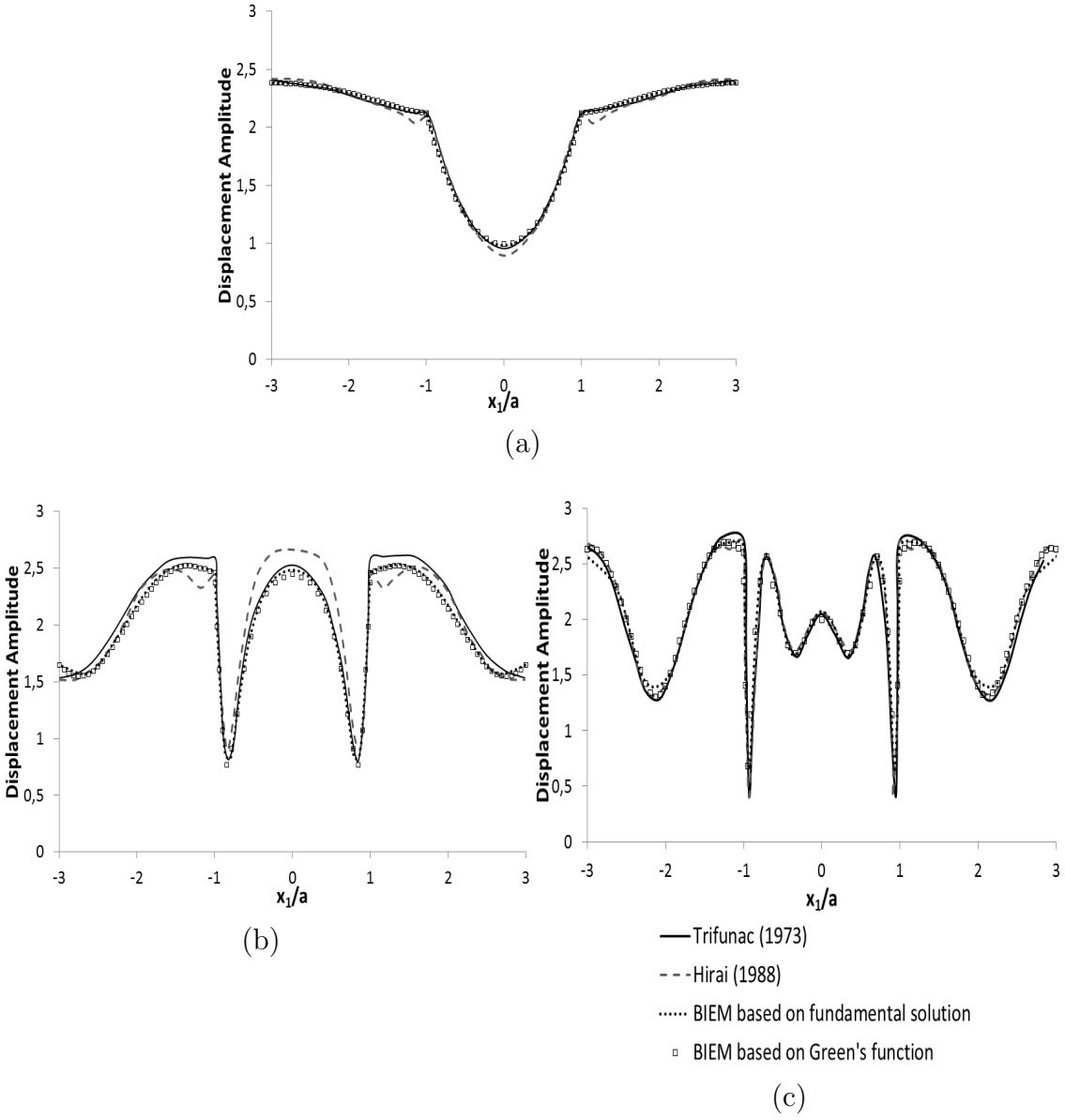

FIGURE 3.3: Displacement amplitude distribution along the free surface of homogeneous half-plane with a relief of semi-circular canyon: comparison of the present method with existing results in the literature and results obtained by BEM based on fundamental solution: (a) $\eta = 0.25$, (b) $\eta = 0.75$ and (c) $\eta = 1.25$

used BEM mesh consists of 12 constant and 24 quadratic boundary elements, when BEM based on Green's function and fundamental solution is applied, respectively. An excellent accuracy of the results obtained by the new developed BEM based on the Green's function is demonstrated.

The third test example solves the problem for seismic wave field in an elastic homogeneous half-plane with material properties $\mu_0 = 123{\cdot}10^7 Pa$ and $\varrho_0 =$

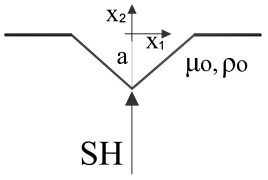

FIGURE 3.4: Geometry of test example 2: Homogeneous elastic isotropic half-plane with a triangle canyon under normal incident SH-wave

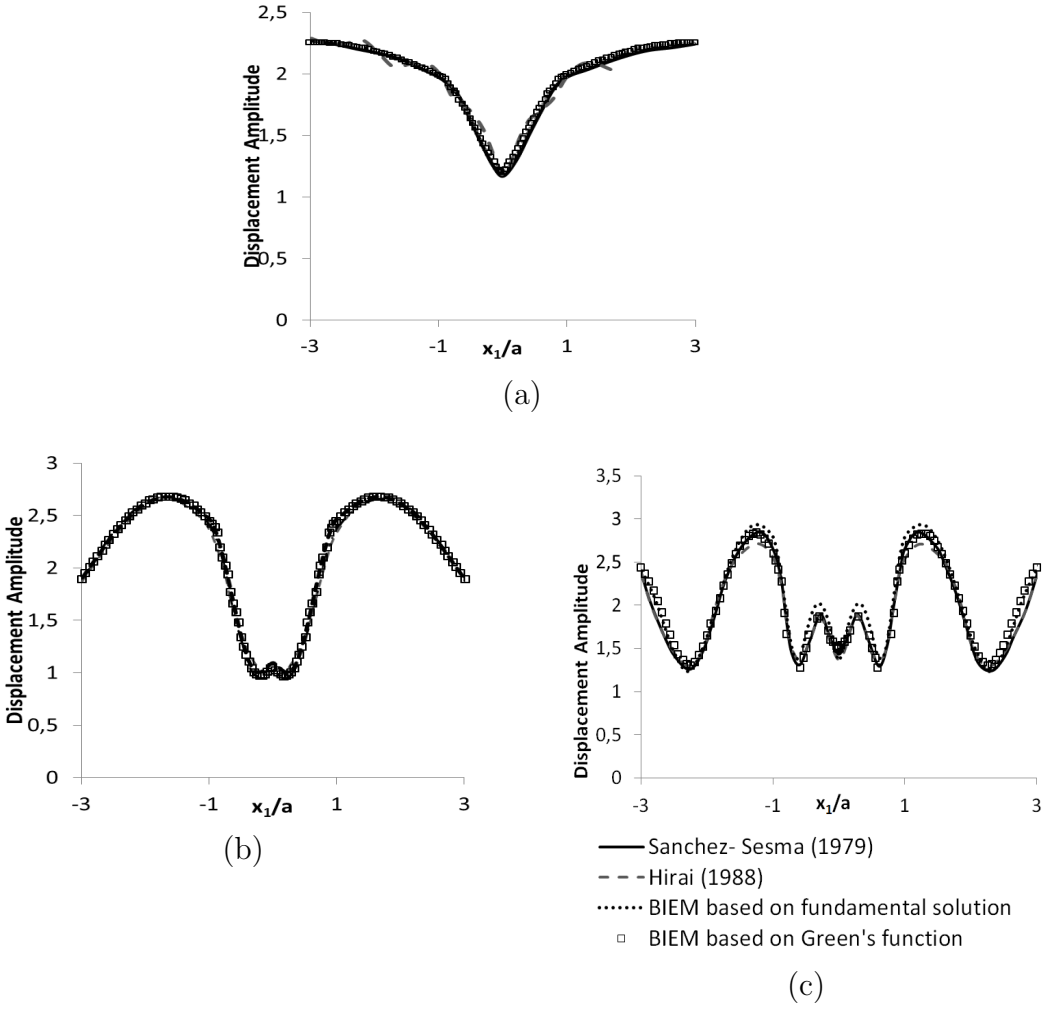

FIGURE 3.5: Displacement amplitude distribution along the free surface of homogeneous half-plane with a relief of triangle canyon: comparison of the present method with existing results in the literature and results obtained by BEM based on fundamental solution: (a) $\eta = 0.25$, (b) $\eta = 0.50$ and (c) $\eta = 1.00$

$1850kg/m^3$ containing an embedded circular cavity with radius a, with center coordinates $(a, -0.7a)$ and also containing a triangle canyon along the free surface, see Fig.3.6. The seismic load is presented by incident time-harmonic SH wave with a prescribed frequency ω and incident angle θ in respect to the coordinate axis Ox_1. Fig.3.6 compares BEM results obtained by fundamental solution and

Green's function with solutions obtained in Shah et al.[98] and in Ohtsu et al. [99]. A hybrid technique which combines a boundary integral representation with the FEM is used by Shah et al.[98] while Ohtsu et al. [99] employ indirect BEM. From Fig.3.6 it can be seen that all solutions are almost identical. The used BEM mesh consists of 24 along S_{can}, 22 along S_{cav} and 116 along the free surface S_2 constant boundary elements when fundamental solution is applied against 34 constant boundary elements along $S_{can} \cup S_{cav}$ when Green's function is employed.

Equivalence of continuous and discrete model: inhom. half-plane

In order to verify the developed method for the case of inhomogeneous half-plane, this section shows and discusses the equivalence of two mechanical models describing inhomogeneous in depth half-plane (without free surface relief) to time harmonic SH-wave. Consider continuously inhomogeneous in depth half-plane with reference material properties $\mu_0 = 180{\cdot}10^6 Pa$ and $\varrho_0 = 2000 kg/m^3$ expressing quadratic type of the material inhomogeneity and subjected to time-harmonic SH-wave with incident angle θ. The seismic signal is evaluated at any point in the half-plane, more especially along the free surface. The soil inhomogeneity in depth can be modeled by two different ways:

1. Model 1: material properties are continuous quadratic function of depth $\mu = \mu_o(bx_2 + 1)^2$ and $\varrho = \varrho_o(bx_2 + 1)^2$, see Fig.3.7(a). The solution for displacement and traction at any point in the considered half-plane is presented by the expressions for the free-field motion, see Eqn.(3.4).

2. Model 2: material properties vary in a discrete way and the inhomogeneity is presented by a stack of flat horizontal layers, where the material properties in each layer are elastic, isotropic and homogeneous, see Fig3.7(b). The boundary value problem describing this model consists of Eqn.(3.1) for the case when the dynamic load is incident time-harmonic wave, plus the following boundary conditions: (a) traction at the free surface is zero; (b) displacement compatibility and traction equilibrium conditions at the interfaces between each two horizontal layers; (c) modeling of the seismic bed by homogeneous half-plane with compatibility and equilibrium conditions for displacement and traction at the interface between the homogeneous and inhomogeneous part of the half-plane; (d) exclusion of incoming waves into the homogeneous part of the half-plane out of depth (seismic bed) in case of absence of a seismic source embedded in homogeneous half-plane (Sommerfeld radiation condition). The computation tool used for solution of the discrete model is wave number integration method (WNIM), see [18]. It is well known that this analytical technique allows the following relation between the seismic signals at the bottom of the geological profile with those at the top:

$$\begin{bmatrix} u_3(x_2 = x^{bottom}) \\ t_3(x_2 = x^{bottom}) \end{bmatrix} = D_N D_{N-1} \dots D_1 \begin{bmatrix} u_3(x_2 = x^{top}) \\ t_3(x_2 = x^{top}) \end{bmatrix}. \tag{3.17}$$

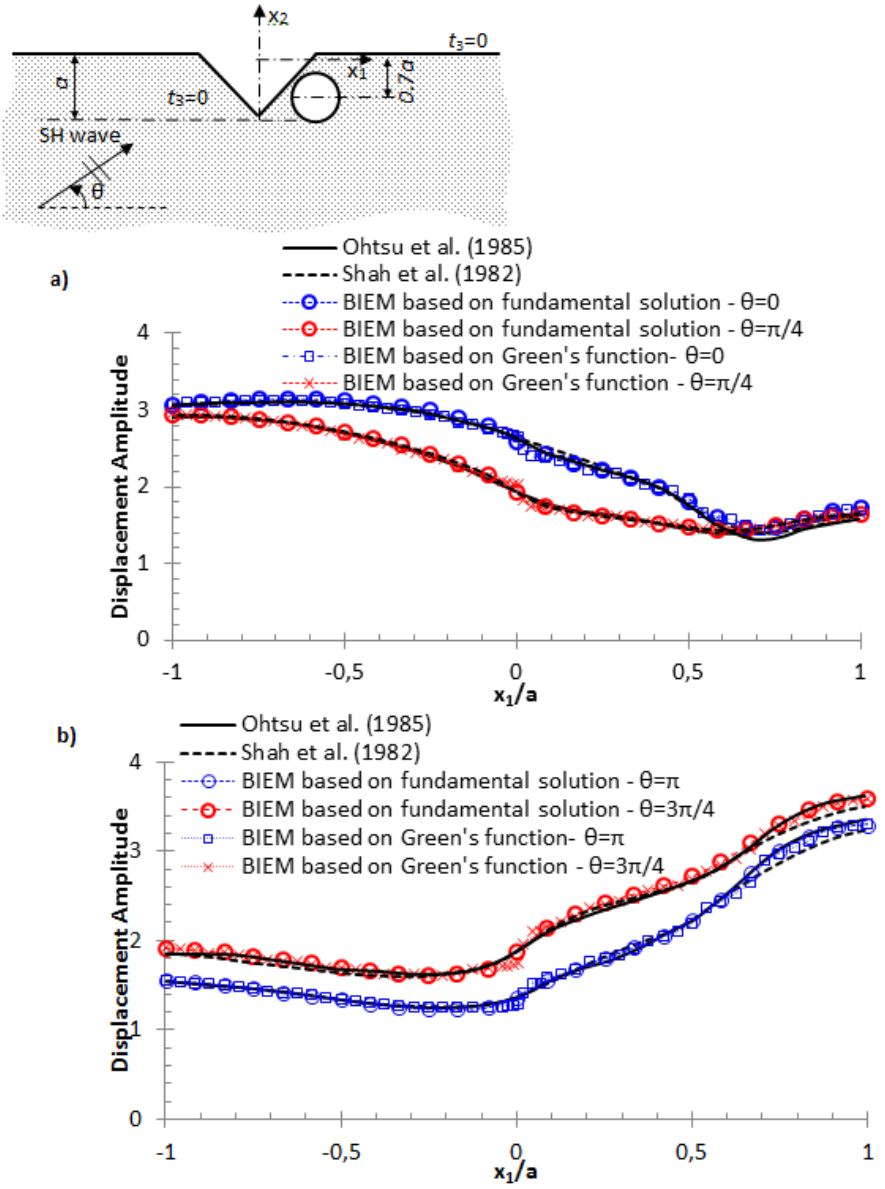

FIGURE 3.6: Displacement amplitudes along free surface of elastic homogeneous half-plane with triangular canyon and a circle cavity subjected to incident time-harmonic with non-dimensional frequency $\eta = 0.25$ SH-wave at incident angle : (a) $\theta = 0^o$; 45^o; (b) $\theta = 135^o$; $\theta = 180^o$. Comparison between solutions in Shah et al. (1982), Ohtsu et al. (1985) and BEM solutions obtained by fundamental solution and Green's function

Here $D_1, i = 1, 2, \ldots, N$ are the matrices depending on the SH–wave characteristics as incident angle θ, frequency ω and material properties for each one layer μ_i, ρ_i.

The aim is to solve this test example by using two different mechanical models accompanied by two different computational techniques based on Eqn.(3.4) and Eqn.(3.17) respectively. The equivalence of these two different approaches is shown

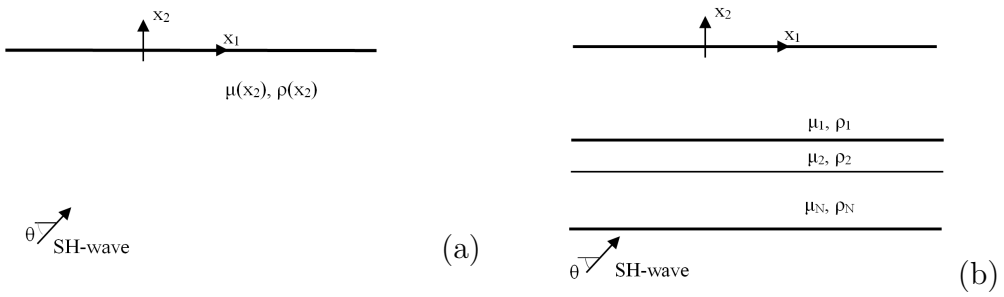

FIGURE 3.7: Inhomogeneous in depth half-plane: (a) Model 1: continuous variation of material characteristics; (b) Model 2: discrete variation of material characteristics

below. The key study parameter is the amplification factor defined as the ratio of the displacement at the free surface $x_2 = 0$ to the displacement at the bottom $x_2 = -100m$. Fig.3.8a,b,c,d show the variation of the material parameters with the depth of the geological profile at fixed inhomogeneity coefficients $b = -0.5$ and $b = -1.0$ in the following cases: (a) continuously in a quadratic way inhomogeneous profile; (b) discrete profile with 2 layers; (c) discrete profile with 10 layers; (d) discrete profile with 100 layers. Fig.3.9 and Fig.3.10 demonstrate evidently the equivalence between both mechanical models at a fixed value of frequency of 1Hz and at different values of the incident angle θ, when the number of discrete layers increases at two different inhomogeneity coefficients $b = -0.5$ (Fig.3.9) and $b = -1.0$ (Fig.3.10). Fig.3.11a,b,c,d depicts the amplification factor at frequency of $10Hz$ versus incident angle θ obtained by the usage of both discrete and inhomogeneous models at inhomogeneous coefficient $b = -1.0$. Note that in case of higher value of frequency, higher number of discrete layers can satisfy the equivalence of both approaches. While the excellent equivalence between both models at frequency of $1Hz$ is reached at 100 horizontal layers, in the case of $10Hz$ the 400 layers can satisfy the discussed equivalence.

Equivalence of continuous and discrete model: inhom. half-plane with free-surface relief

Equivalence of solutions obtained by the usage of two different models (discrete and continuously inhomogeneous) for half–plane with material properties varying in respect to depth and containing a semi–circular canyon under SH–wave is discussed.

Consider continuously inhomogeneous in depth half–plane with semi–circular canyon with radius $a = 15m$ subjected to time–harmonic SH–wave propagating under incident angle $\theta = \pi/2$, see Fig.3.12. The reference material properties are $\mu_0 = 180{\cdot}10^6 Pa$, $\varrho_0 = 2000kg/m^3$ and quadratic type of the material inhomogeneity is assumed. The inhomogeneous in depth geological region is described

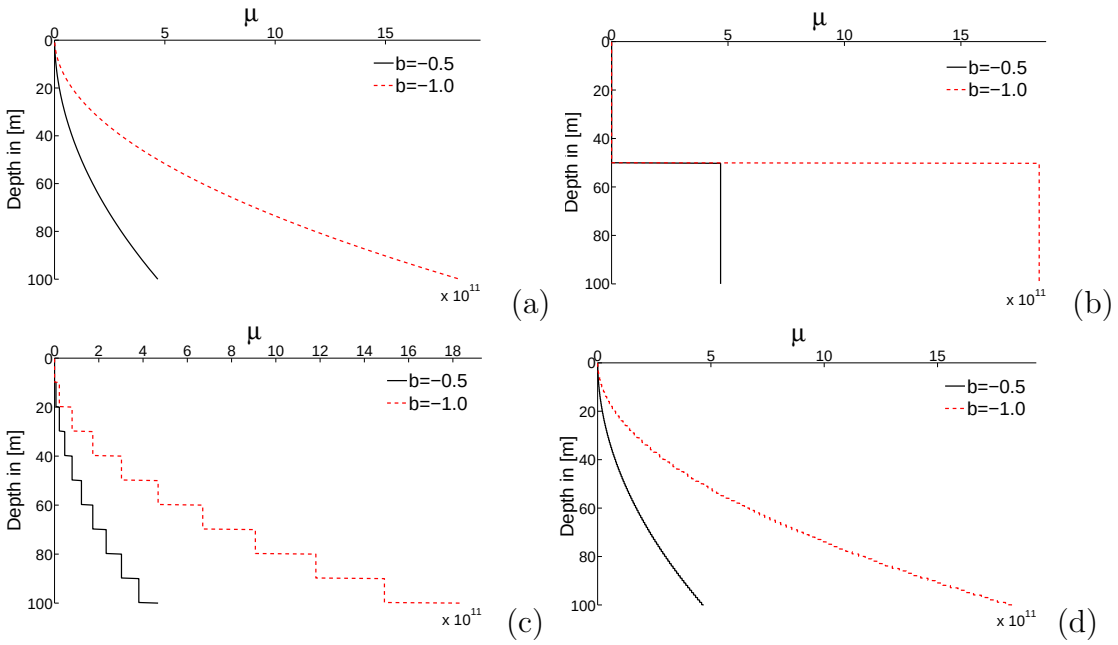

FIGURE 3.8: Variation of material properties in depth by: (a) continuously inhomogeneous profile; (b) discrete inhomogeneous profile with 2 layers; (c) discrete inhomogeneous profile with 10 layers; (d) discrete inhomogeneous profile with 100 layers

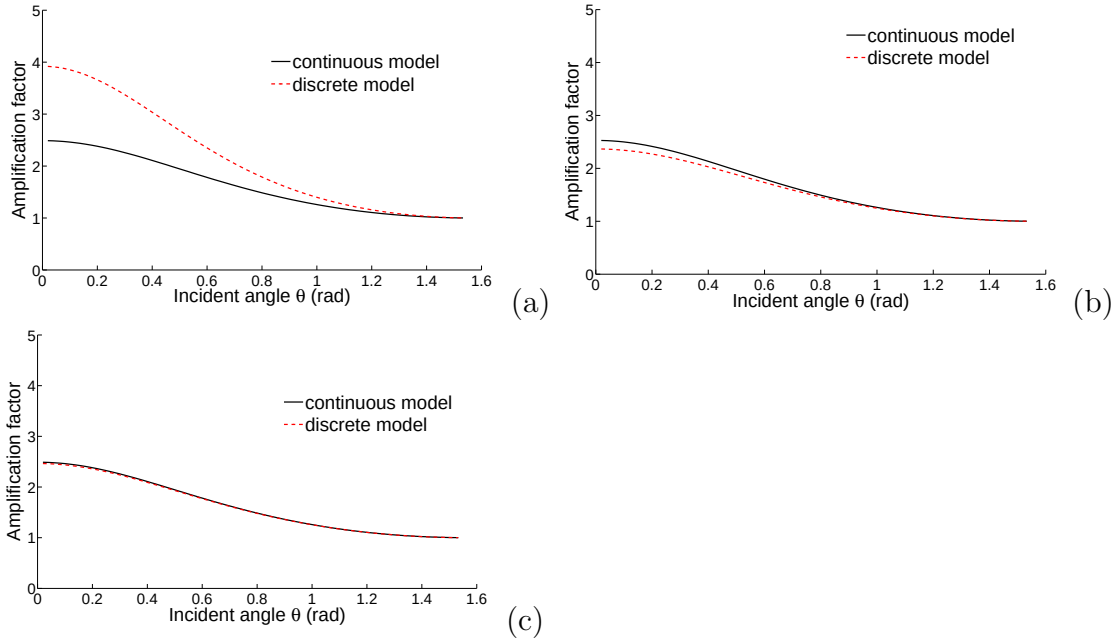

FIGURE 3.9: Amplification factor at $f = 1Hz$ versus incident angle obtained analytically by Eq.(3.4) and by WNIM for the case of inhomogeneous coefficient $b = -0.5$: (a) discrete model with 2 layers; (b) discrete model with 10 layers; (c) discrete model with 100 layers

by model 1 presented in Fig.3.12.a and model 2 shown in Fig.3.12.b. Two different computational techniques are applied. The boundary–value problem concerning model 1 (Fig.3.12a) is solved by the BEM based on the Green's function

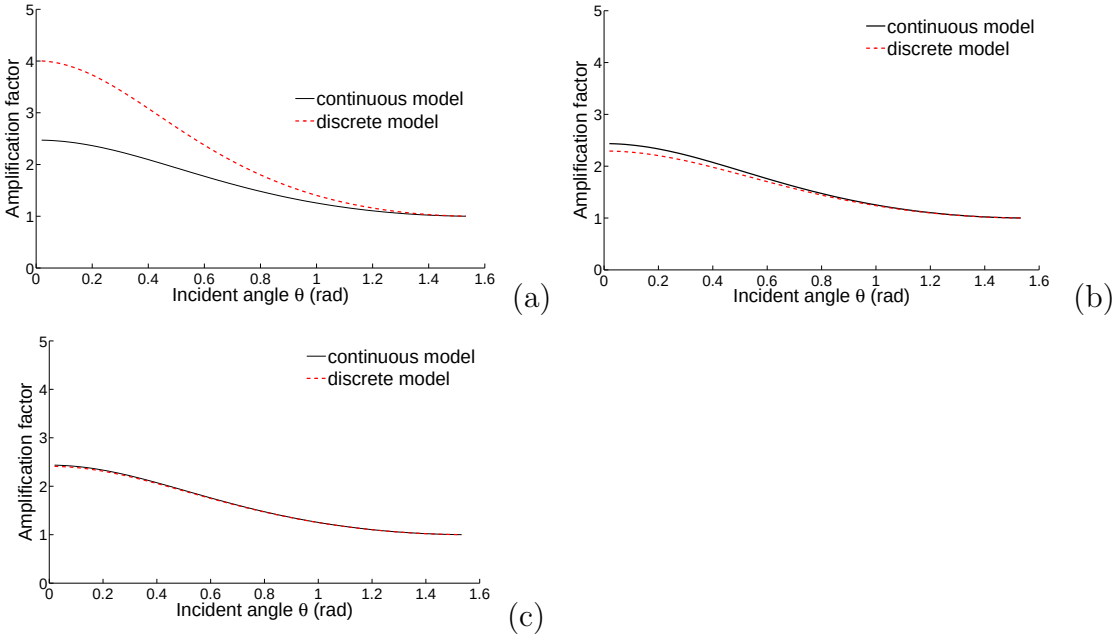

FIGURE 3.10: Amplification factor at $f = 1Hz$ versus incident angle obtained analytically by Eq.(3.4) and by WNIM for the case of inhomogeneous coefficient $b = -1.0$: (a) discrete model with 2 layers; (b) discrete model with 10 layers; (c) discrete model with 100 layers

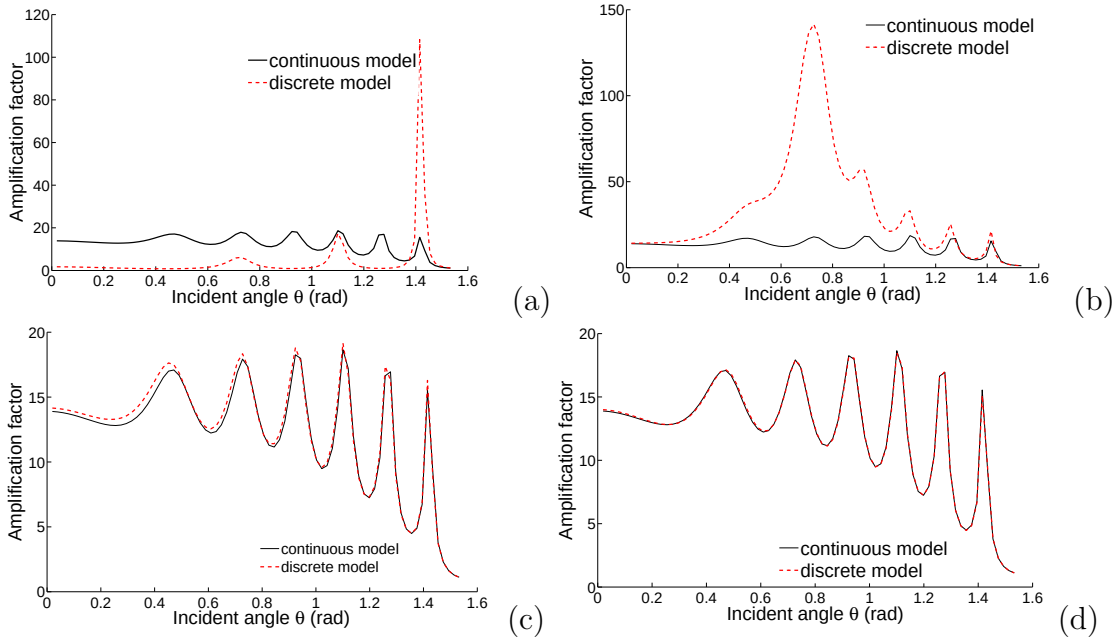

FIGURE 3.11: Amplification factor at $f = 10Hz$ versus incident angle obtained analytically by Eq.(3.4) and by WNIM for the case of inhomogeneous coefficient $b = -1.0$: (a) discrete model with 2 layers; (b) discrete model with 10 layers; (c) discrete model with 100 layers;(d) discrete model with 400 layers

for quadratically inhomogeneous in depth half–plane. Hybrid WNIM–BEM proposed in [27] is applied to treat the model 2 (Fig.3.12b). To compute the total

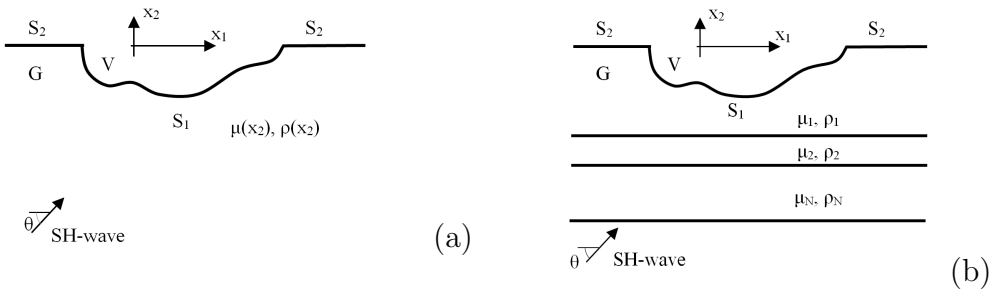

FIGURE 3.12: Inhomogeneous in depth half-plane with free surface relief: (a) Model 1: continuous variation of material characteristics; (b) Model 2: discrete variation of material characteristics

displacement at the canyon site, the following steps should be realized when the hybrid technique is applied: (1) determine by WNIM displacement due to free–field motion, defined in this case as wave field in the stratified half–plane without the canyon, see Figure 3.7b. Closed–form solution is available for the displacement along the points laying at the hypothetic canyon boundary S_1 in the geometry presented in Fig.3.12b; (2) determine by WNIM the tractions along the boundary S_1; (3) apply these tractions with opposite sign at the base of the canyon (boundary S_1) as a traction boundary condition and obtain the displacement $u_3^{sc}(x)$ along the free surface by the BEM using the classical fundamental solution of elastodynamics ([23]); (4) compute the total displacement by superposition of the wave fields obtained in steps 1 and 3, i.e. $u_3 = u_3^{ff} + u_3^{sc}$, $t_3 = t_3^{ff} + t_3^{sc}$. The hybrid WNIM-BEM is applied here for a stack of horizontal elastic isotropic homogeneous layers with a fixed number that satisfies the equivalence of the solutions for continuous inhomogeneous half–plane (Fig.3.7a) and horizontally layered half–plane (Fig.3.7b). The equivalence of the solutions along the free surface at frequency of $1Hz$ by using models presented in Fig.3.12a and Fig.3.12b is demonstrated by Fig.3.13 for inhomogeneity coefficient $b = -0.01666$ and for $b = -0.5$. This figure shows that hybrid WNIM–BEM applied for the geometry in Fig.3.12b gives the same results as the proposed here (Fig.3.12a) BEM based on the Green's function for inhomogeneous in depth half–plane.

The advantages of the BEM based on the Green's function in comparison with the hybrid WNIM–BEM technique are as follows: (a) the proposed here continuously inhomogeneous mechanical model and the developed and verified computational tool based on the non-conventional BEM avoids considering the horizontal interfaces in stratified half-plane and the only surface where the discretization is applied is the canyon's boundary; (b) the proposed here technique is semi-analytical because is based on the analytically derived Green's function for the continuously inhomogeneous in depth half-plane; (c) when hybrid technique is used, the backscattering phenomena are not take into consideration and this disadvantage of the hybrid approach is overcome by the proposed here non-conventional

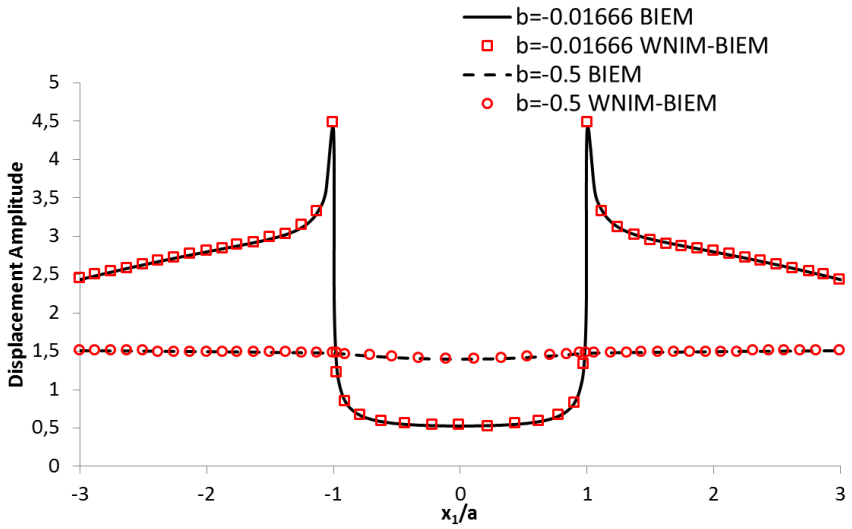

FIGURE 3.13: Displacement amplitude along the free surface of quadratically inhomogeneous in depth half–plane with $b = -0.01666$ and $b = -0.5$ containing a semi-circle canyon. Comparison of solutions obtained by hybrid WNIM–BEM applied for discrete model and BEM based on Green's function used for the continuous model

BEM; (d) the derived in a closed form Green's function has much simpler mathematical form than the Green's function derived by [15] or [16, 17] for the stratified half–plane; (e) The derived in a closed form Green's function satisfied the Sommerfeld's radiation condition and thus infinitely extended boundaries are automatically incorporated. This well-known benefit of the BEM gives a great advantage of the method in comparison with other numerical methods as FEM and FDM where special transmitting boundaries should be inserted in order to satisfy the radiation conditions at infinite.

3.3.2 Verification: Wave radiating from seismic source

Considering the fact that there are no results in the literature for quadratically inhomogeneous half-plane with embedded seismic source and with free- and subsurface relief peculiarities, the verification of the new numerical scheme is done by test examples for homogeneous case, using the codes developed for inhomogeneous material, but working with zero inhomogeneous coefficient, i.e. $b = 0$ [100]. Solution of wave propagation from a seismic source located at a point along the traction-free surface is given in Lamb [101]. The Lamb's analytical solution can be found in Achenbach [43]. The first test example concerns scenario of the Lamb's problem, see Fig.3.14, where it considers the wave field along the free surface of elastic homogeneous half-plane due to out of plane time-harmonic line seismic load acting at a point on the free-surface. Graphically this solution is illustrated

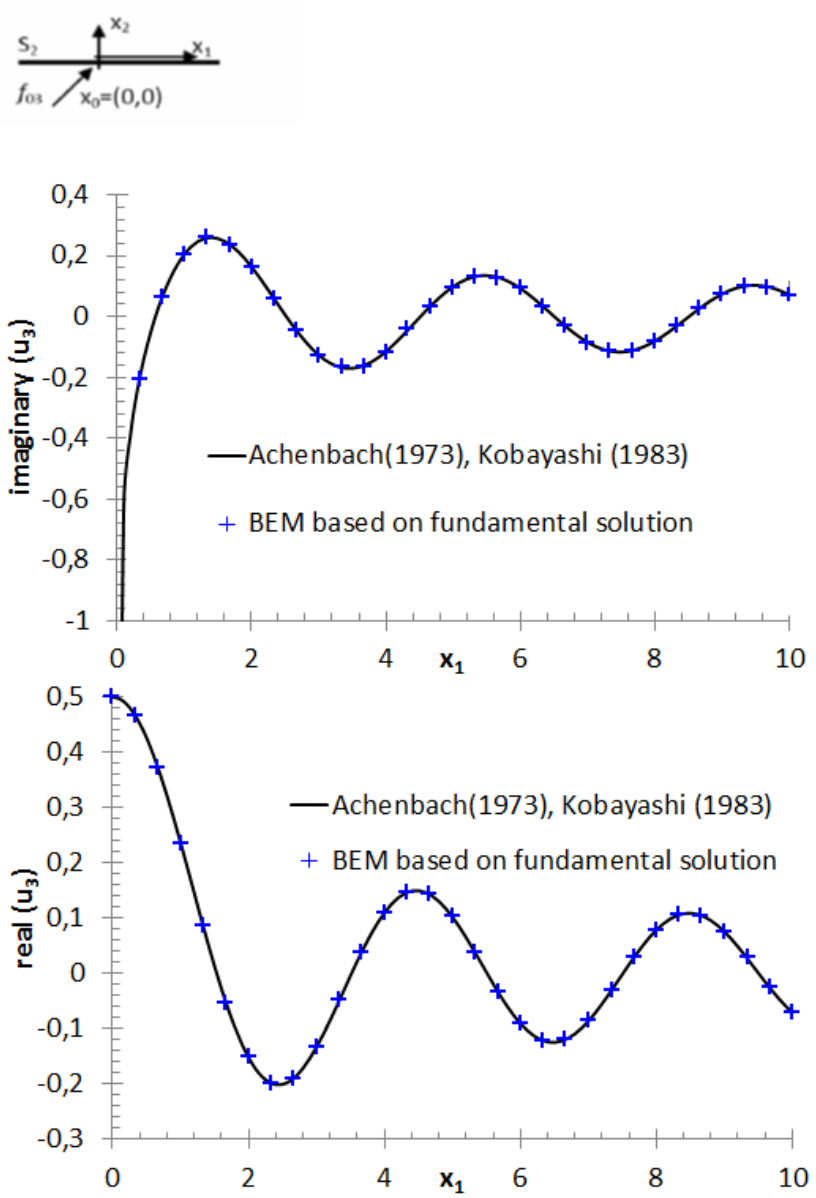

FIGURE 3.14: Comparison with Lamb's solution

in Yeh et al. [102]. Fig.3.14a,b presents real and imaginary parts of the normalized free surface displacement for fixed wave number $k = (\omega\sqrt{\varrho_0/\mu_0}) = \pi/2$ of time-harmonic seismic source located at the point $(0, 0)$ along the free surface of a homogeneous half-plane. Comparison is conducted between results obtained by two different computational tools: (a) analytical solution for homogeneous half-plane expressed by Eqn.(3.16). The corresponding solution for quadratically inhomogeneous case at zero value of the inhomogeneous coefficient $b = 0$ recovers the solution presented by Eqn.(3.16); (b) numerical solution by direct BEM based on the elastodynamic fundamental solution for the full plane with the mesh along free surface consisting of 30 quadratic boundary elements. Fig.3.14 demonstrates that both solutions are indistinguishable. With this test example the BEM code

based on the fundamental solution is validated and it is applied further below for a half-plane with a relief, considering the fact that there is no published test example for homogeneous half-plane with surface relief under wave radiating from seismic source.

The second test example considers the wave field in an elastic homogeneous half-plane with material properties $\mu_0 = 123{\cdot}10^7 Pa$, $\varrho_0 = 1850 N/m^2$ containing a semi-circle canyon with radius a and subjected to waves radiating from an embedded at point x_0(0,-5a) time-harmonic seismic source. This problem is solved by two different BEM codes using fundamental solution and Green's function correspondingly. Fig.3.15a-e compares solutions for displacement amplitudes along the free surface of the half-plane at different values of the non-dimensional frequency η=2a/λ. Fig.3.15 demonstrates the high accuracy of both solutions. The used BEM mesh consists of 24 along S_{can} and 108 along S_2 constant boundary elements when employ fundamental solution against 14 along S_{can} constant boundary elements when employ Green's function.

The third test example compares again BEM results obtained via fundamental solution and Green's function for the problem presented in Fig.3.16. It considers elastic homogeneous half-plane without free surface but containing a circular cavity with radius a and center coordinates (0,-5a) subjected to waves radiated from an embedded at point x_0(0,-5a) seismic source with a prescribed frequency $\eta = 0.25$. Both solutions are fully covered. The used BEM mesh consists of 22 along S_{cav} and 140 along S_2 constant boundary elements when use fundamental solution against 22 along S_{cav} constant boundary elements when use Green's function.

The verification results presented in Fig.3.2-3.16 show that the developed numerical scheme and accompanied created software work with high accuracy and a further simulation study can be conducted. In all considered above numerical examples is evident that the non-conventional BEM proposed here is an efficient strong mesh reducing technique comparing with the conventional BEM technique.

3.4 Parametric study

The aim of this section is to demonstrate the potential of the non-conventional BEM to study wave propagation phenomena in complex geological profiles accounting for all three components of the problem (source–wave path inhomogeneity and heterogeneity–subsurface geology). The sensitivity of the seismic field to the following key factors is revealed: (a) inhomogeneity in terms of quadratic variation of material properties, (b) type (incident or concentrated load) and characteristics (frequency, wave length, incident angle) of the applied load, (c) geometry of the

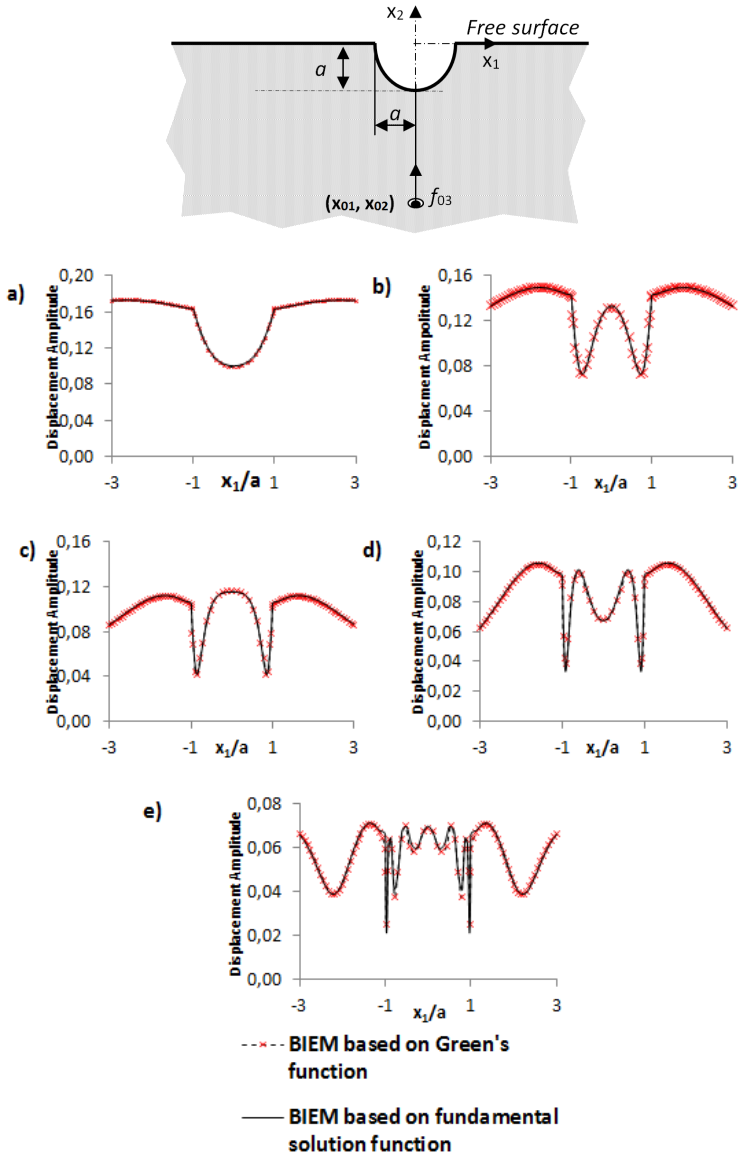

FIGURE 3.15: Displacement amplitude along the free surface of elastic homogeneous half-plane with a semi-circle canyon with radius a subjected to waves radiating from an embedded time-harmonic seismic source with non-dimensional frequency η at point (0, -5a): (a) $\eta = 0.25$; (b) $\eta = 0.50$; (c) $\eta = 0.75$; (d) $\eta = 1.0$; (e) $\eta = 2.0$

free-surface relief and (d) geological media heterogeneity: existence of cavities or tunnels [95, 103, 104].

First, results for the case when the seismic excitation is presented by incident time-harmonic SH-wave are presented in Fig.3.17-3.24. Note here that for the illustration of the results the inhomogeneity parameter b is presented while all simulations are conducted considering the normalized inhomogeneity parameter defined as $\beta = -b/2a$, where a is the characteristic size of the free- or sub-surface

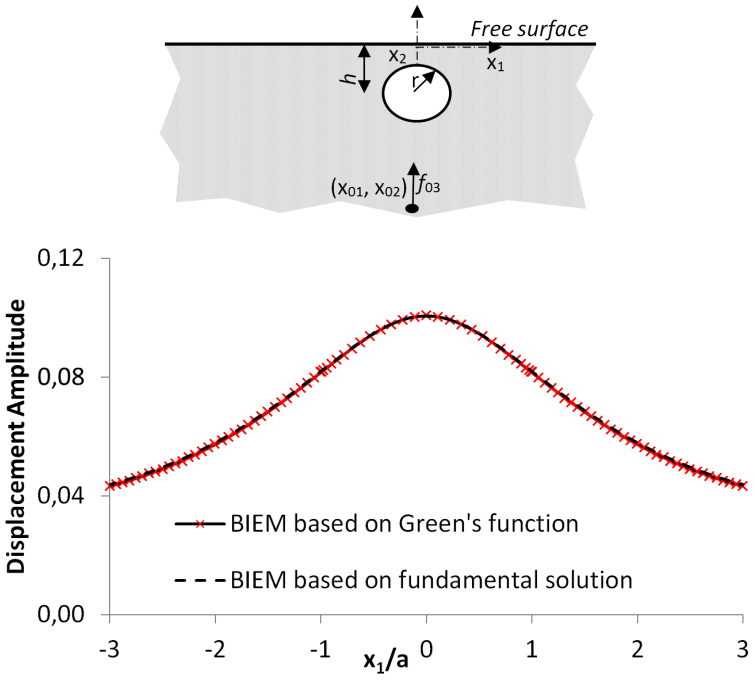

FIGURE 3.16: Displacement amplitude along the free surface of elastic homogeneous half-plane with an embedded circle cavity subjected to waves radiating from an embedded time-harmonic seismic source located at point (0, -5a) with non-dimensional frequency $\eta = 0.25$

relief. The influence of the material inhomogeneity on the seismic wave field along the free surface of the half-plane can be seen in Fig.3.17 for a circular canyon and in Fig.3.18 for a triangle canyon. Observe that the seismic signal depends strongly on the magnitude of the material gradient and this effect is sensitive to the frequency of the propagating SH-wave. For instance, in Fig.3.17b, at non-dimensional frequency $\eta = 0.75$ the percentage difference between displacement amplitudes for homogeneous case (b=0) and for inhomogeneous case $b = -2.5$ is approximately 70% at site x/a=$\pm$1.0. For $\eta = 0.75$, with increasing the inhomogeneity magnitude, the displacement amplitude also increases, while for frequency $\eta = 0.25$ (Fig.3.17a) with increasing the inhomogeneity magnitude the displacement amplitude decreases. The combination of material inhomogeneity with the type of the free surface relief can modify significantly the shape of the seismic signal computed at the free surface (compare Fig.3.17 with Fig.3.18). In general, the shape of the overall seismic signal keeps one and the same, only the site effects with increasing the inhomogeneity magnitude are amplified for some frequency values or de-amplified for other frequency values.

Furthermore, the strong influence of the geometrical shape on the seismic field can be seen in Fig.3.19 and 3.20 where the shape of the cavity is horizontally or vertically elongated semi-elliptic, respectively. The ratios of semi-axes in the case of horizontally and vertically elongated semi-elliptic canyons are 2 and 1/2, respectively. It is obvious that all three factors, the ratio a/λ, material gradient

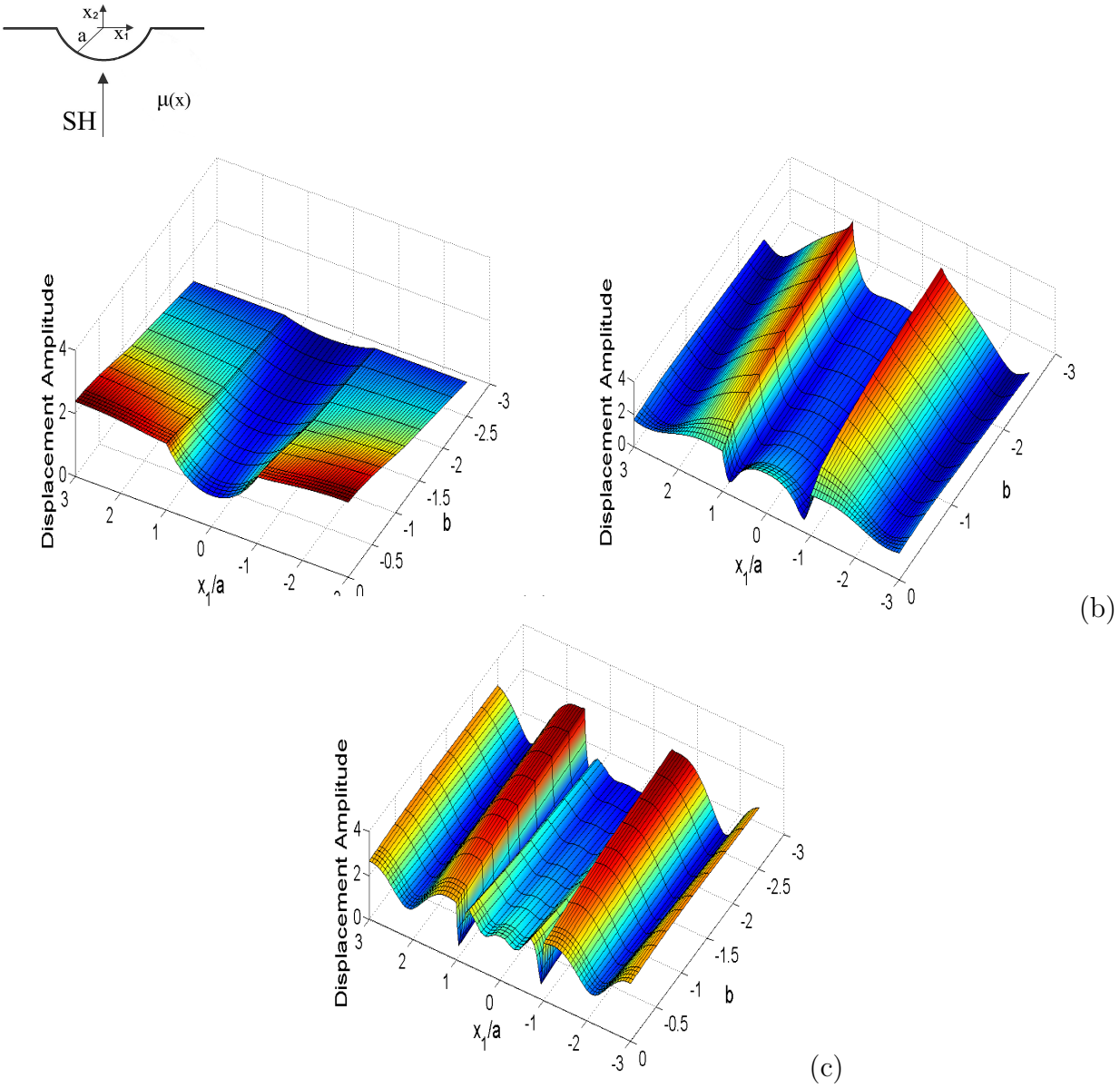

FIGURE 3.17: Displacement amplitude along the free surface of quadratically inhomogeneous half-plane containing a semi-circle canyon with radius a. The frequency of normal incident SH-wave is: (a) $\eta = 0.25$; (b) $\eta = 0.75$; (c) $\eta = 1.25$

and geometrical shape of the free surface canyon play together and as a result a complex wave field picture is obtained. The seismic signal changes its form, frequency behavior and amplification when the free surface relief varies from circular canyon (Fig.3.17) to horizontally elongated canyon (Fig.3.19) or to vertically elongated canyon (Fig.3.20). The characteristic behavior of the seismic field near the corners of the canyon (at point x =a, where a is the size of the smaller semi-axes) is demonstrated in Fig.3.20. Such type of pictures can be effectively used to identify the shape and size of the free surface relief. Moreover, the sensitivity of the seismic field to the direction of the SH-wave propagation for different values of frequency and magnitude of material gradient is shown in Figs.3.21-3.23. The wave picture differs significantly for different incident angles of the propagating wave.

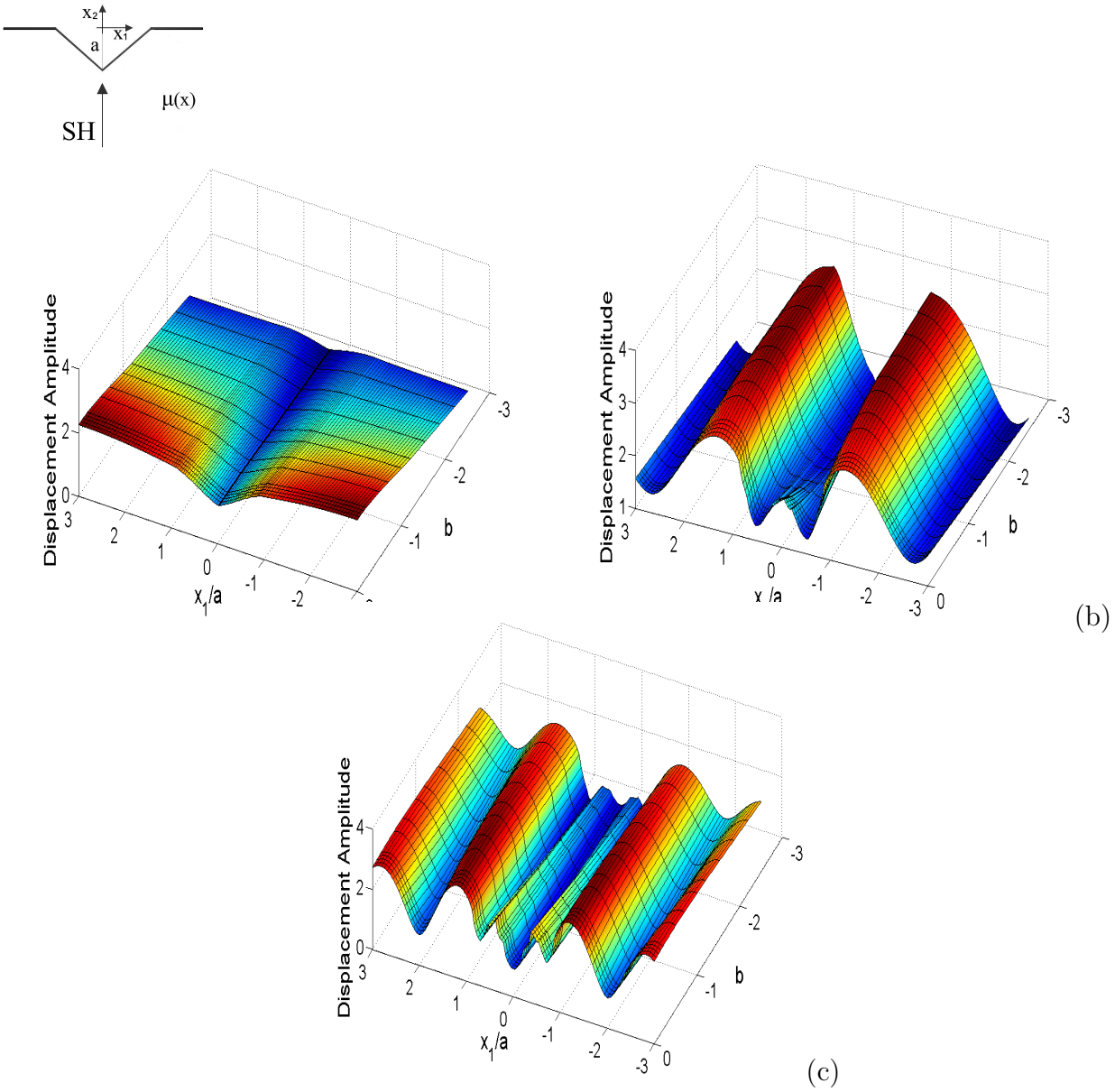

FIGURE 3.18: Displacement amplitude along the free surface of quadratically inhomogeneous half-plane containing a triangle canyon with radius a. The frequency of normal incident SH-wave is: (a) $\eta = 0.25$; (b) $\eta = 0.75$; (c) $\eta = 1.25$

As expected for higher values of frequency the displacement amplitude has a more oscillating behavior. Additionally the presence of an embedded circular cavity (with radius 0.4a) to a quadratically inhomogeneous half-plane containing a triangle canyon with radius a, is plotted in Fig.3.24. The interaction between the free- and sub- surface relief under normal SH-wave propagation influences significantly the seismic field along the free surface. However, the effect of the inhomogeneity in this plot is minor compared to the site effect due to this interaction.

Next, results for SH-wave propagating from an embedded seismic source are presented in Fig.3.25-3.27. The reference data of the material characteristics are:

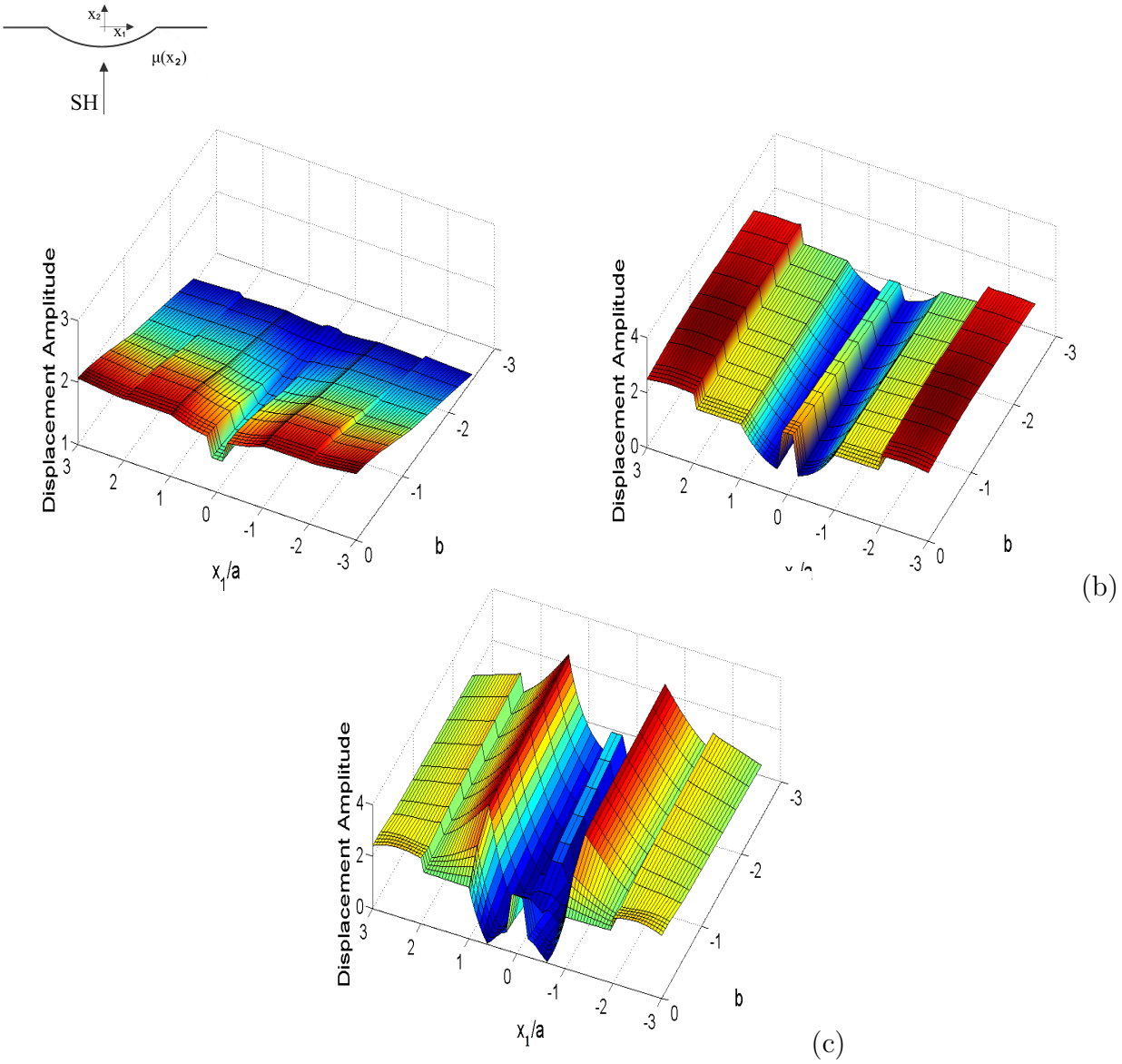

FIGURE 3.19: Displacement amplitude along the free surface of quadratically inhomogeneous half-plane containing a horizontally elongated semi-elliptic canyon with radius a. The frequency of normal incident SH-wave is: (a) $\eta = 0.25$; (b) $\eta = 0.75$; (c) $\eta = 1.25$

$\mu_o = 1.23 \cdot 10^9$ Pa, $\rho_o = 1.85 \cdot 10^3 kg/m^3$ and the magnitude of the applied concentrated force is $f_{03} = 10^9 N$. Two locations of the seismic source are considered: x_{0A}(0, -5a) and x_{0B}(-5a, 0), where a is the characteristic size of the canyon. The great importance of the position of the seismic source on the seismic field is shown in Fig.3.25 and Fig.3.26, where the picture of the wave field is symmetric and non-symmetric, with stronger site effects in the zone of source locations, respectively. As can be seen the material gradient effect is more pronounced when the seismic source is located at point (0, -5a) compared with the seismic field obtained for seismic source at point (-5a, 0). Figure 3.27 depicts the strong site effects due to the combined effects of sub- and free-surface relief, material gradient and seismic source location.

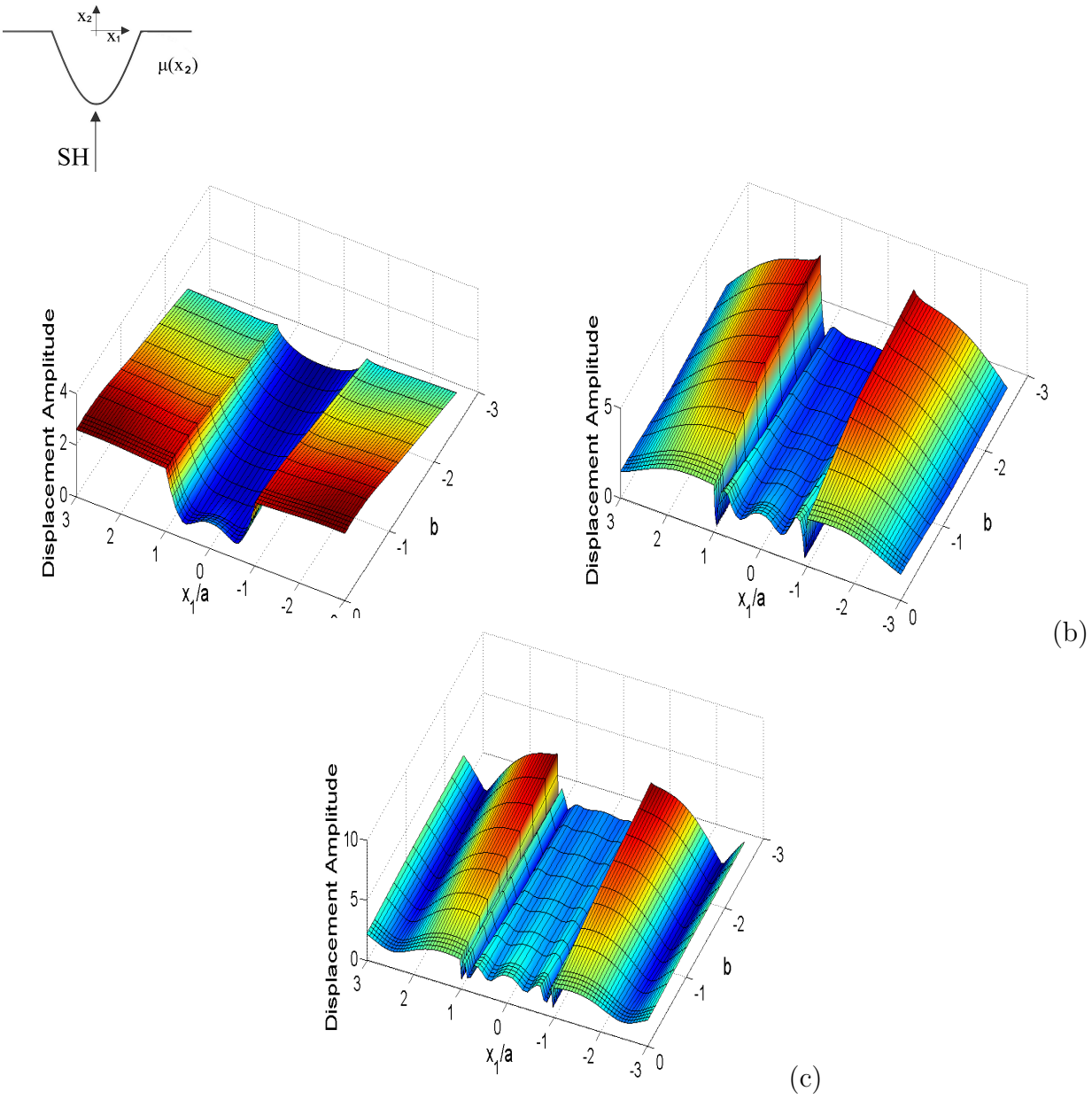

FIGURE 3.20: Displacement amplitude along the free surface of quadratically inhomogeneous half-plane containing a vertically elongated semi-elliptic canyon with radius a. The frequency of normal incident SH-wave is: (a) $\eta = 0.25$; (b) $\eta = 0.75$; (c) $\eta = 1.25$

3.5 Seismic signal synthesis

The developed here numerical tool has the potential to generate seismic signals in complex geological profiles since it describes efficiently all three components of the Earth system: seismic source, inhomogeneous and heterogeneous wave path and the local geological region of interest. The recovery of transient signals is accomplished by first solving the BVP in the frequency domain, in which case the Fast Fourier Transform (FFT) is applied to the time history signal. This

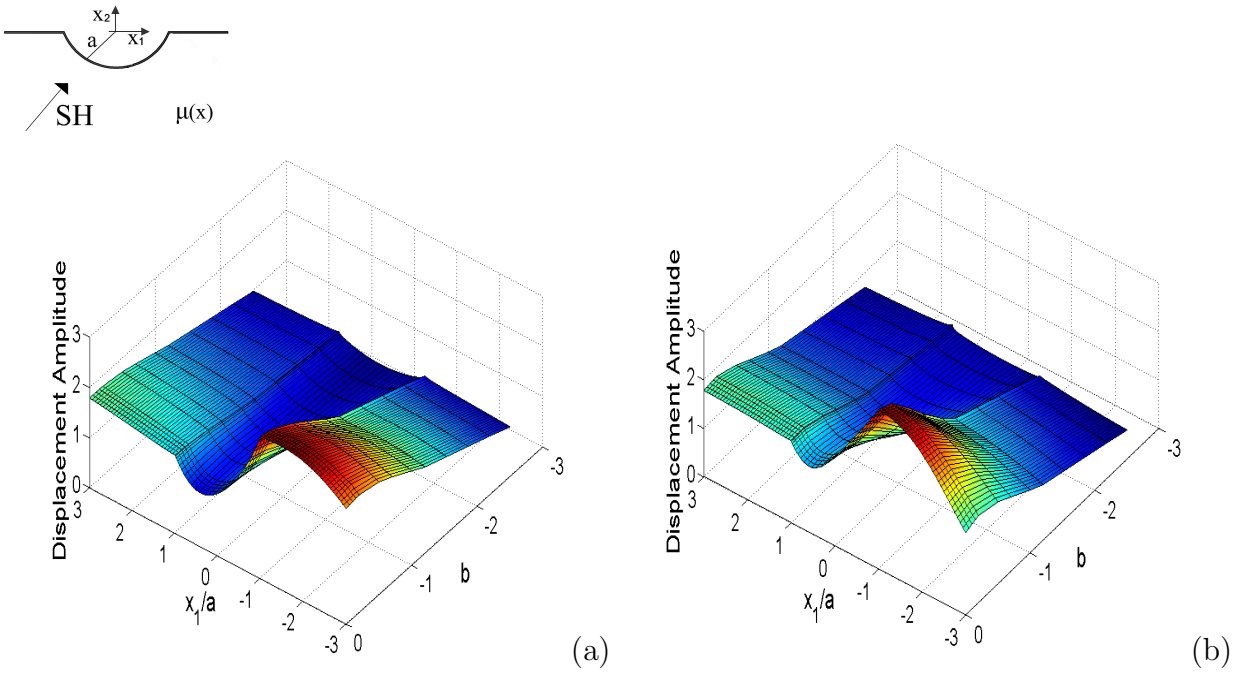

FIGURE 3.21: Displacement amplitude along the free surface of quadratically inhomogeneous half-plane containing a semi-circle canyon with radius a. Incident SH-wave propagates with normalized frequency $\eta = 0.25$ and incident angle θ: (a) $\pi/6$; (b) $\pi/3$

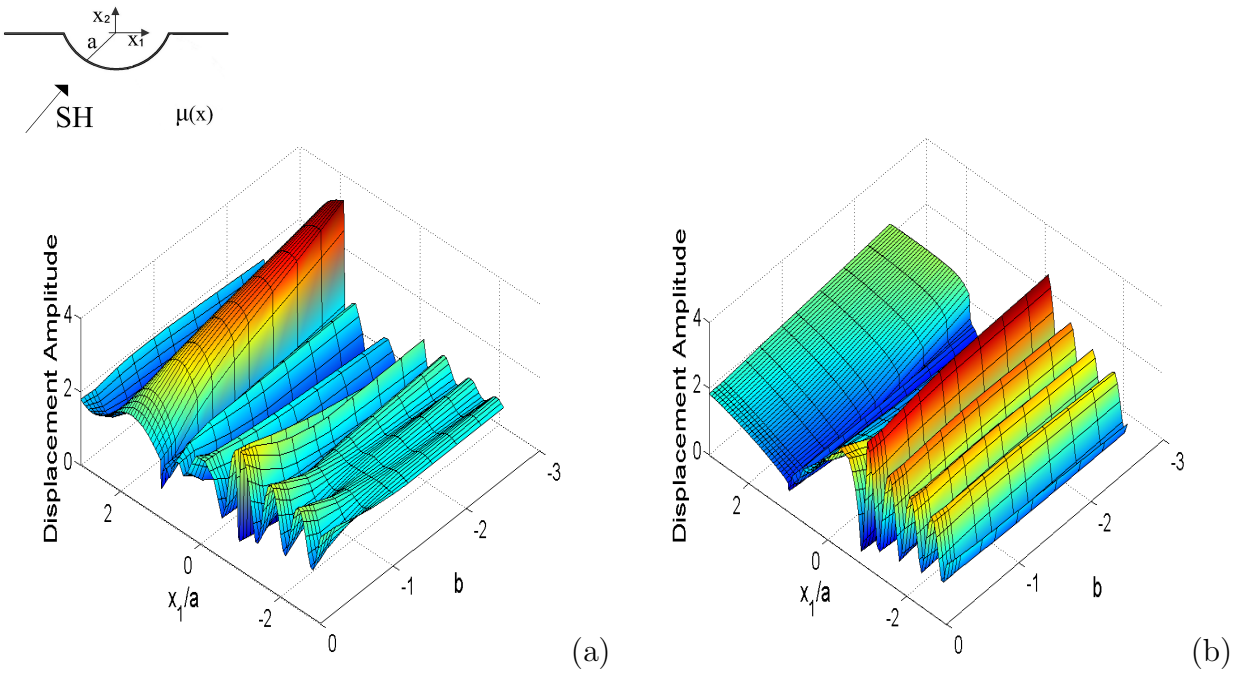

FIGURE 3.22: Displacement amplitude along the free surface of quadratically inhomogeneous half-plane containing a semi-circle canyon with radius a. Incident SH-wave propagates with normalized frequency $\eta = 2$ and incident angle θ: (a) $\pi/6$; (b) $\pi/3$

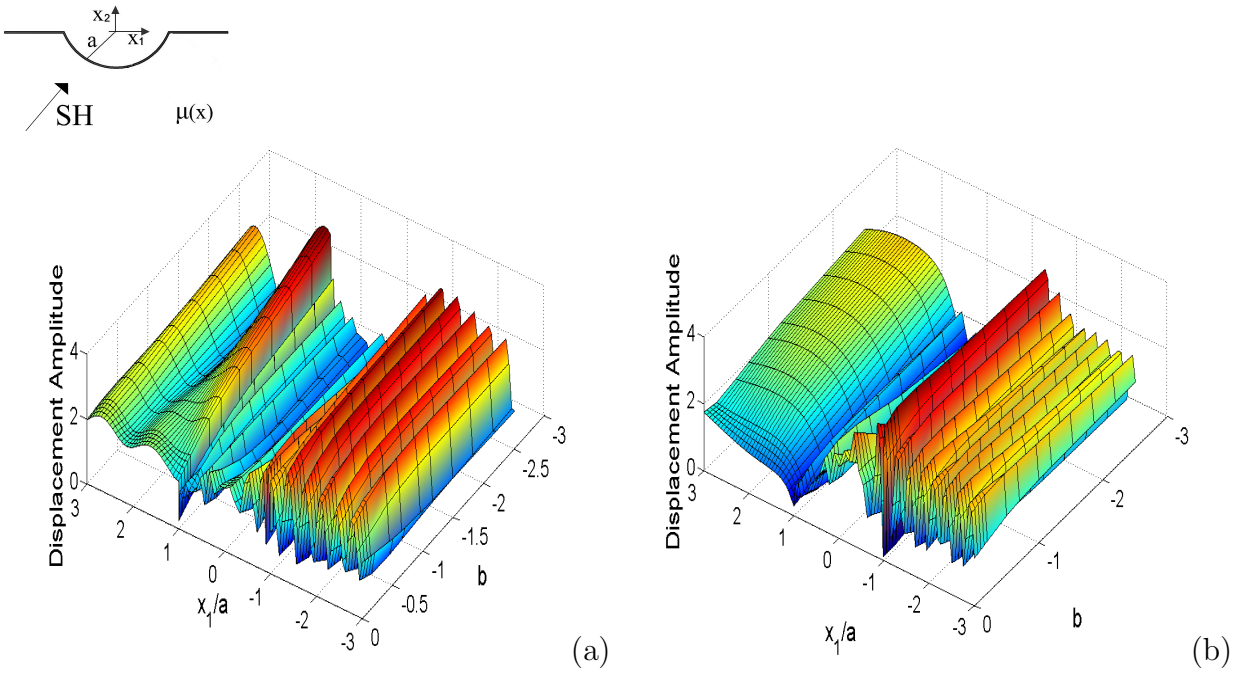

FIGURE 3.23: Displacement amplitude along the free surface of quadratically inhomogeneous half-plane containing a semi-circle canyon with radius a. Incident SH-wave propagates with normalized frequency $\eta = 4$ and incident angle θ: (a) $\pi/6$; (b) $\pi/3$

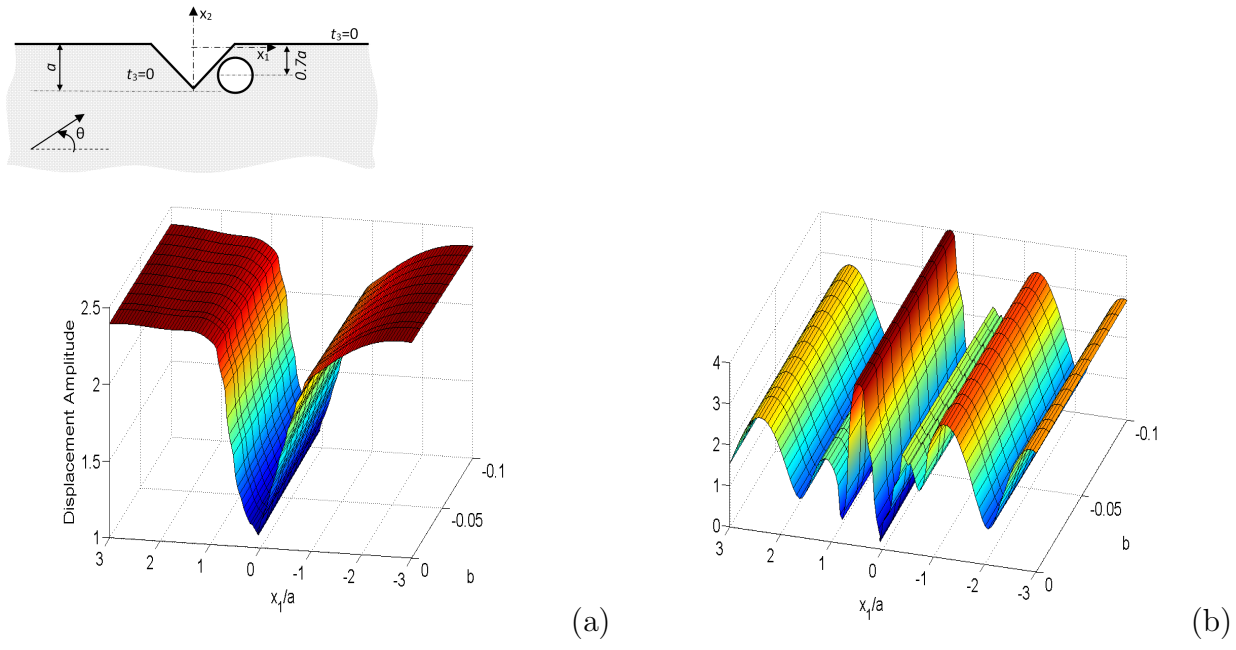

FIGURE 3.24: Displacement amplitude along the free surface of quadratically inhomogeneous half-plane containing a triangle canyon with radius a and an embedded circular cavity with radius 0.4a. The frequency of normal incident SH-wave is: (a) $\eta = 0.25$; (b) $\eta = 1.25$

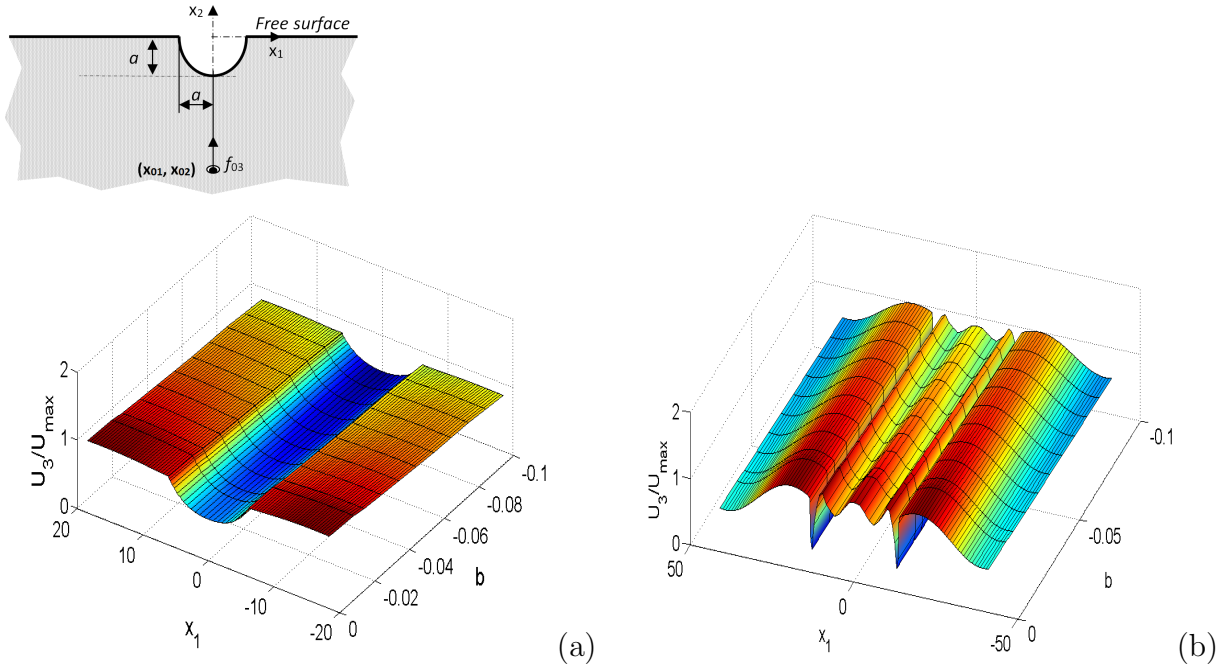

FIGURE 3.25: Displacement amplitude along the free surface of quadratically inhomogeneous half-plane containing a semi-circular canyon with radius a subjected to waves radiating from a seismic source located at point (0, -5a) with non-dimensional frequency: (a) $\eta = 0.25$; (b) $\eta = 1.25$

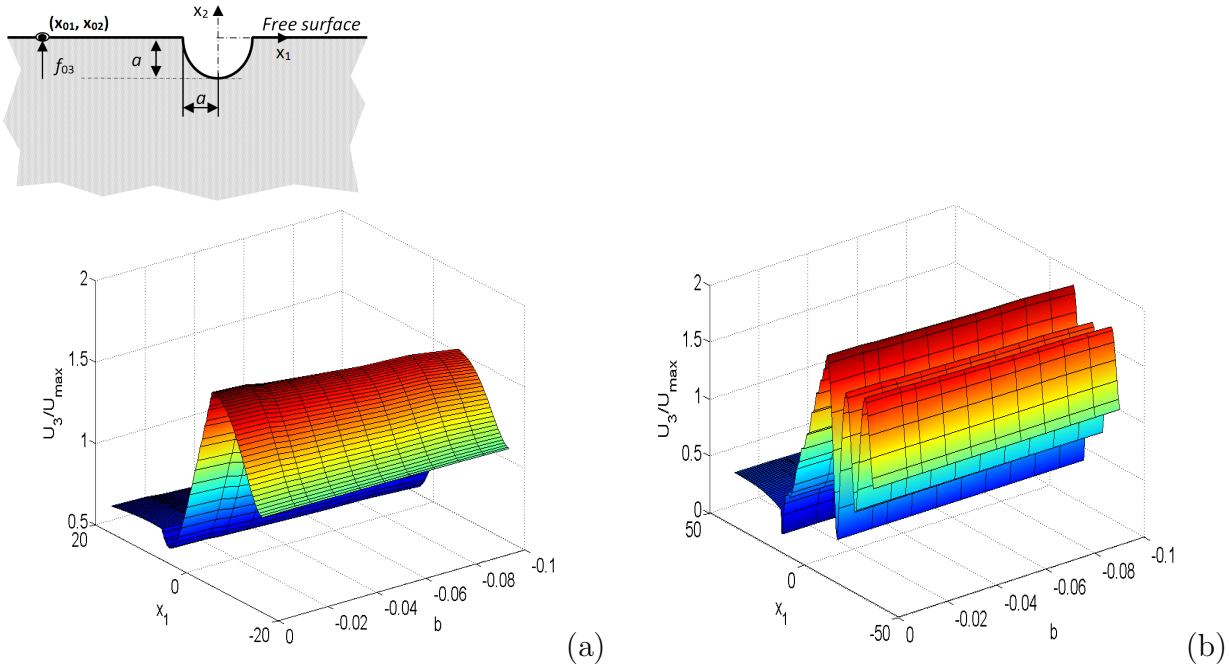

FIGURE 3.26: Displacement amplitude along the free surface of quadratically inhomogeneous half-plane containing a semi-circular canyon with radius a subjected to waves radiating from a seismic source located at point (5a, 0) with non-dimensional frequency: (a) $\eta = 0.25$; (b) $\eta = 1.25$

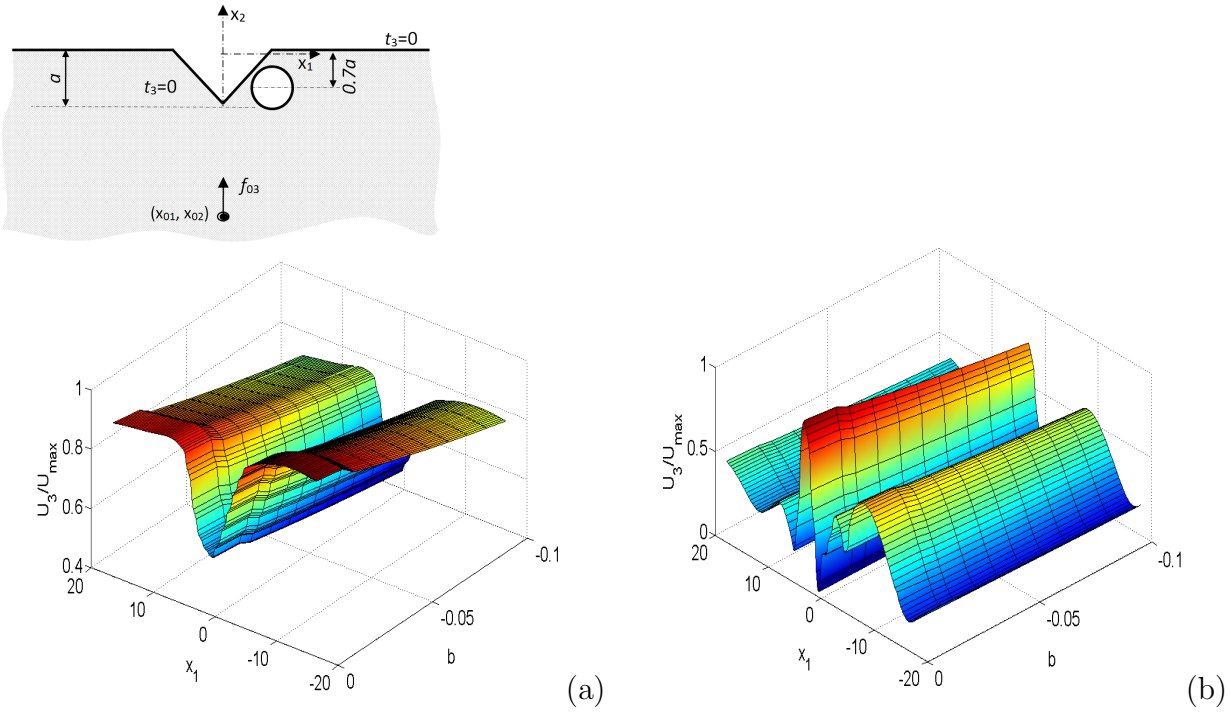

FIGURE 3.27: Displacement amplitude along the free surface of quadratically inhomogeneous half-plane containing a triangle canyon with radius a and an embedded circular cavity with radius 0.4a, subjected to waves radiating from a seismic source located at point (0, -5a) with non-dimensional frequency: (a) $\eta = 0.25$; (b) $\eta = 1.25$

is followed by application of the BEM so as to generate a spectrum comprising kinematic field values at discrete frequencies. Finally, the IFFT is applied to the frequency domain solution to recover displacements, velocities and accelerations in the time-domain.

First numerical example, that serves also to demonstrate the verification of the presented here numerical tool, consists of elastic half-plane with semi-circular canyon subjected to incident normal transient SH wave with time function $f(t)$. In Figure 3.28 the form of the time function and its Fourier spectrum are plotted. An excellent comparison is shown in Figure 3.29a between solutions for homogeneous half-plane ($b = 0$) obtained by two different BEM techniques for displacement in time domain at receiver point 1 (edge of the canyon) and at receiver point 2 (bottom of the canyon). The developed here BEM based on Green's function for quadratically inhomogenous in depth half-plane is validated with the conventional BEM based on the elastodynamic fundamental solution for results in time domain. Next, synthetic seismograms are plotted in Figure 3.29b obtained only by BEM based on Green's function at two different receiver points along the canyon for several values of inhomogeneity magnitude b.

Results from transient seismic source are shown in Figures 3.30 and 3.31, where the seismic excitation is a vertically, planar Gabor pulse described by the following equation:

$$f(t) = exp(-\alpha)cos(\omega_p(t-t_s)+\chi); \quad \alpha = \omega_p(t-t_s)/\gamma)^2 \tag{3.18}$$

The following numerical values are assigned to the parameters appearing in the above equation: $f_p = \omega_p/2\pi = 0.23$; $\chi = 0$; $t_s = 0.25sec$; $\gamma = 0.15$. The geological domain consists of homogeneous half-plane containing: (a) free surface relief presented by an elliptic canyon with prescribed ratio $\kappa = (b_1/\text{a})$=1.5, where a=50m and $b_1 = \kappa a$ are the semi-axes (Fig.3.30a) and (b) free surface relief presented by an elliptic canyon with prescribed ratio $\kappa = (b_1/\text{a})$=1.5 plus a sub-surface relief as a circular cavity with radius $r = 20m$ and center coordinates $(100, -35)$ (Fig.3.30a). Reference data for the material characteristics are $\mu_o = 10^9$ Pa and $\rho_o = 2.5 \cdot 10^3 kg/m^3$ and the source is located at point (0, 2a). Normalized displacement seismograms and response spectra are presented in Fig.3.30c and Fig.3.31 respectively, for two different receiver sites along the canyon. The normalization is done by the maximum response value at the surface of the homogeneous half-plane without free and sub surface relief and the same material properties and load.

All synthetic seismic signals presented here reveal the sensitivity of the seismic response to the material inhomogeneity of the wave path, to the type of the seismic load, to the location of the seismic source and to the existence of any relief peculiarities of arbitrary shape in the geological region. Site effects have a significant influence on the ground motions recorded along the free surface in terms of resonance frequencies and amplification levels.

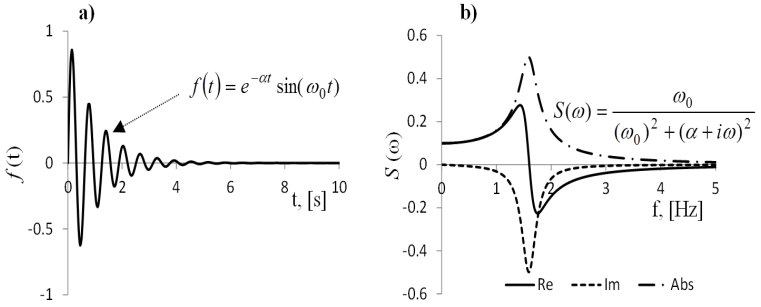

FIGURE 3.28: Time function: a) input signal f(t); (b) Continuous Fourier transform of f(t).

3.6 Conclusions

2D out of plane wave propagation problem is solved for quadratically inhomogeneous in depth half-plane with free- or/and sub-surface relief due to plane

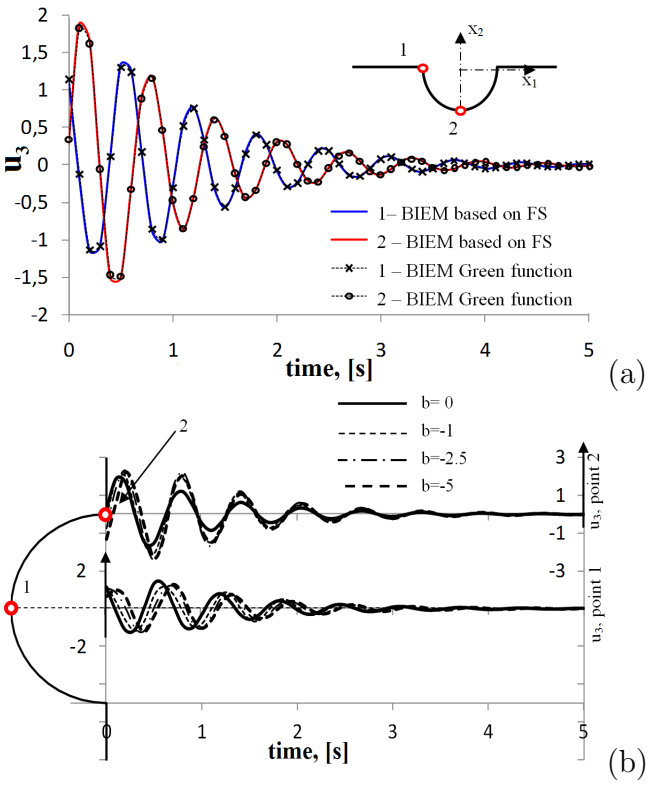

FIGURE 3.29: Synthetic seismograms at point 1 (canyon's edge) and point 2 (canyon's bottom) (a) for a homogeneous half-plane and (b) for an quadratically inhomogeneous half-plane, with semi-circle canyon due to normal SH waves with time-function $f(t)$

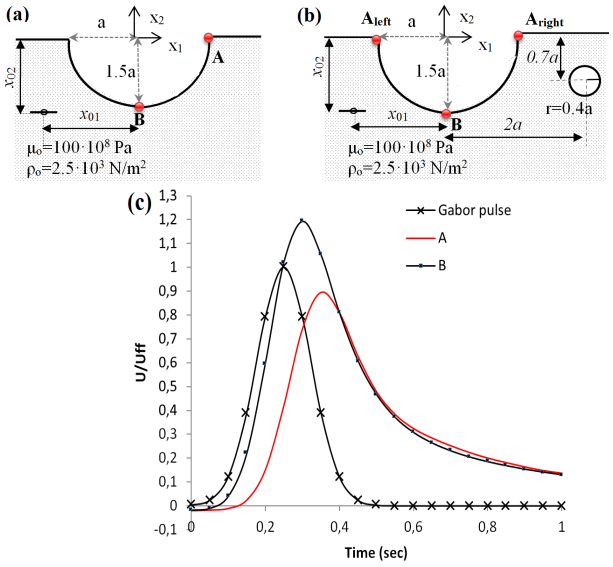

FIGURE 3.30: Geometry of the problem Case (a) and Case (b); (c) normalized displacement seismograms for receiver sites A_{right} (right rim of the canyon) and B (bottom of the canyon) in the homogeneous half-plane with an elliptic canyon under normalized Gabor pulse

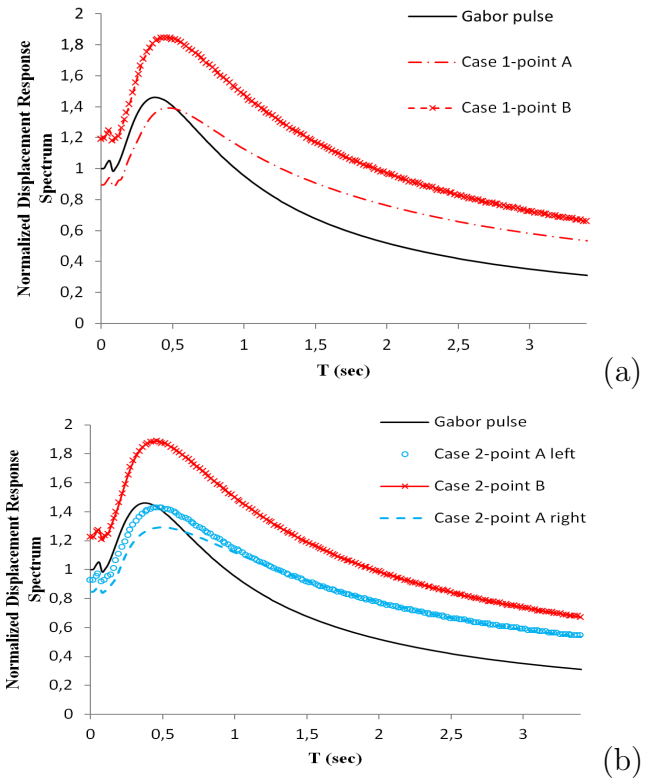

FIGURE 3.31: Normalized displacement response spectra for: (a) receiver sites A_{right} (right rim of the canyon) and B (bottom of the canyon) in the homogeneous half-plane with elliptic canyon and (b) receiver sites A_{right} (right rim of the canyon), A_{left} (left rim of the canyon) and B (bottom of the canyon) in the homogeneous half-plane with elliptic canyon and circular cavity

time-harmonic or transient SH-waves or waves generated from an embedded time-harmonic or transient seismic source. BEM appropriate to deal with this problem is proposed, validated and applied for several geological configurations and seismic scenarios. The obtained results reveal convincingly the potential of the BEM based on Green's function to study efficiently this problem due to many advantages compared to other techniques, namely: (a) reduction of the problem dimensionality because the discretization is applied only along the existing boundaries (free- and sub-surface relief) without the need to discretize additionally the free-surface as in conventional BEM or the whole domain area as in FEM; (b) direct modeling of inhomogeneity through the use of Green's function for quadratically inhomogeneous half-plane; (c) the mathematical form of the Green's function is not complex and there is no problem to be inserted in the BEM software; (d) the Green's function satisfies the Sommerfeld radiation condition and thus infinitely extended boundaries are automatically incorporated; (e) the method is based on the Green's function for the inhomogeneous half-plane and thus it can be considered as semi-analytical approach.

Chapter 4

BEM for geological media with variable velocity profile

The present chapter concerns the development and verification of a novel type of BEM that employs a closed form fundamental solution for continuously inhomogeneous media with variable wave velocity profile. More specifically, the geological medium possesses a variable velocity profile assuming both a depth-dependent shear modulus and material density. In addition the geological region contains either parallel or nonparallel graded layers, surface relief, and buried cavities and tunnels. The present chapter is structured as follows: Statement of the problem; BEM formulation; Verification and parametric study. The developed BEM numerical implementation is successfully verified and then a series of parametric studies are conducted and numerical results are generated in the form of synthetic signals in complex geological media. The proposed approach allows to investigate the influence of the material gradient and the wave velocity, the presence of graded layers, multiple canyons and cavities of different number, shape and location and the frequency content of the incoming signal on the seismic response of an inhomogeneous and heterogeneous geological medium.

4.1 Statement of the problem

Consider time-harmonic elastic waves in a viscoelastic half-plane comprising N stratified layers Ω_n (n=0, 1, 2...N) with non-parallel boundaries Λ_n of arbitrary shape extending to infinity. The geometry of the problem is presented in Fig.4.1. As can be seen the top layer Ω_N is bounded by the free surface Λ_N, with relief in the form of a canyon (boundary S_{canyon}), plus a buried cavity (boundary S_{cav}). It is assumed that each layer Ω_n is continuously inhomogeneous along the vertical axis, with a shear modulus $\mu(x_2)$ and a density $\varrho_n(x_2)$, yielding a shear wave velocity $C_{Sn}(x_2)$ that is also position-dependent. Thus, the geological region has a wave

velocity profile $C_S(x_2) = \cup_{n=1}^{N} C_{Sn}(x_2); x_2 \in \Omega_n$. The upper and lower boundary of each finite-thickness layer Ω_n is denoted by Λ_n and Λ_{n-1}., respectively. Next, ratio $c_n = C_{Sn}^{bottom(\Lambda_{n-1})}/C_{Sn}^{top(\Lambda_n)}$ is defined for the velocities at bottom and top of the layer Ω_n. The boundaries for the deepest layer Ω_1 are denoted as Λ_1 and Λ_0, where the latter boundary is the interface between Ω_1 and the underlying homogeneous half-space Ω_0, with constant material properties μ_0, ϱ_0. Finally, the dynamic loads comprise either (a) an incident time-harmonic SH wave tracing an incident angle θ with respect to axis Ox_1 or (b) waves generated by an embedded seismic line source $x_0(x_{01}, x_{02}) \in \Omega_0$.

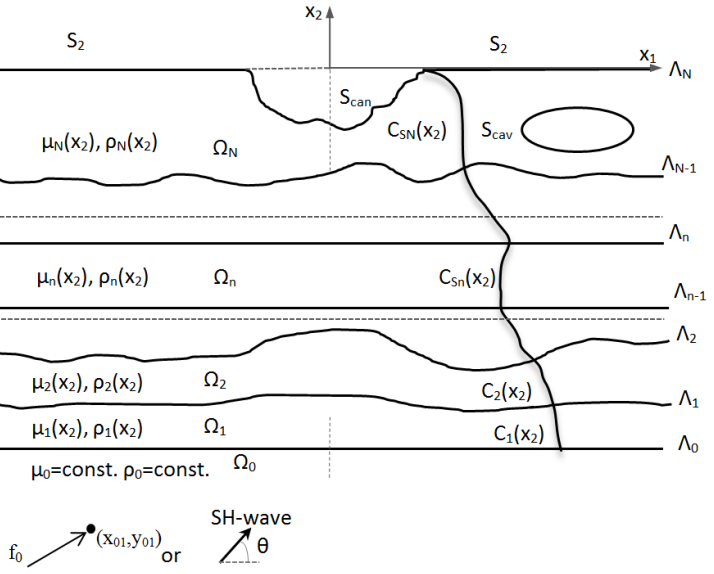

FIGURE 4.1: Geological region with graded layers, surface topography and buried inclusions

Since anti-plane strain conditions are assumed to hold, the only non-zero field quantities are the displacement $u_3(x, \omega)$ and the shear stresses σ_{i3}, i=1, 2, all dependent on position vector $x = x(x_1, x_2)$ and on frequency ω. The governing equation of motion and corresponding boundary conditions are as follows:

$$\nabla \cdot \{\mu_k(\mathbf{x}, \omega) \nabla u_3(\mathbf{x}, \omega)\} = -\varrho_k(x_2)\omega^2 u_3(\mathbf{x}, \omega); \quad x \in \Omega_k; \quad k = 1, 2, ...N \tag{4.1}$$

$$\nabla \cdot \{\mu_0 \nabla u_3(\mathbf{x}, \omega)\} = -\varrho_0 \omega^2 u_3(\mathbf{x}, \omega) - \psi f_{03} \delta(\mathbf{x}, x_0); \quad x \in \Omega_0 \tag{4.2}$$

$$t_3(x_1, x_2, \omega) = \sigma_{3,j}(x_1, x_2, \omega) n_j(x_1, x_2) = 0 \quad for \quad \mathbf{x} \in S_2 \cup S_{can} \cup S_{cav} \tag{4.3}$$

In addition, compatibility conditions for displacements and equilibrium conditions for tractions are satisfied along all interfaces Λ_n (n=0, 1, 2N), plus the Sommerfeld radiation condition holds for waves at infinity. In the above equations, n_i are the components of the outward pointing normal vector, while $\psi = 0$ when seismic

loads are represented by an incident wave and $\psi = 1$ when seismic loads are waves radiating from an embedded line source placed at point x_0 with magnitude f_{03}. Next, the summation convention over repeated indices is implied, $\bigtriangledown$ is the gradient and $(\bullet)$ is the inner product. In all the above equations, shear modulus μ is complex-valued and defined as $\mu = \mu^* = Re(\mu^*) - i\omega\bar{\mu}$, where the real part is position-dependent, while $\bar{\mu}$ is the dissipative part evaluated from the logarithmic decrement in amplitude $\delta = \pi/Q = 2\pi\sqrt{\omega\bar{\mu}/Re(\mu^*)}$, where Q is the dimensionless quality factor.

A number of configurations for the model described above are now considered in Fig.4.2, namely: (a) BVP-1 and BVP-4 describe a graded half-plane Ω_1 with velocity profile $C_{S1}(x_2)$, containing free-surface relief along boundary Λ_1 in the form of a canyon (S_{can}) plus an embedded cavity (S_{cav}); (2) BVP-2 and BVP-5, where a graded layer Ω_1 of finite depth H_1 and velocity profile $C_{S1}(x_2)$, in the presence of a canyon, rests on bedrock that in turn is modeled as a homogeneous half-space Ω_0 with constant properties μ_0 and ϱ_0; (3) BVP-3 and BVP-6 describe two finite-depth graded layers Ω_1 and Ω_2 with thickness H_i (i=1, 2), as well as a canyon, and this layered system rests on bedrock (i.e., the previously mentioned homogeneous half-space Ω_0). The velocity profiles in layers Ω_1 and Ω_2 are denoted as $C_{S1}(x_2)$ and $C_{S2}(x_2)$, respectively. Finally, for BVP-1, 2, 3 the dynamic loading is an incident SH wave, while for BVP-4, 5, 6 is expressed by time-harmonic waves generated from a seismic source embedded in bedrock.

Variable wave velocity profile

The particular depth profiles of shear modulus, density and wave speed follow the inhomogeneous model proposed in Karakostas and Manolis [72], where the fundamental solution of equation of motion Eqn.(4.1) was analytically derived based on earlier work by Manolis and Shaw [41, 42]. Short description of the derivation steps is given in section 4.2.1. The acceptable material parameter profiles are given in [41]. In what follows, the material profiles are recovered by imposing the condition that the wave number k^∞ depends on the value of the stiffness and density at large depth ($x_2 \to \infty$), where the material attains a homogeneous structure:

$$\begin{aligned} \mu^{1/2}(x_2) &= (\mu^\infty)^{1/2} + H_1 exp(-\gamma x_2) + H_2 exp(ik^\infty x_2) \\ \varrho(x_2) &= (\tfrac{1}{\omega})^2 \mu^{1/2} \Big[(k^\infty)^2 \mu^\infty)^{1/2} + (k^0)^2 \mu^0)^{1/2} - (k^\infty)^2 (\mu^\infty)^{1/2} exp(-\gamma x_2) \Big] \end{aligned} \tag{4.4}$$

where

$$\begin{aligned} H_1 &= \frac{\left((k^0)^2 (\mu^0)^{1/2} - (k^\infty)^2 (\mu^\infty)^{1/2} \right)}{\gamma^2 + (k^\infty)^2} \\ H_2 &= (\mu^0)^{1/2} - (\mu^\infty)^{1/2} - \frac{\left((k^0)^2 (\mu^0)^{1/2} - (k^\infty)^2 (\mu^\infty)^{1/2} \right)}{\gamma^2 + (k^\infty)^2} \end{aligned} \tag{4.5}$$

Note that $C_S^0 = \sqrt{\mu^0/\varrho^0}$ and $k^0 = \omega/C_S^0$ respectively are the wave velocity and wave number at the free surface $x_2 = 0$, while $C_S^\infty = \sqrt{\mu^\infty/\varrho^\infty}$ and $k^\infty = \omega/C_S^\infty$

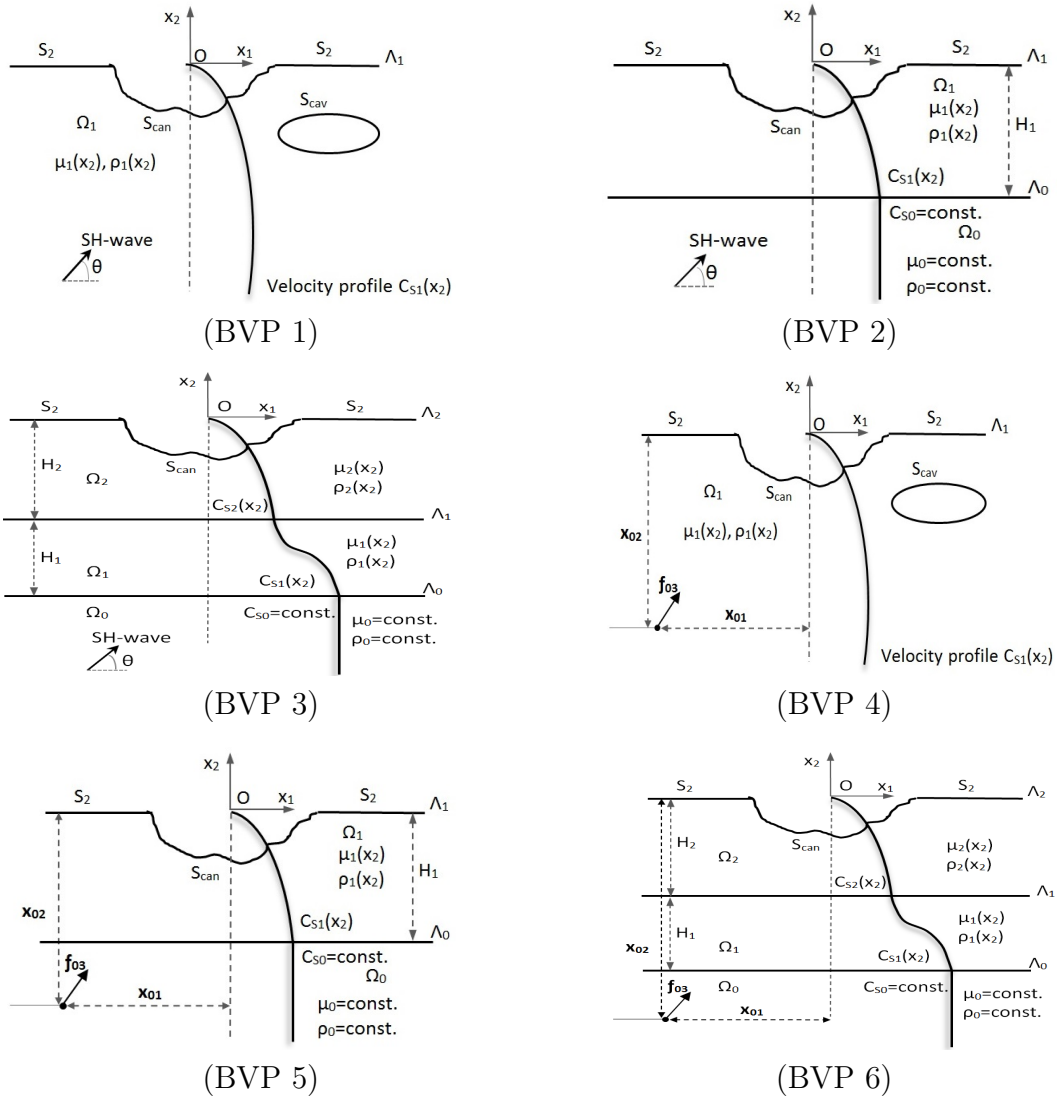

FIGURE 4.2: Six geological deposit configurations: (BVP-1) a single inhomogeneous layer under SH incident waves; (BVP-2) a single inhomogeneous layer on bedrock under SH incident waves; (BVP-3) two inhomogeneous layers on bedrock under SH incident waves; (BVP-4) a single inhomogeneous layer under waves radiated from a seismic source; (BVP-5) a single inhomogeneous layer on bedrock under waves radiated from a seismic source (BVP-6) two inhomogeneous layers on bedrock under waves radiated from a seismic source

are their counterparts at great depth $x_2 = \infty$. Coefficient γ is a small number taken as equal to 0.1 here so as to recover a smooth wave speed profile with depth, i.e., $C_S(x_2) = \sqrt{\mu(x_2)/\varrho(x_2)}$. Note that the wave number k is complex-valued since the material is viscoelastic. Thus, there are two mechanisms to account for wave dispersion phenomena, namely non-elastic material behaviour and position-dependent material properties.

Free-field motion

When seismic loads are modeled as incoming SH waves, then the total wave field is a superposition of the free-field motion (u_3^{ff}, t_3^{ff}) plus the scattered wave field (u_3^{sc}, t_3^{sc}) from both the material inhomogeneity plus from existing heterogeneities such as layering, free-surface relief, buried structures, etc. Thus,

$$u_3(\mathbf{x},t) = u_3^{ff}(\mathbf{x},t) + u_3^{sc}(\mathbf{x},t); \quad t_3(\mathbf{x},t) = t_3^{ff}(\mathbf{x},t) + t_3^{sc}(\mathbf{x},t) \tag{4.6}$$

The free-field motion when we solve the BVP-1 (Fig.4.2) describes wave propagation in a continuously inhomogeneous half-plane with position-dependent material characteristics and without any type of heterogeneities as free or sub-surface relief. The free field motion in this case is computed numerically via boundary integral equations along the flat free surface with respect to u_3^{ff}. The quantities for (u_3^{ff}, t_3^{ff}) at any receiver point in the half-plane can be computed by the usage of well-known integral representation formulas. In the presence of layered structure (e.g., BVP-2, 3 of Fig.4.2), the free field motion is the wave field in a homogeneous half-plane with constants μ_0 and ϱ_0 and without any heterogeneities. In this case, the displacement u_3^{ff} are known (see [43]):

$$u_3^{ff}(x) = U_{30}[e^{-ik(x_1 cos\theta + x_2 sin\theta)} + e^{-ik(x_1 cos\theta - x_2 sin\theta)}] \tag{4.7}$$

In the above, U_{30} is the unit displacement amplitude, $k = \omega / C_S^{bed}$ the wave number and $C_S^{bed} = \sqrt{\mu_0/\varrho_0}$ is the velocity, while the corresponding traction field is $t_3^{ff} = \sigma_{i3}^{ff} n_i$, $\sigma_{i3}^{ff} = \mu_0 u_{3,i}^{ff}$. In addition, the following boundary conditions along the interface boundary Λ_0 between the bottom soil layer Ω_1 and the seismic bed Ω_0 must be satisfied:

$$t_3^{ff(0)} + t_3^{sc(0)} = t_3^{(0)} = -t_3^{(1)}; \quad u_3^{ff(0)} + u_3^{sc(0)} = u_3^{(0)} = u_3^{(1)}; \quad for \quad (x_1, x_2) \in \Lambda_0 \tag{4.8}$$

In the above, the pairs $(u_3^{(0)}, t_3^{(0)})$ and $(u_3^{(1)}, t_3^{(1)})$ are total displacements and tractions at boundary Λ_0 in region Ω_0 and in the layer Ω_1, respectively. The total displacement $u_3^{(0)}$ and traction $t_3^{(0)}$, plus the free field traction $t_3^{ff(0)}$ and the free field displacement $t_3^{ff(0)}$, are all determined for region Ω_0. Finally, in the interior of the layers, the scattered and total wave fields are equal.

4.2 BEM formulation

The aforementioned family of BVPs is reformulated via boundary integral equations (BIE) using Betti's reciprocal theorem [23] in conjunction with the new type of fundamental solution for continuously inhomogeneous media with variable wave velocity profile. In what follows, BVPs 1-6 (see Fig.4.2) outlined in the previous

section are all discussed separately and the problem is classified into two categories in respect to the type of the seismic excitation: (a) Incident SH-wave and (b) SH-wave radiating from an embedded seismic source.

(a) Incident SH-wave

- BVP-1

The BIE is written in terms of the scattered wave field as follows:

$$cu_3^{sc}(x,\omega) = \int_\Gamma U_3^*(x,y,\omega)t_3^{sc}(y,\omega)d\Gamma - \int_\Gamma P_3^*(x,y,\omega)u_3^{sc}(y,\omega)d\Gamma; \quad x \in \Gamma = S_2 \cup S_{can} \cup S_{cav} \tag{4.9}$$

In the above, x, y are source and field points, respectively, c is the jump term, U_3^* is the fundamental solution of Eqn.(4.1), while $P_3^*(x,y,\omega) = \mu(x_2)U_{3,i}^* n_i(x)$ is the corresponding traction fundamental solution. Taking into account Eqn.(4.6) and the traction-free boundary conditions, Eqn.(4.3), the above BIE can be written for the total wave field u_3 as

$$c\Big(u_3(x,\omega) - u_3^{ff}(x,\omega)\Big) = -\int_\Gamma U_3^*(x,y,\omega)t_3^{ff}(y,\omega)d\Gamma - \int_\Gamma P_3^*(x,y,\omega)\Big(u_3(x,\omega) - u_3^{ff}(x,\omega)\Big)d\Gamma; \quad x \in \Gamma = S_2 \cup S_{can} \cup S_{cav} \tag{4.10}$$

The free-field wave motion appearing above is computed numerically, as described in the previous section.

- BVP-2 and BVP-3

The BIE is written for any continuously inhomogeneous layers as follows:

$$cu_3^i(x,\omega) = \int_{S_{\Omega_i}} U_3^{*(i)}(x,y,\omega)t_3^i(y,\omega)dS_{\Omega_i} - \int_{S_{\Omega_i}} P_3^{*(i)}(x,y,\omega)u_3^i(y,\omega)dS_{\Omega_i}; \quad x \in S_{\Omega_i} \tag{4.11}$$

Index i=1 for BVP-2 and i=1, 2 for BVP-3, while any surface is denoted by $S_{\Omega_i} = \Lambda_{i-1} \cup \Lambda_i$. Note that inside the continuously inhomogeneous layers we have that $u_3^{sc} = u_3$ and $t_3^{sc} = t_3$. In the case of N layers the above equation is generalized for i=1, 2...N. For semi-infinite domain Ω_0 with boundary Λ_0, the BIE formulation is as follows:

$$c\Big(u_3^{(0)}(y,\omega) - u_3^{ff}(y,\omega)\Big) = -\int_{\Lambda_0} U_3^*(x,y,\omega)\Big(t_3^{(0)}(y,\omega) - t_3^{ff}(y,\omega)\Big)d\Lambda_0 - \int_\Gamma P_3^{*(0)}(x,y,\omega)\Big(u_3^{(0)}(y,\omega) - u_3^{ff}(y,\omega)\Big)d\Lambda_0; \tag{4.12}$$

Here, the boundary condition given in Eq.4.8 is satisfied along the interface Λ_0 between the last soil layer Ω_1 and the elastic half-space (i.e., the seismic bed).

(b) SH-wave radiating from embedded seismic source

- BVP-4

Consider elastic waves emanating from a seismic source embedded at point (x_{01}, x_{02}). The BIE formulation for the total wave field is as follows:

$$cu_3(x,\omega) = \int_\Gamma U_3^*(x,y,\omega)t_3(y,\omega)d\Gamma - \int_\Gamma P_3^*(x,y,\omega)u_3(y,\omega)d\Gamma + f_{03}U_3^*(x,x_0,\omega); \quad x \in \Gamma = S_2 \cup S_{can} \cup S_{cav} \tag{4.13}$$

- BVP-5 and BVP-6

The BIE formulation for continuously inhomogeneous layers is the same as Eqn.(4.11), while the corresponding formulation for a homogeneous semi-infinite domain Ω_0 with a single boundary Λ_0 is as follows:

$$cu_3(x,\omega) = \int_{\Lambda_0} U_3^*(x,y,\omega)t_3(y,\omega)d\Gamma - \int_{\Lambda_0} P_3^*(x,y,\omega)u_3(y,\omega)d\Gamma + f_{03}U_3^*(x,x_0,\omega); \quad x \in \Lambda_0 \tag{4.14}$$

The numerical procedure followed here proceeds with discretization of all boundaries using simple "constant" type boundary elements (BE), and impose nodal collocation on Eqs.4.9-4.14. Thus, the following matrix equation system is formed for a given BVP, which can be used to solve all unknowns in terms of prescribed boundary conditions:

$$[\mathbf{G}]\mathbf{t} - [\mathbf{H}]\mathbf{u} = \mathbf{0} \tag{4.15}$$

The above system matrices **G** and **H** are the influence matrices that result from numerical integration using Gaussian quadrature of surface integrals containing the products of fundamental solutions and interpolation functions used for approximation of the field variables. They are fully populated matrices of size NxN, where N is the total number of nodes used in the discretization of all surfaces and interfaces, while vectors **u** and **t** now contain the nodal values of displacements and tractions at all boundaries.

Note that the displacement and traction fundamental solutions for the inhomogeneous model considered here exhibit the same singular behavior as those for the homogeneous case. By keeping in mind the asymptotic behavior of the frequency dependent fundamental solutions for small arguments, two types of singular integrals appear:

1. $\int_S U_3^*(x,y,\omega)t_3(y,\omega)dS$ with a weak singularity of order $O(lnr)$ and
2. $\int_S P_3^*(x,y,\omega)u_3(y,\omega)dS$ with a strong singularity of order $O(1/r)$

where r is the distance between source and receiver points. When using constant-type BE, Hoelder continuity conditions are satisfied at all collocation points along

smooth boundaries, so the singular integrals are of the Cauchy Principal Value type. Following the aforementioned computational steps of surface discretization, nodal collocation, evaluation of all surface integrals by numerical quadrature and imposition of the boundary conditions, a linear system of algebraic equations is obtained with respect to all unknowns of the BVP in question. Finally, the BEM numerical implementation is programmed using the Matlab [94] software code.

4.2.1 Fundamental solution for inhomogeneous media with variable wave velocity profile

The developed here BEM formulation employs a novel type of analytically derived fundamental solution proposed by Manolis and Shaw [41, 42]. As usual, the fundamental solution is a solution of the equation of motion (Eq.4.1) under a point load (with Dirac delta function $\delta(x-\xi)$ in the right-hand-side). The methodology is based on an appropriate algebraic transformation of the displacement vector of the type $u_3(x,\omega) = \mu^{-1/2}(x,\omega)U_3(x,\omega)$, which also modifies the right-hand-side of the equation of motion as $\mu^{-1/2}(x,\omega)\delta(x-\xi)$, where x,ξ is the source-receiver pair. This procedure results in a reduction of the original equation of motion with variable coefficients to one with constant coefficients with respect to the transformed displacement vector. Solution of the latter type of equations defined for an "equivalent" homogeneous medium are readily available, see Dominguez [23]:

$$\begin{gathered} U_3^{*hom}(R,\omega) = \frac{1}{2\pi\mu(x_2\to\infty)} K_0\left(\frac{i\omega R}{C_s(x_2\to\infty)}\right); \\ R = sqrt(x_1-\xi_1)^2 + (x_2-\xi_2)^2 \end{gathered} \tag{4.16}$$

where, K_0 is the modified Bessel function of second kind and zero order. Thus, the fundamental solution of Eq.4.1 attains the following form:

$$u_3^*(x,\xi,\omega) = \mu(x_2\to\infty)\mu^{-1/2}(x_2)\mu^{-1/2}(\xi_2)U_3^{*hom}(R,\omega) \tag{4.17}$$

The above form is conditional on the shear modulus and the density satisfying the following constraint equation, which dictates acceptable depth profiles for material parameters $\mu(x_2)$, $\varrho(x_2)$:

$$\frac{1}{4}\mu^{-1}\left(\frac{d\mu}{dx_2}\right)^2 - \frac{1}{2}\frac{d^2\mu}{dx_2^2} + \omega^2\varrho = \mu k^2 \tag{4.18}$$

The rather simple structure of Eq.4.17 indicates that the solution for an "equivalent" homogeneous medium is being scaled by the inverse of the square root of the shear modulus at both source and receiver locations.

4.3 Verification

Necessary first step consists of the validation procedure on the accuracy and convergence characteristics of the present BEM implementation. To this end, three test examples are conducted for which analytical and/or numerical solutions can be found in the literature. Given that, no results are currently available for the types of continuously inhomogeneous deposits depicted by the six BVP formulated above, the proposed methodology is verified by tests examples for homogeneous case. In particular, the velocity profiles used for inhomogeneous materials in the comparison studies is constant, i.e., $c = C_S^{bottom}/C_S^{top} = 1$, for wave velocities at the top and bottom of a soil layer.

As first test example here is considered half-plane with a semi-circle canyon of radius a subjected to time-harmonic SH waves of normal incidence, see Fig.4.3 for two variations of this BVP. The first is the same as the original BVP-1 in Fig.4.2, but for the homogeneous half-plane with material constants $\mu_0 = 123{\cdot}10^7 Pa$ and $\varrho_0 = 1850 kg/m^3$. Likewise, the second is essentially BVP-2 in Fig.4.2, but for a homogeneous finite layer of depth H_1=3a with the same values of material properties as before, i.e., $\mu_0 = 123{\cdot}10^7 Pa$ and $\varrho_0 = 1850 kg/m^3$. This layer rests on a half-plane, again with material properties μ_0 and ϱ_0. A non-dimensional frequency is introduced here as η=2a/λ_{S0}, where the wave length is $\lambda_{S0} = (2\pi/\omega)\sqrt{\mu_0/\varrho_0}$. This test example was solved analytically by Trifunac [4]. In Fig.4.3, the surface displacement amplitude $|u_3|$ is plotted versus normalized distance x_1/a at two fixed values of the normalized frequency, namely $\eta = 0.25$ (Fig.4.3c) and $\eta = 1.25$ (Fig.4.3d). A comparison between the two sets of results, and for both BVP, shows that they are practically identical, irrespective of frequency.

The BEM good accuracy and fast convergence characteristics were realized by a mesh refinement procedure that lead to 120 constant BE for BVP-1. More specifically, 24 BE were placed along the circumference of the semi-circular canyon, and the remaining along the free surface, split evenly and extending for a distance L = 20a from both sides of the canyon. For BVP-2, different meshes were used for different frequencies: (a) For $\eta = 0.25$ are used 82 BE along the free surface and another 82 BE along the layer-seismic bed interface extending to a distance L = 34a; (b) for $\eta = 1.25$ the number of BE went up to 219 along the free surface and another 219 BE along the interface extending to L = 22a.

Second test example considers the same topography as the previous one, with the difference that seismic waves are emanating from a line source of magnitude $f_{03} = 10^9 N$ embedded at point x_0(0,-5a), see Fig.4.4. The input data for the two BVP examined here are also the same as before. This particular problem was solved in Chapter 3 using two alternative BEM techniques, one employing

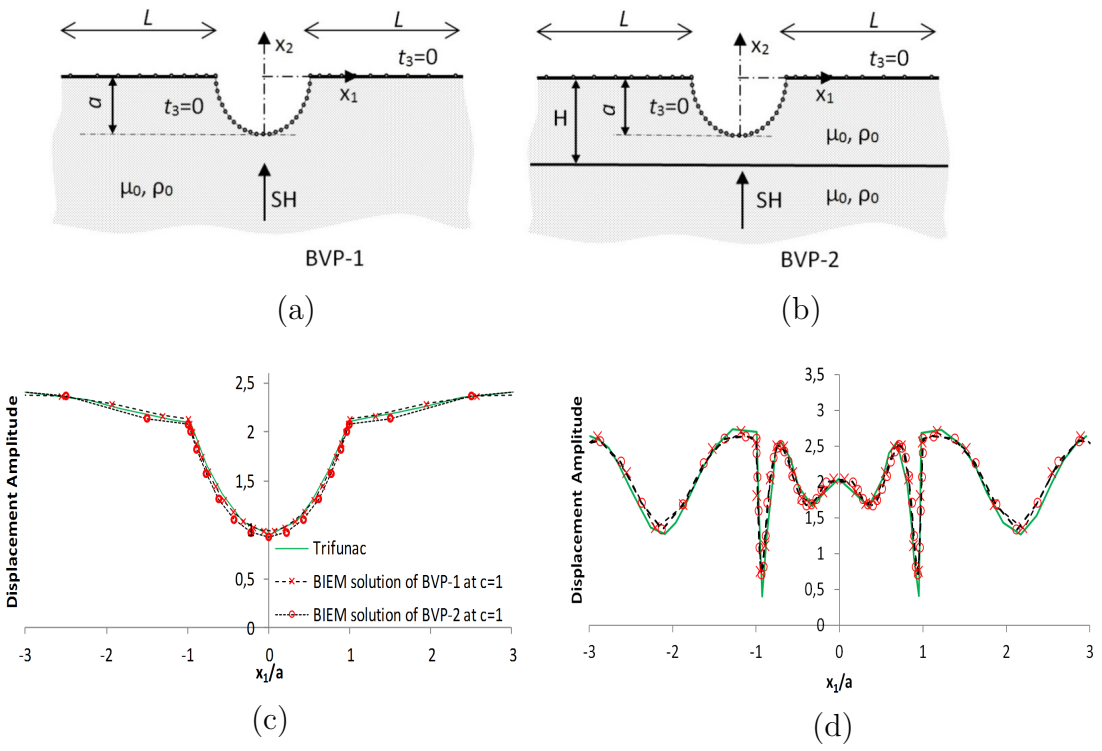

FIGURE 4.3: (a) Homogeneous half-plane; (b) homogeneous layer resting on bedrock: Displacement amplitude distribution along the free surface with a semi-circle canyon of radius a under a normally incident SH-wave with non-dimensional frequency (c) $\eta = 0.25$ and (d) $\eta = 1.25$

a Green's function for a half-plane and the other the fundamental solution for a full elastic space (i.e., basically the same approach as that used in this BEM formulation). The comparison in Fig.4.4 is therefore between these two BEM solutions and results are plotted for the displacement amplitude along the free surface of elastic homogeneous half-plane with the semi-circular canyon at two values of non-dimensional frequency $\eta = 0.25$ and $\eta = 0.5$. The BEM mesh used here comprised 140 BE along the free surface and another 140 ones along the interface boundary between the finite layer and the supporting half-space. The lateral extent of this mesh is $L = 20$a to both left and right of the edges of the canyon. In all cases, the results obtained here are in perfect agreement.

Equivalence of continuous and discrete model

In this section two different mechanical models, able to describe the inhomogeneous half-plane, are compared: (a) the continuously inhomogeneous model described in the present chapter with variable wave velocity profile and (b) the discrete model, which uses a stack of N flat horizontal layers of total height H that are isotropic and homogeneous with material properties μ_i, ϱ_i=1,2,...N. This stack rests on the elastic half-plane (i.e., the seismic bed) with shear modulus μ_0 and density ϱ_0. The dynamic load is a normally incident SH-wave of unit amplitude. As far as the latter model is concerned, the numerical model used is the wave number integration

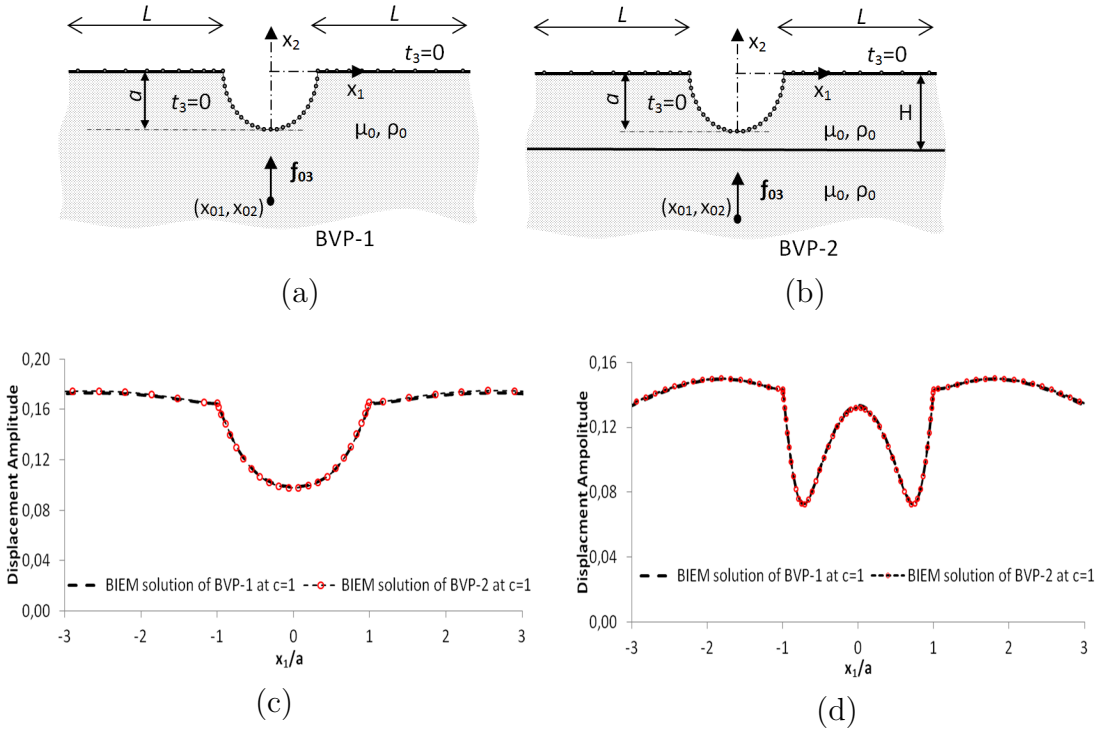

FIGURE 4.4: (a) Homogeneous half-plane; (b) homogeneous layer resting on bedrock: Displacement amplitude distribution along the free surface with a semi-circle canyon of radius a under waves radiating from a seismic source embedded at point (0,-5a) with non-dimensional frequency (c) $\eta = 0.25$; (d) $\eta = 0.50$

method (WNIM) [18] described and employed also in the previous chapter. For the former mechanical model, it is applied BEM based on fundamental solution for continuously inhomogeneous media developed herein. More specifically, the material properties at the top ($x_2 = 0$) of the continuously inhomogeneous deposit of depth H are denoted as μ_1, ϱ_1, while those at the bottom ($x_2 = H$) as μ_0, ϱ_0. Fig.4.5 depicts both these models, as well as the resulting SH wave velocity depth profiles for different frequencies in the interval $1-20Hz$. Next, the inhomogeneity coefficient is defined as $c = C_S^{bottom}/C_S^{top}$ for both discrete and continuous models and for a fixed value of the frequency f (in Hz). For a given value of the frequency f, the number of layers in the discrete model is adjusted so that the same velocity profile as is in the continuous model is reproduced. Finally, Fig.4.5 plots the displacement amplification factors, defined as the ratio of the displacement at the top to the displacement at the bottom, computed by both the WNIM utilizing the discrete model and by the BEM utilizing he continuous model. Good agreement in the results obtained for both mechanical models is observed, indicating the correct implementation of the proposed here BEM.

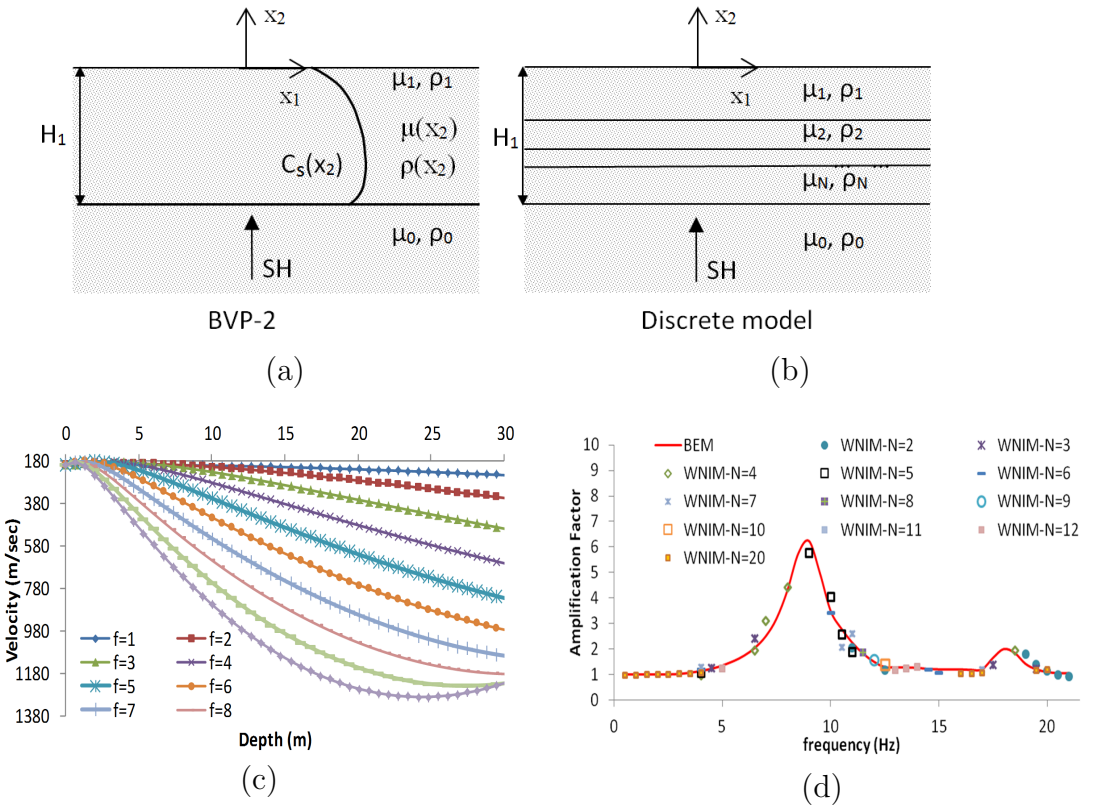

FIGURE 4.5: Comparison of the displacement amplification factor versus frequency f as computed for the continuous model of BVP-2 and for the "equivalent" layered model with sufficient number N of layers yielding the above velocity profiles as functions of depth and frequency

4.4 Parametric study

The aim of this section is to present results from several numerical simulations conducted in reference to the BVPs defined in Fig.4.2, which provide some insight on the effect of various parameters on the generation of synthetic seismic signals along the free surface of complex geological deposits. These key parameters are: (i) type and frequency of the propagating seismic wave; (ii) material inhomogeneity magnitude, as expressed with inhomogeneity parameter $c_n = C_{Sn}^{bottom(\Lambda_{n-1})}/C_{Sn}^{top(\Lambda_n)}$ for the n-th layer of the deposit; (iii) layering with interface boundaries of arbitrary shape; (iv) existence of free surface relief; (v) presence of buried cavities; (vi) overall geometric configuration of the deposit, and (vii) variability of the shear wave velocity with respect to depth and frequency of vibration.

In all numerical examples, free surface relief is in the form of a circular cylindrical canyon of radius a= $10m$. Either a single inhomogeneous soil layer of depth H = 3a (Fig.4.2 BVP2, BVP5) or two soil layers (Fig.4.2 BVP3, BVP6),

each of depth $H = 1.5$a is considered. The material properties have values of $\mu_{10} = Re(\mu_{10}) - i\omega\mu_{10}^{-} = 72{\cdot}10^6 - i\omega{\cdot}0.15Pa$, ϱ_{10}=$1800kgr/m^3$ at points ($x_1{\in}S_2$, $x_2 = 0$) for the BVPs with a single layer (Fig.4.2 BVP2, BVP5) and $\mu_{20} = Re(\mu_{20})i\omega\mu_{20}^{-} = 72{\cdot}10^6 - i\omega{\cdot}0.15Pa$, ϱ_{10}=$1800kgr/m^3$, again at points ($x_1{\in}S_2$, $x_2 = 0$) for the BVPs with two layers (Fig.4.2 BVP3, BVP6). In both cases, the layered structure rests on either a rigid or an elastic homogeneous substratum (i.e., a half-plane) with constant phase velocity $C_{S0}{\equiv}C_{S1}(\mathbf{x}{\in}\Lambda_0)$. Two sources of dynamic disturbance are considered, a normally incident SH wave or a seismic wave radiated by a source embedded in the homogeneous semi-infinite base at point (x_{01}, x_{01}). The layers above the base are continuously inhomogeneous with the inhomogeneity coefficient defined in the first and second layers as $c_1 = C_{S1}(\mathbf{x}{\in}\Lambda_0)/C_{S1}(\mathbf{x}{\in}\Lambda_1)$; $c_2 = C_{S2}(\mathbf{x}{\in}\Lambda_1)/C_{S2}(\mathbf{x}{\in}S_2)$, respectively, see Fig.4.2(BVP3, BVP6). In the case of a single layer (Fig.4.2 (BVP2, BVP5)) the inhomogeneity coefficient is defined as $c_1 = C_{S1}(\mathbf{x}{\in}\Lambda_0)/C_{S1}(\mathbf{x}{\in}S_2)$. Finally, the non-dimensional frequency is defined as η=2a/λ_{10}; $\lambda_{10} = 2\pi/\omega{\cdot}\sqrt{\mu_{10}/\varrho_{10}}$ in the case of a single layer structure (Fig.4.2 BVP2, BVP5) and η=2a/λ_{20}; $\lambda_{20} = 2\pi/\omega{\cdot}\sqrt{\mu_{20}/\varrho_{20}}$ in the case of two-layered structure (Fig.4.2 BVP3, BVP6).

The first series of numerical results present the displacement amplitude that develops along the free surface of a single, continuously inhomogeneous layer containing a semi-circular canyon, and resting over a perfectly rigid base (Figs.4.6 and 4.8) or on an elastic half-plane (Fig.4.7). The upward moving SH wave has either a low frequency of $\eta = 0.25$ (see Figs.4.6 and 4.7) or a high one of $\eta = 1.25$ (see Fig.4.8). The velocity profile for these solutions is a function of inhomogeneity coefficient c_1, and this profile becomes steeper as either c_1 or ω (or both) increase. The basic observations here are that (a) the presence of the canyon strongly perturbs the amplitude distribution in its immediate vicinity; (b) the presence of inhomogeneity serves to counteract this effect, in the sense that for high c_1 values the displacement amplitude profile becomes smoother; (c) a high frequency content in the incoming wave changes the rather smooth amplitude distribution into a highly irregular one; and (d) the presence of an elastic base results in a lowering of the amplitude values by almost 50% as compared to the rigid base. In essence, we have two mechanical phenomena occurring simultaneously, namely wave scattering due to the canyon geometry and wave dispersion due to the continuous layer inhomogeneity. Next, the influence of the presence of a buried line source is examined in Fig.4.9, where seismic waves at a low dimensionless frequency of $\eta = 0.25$ radiate from a point at depth (0,-4a) and from a point (4a, 0) along the horizontal plane. The amplitude of the displacement field is more pronounced in the former case, which resembles the vertically propagating SH-waves previously examined, as compared to the latter case. Also, in the latter case the influence of the canyon is more localized.

The presence of a buried circular cylindrical cavity simultaneously with a semi-circular canyon is next examined in Fig.4.10. The radius of the cavity is smaller

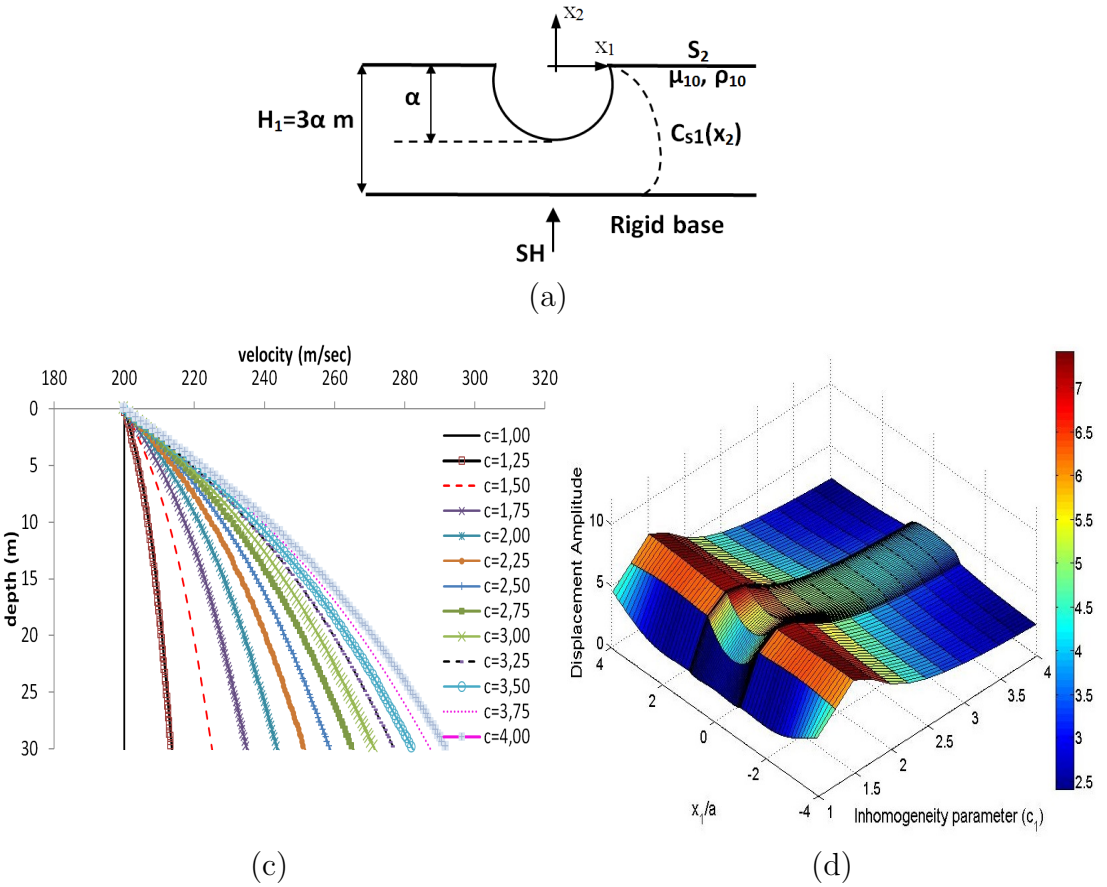

FIGURE 4.6: Displacement amplitude along the free surface of a continuously inhomogeneous layer containing a semi-circular canyon and resting on rigid base: The shear wave velocity profiles are shown above and the layer is swept by a normally incident SH wave with frequency $\eta = 0.25$

than that of the canyon and equal to $r_1 = 0.7$a, with two cases examined: (a) the cavity is centered at a shallow point with coordinates (2.5a, 0.95a) and (b) at a deeper point with coordinates (5a, 0.95a). Also, the continuously inhomogeneous deposit rests on a rigid base. Observe that the presence of subsurface discontinuity in relatively close proximity to the free surface produces non-negligible site effects, as can be seen by comparing Figs.4.6 and 4.10. The most striking feature is the high amplification (e.g., near doubling) in the surface displacement amplitudes. As before, the presence of material inhomogeneity serves to ameliorate this effect by smoothening the displacement distribution to values not much different from that of the incoming SH-wave, i.e., little amplification is observed. Furthermore, the cavity depth seems to have a rather minor influence on the surface amplitude spatial distribution in the present investigated case.

Next the two layer profile case is examined, as shown in Figs.4.11-4.13. At first, it is plotted the free surface displacement amplitude for this deposit resting on rigid base, and in the presence of a semi-circular canyon. The thickness of each layer is

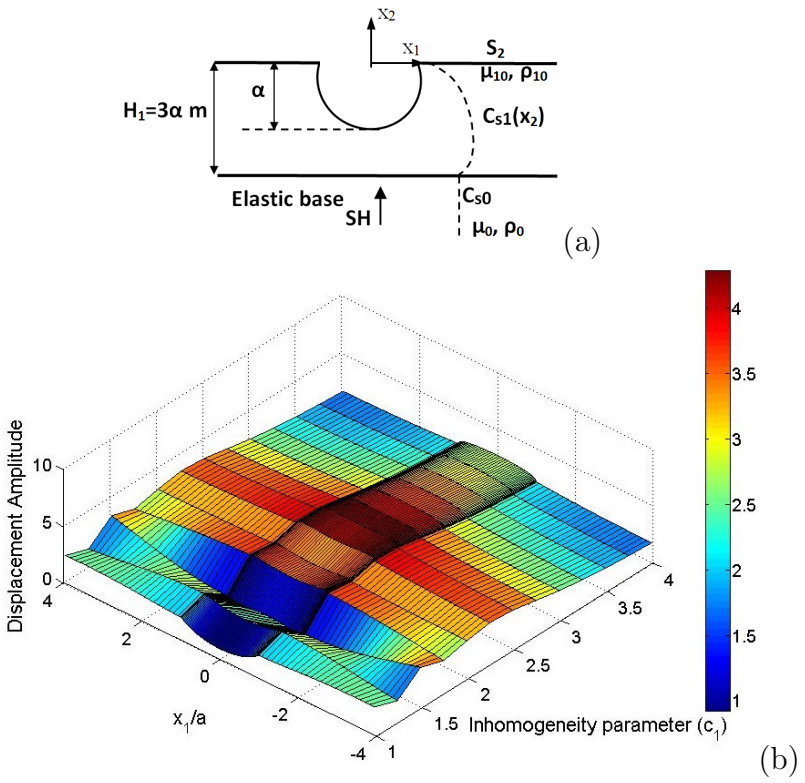

FIGURE 4.7: Displacement amplitude along the free surface of continuously inhomogeneous layer containing a semi-circular canyon and resting on an elastic base: The shear wave velocity profile was shown in the previous figure and the layer is swept by a normally incident SH wave with dimensionless frequency $\eta = 0.25$

$H = 1.5$a, so that the entire deposit thickness is the same as that in Fig.4.6. The dynamic input is a normally incident SH wave at a dimensionless frequency of $\eta = 0.25$. In Fig.4.11 three different inhomogeneity combinations are investigated for the two layers by specifying the following values to the inhomogeneity coefficients: (a) $c_1 = 2$; $c_2 = 4$; (b) $c_1 = 4$; $c_2 = 2$; and (c) $c_1 = 2$; $c_2 = 0.4$. These combinations result in increasing (case a) or decreasing (cases b, c) velocity profiles with depth, and in each case lead to markedly different response. The first case produces very high amplification, nearly triple the amount observed in Fig.4.6. The softening layers produce a nearly flat amplitude distribution, thus rendering the presence of the canyon practically irrelevant.

A more complete picture for the two-layer deposit previously described emerges in Figs.4.12 and 4.13, where the frequency variation is introduced in the results plotted for the free surface displacement amplitude. More specifically, the former figure is for the stiffening deposit with depth, case (a) with $c_1 = 2$; $c_2 = 4$ and the latter one for the softening deposit, case (b) with $c_1 = 4$; $c_2 = 2$. Observe high amplification values in all cases, the difference being that in the former case, they occur across the entire frequency range with factors ranging from $6 - 8$. In the

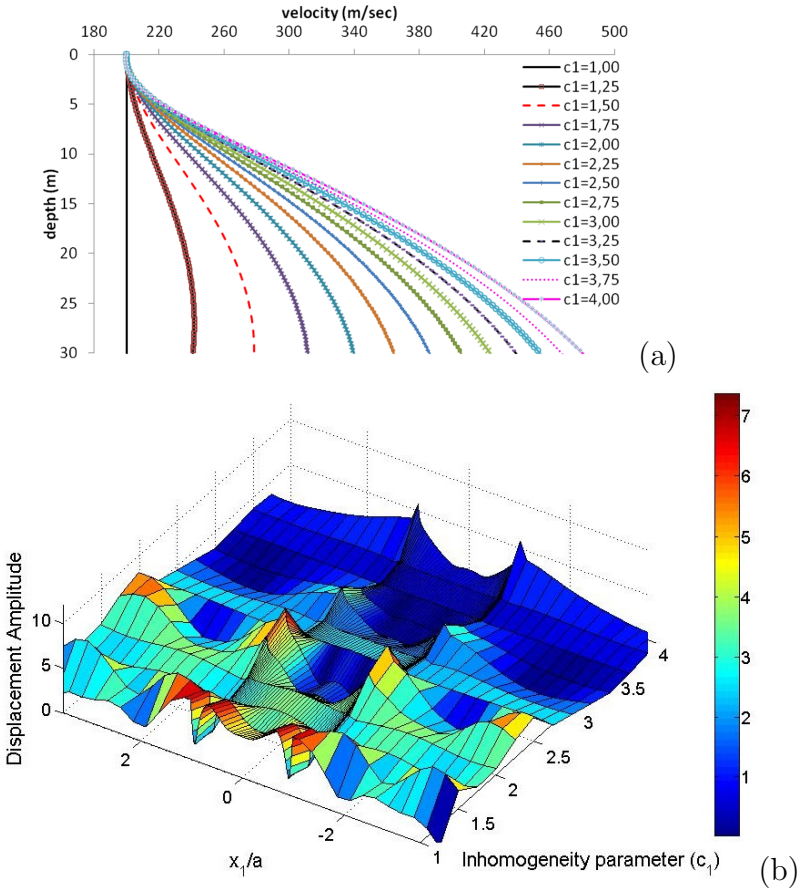

FIGURE 4.8: Displacement amplitude along the free surface of continuously inhomogeneous layer containing a semi-circular canyon and resting on rigid base: The shear wave velocity profile is shown above and the layer is swept by a normally incident SH wave with dimensionless frequency $\eta = 1.25$

latter case, these occur at low frequencies with amplification factors well in excess of 12, but dropping fast to 6 or less.

Figure 4.14 examines the influence of non-horizontal interfaces within the layered deposit that comprises two layers resting on bedrock and in the presence of a canyon. More specifically, the configuration (a) with $c_1 = 2$; $c_2 = 4$ is considered that corresponds to a stiffening wave velocity profile. The curved interface geometry has dimensions comparable to the canyon radius, in the sense that the peaks and troughs are of height 0.35a, while the width of a specific curve is 2a. This type of deposit is subjected to a normally incident SH wave and results are for the free surface displacement amplitude as a function of normalized frequency η. A comparison between Figs.4.12 and 4.14 reveals that the influence of non-flat interfaces is not that important, although noticeable: slightly higher amplification values are noticed on the free surface of the deposit across the frequency range examined herein.

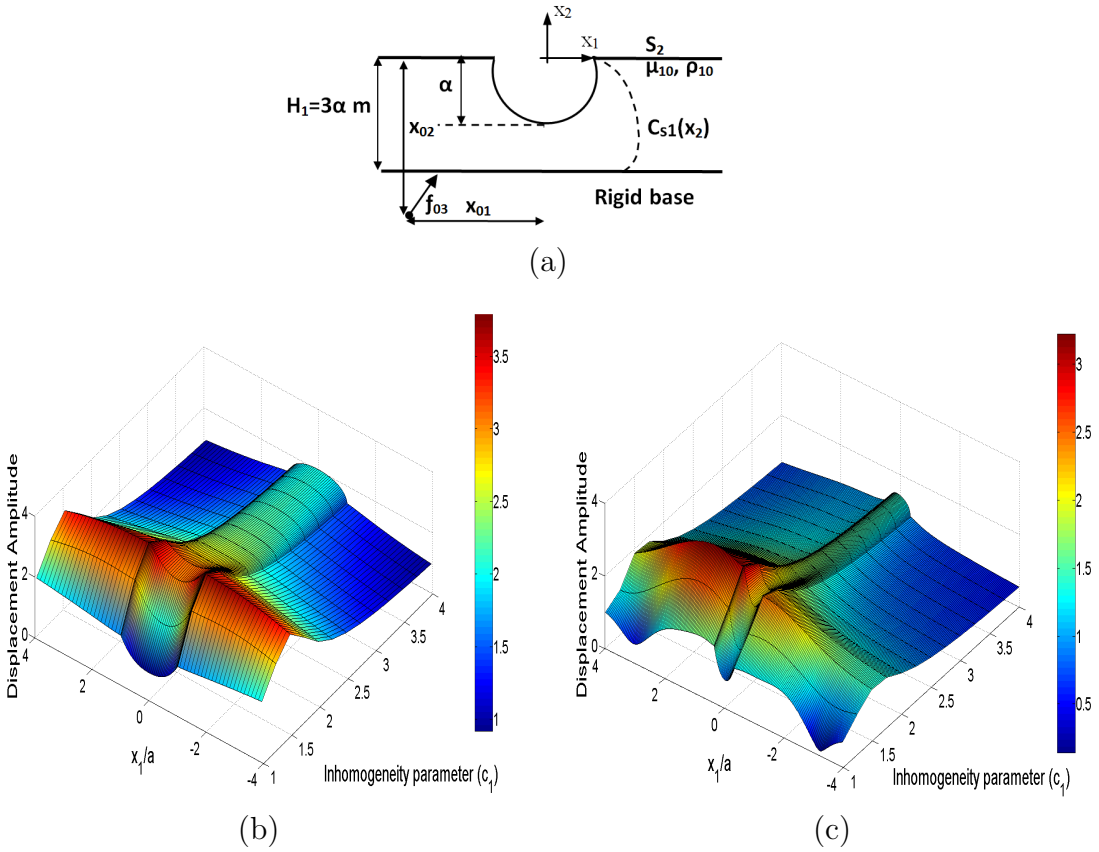

FIGURE 4.9: Displacement amplitude along the free surface of a continuously inhomogeneous layer with a semi-circular canyon and resting on rigid base: The input are seismic waves at dimensionless frequency $\eta = 0.25$ emanating from an embedded source located at points: (b) (0,-4a); (c) (4a,0)

Finally, Fig.4.15 plots transient seismic signals at the free surface and more specifically at both bottom and rim of the semi-circular canyon in a two-layer deposit resting on a rigid base. Consider the layer configuration that corresponds to a stiffening wave velocity profile with depth, i.e., case (a) with $c_1 = 2$; $c_2 = 4$. Also, both a horizontal and a curved boundary Λ_1 between the two layers is considered. The input is a normally incident Gabor pulse. Detailed description of the Gabor pulse and the input parameter are given in Chapter 3, Eq.(3.18). The solution for recovery of transient signals is accomplished by following the well-known numerical procedure as mentioned in the previous chapter. First Fast Fourier Transform (FFT) is applied to the governing equations of motion and the corresponding BVP in frequency domain is solved by BEM based on the frequency dependent fundamental solution for discrete values of frequencies. Finally, the inverse FFT is applied to the frequency domain solution to recover displacements, velocities and accelerations in the time-domain. Returning to Fig.4.15, observe that the Gabor pulse (whose frequency content is nearly white noise), at the free surface is hugely magnified due to the combination of complex geological deposit topography and material inhomogeneity, leading to wave dispersion phenomenon. More specifically, the aforementioned amplification effect registers values of over

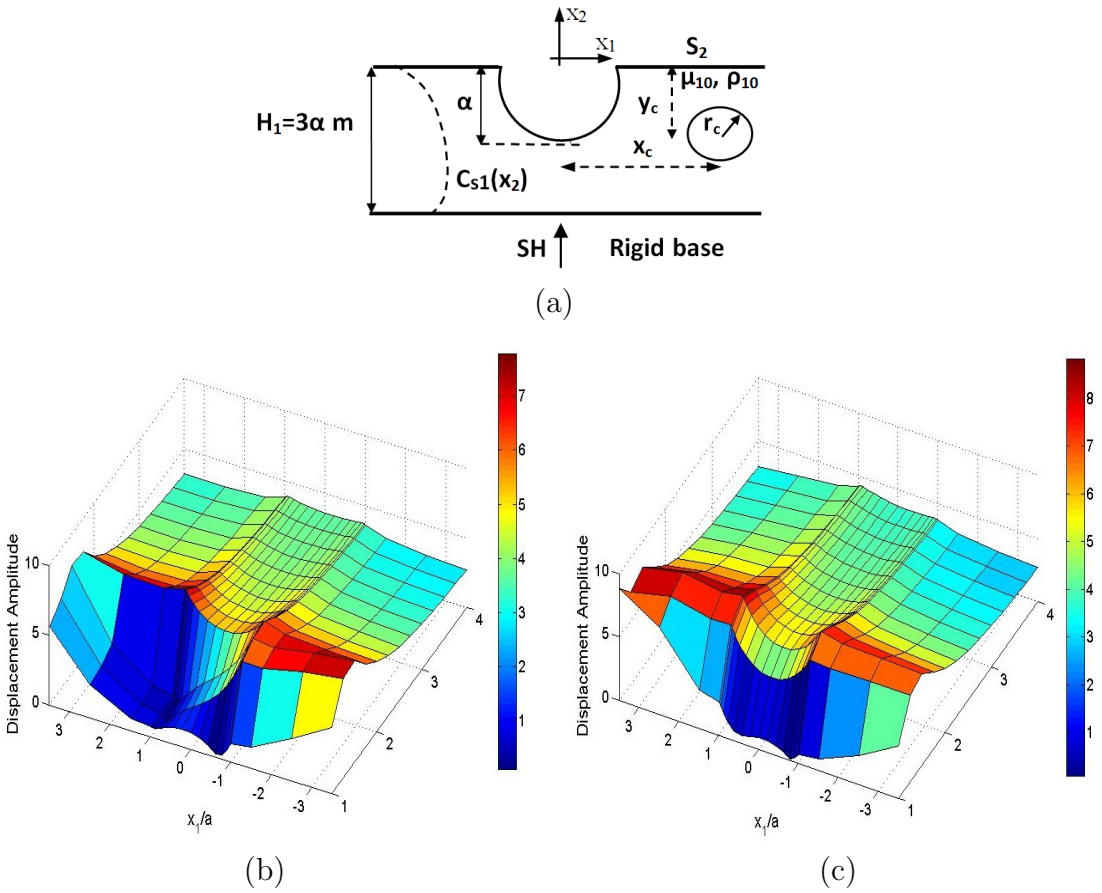

FIGURE 4.10: Displacement amplitude along the free surface of the continuously inhomogeneous layer resting on rigid base in the presence of both a semi-circular canyon and a circular cavity: SH waves with normal incidence and dimensionless frequency $\eta = 0.25$. The cavity radius is $r_1 = 0.7$a and centered at a point with coordinates (a) (5a, 0.95a); (b) (2.5a, 0.95a)

3 at the canyon bottom and of about 6 at the canyon rim, both occurring at a time interval comparable to the total duration of the Gabor pulse, i.e., $0.5sec$. As previously mentioned, the presence of curved instead of flat layer interface boundaries is of secondary importance.

4.5 Conclusions

Seismically induced wave motion in complex geological media comprising graded, non-parallel layers with different types of buried heterogeneities, plus the presence of free-surface relief is investigated. Numerical solution is accomplished by means of a new developed BEM defined in the frequency domain. The novelty of the proposed method lies in the use of a novel type fundamental solution for wave propagation in a continuum whose material properties vary continuously

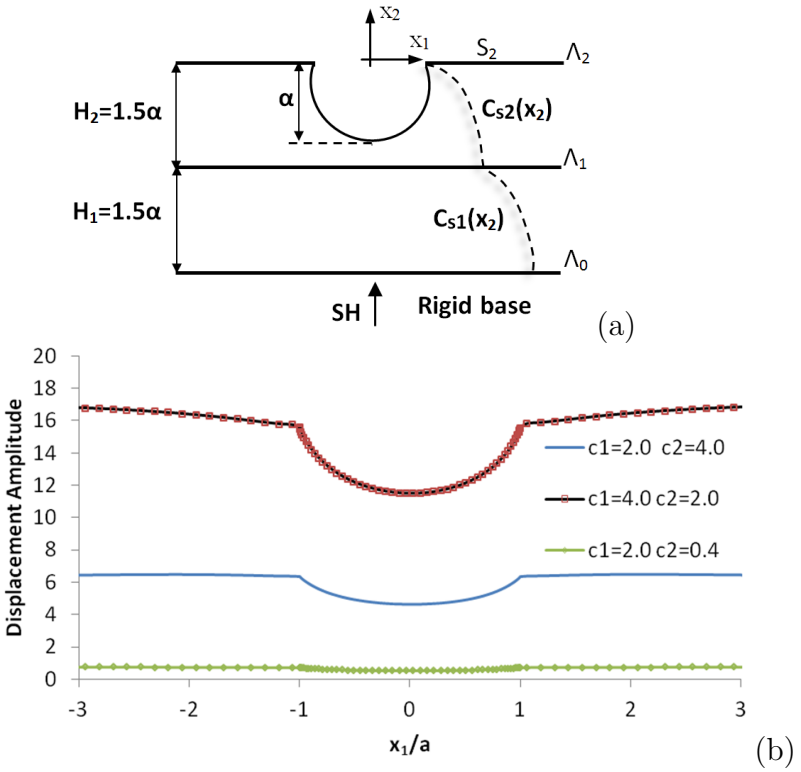

FIGURE 4.11: Displacement amplitude along the free surface of a two layer deposit containing a semi-circular canyon and resting on rigid base, under a normally incident SH wave with frequency $\eta = 0.25$. Results are plotted for different amounts of layer inhomogeneity

with depth, resulting in a wave velocity that is position-dependent. More specifically, direct modeling of inhomogeneity in term of soil velocity profile variation is achieved. Source code for the proposed BEM implementation is produced and its accuracy is verified against a series of benchmark-type problems appearing in the literature. From the numerical simulation results, the followings can be stated: (i) the magnitude of the material inhomogeneity and the resulting wave velocity variation with depth in a geological deposit, in combination with geometric discontinuities, leads to complex wave phenomena on the free surface that in turn are a strong indicator of near site effects; (ii) all three components of the problem, namely seismic source location, wave path inhomogeneity and local site heterogeneity are important in the generation of seismically-induced, free surface signals; (ii) the presence of non-parallel layers, free-surface relief and sub-surface cavities also add to the intensity of the free surface signals.

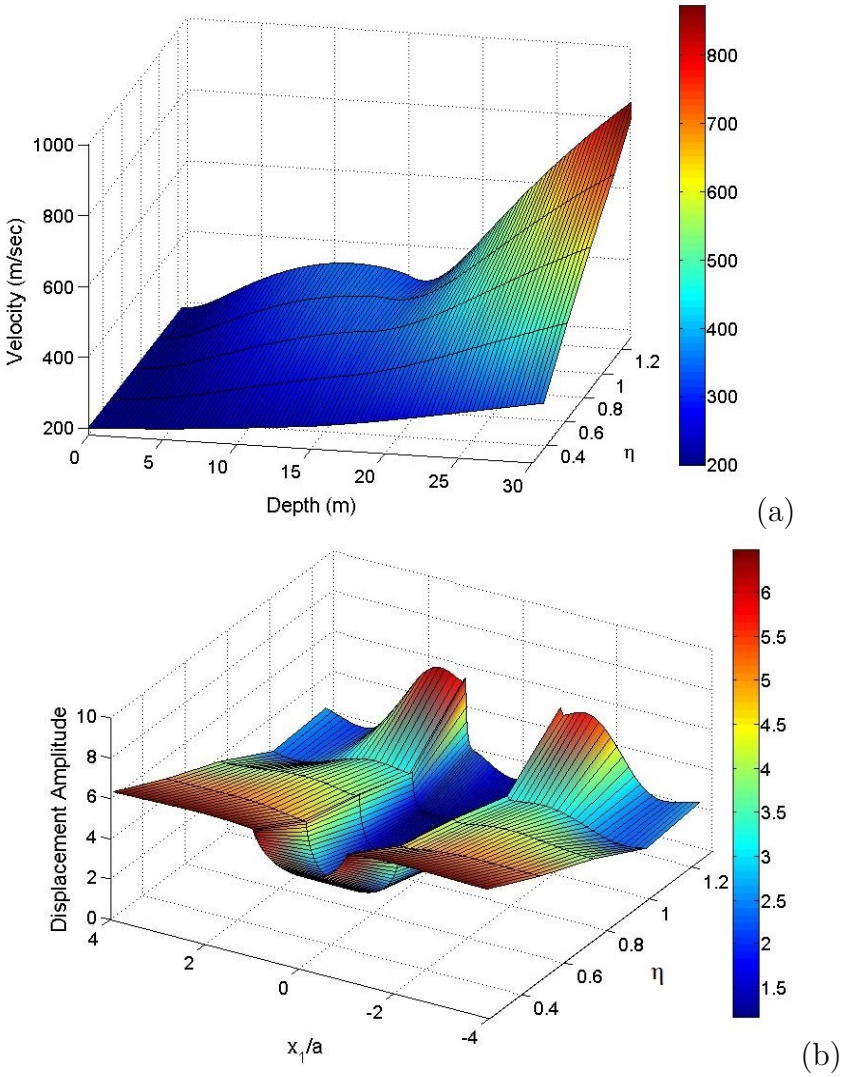

FIGURE 4.12: Two-layer deposit with inhomogeneity coefficients $c_1 = 4$, $c_2 = 2$, containing a semi-circular canyon and resting on rigid base, under SH wave with normal incidence: (top) The velocity profile; (bottom) displacement amplitude along the free surface as a function of frequency η

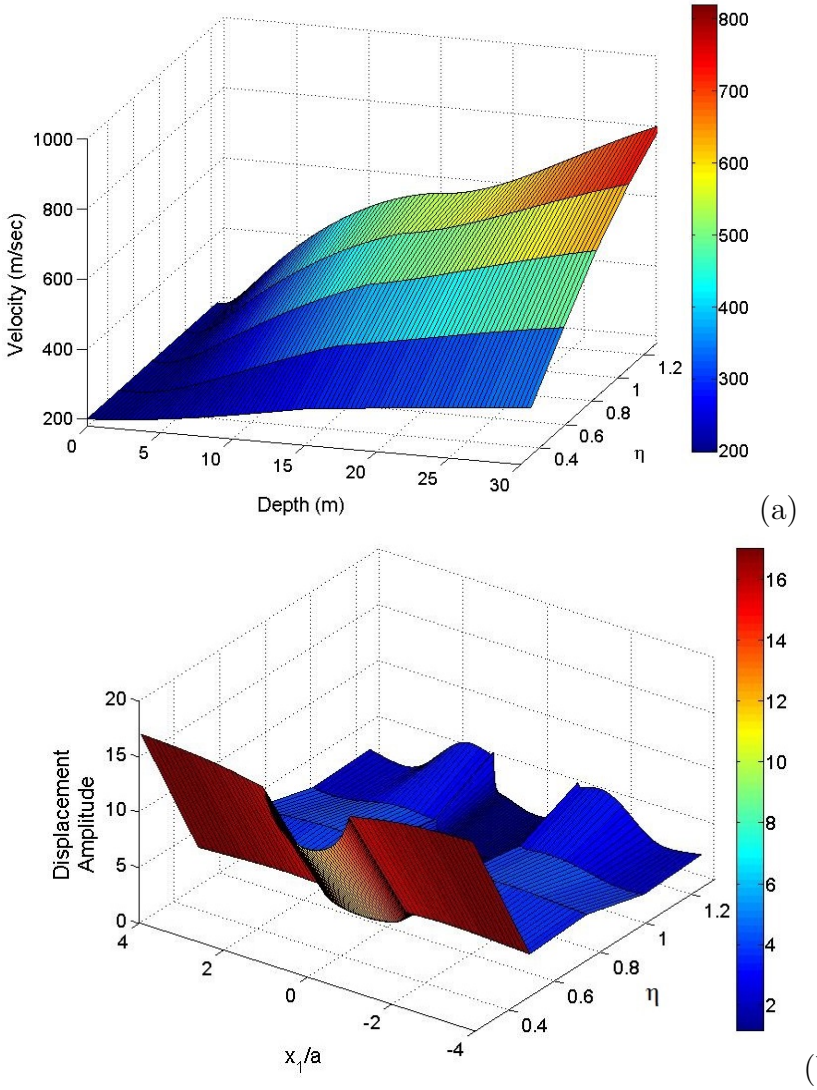

FIGURE 4.13: Two-layer deposit with inhomogeneity coefficients $c_1 = 2$, $c_2 = 4$, containing a semi-circular canyon and resting on rigid base, under SH wave with normal incidence: (top) The velocity profile; (bottom) displacement amplitude along the free surface as a function of frequency η

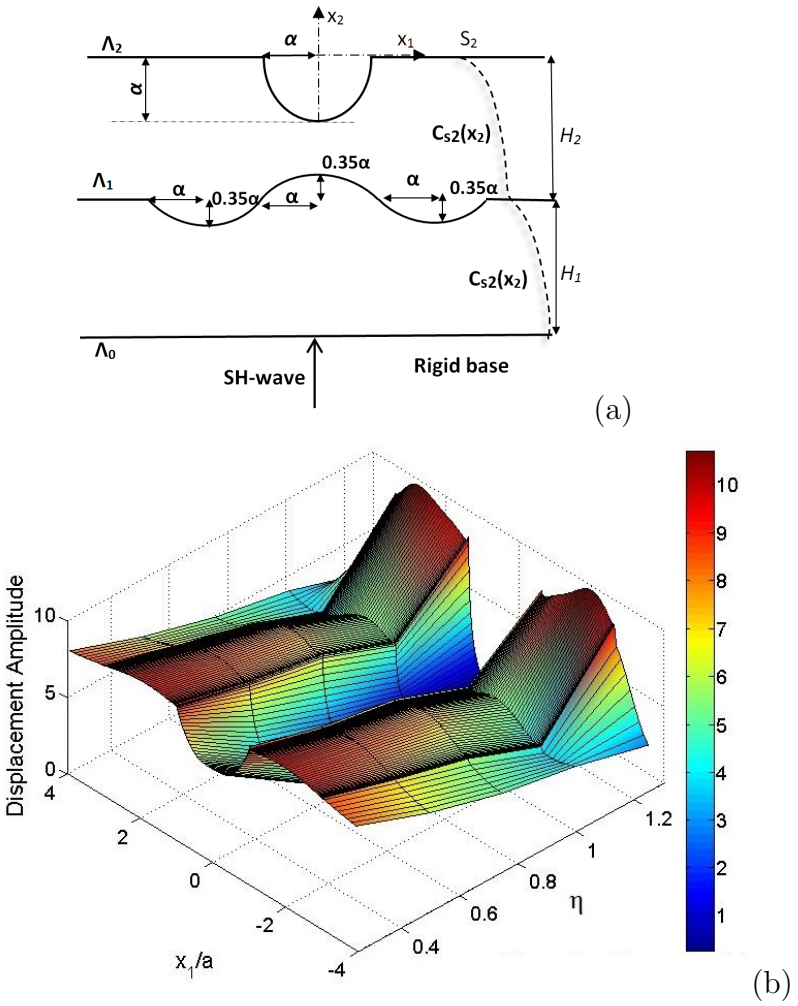

FIGURE 4.14: Displacement amplitude versus normalized frequency η along the free surface of a two layer profile with curved interface containing a semi-circular canyon, resting on rigid base and under SH wave with normal incidence: The inhomogeneity coefficients for the two layers are $c_1 = 2$, $c_2 = 4$

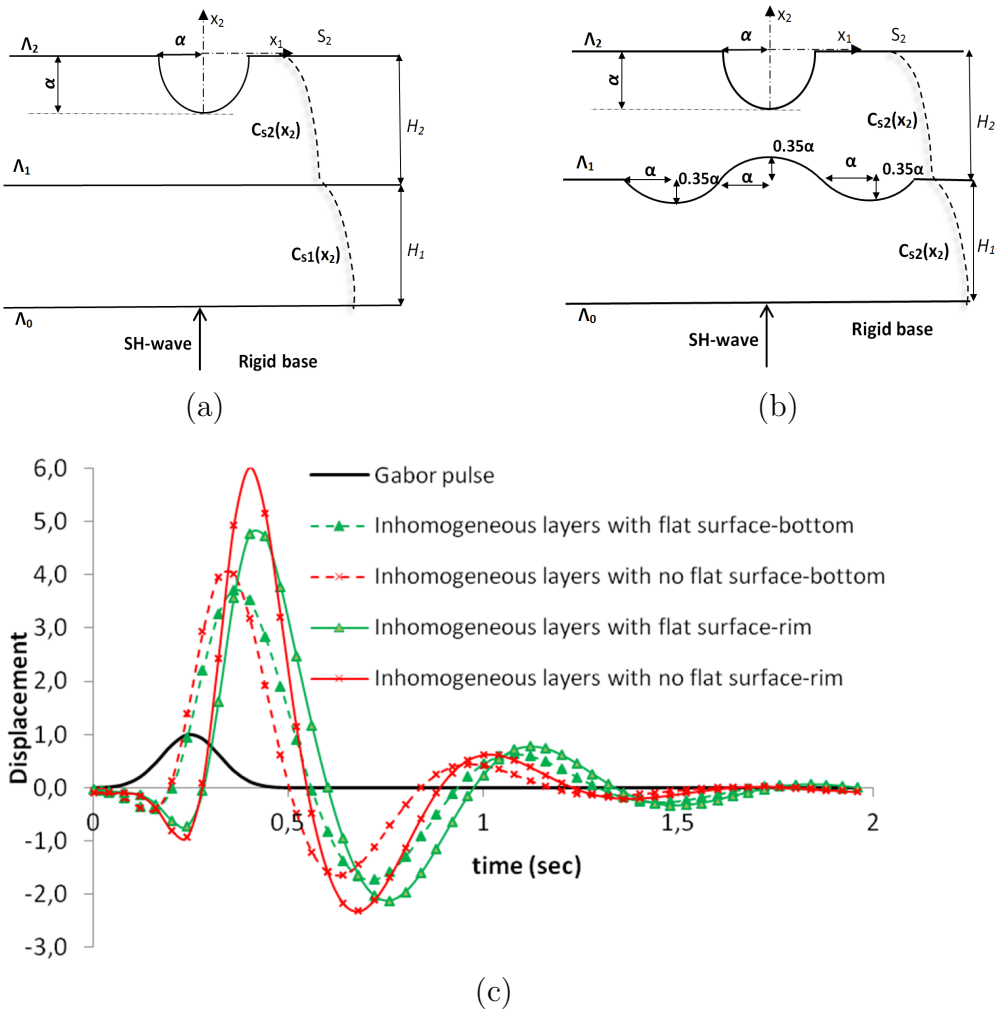

FIGURE 4.15: Synthetic seismic signals at the bottom and rim of a semi-circular canyon on the free surface of a two layer deposit with inhomogeneity coefficients $c_1 = 2$, $c_2 = 4$, resting on rigid base: Case 1 is for two inhomogeneous layers with horizontal interface and Case 2 is for two inhomogeneous layers with serrated interface

Chapter 5

Material modeling in geophysics

The present chapter gives an application in material modeling in seismic geology and serves to demonstrate the potential of the developed and proposed in the present thesis BEM models in reproducing wave motion phenomena in a continuous matrix with position-dependent material profiles, and containing any number, shape and configuration of cavities. The structure of this chapter has the following form: short introduction; problem statement; and numerical results. A number of cases involving perforated semi-infinite slab with position-dependent material properties and any number of cavities of arbitrary shape and position are solved in the frequency domain for pure elastic and poroelastic geological materials.

5.1 Introduction

The basic categories of materials used nowadays are man-made as metals, ceramics, polymers, composites and natural materials as the geomaterials. The structure of each category of all these materials is obviously different, while the stress and temperature fields that develop during their manufacturing, as well as during their use or due to their geological environment, affects them in different ways [105]. A paramount concern of modern manufacturing techniques for man-made materials is optimization of the material structure by using all available information, such as equilibrium data (i.e., phase diagrams) and non-equilibrium conditions (e.g., precipitation hardening). Equally important is the performance of components during their life cycle, as different engineering fields require materials with very specific characteristics. Problems that are common to all materials include corrosion and oxidation, failure analysis, degradation of electrical and magnetic properties, accurate specification of their characteristics, etc. All these problems concern also the geomaterials, of course having in mind their specific properties, environment, geological location, structure, etc. More specifically, when dealing with structural

type of components, the kinematic and stress fields that are generated in the material due to the influence of dynamically-induced loads are considered as key design parameters.

It is well known that abrupt change in material properties across interfaces between layers in composites and other types materials may result in large interlaminar stresses, which often lead to delamination phenomena and failure [106]. One way to overcome these effects is to produce functionally graded materials (FGM) with position dependent material properties. In principle, controlling the material gradation during the manufacturing process leads to the desired mechanical response characteristics. This feature provides freedom in the design of novel structural and mechanical components, so that FGM are believed to be the next generation of high performance materials [107]. As their use is extended to new frontiers, FGM structural integrity is fast becoming an increasingly important design criterion. In particular, FGM subjected to different type of mechanical loads during service may fail due to the presence of defects such as cracks, holes, inclusions, as well as the presence of sharp corners, joints, pores, etc., all arising during their manufacturing process. These defects become regions for potential stress field concentrations that initiate sudden brittle failure, which is a well-known fact in material science. Thus, a great deal of research has been conducted in recent decades to determine the formation of complex wave fields in solids with discontinuities of all types, see Zhang and Gross [108]. Note here, that geomaterials are naturally graded and strongly heterogeneous materials.

From another point of view, dynamically induced deformations in an elastic half-space (or in a specimen with finite dimensions) containing different types of heterogeneities is also of interest in solid mechanics and material science. The reconstruction of the displacement field along the free surfaces of the solid matrix and along the interfaces between the solid matrix and the heterogeneities forms the basis for nondestructive testing evaluation techniques used in establishing material reliability and performance issues [109]. More specifically, measurements of these dynamic displacement fields are used in calibrating numerical models of the specimens in question, which are subsequently used in tracing the evolution of damage. The problem of determining localized kinematic and stress distributions in an elastic matrix containing inclusions has been discussed in details in the past, but only for a homogeneous material structure. For inhomogeneous material structure one can read the study of Gao et al.[110] and Dineva et al.[86] where two dimensional crack analysis in inhomogeneous, isotropic and linear elastic FGM via BEM is presented. Exponential variation of Young's modulus and constant Poisson's ratio is considered. However, these studies are restricted to constant variation of the material wave velocity. Similar studies which employ FEM can be found in [111, 112]. In sum there is a limited number of results available for dynamic problems in graded solids with cavities or inclusions.

Along these lines, the aim of the present chapter is to demonstrate the efficiency of the herein developed BEM to deal with dynamic problems in graded half-plane with position-dependent material properties and pure elastic or poroelastic material.

5.2 Problem Statement and BEM solution

Consider in Fig.5.1 the material half-plane Ω with free surface S_f containing N cavities of arbitrary shape with common boundary $\Gamma = \bigcup_{k=1}^{N} \Gamma_k$, $k = 1, 2, \ldots N$, which is subjected to the following loads: (a) SH wave propagating in the plane $x_3 = 0$, tracing an incident angle θ with respect to the coordinate axis Ox_1; (b) a point force at source $x_0 = (x_{01}, x_{02})$. In both cases, time harmonic conditions are assumed to hold and the loads are functions of frequency ω. Next, the deformation mode is anti-plane strain and the only non-zero variables are the out-of-plane displacement component $u_3(x, \omega)$ and the stresses $\sigma_{i3}(x, \omega)$, $i = 1, 2$. The material is described by a position-dependent shear module $\mu(x_2)$ and a density $\varrho(x_2)$. The governing equation and corresponding boundary conditions are as follows:

$$\bigtriangledown \cdot \{\mu_0 \bigtriangledown u_3(\mathbf{x}, \omega)\} = -\varrho_0 \omega^2 u_3(\mathbf{x}, \omega) - \psi f_{03} \delta(\mathbf{x}, x_0); \quad x \in \Omega_0 \tag{5.1}$$

$$t_3(x_1, x_2, \omega) = \sigma_{3,j}(x_1, x_2, \omega) n_j(x_1, x_2) = 0 \quad for \quad \mathbf{x} \in S_f \cup \Gamma \tag{5.2}$$

In the above, n_i are the components of the outward pointing normal vector along a surface, index ψ is either equal 0 or 1 when the load is respectively an incident wave or a point load at x_0 with magnitude f_{03}. Also, $\bigtriangledown$ is the gradient operator, $(\bullet)$ is the inner product and a summation convention over repeated indices is implied. For an infinitely extending boundary, the Sommerfeld radiation condition is satisfied.

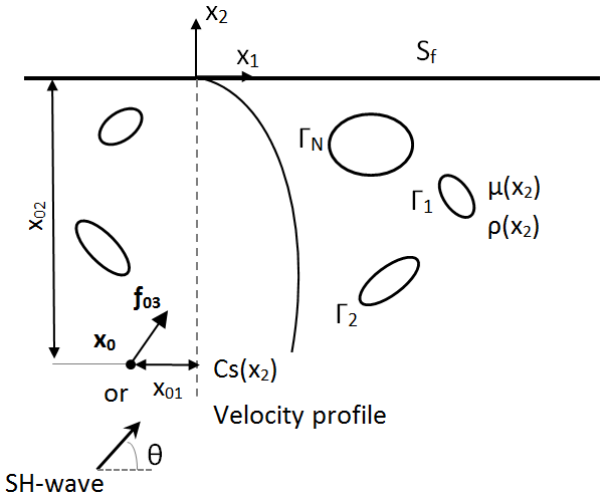

FIGURE 5.1: Perforated material slab with a variable shear wave speed profile

Three different types of inhomogeneity (i.e., material gradient) are now considered:
[1] *Type A*, where the material is isotropic elastic, but its density and shear modulus vary proportionally in a quadratic way in respect to the depth of the slab, yielding a macroscopically constant wave speed. The type A material gradient model is described in details in Chapter 3 and its magnitude is defined by the parameter b.
[2] *Type B*, where the material is viscoelastic (Kelvin-Voigt model) type and the shear modulus and density have an arbitrary variation with respect to depth. This yields a wave speed that is both frequency and position dependent. The type B material gradient model and its reference data are described in details in Chapter 4. Note that in the examined case here, the reference wave speed and wave number are defined as $C_S^0 = \sqrt{\mu^0/\varrho^0}$ and $k^0 = \omega/C_S^0$, respectively, at the free surface $x_2 = 0$, while $C_S^\infty = \sqrt{\mu^\infty/\varrho^\infty}$ and $k^\infty = \omega/C_S^\infty$ are their counterparts at great depth $x_2 = \infty$ and the magnitude of the material gradient is defined by the parameter $c = C_S^\infty/C_S^0$.
[3] *Type C*, with position-dependent shear modulus and constant density, i.e., $\mu = \mu(x_2)$, $\varrho = \varrho^0(0)$, yielding linear profiles in the wave speed as $C_S(x_2) = C_S^0(x_2)(1 + x_2/H)$. The magnitude of the material gradient is expressed by the parameter $H > 0$ defined in the interval $10^{-7} < H/\alpha < 10^{+7}$, where α is the characteristic heterogeneity length, see Luzon et al.[81], and $C_S(-H) = 0$.

Two BEM schemes are formulated, one using a Green's function for a graded half-plane [40] in the case of the material profile of Type A and another using a fundamental solution for the graded full-plane in the case of material profiles of Type B [40] and Type C [71]. Both of them are already described in Chapter 3, Eqn.(3.5) and Eqn.(3.6) and Chapter 4, Eqn.(4.13). Regarding the Type C material profile, a fundamental solution for media with linear variation of velocity profile is inserted in the BIE. This fundamental solution is developed by Sanchez-Sesma et al. [71] and later modified by Luzon et al. [81] and has the following form:

$$\begin{gathered} U_3^* = \Lambda \tfrac{i}{4mu^0} H_0^{(1)}(\omega\tau_S) \\ \Lambda = \tfrac{(H+x_2)}{H+\xi_2)}\sqrt{\tfrac{\tau_S C_S^0}{R_w}} = \tfrac{(H+x_2)}{(H+\xi_2)}\sqrt{2ln\left(\tfrac{R_2+R}{R_2-R}\right)\tfrac{(xi_2+H)(x_2+H)}{RR_2}} \\ \tau_S = t_S^0 \ln\tfrac{R_2+R}{R_2-R}; \quad t_S^0 = \tfrac{H}{C_S^0}; \quad R_2 = sqrt(\xi_1 - x_1)^2 + (\xi_2 + x_2 + 2H)^2 \\ (R_w)^2 = (\xi_1 - x_1)^2 + \xi_2 - [(x_2 + H)\cosh(\gamma\beta(0)\tau) - H]^2 \end{gathered} \tag{5.3}$$

In the above, x and ξ are source and receiver point respectively, $H_0^{(1)}$ is the Hankel's function of the first kind and zero order, τ_S is the travel time and R_w is the radius of the moving wave front. The derivation is based on the use of asymptotic ray theory. Note here that the fundamental solution for displacement and their corresponding traction in the inhomogeneous model exhibit the same singular behavior as in the homogeneous case, as the radial distance between source and receiver points tends

to zero. The corresponding computational steps for solving the formulated above BVP via BEM based on fundamental solution can be found in Chapter 4.

5.3 Verification study

Given the fact that there are no results in the literature for graded half-plane geomaterial profiles of Type A, B, C, even for the case of a single cavity, the developed BEM numerical schemes are validated by using test example for homogeneous half-plane as the degenerate case of all three types of profiles previously mentioned. In particular, Type A material profile degenerates to the homogeneous material structure when the inhomogeneity coefficient is $b = 0$, while the necessary value for this to happen for Type B material is $c = C_S^{\infty}/C_S^0 = 1$, and for Type C material it must be that $H \to \infty$; $\gamma = (1/H) \to 0$ and $\mu = \mu^0$; $C_S = C_S^0$, as well as $\Lambda \to 1$; $\omega\tau_S \to \omega r/C_S^0$; $R_w \to R$.

In order to verify the accuracy of both numerical BEM implementations that utilize the full-space fundamental solution and the half-space Green's function, results are compared with those obtained by Luco and de Barros [113]. These researchers applied an indirect BEM formulation to investigate the response of a homogeneous half-plane with a single circular cavity of radius a under normally incident SH waves. Fig.5.2 clearly establishes the high accuracy of the present BEM in terms of the absolute value of the normalized displacements $|u_3/u_{30}|$ along the free surface of the half-plane for two values of the incident SH wave frequency, namely $\eta = 0.5$ and $\eta = 1$. An additional parameter in this study is the cavity depth of embedment, where two values are used, namely $h/\mathrm{a} = 1.5$; $h/\mathrm{a} = 5$ corresponding to shallow and deep burial, respectively. The data for the reference matrix material are $\mu^0 = 123{\cdot}10^7 Pa$ and $\varrho^0 = 1850 kg/m^3$.

Starting with the BEM implementation based on the full-space fundamental solution, the mesh used to discretize the problem surfaces comprised 124 single-node (i.e., "constant") BE along the free surface and 44 BE along the cavity perimeter. The size of the discretized horizontal free surface is ± 22a from the center of the mesh, with the radiation boundary condition obviating the need for a larger surface mesh. For the BEM implementation based on the Green's function, the mesh comprises of only 22 constant BE along the circular cavity perimeter, since the presence of the free surface is automatically accounted for. To complete the picture, Fig.5.3 plots a comparison for the stress field normalized by the incident stress carried by the SH-wave along the cavity perimeter at observer points with polar angle ϕ in the case of homogeneous half-plane without any type of heterogeneities. Again, the resulting SCF is in excellent agreement with the results obtained by Luco and Barros [113].

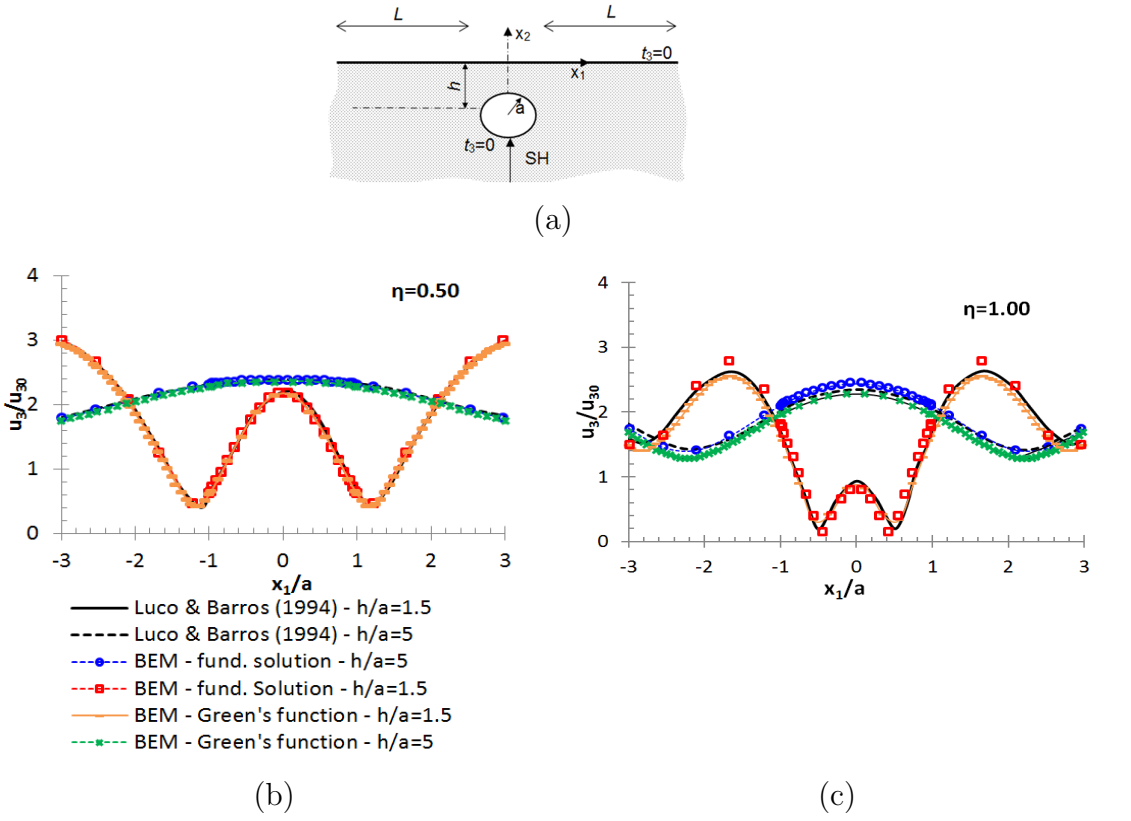

FIGURE 5.2: Displacement amplitude variation along the free surface of an elastic homogeneous half-plane with an embedded circular cavity of radius a under a normally incident SH wave with dimensionless frequency $\eta = 0.5$

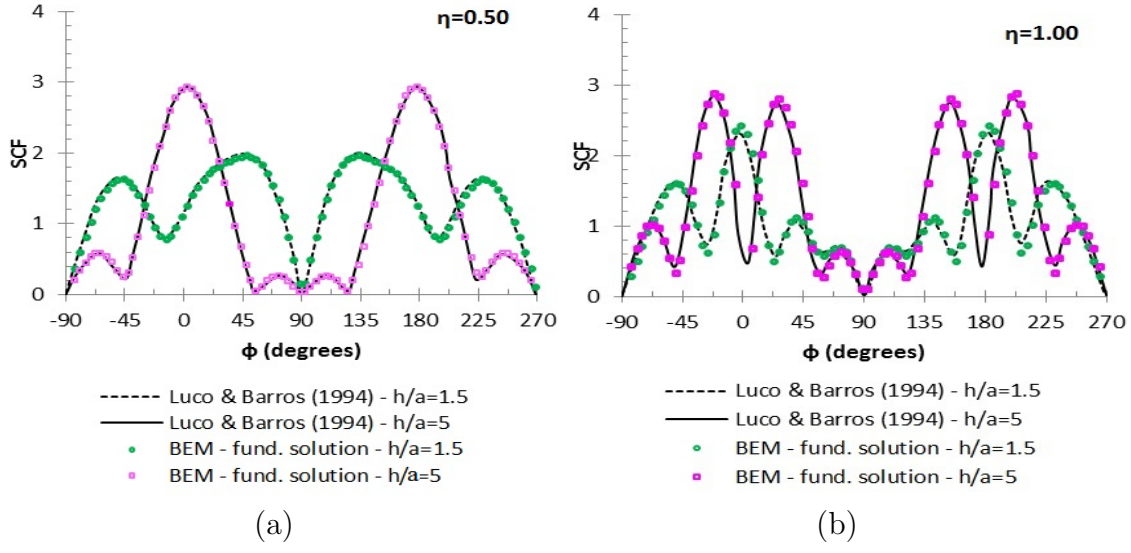

FIGURE 5.3: SCF along the perimeter of an embedded cavity of radius a in a homogeneous half-plane under a normally incident SH wave

The dynamic SCF along the perimeter of the circular cavity is defined according to Pao and Maw [114], as the ratio of the stress $\sigma_{\gamma\theta}$ along the circumference to the

amplitude of the incident wave's stress component $\sigma_0 = \omega\sqrt{\mu^0\varrho^0}$ at the same point when the cavity is in infinite homogeneous half-plane with μ^0, ϱ^0 and without any types of boundaries and heterogeneities. The stress along the circumference $\sigma_{\gamma\theta}$ is computed by the following formulae:

$$\sigma_{\gamma\theta} = -\sigma_{13}\sin(\theta-\gamma) + \sigma_{23}\cos(\theta-\gamma) \tag{5.4}$$

where θ is the incident wave angle and γ the polar angle of the observation point.

The same benchmark example is now solved for the case of a dynamic load concentrated at point (0, -5a) and for the normalized displacement amplitude that develops along the free surface, as obtained by both BEM numerical implementations. More specifically, Fig.5.4 gives two plots corresponding to two values of the load frequency η, and for a cavity with shallow burial. This way, the presence of the cavity is clearly manifested at the free surface, and especially so at the higher frequency value that corresponds to a wave length comparable to both cavity radius and depth of cover. Although there are some minor differences in the numerical results as obtained by the two basic BEM implementations using the basic fundamental solution and the Green's function for $\eta = 1.25$, agreement is satisfactory and can be further improved by extending the free surface discretization for the former implementation. Note that this particular example for a single cavity serves as the degenerate case for multiple cavities with the same radius a.

5.4 Simulation results

A series of numerical examples that follow serves to demonstrate the potential of the basic mechanical models described above in reproducing wave motion phenomena in a continuous matrix with position-dependent material profiles, and containing any number, shape and configuration of cavities [115]. The loads are assumed to be time harmonic and comprise both an incident wave sweeping the perforated slab or an embedded point load. Both kinematic and stress fields in the perforated matrix are recovered using the above mentioned BEM formulations as numerical tool. For the medium under consideration, the following data are used as the reference case, which corresponds to an equivalent homogeneous material with properties those defined at the free surface, namely, $\mu_0 = 72{\cdot}10^6 Pa$ and $\varrho_0 = 1800 kg/m^3$. The load consists of a concentrated force with magnitude $f_{03} = 10^9 N$ located at point (0, -5a). The material profiles under investigation are shown in Fig.5.5 for the shear modulus, the density and the wave speed. As previously mentioned, three basic material profiles are considered, namely Type A for which the stiffness is quadratic in terms of the depth coordinate, Type B for which it is variable and Type C for which it is linear. The last two types of material profiles exhibit a variation in the wave velocity profile.

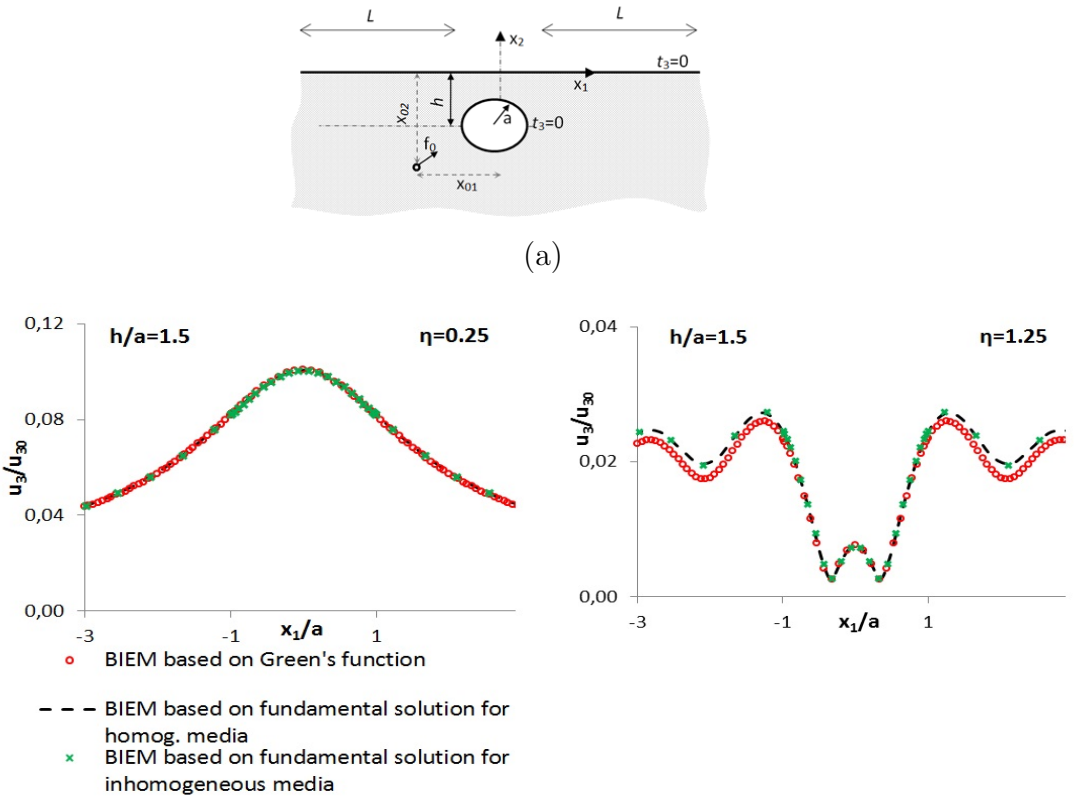

FIGURE 5.4: Displacement amplitude variation along the free surface of an elastic homogeneous half-plane with an embedded circular cavity of radius a subjected to a concentrated load at point x_0(0, -50a) for two values of the dimensionless frequency: $\eta = 0.25$ and $\eta = 1.25$

Figure 5.6 shows the influence of different models of inhomogeneity on the dynamic wave field of a perforated slab. In particular, displacement amplitudes are plotted across the free surface of an elastic, inhomogeneous graded half-plane with a single embedded circular cavity. There is a load applied at point x_0(0, -15a) at two frequency values of $\eta = 0.25$ and $\eta = 1.25$. All three material types are contrasted with the reference homogeneous case, and all have the same value of the material stiffness at the top and at a certain depth equal to $h = 150m$. It is clearly seen that the Type B material profile response diverges the most from the response of the equivalent homogeneous slab. In fact, at the higher frequency of $\eta = 1.25$ the difference between Type A, Type C and the equivalent homogeneous type is minimal, and it would be very difficult to distinguish the type of the material matrix is made of, if this plot was due to actual measurements. At the lower frequency of $\eta = 0.25$, the Type A material response is the one closer to the equivalent homogeneous case, simply because macroscopically the wave speeds are the same for these two materials. From here on, all results will be for Type B material profile, since this case results diverge the most from those obtained for a homogeneous material.

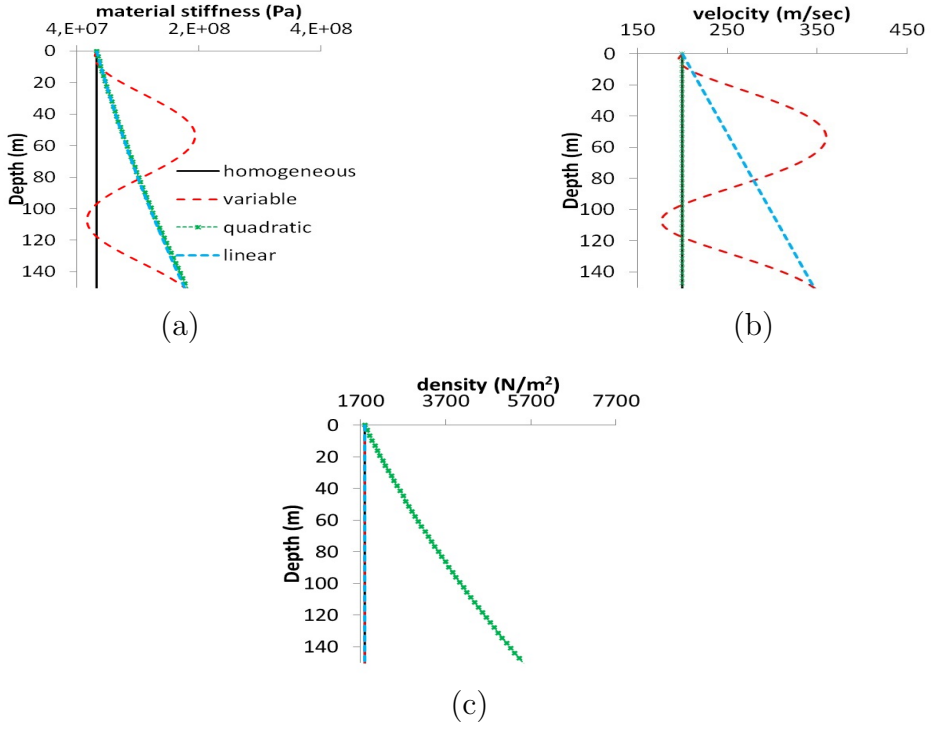

FIGURE 5.5: Three different material profiles used in the numerical simulations with the homogeneous medium serving as the reference case

In what follows, a series of numerical simulations are conducted to recover the dynamic wave fields that develop in a perforated slab, i.e., a half-plane with cavities. As will be seen, both kinematic and stress fields are highly dependent on wave interaction phenomena manifested between a cavity and the free surface, and between cavities. Furthermore, wave diffraction phenomena are added to the picture because of the inhomogeneous structure of the matrix material. Finally, the type of external load and its frequency content are also important parameters in this mechanical problem. The basic configuration consists of a perforated material slab with a free surface (i.e., a half-plane), as shown in Fig.5.7. More specifically, a single cylindrical cavity is chosen as the reference case to study cavity-free surface interaction phenomena, where points 1 and 2 along its boundary serve as observation positions. Next, two cavities arranged in the horizontally direction, and then again in the vertical direction, serve as the basic configuration for investigating cavity interaction phenomena. Finally, their combination in a three-cavity configuration serves as the final case. In addition, the cavity shape is investigated by considering, besides the circular cylindrical cavity, an elliptic cavity with horizontal semi-axis a and vertical semi-axis χa. This way, the cavity shape varies from a vertically elongated ellipse ($\chi > 1$) to horizontally elongated ellipse ($\chi > 1$). In the case of circular cavities, their center coordinates are placed at: (a) for one cavity $(0, -h)$; (b) for two cavities arranged vertically $(0, -h)$ and $(0, -h - d)$, where the depth from the free surface to the center of a cavity is $h = 0.5$a and the center-to-center distance between two cavities is $d = 2$a+0.5a; (c) for two cavities arranged horizontally $(0, -h)$ and $(d, -h)$; and (d) for three

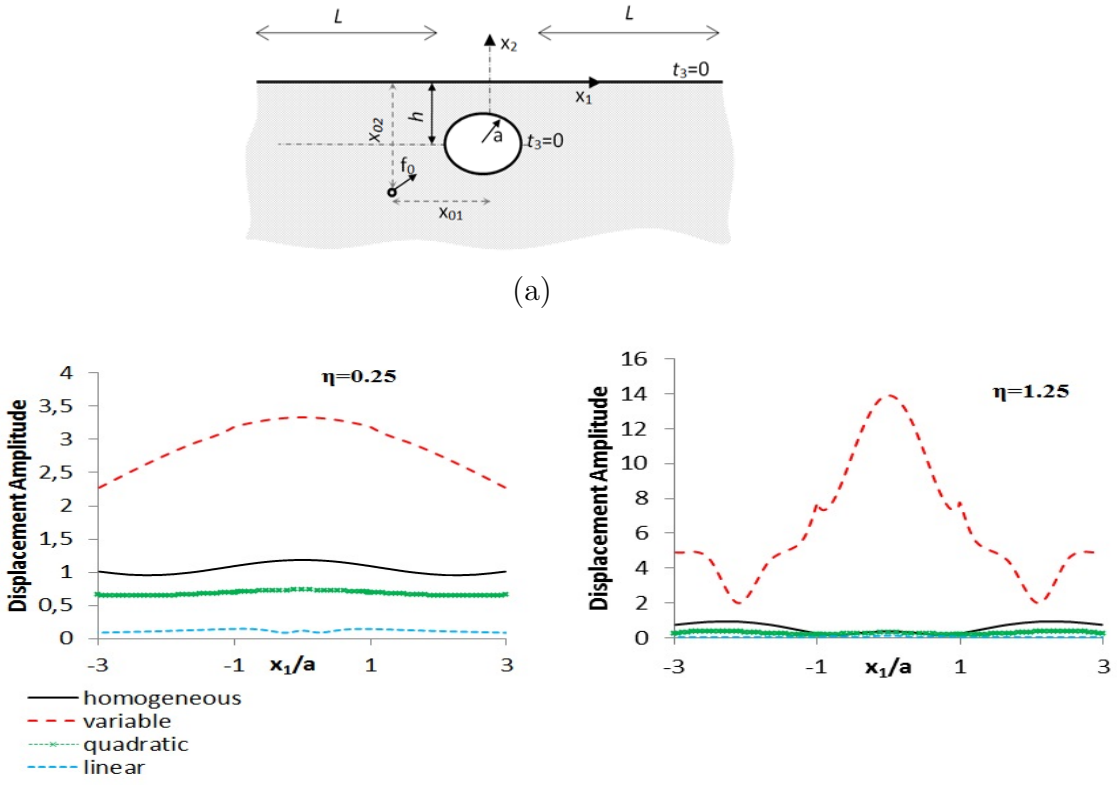

FIGURE 5.6: Displacement amplitudes along the free surface of the half-plane with an embedded circular cavity of radius a under a concentrated load at point x_0(0, -50a) for two values of the dimensionless frequency: $\eta = 0.25$ and $\eta = 1.25$: Comparison is between results obtained by model Types A,B,C for the case $\mu(x_1, 0)/\mu(x_1, h) = 1/2$

cavities $(0, -h)$, $(d, -h)$ and $(0, -h - d)$.

In Fig.5.8-5.10 the combined effects of multiple cavities of circular, horizontally and vertically elliptic shape, and the material gradient of the matrix on the displacement amplitude variation along the free surface are examined. The frequency of excitation of the incoming SH-wave has an intermediate value of $\eta = 0.5$. The first observation is that for circular cavities (Fig.5.8), the surface distribution of the displacements is quite similar, irrespective of the number of buried cavities. Basically, the amplitude magnitude increases with increasing inhomogeneity parameter c in all cases. This, however, is not true for elliptic cavities where the number of cavities and their orientation is just as important as the inhomogeneity.

Next, the same problem is investigated for multiple cavities of circular, horizontally elliptic and vertically elliptic shape, however in Fig.5.11-5.13 the stress

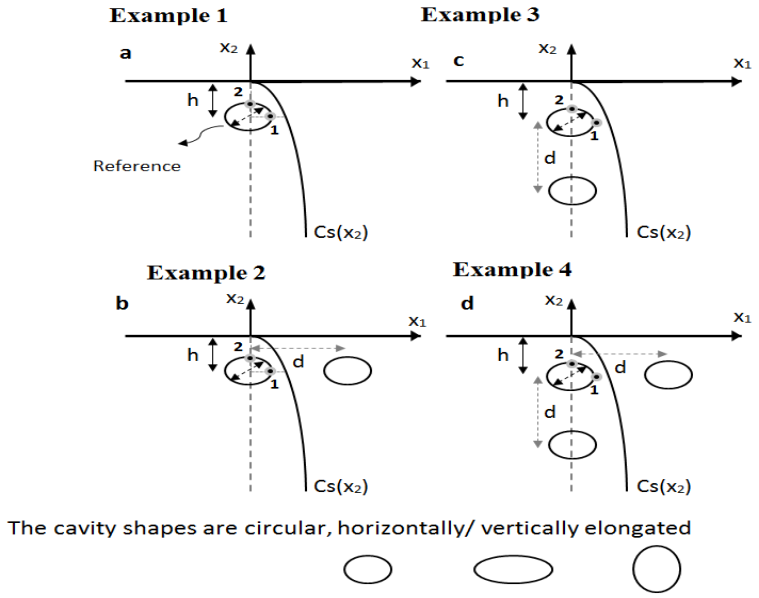

FIGURE 5.7: Four configurations (examples 1-4) ranging from one to three embedded cavities with two fixed receiver points (1 and 2) along the contour of the reference cavity

field distributions along the reference cavity perimeter for homogeneous case and two different values of inhomogeneity parameter c=3, 4 are presented. First, the effect of parameter c is indisputable: as its value increases, markedly different stress distributions are observed for a given cavity configuration. Next, stresses for circular cavities change slightly between one or two cavities, and only when a third is added do results start to differentiate considerably. This is not true for elliptic cavities, and especially if their placement is vertical: two cavities produce quite a different pattern compared to a single one, especially if they are placed one below the other. When three elliptic cavities are present, then stress distributions become markedly different.

The influence of frequency variation of displacement amplitude along the reference (first) circular cavity perimeter in the absence and presence of additional cavities, respectively, for both homogeneous ($c = 1$) and inhomogeneous ($c = 2$) materials is shown in Fig.5.11 and Fig.5.12 respectively. Observe in Fig.5.12 that the presence of additional cavities does not change the displacement distribution in the reference cavity when the slab material is homogeneous. In the presence of inhomogeneity in Fig.5.13, however, this is no longer true. The addition of extra cavities, especially when they are located parallel to the free surface, affects the reference cavity by a near tripling of the amplitude, and again at discrete frequency values. Strangely enough, the addition of an extra cavity directly below the reference one seems to have a beneficial result in sense that maximum recorded amplitude values are nearly half now, although both their spatial and frequency distributions are different.

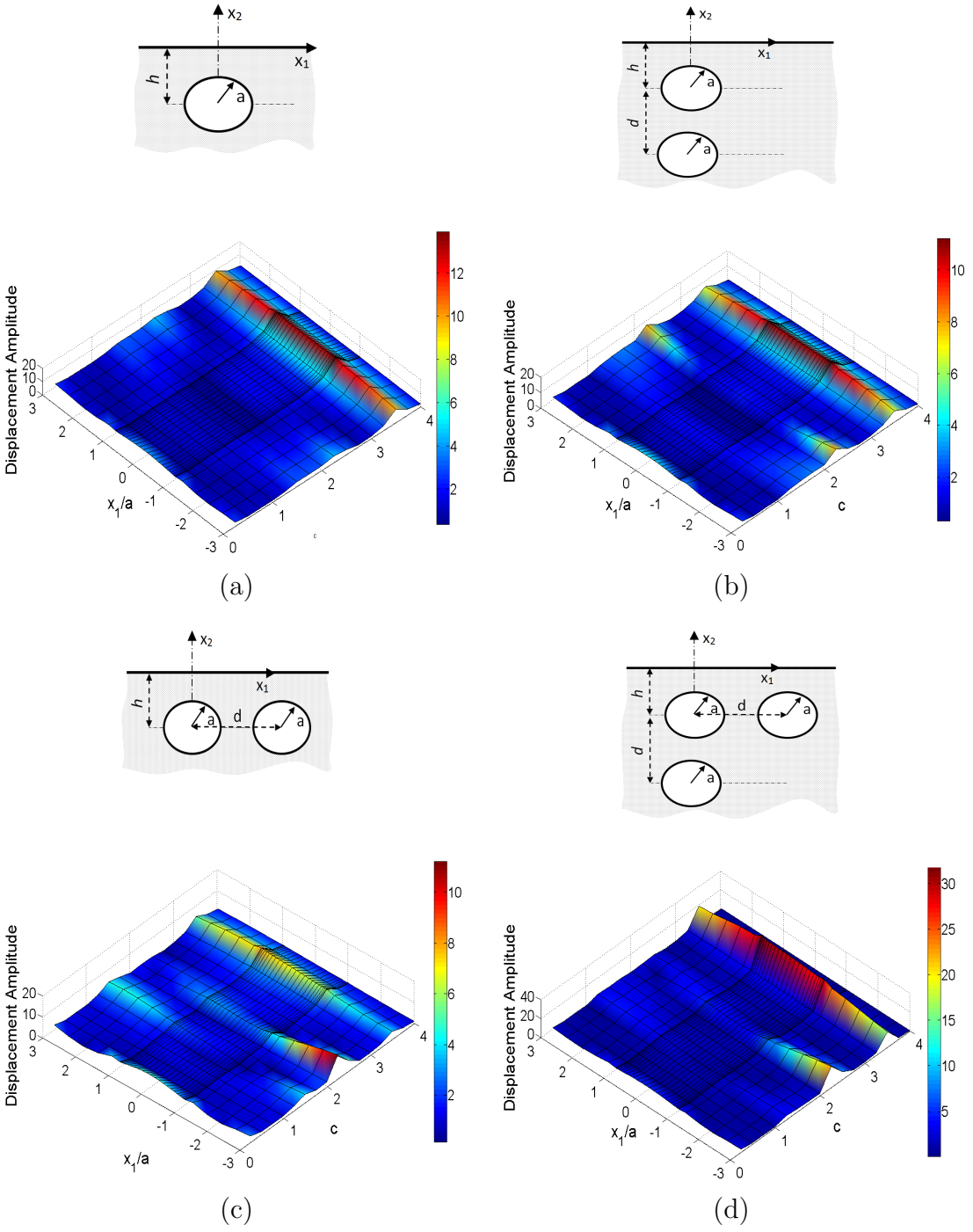

FIGURE 5.8: Displacement amplitude along the free surface of Type B half-plane with inhomogeneity parameter c due to a concentrated load at point x_0(0, -15a) with dimensionless frequency $\eta = 0.5$: All embedded cavities are circular with radius a

5.5 Poroelastic graded geological media

The present section addresses the problem of wave propagation in a graded half-plane containing multiple cavities and considering pure elastic and poroelastic

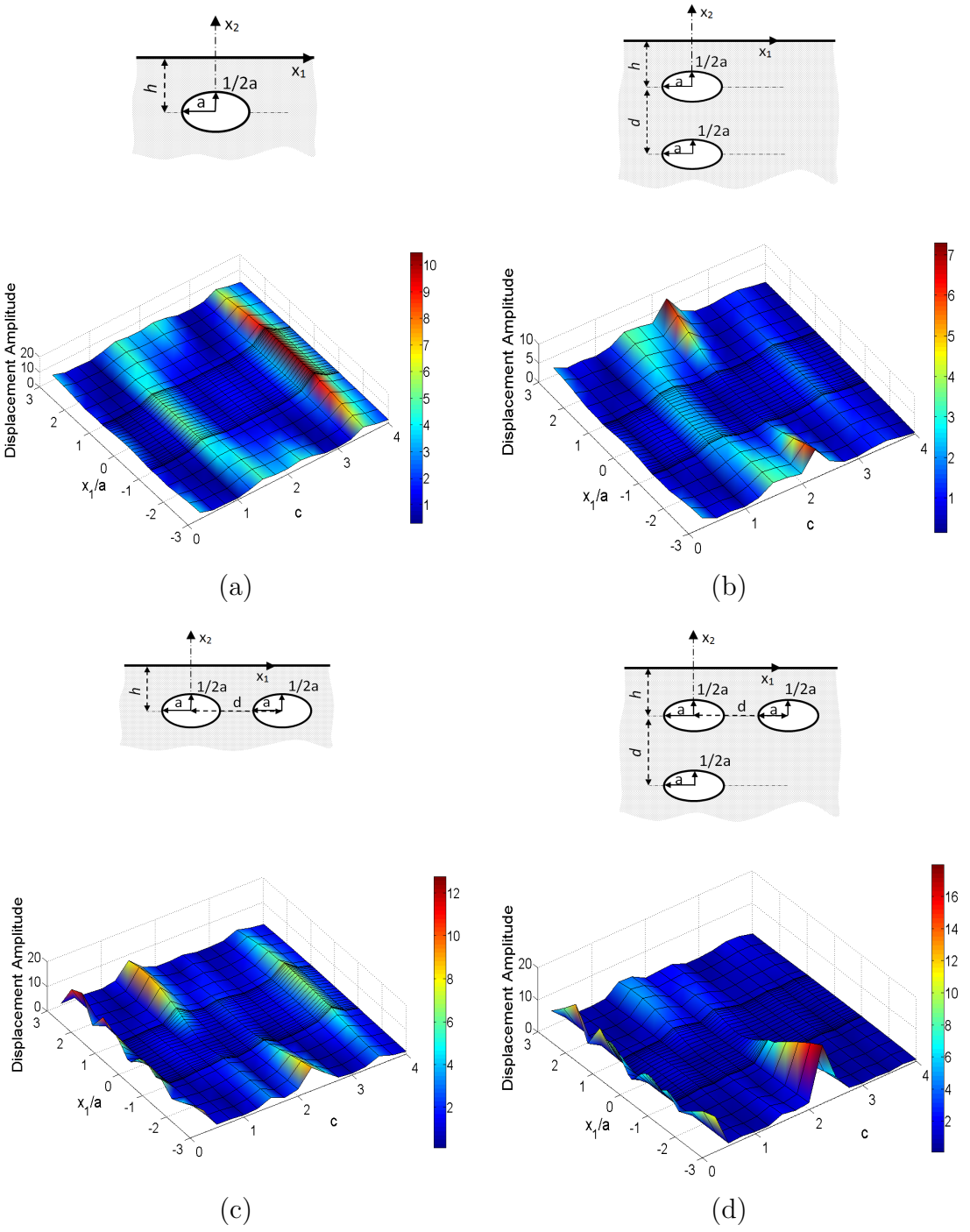

FIGURE 5.9: Displacement amplitude along the free surface of Type B half-plane with inhomogeneity parameter c due to a concentrated load at point x_0(0, -15a) with dimensionless frequency $\eta = 0.5$: All embedded cavities are horizontally elongated ellipses with semi-axes 0.5a and a

geological material [115, 116]. The poroelasticity is taken into consideration by the Bardet model [117]. The two-phase poroelastic dynamic behavior described

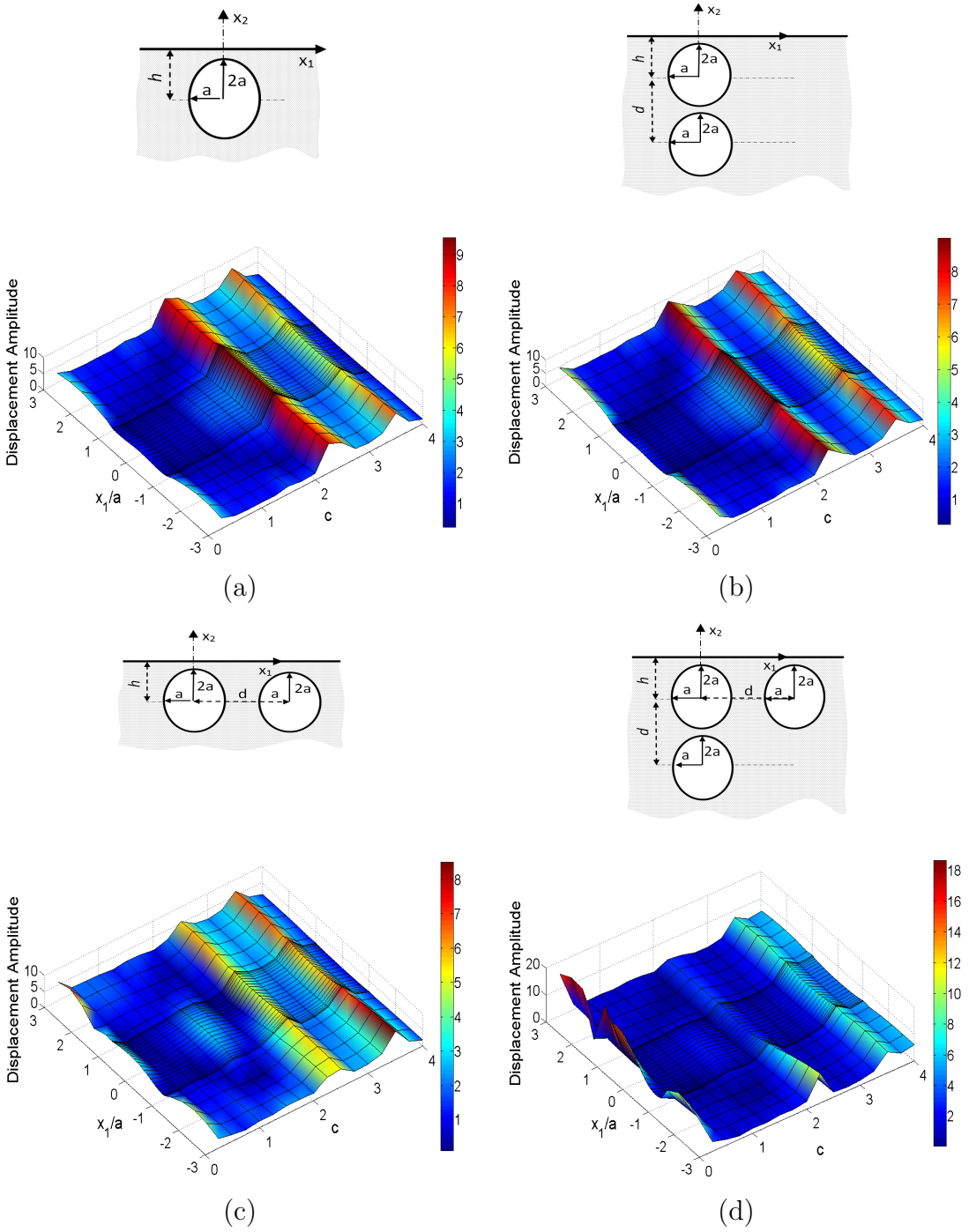

FIGURE 5.10: Displacement amplitude along the free surface of Type B half-plane with inhomogeneity parameter c due to a concentrated load at point x_0(0, -15a) with dimensionless frequency $\eta = 0.5$: All embedded cavities are vertically elongated ellipses with semi-axes a and 2a

by Biot's model [118] is approximated by the dynamic response of one-phase viscoelastic material.

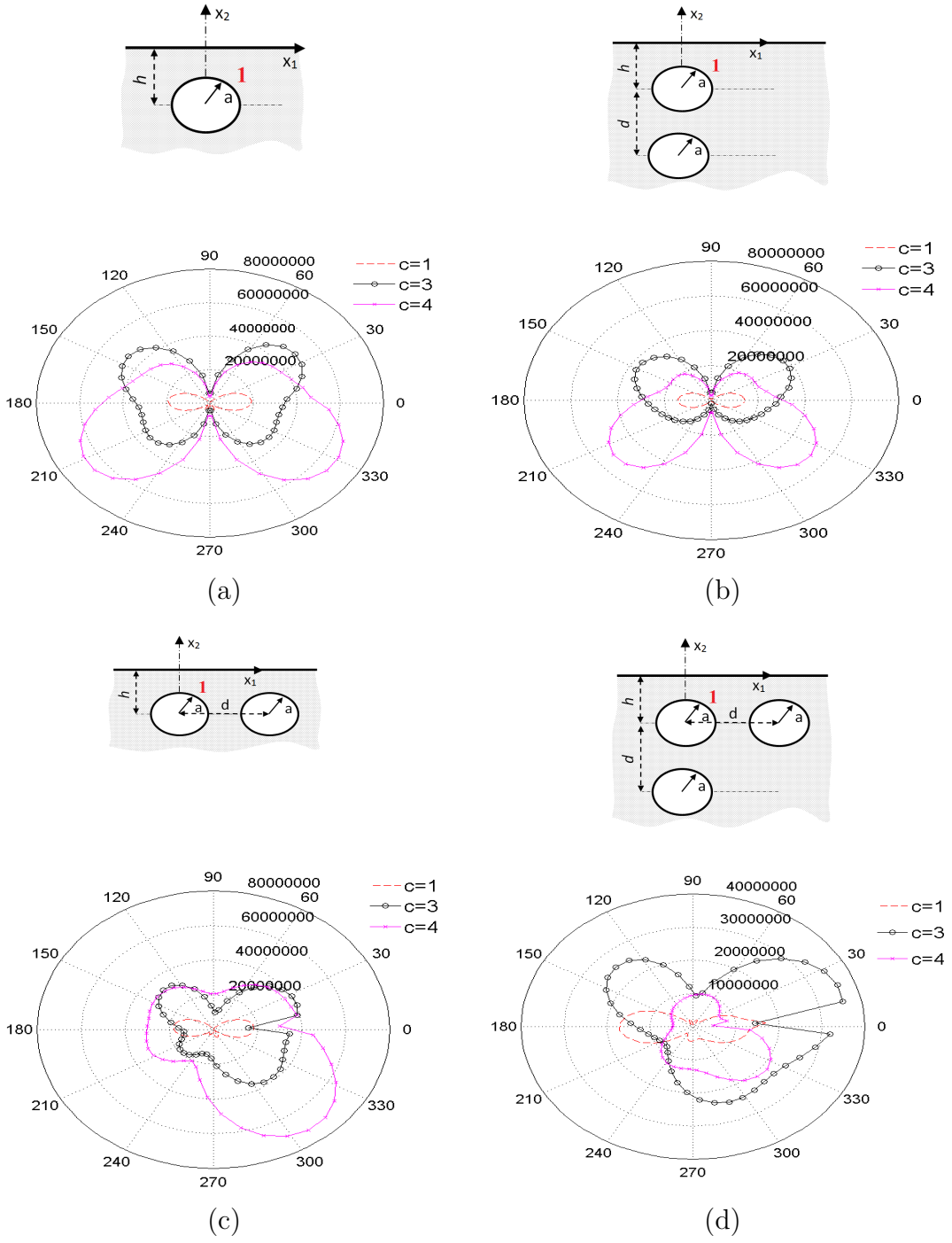

FIGURE 5.11: Stress distribution along the perimeter of a cavity in a half plane with inhomogeneity magnitude c at dimensionless frequency $\eta = 0.5$ due to an SH-wave emanating from an embedded source located at point x_0(0, -15a): All cavities are circular with radius a

Consider graded in respect to the depth viscoelastic half-plane Ω with free surface S_f containing N cylindrical unlined tunnels (or pipelines) with common boundary $\Gamma = \bigcup_{k=1}^{N} \Gamma_k$, $k = 1, 2, \ldots N$, subjected to seismic SH wave radiated

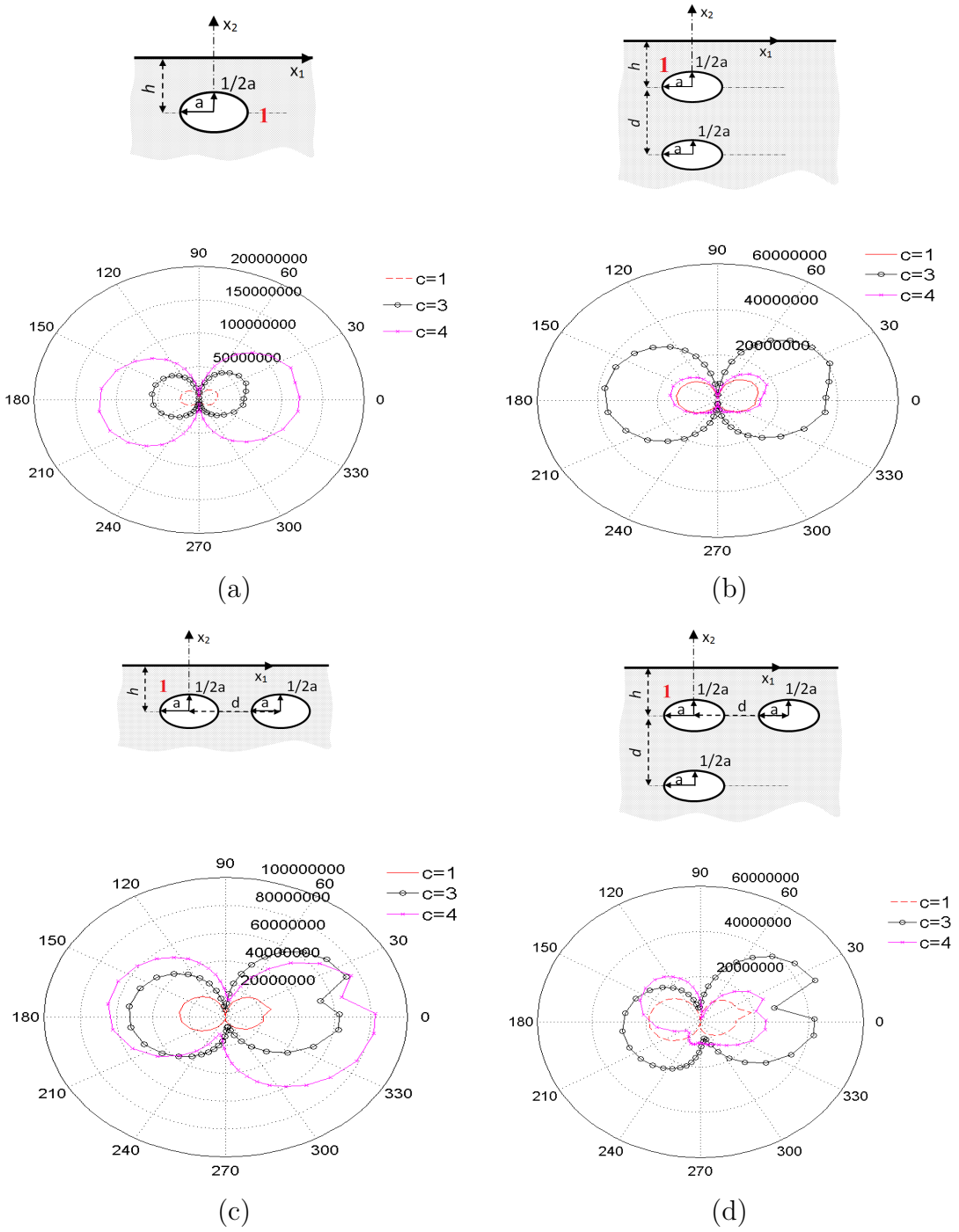

FIGURE 5.12: Stress distribution along the perimeter of a cavity in a half plane with inhomogeneity magnitude c at dimensionless frequency $\eta = 0.5$ due to an SH-wave emanating from an embedded source located at point x_0(0, -15a): All embedded cavities are horizontally elongated ellipses with semi-axes 0.5a and a

from a line seismic source acting as a time-harmonic body force with magnitude f_{03}, frequency ω and concentrated at a prescribed point $x_0 = x_0(x_{01}, x_{02})$, see Fig.5.1. For the state of anti-plane wave motion, the only non-zero field quantities

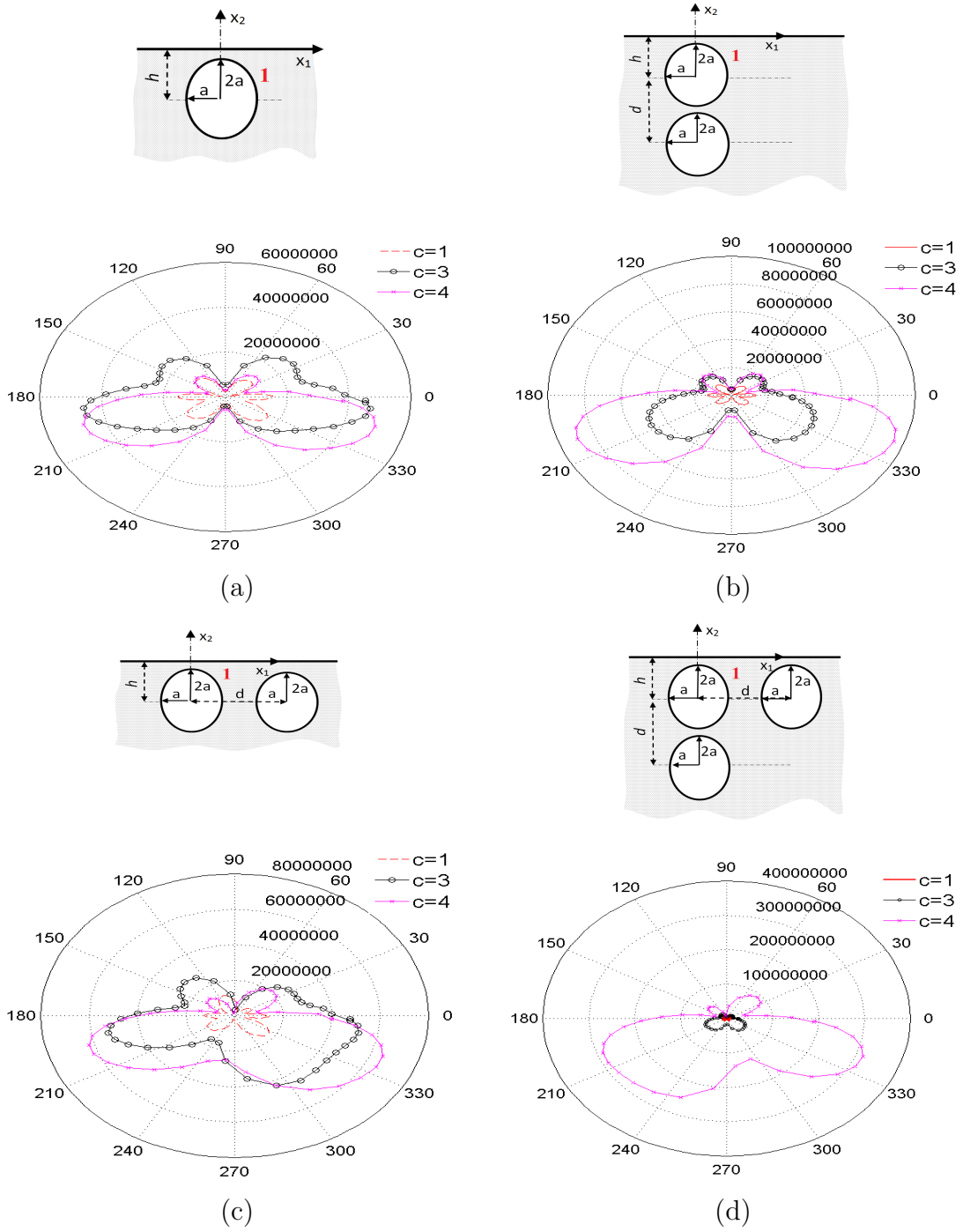

FIGURE 5.13: Stress distribution along the perimeter of a cavity in a half plane with inhomogeneity magnitude c at dimensionless frequency $\eta = 0.5$ due to an SH-wave emanating from an embedded source located at point $x_0(0, -15a)$: All embedded cavities are horizontally elongated ellipses with semi-axes a and 2a

are displacement component u_3 and stresses $\sigma_{i3} = \mu(x_2)u_{3,i}$ $i = 1, 2$ all depending on the coordinates (x_1, x_2). The viscoelastic shear modulus is complex-valued with the same real part as in its elastic counterpart, while its imaginary part is due to the dissipative processes developed during wave propagation in soils. For a

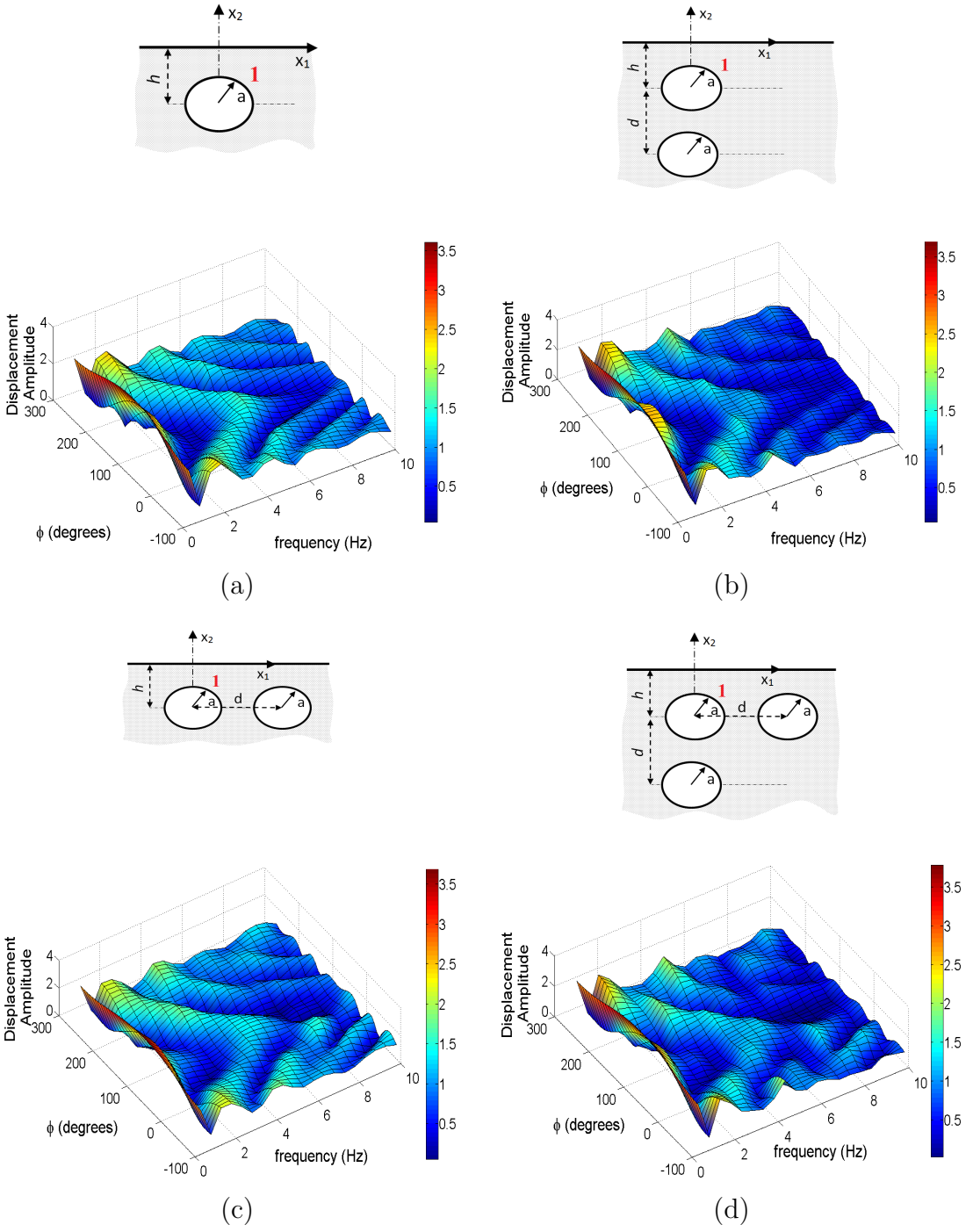

FIGURE 5.14: Displacement amplitude along cavity No. 1 embedded in a homogeneous half plane versus frequency due to SH-wave emanating from a source located at x_0(0, -15a). All embedded cavities are circular with radius a

Kelvin-Voigt model the wave number is $k_S^2 = \frac{\omega^2}{C_S^2(1-i\omega\xi_S)}$, where $C_S(x_2) = \sqrt{\frac{\mu(x_2)}{\varrho(x_2)}}$ is the real part of the SH wave, while ξ_S is the corresponding attenuation coefficient representing a small amount of hysteretic damping. In the low frequency

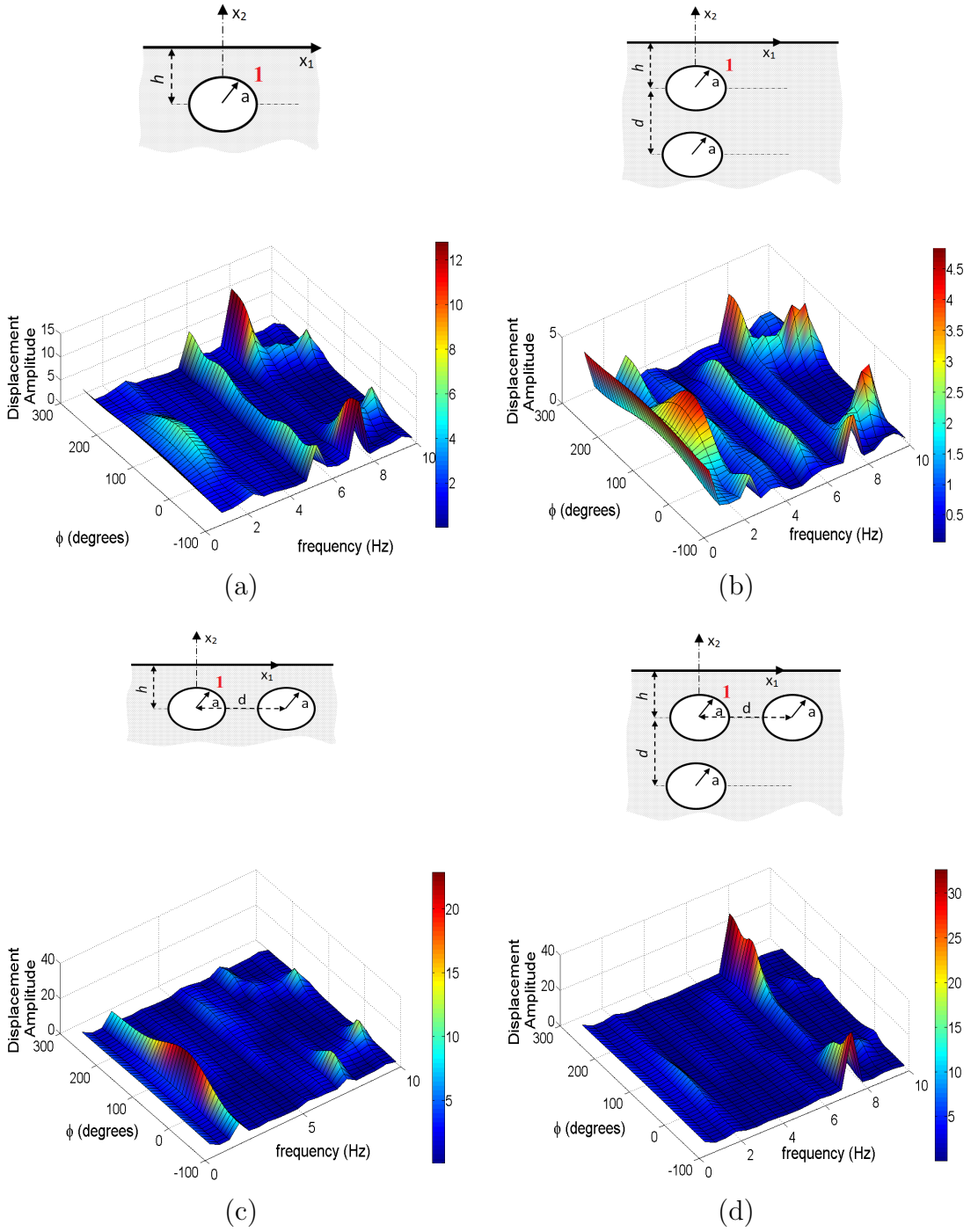

FIGURE 5.15: Displacement amplitude along cavity No. 1 embedded in a inhomogeneous half plane with Type B inhomogeneity magnitude $c = 2$ versus frequency due to SH-wave emanating from a source located at $x_0(0, -15a)$. All embedded cavities are circular with radius a

range, i.e $\omega\xi_S << 1$, the wave number reduces to:

$$k_S \approx \frac{\omega(1 + 0.5\omega\xi_S)}{C_S} \tag{5.5}$$

The material properties of the graded half-plane are depth dependent shear module $\mu(x_2)$ and density $\varrho(x_2)$. Assume that attenuation coefficient ξ_S is constant. Two different mechanical models for the material gradient are considered:
[1] *Type A*, where the density and shear modulus vary proportionally in a quadratic way in respect to the depth, yielding a macroscopically constant wave speed. The type A material gradient model is described in details in Chapter 3.
[2] *Type B*, where the shear modulus and density have an arbitrary variation with respect to depth. This yields a wave speed that is both frequency and position dependent. The type B material gradient model and its reference data are described in details in Chapter 4.

The governing equation of motion and the corresponding boundary conditions are expressed by Eqn.(5.1) and Eqn.(5.2), respectively. In addition, the Sommerfeld radiation condition holds for waves at infinity. The aim is to obtain displacements at any point of the graded poroelastic half-plane with cavities using the viscoelastic isomorphism of Bardet [117] to Biot's [118] equations of dynamic poroelasticity.

First Biot derived the frequency dependent equations of motion for fluid-saturated materials considered as two-phase ones. A characteristic equation for the wave numbers in the frame of the Biot's model was obtained in Bardet [117] and Lin et al. [119]. Three solutions of Biot's wave equation have been identified, corresponding to shear wave S transmitted through the solid skeleton, fast dilatational P wave and slow dilatational P wave. The corresponding wave velocities are complex and frequency dependent, hence they correspond to dissipative and dispersive waves. Finally, the solid and fluid dilatations are in phase for the first arriving P wave, and in reverse phase for the slower P wave, which damps out quickly. In a series of publications, Bardet [117] discussed the applicability of the viscoelastic behavior equivalent to Biot's model of dynamic poroelasticity in the low frequency range. In particular, Bardet proposed a single-phase viscoelastic material representation for saturated soils. The viscoelastic material constants are complex-valued with the same real part as in their elastic counterparts. The same holds true for the governing viscoelastic wave equation, with wave numbers which are complex-valued, frequency dependent functions that satisfy causality conditions.

Briefly is presented the terminology used for description of solid-fluid continuum in poroelasticity. A representative volume V for the solid-fluid continuum comprises an elastic, isotropic solid skeleton (matrix) with porosity $n = V_p/V$, where V_p is the pore volume. The "dry rock" approximation is the case of an air-filled solid skeleton, while the "solid grain" characteristics are the properties of the skeleton material. The elastic bulk modulus and density are denoted as follows for dry rock K_{dry}, $\varrho_{dry} = (1-n)\varrho_g$, solid grain K_g, ϱ_g and fluid K_f, ϱ_f. The solid-fluid system density is $\varrho_{sat} = \varrho_{dry} + n\varrho_f = (1+n)\varrho_g + n\varrho_f$. The shear strength of the

porous material is provided by the solid skeleton and is not affected by the fluid, since fluids sustain dilatational deformations only. Thus, both dry and saturated soils are described by the same shear modulus, i.e. $\mu = \mu_{sat}{=}\mu_{dry}{=}\frac{3(1-2\nu)}{2(1+\nu)}K_{dry}$, where ν is the Poisson's ratio for the dry skeleton.

The poroelastic-viscoelastic isomorphism proposed in Bardet [117] is based on the equating of the wave numbers in Biot's poroelastic model with those in viscoelastic Kelvin-Voigt model. This process gives the following equivalence relations between the characteristics of the poroelastic and viscoelastic materials:

$$C_P = \sqrt{\frac{P+2Q+R}{\varrho_{sat}}}; \quad C_S = \sqrt{\frac{\mu}{\varrho_{sat}}} \tag{5.6}$$

$$\xi_P = \frac{\varrho_{sat}}{b}\left(\frac{Q+R}{P+2Q+R}\cdot\frac{n\varrho_f}{\varrho_{sat}}\right)^2; \quad \xi_S = \frac{\varrho_{sat}}{b}\left(\frac{n\varrho_f}{\varrho_{sat}}\right) \tag{5.7}$$

$$P = \frac{3(1-\nu)}{1+\nu}K_{dry} + \frac{Q^2}{R}; \quad Q = \frac{n(1-n-K_{dry}/K_g)}{(1-n-K_{dry}/K_g+nK_g/K_f)}K_g \tag{5.8}$$

$$R = \frac{n^2K_g}{1-n-K_{dry}/K_g+nK_g/K_f}; \quad N = \frac{3}{2}\frac{1-2\nu}{1+\nu}K_{dry}; \quad K_{dry} = \frac{2}{3}\frac{\mu(1+\nu)}{1-n\nu} \tag{5.9}$$

$$\lambda_{sat} = \lambda_{dry} + \frac{Q^2}{R}; \quad b = \frac{n^2 g\varrho_f}{k} \tag{5.10}$$

where g is the acceleration of gravity and k is the soil permeability with values in the interval $10^{-10} - 10^{-2} m/sec$. The above approximate expressions are correct when the following condition is satisfied: $\omega\varrho_{sat}/b << 1$ and it is always satisfied in earthquake engineering field since permeability values for most soils is small. Figure 5.16 shows the sensitivity of the SH phase velocity for dry and saturated sandstone to the porosity. It is used the sandstone with the following characteristics: $K_g = 36000MPa$, $\varrho_g{=}2650kg/m^3$, $K_f = 2000MPa$, $\varrho_f = 1000kg/m^3$, $K_{dry}{=}K_{cr} + (1-n/n_{cr})(K_g - K_{cr})$, $n_{cr}{=}0.36$, $K_{cr}{=}200MPa$, see Lin et al.[119]. All simulation results presented in this section are for sandstone with the aforementioned properties. The BEM formulations addressed previously for pure elastic soil material are employed now for the equivalent soil parameters of a poroelastic soil according to Bardet model.

Next, the sensitivity of the wave field to the type of inhomogeneity model, to the type of material profile and to the poroelasticity of the material is demonstrated in Fig.5.17. Velocity profile along the depth for homogeneous and inhomogeneous (type A and type B at a fixed frequency $\eta = 0.25$), pure elastic, dry and saturated (with porosity $n = 0.2$) half-plane is given in Figure 5.17b. For the inhomogeneous model of type B the velocity profile depends also on the frequency since this model takes into account wave dispersion phenomena. Displacement amplitudes along free surface of elastic inhomogeneous graded poroelastic half-plane with an

embedded single circular cavity subjected to concentrated at point $x_0(0, -15a)$ body force with frequency $\eta = 0.25$ are drawn in Fig.5.17c. The presented results are obtained for homogeneous case and for two different material profiles of type A (quadratic) and B (variable). The porosity is $n = 0.2$, and the Poisson ration is 0.25. Both material types are contrasted with the reference homogeneous case, and all have the same value of material stiffness at the top and at a certain depth equal to $h = 150m$. The difference between the dry and saturated case is insignificant due to the low value of porosity, however the difference increases at higher porosities. It is clearly seen that the response for the Type B material profile diverges the most from the response of the homogeneous case. The difference in terms of displacements between Type A and the homogeneous case is smaller and even negligible at higher frequency, because macroscopically the wave speeds are the same for these two materials.

Figure 5.18 draws the normalized displacement amplitude $|u_{3_{poroelastic}}/u_{3_{poroelastic}}|$ along the free surface of continuously inhomogeneous poroelastic half plane of type B with inhomogeneity coefficient in the interval $c = 0.25 - 4$ due to SH-wave propagating from an embedded seismic source located at $x_0(0, -15a)$ with frequency $\eta = 0.25$ in the case of a single and two cavities with radius a. The obtained results are for pure elastic and poroelastic case with porosity $n = 0.3$ and $n = 0.35$. The normalization is done with respect to the maximal displacement for the pure elastic case. With increasing the porosity the displacement along the free surface increases significantly in respect to the displacement in the elastic case. Additionally with increasing the inhomogeneity coefficient the displacement also increases and attains its maximum value at inhomogeneity coefficient $c = 0.3$. Observe that when the poroelasticity and the inhomogeneity effect are combined the material response may lead to 30 times greater value than the pure elastic homogeneous case.

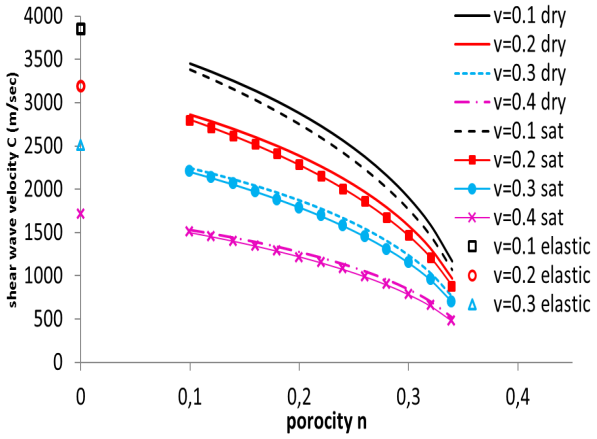

FIGURE 5.16: SH-wave velocity variation with porosity for homogeneous pure elastic, dry and saturated soil by Bardet (1992) model.

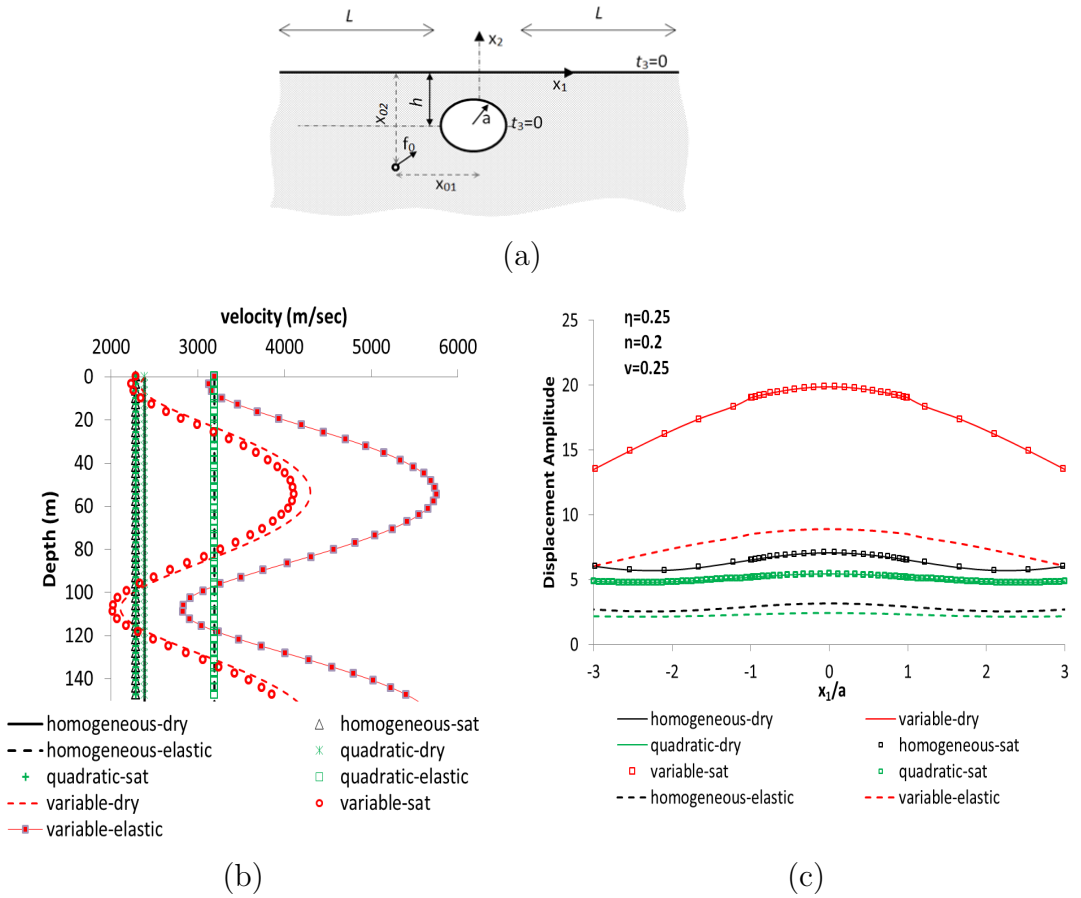

FIGURE 5.17: Velocity profile along the depth for elastic and poroelastic (with porosity $n = 0.2$) material. Displacement amplitude along the free surface of an elastic and poroelastic ($n = 0.2$) graded half-plane with a single circular tunnel due to waves radiating from an embedded at point x_0(0, -15a) and frequencies η=0.25. Comparison is between results obtained by homogeneous and inhomogeneous models of type A (quadratic) and B (variable)

5.6 Conclusions

In the present chapter, the potential of the new developed BEM schemes to produce highly accurate results for applications in material geoscience is demonstrated. Wave propagation problems in a graded, pure elastic or poroelastic half-plane containing multiple cavities under time-harmonic incident shear waves or to body waves radiating from a point source are investigated. Three different types of material gradient are considered: (a) density and shear modulus vary proportionally as quadratic functions of depth, but the wave velocity remains constant; (b) shear modulus and density vary with respect to the spatial coordinates in an arbitrary fashion, so that the wave velocity is both frequency and position-dependent; and (c) position-dependent shear modulus and constant density, yielding to a

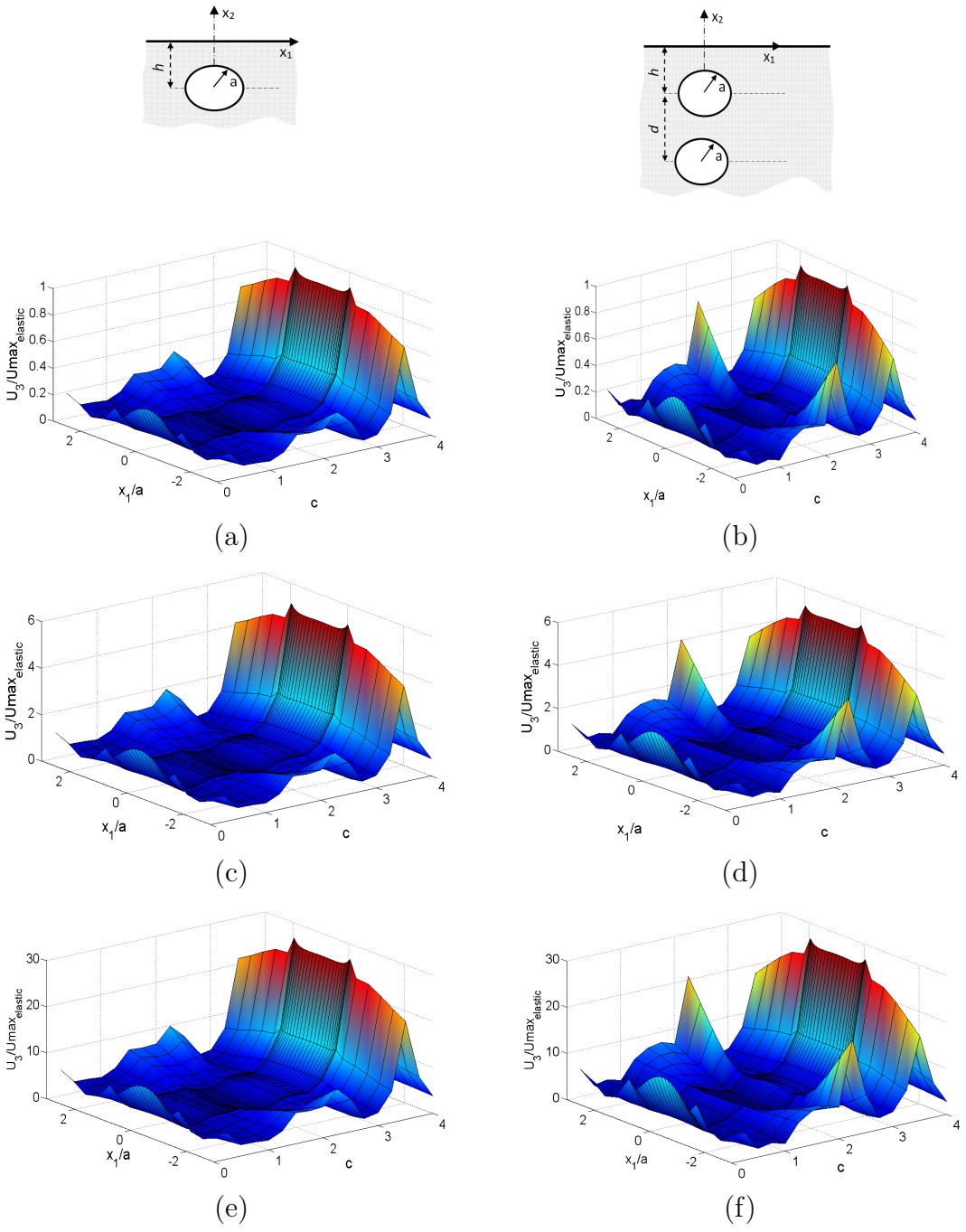

FIGURE 5.18: Normalized displacement amplitude along the free surface of continuously inhomogeneous of type B half plane with inhomogeneity coefficient $c = 0.25 - 4$ due to SH-wave propagating from embedded seismic source located at x_0(0, -15a) with frequency $\eta = 0.50$ in the case of a single and two tunnels. The obtained results are for pure elastic and poroelastic cases with $n = 0.3$ and $n = 0.35$

linear profile for the wave velocity. The aforementioned mechanical models are developed and the accompanied three different BEM formulations are applied.

From the numerical simulation results the followings can be stated. The presence, shape and spatial distribution of cavities in a slab is a key parameter in the development of the scattered displacement field and of localization effects in the stress field. Additionally the presence of inhomogeneous structure in the material matrix complicates further the picture of the wave field. The type of material gradient affects significantly the material response. Next, the parameter of poroelasticity of the soil material may greatly amplify its response for high values of porosity. The combined effect of poroelasticity and material gradient complicates further the picture of the wave field.

The results obtained in the present chapter are of interest to both solid mechanics and material science researchers. In all cases, the dynamic kinematic and stress fields which form in the perforated materials that exhibit a marked inhomogeneous structure, is an essential piece of information in their design and development, leading to specialized materials capable of withstanding very stringent performance criteria.

Chapter 6

Applications in earthquake engineering and structural dynamics

The present chapter gives applications in earthquake engineering and serves to demonstrate the potential of the developed and proposed here BEM models in investigating the influence of local soil conditions on structural damage, considering 2D analysis of the soil profile. In particular, two cases are examined: effects of site conditions on (i) structural damage of conventional multi-storey reinforced concrete buildings and (ii) nonlinear response of reinforced concrete bridges. A brief introduction to the topic is given and separately for the two examined cases mentioned above the followings are presented: seismic signal recovering methodology; geological profiles; ground motions; description of the structural models; dynamic response of the models and final conclusions arising from the numerical results. Several complex 2D geological configurations are considered under a suite of earthquake excitation and the structural response is computed in order to demonstrate the importance of site effects in earthquake resistant design of structures.

6.1 Introduction

During an earthquake, seismic waves radiate from a fault and travel through the earth's crust. As seismic waves travel through bedrock and soil deposits, the various complex geological profiles produce local distortions in the incoming wave field which lead to large amplifications as well as strong spatial variations in frequency, amplitude and phase along the surface in the seismic motions. For elongated structures such as bridges, pipelines, communication and power transmission grids, dams etc., the effects of local site conditions become especially important because

spatial variations of ground motion would lead to multiple support excitation of the structure. The structure would respond differently to a variety of input motions due to its dynamic characteristics that tend to be triggered differently under uniform and non-uniform earthquake excitation patterns. This relative difference between the motions of the soil and the structure is further pronounced by the fact that soil-structure-interaction phenomenon at each pier foundation-soil interface is strongly frequency-dependent, hence, inherently sensitive to the variations of seismic input along the bridge length.

So far, seismic codes for bridge design do not prescribe explicit procedures to simultaneously account for spatial variability, site effects and SSI phenomena maybe with the exception of some sporadic provisions to generate asynchronous ground motions (i.e., Eurocode 8 Part 2 [120]) and some rough guidelines to account for soil compliance in the above code Annex.

During the past decades, work on identification of the aforementioned phenomena and on the interpretation of the ensuing structural damage has become quite intensive. Studies can be classified into two categories: (a) experimental or probabilistic site studies and their correlation with the observed structural damage, e.g., [121–124] (b) studies based on numerical simulation of the structure and the subsoil domain. Investigations belonging to the second category are more relevant with respect to damage interpretation and its practical application for engineering purposes.

Considering the effects on the seismic response of buildings, Lang [125] investigated the damage potential of multi-storey R/C frame structures under selected ground motions suitable for the given site and subsoil conditions. Manolis and Athanatopoulou [126] examined the elastic and inelastic response of 3D multistorey R/C buildings subjected to synthetic ground motions which account for the presence of complex geological profiles. Considering the effects on the seismic response of extended structures like bridges, Sextos et al [127, 128] developed a general methodology for deriving appropriate modified time histories that account for spatial variability, site effects and soil structure interaction phenomena. Parametric analyses were conducted and demonstrated that the presence of site effects, spatial variability and soil-foundation superstructure interaction strongly influences the input seismic motion and the ensuing dynamic response of the bridge. Jeremic et al. [129] proposed a numerical simulation methodology and conducted numerical investigations of seismic SSI for a bridge structure on non-uniform soil. It was then stated that the dynamic characteristics of earthquakes, soil and structure all play a crucial role in determining the seismic behavior of an extended construction. Bi et al. [130] studied the simultaneous effect of SSI and ground motion spatial variation on bridge response and estimated the required separation distance that modular expansion joints must provide in order to avoid seismic

pounding. Soyluk and Sicacik [131] further investigated the effects of SSI and multiple support excitation on the seismic response of a cable-stayed bridge.

However, in all the above mentioned studies the influence of local site conditions on structural response is evaluated using models based on a uni-dimensional description of the local soil profile as a soil column and similarly for the seismic wave propagation path. Limited papers can be found which deal with the effects of local site conditions on structural response considering 2D analysis of the soil profile. Esquivel and Sanchez-Sesma [132] studied the influence of a semi-circular cylindrical canyon on the dynamic soil-bridge interaction for the case of incident harmonic plane SH waves. Analytical scattered and free-field solutions are used to determine the driving forces and impedance stiffness matrix for the bridge foundation, while the bridge is modeled as a shear beam and solved analytically. Zhou et al. [133] investigated canyon topography effects on the linear response of continuous, rigid frame bridges under obliquely incident SV waves. The seismic response of the canyon was analyzed using the FEM, while the response of the bridge was computed by the "large mass" method. It was shown that the distribution of ground motions is affected by canyon topographic features and the incident angle of the waves. In case of vertical incident SV waves, the peak ground accelerations increase greatly at the upper edges of the canyon and decrease at its bottom lateral boundaries. Note here that these studies are restricted to either very simple geometry of the topographic effects (so that can be solved analytically) or to a simple frame-like bridge model which typically neglects salient features of a real bridge.

Along these lines, the main objective of the present chapter is to investigate the effects of (a) spatial variability of earthquake ground motion, (b) local site conditions and (c) SSI on the dynamic response of reinforced concrete buildings and bridges, considering 2D analysis of the soil profile via the new developed BEM schemes. Several complex geological configurations are considered that account for (a) canyon topography, (b) soil layering and (c) material gradient effect. The structural dynamic response of r/c building and bridge models due to site dependent ground motions is determined and the results are interpreted to establish changes in terms of what would be observed for a homogeneous soil deposit.

6.2 Effects of site conditions and canyon topography on multi-storey buildings

The present section investigates the influence of local site effects and canyon topography on the nonlinear response of conventional multi-storey R/C buildings

[134]. The first step is to model seismic waves propagating through complex geological profiles with canyon topography by the Boundary Element Method based on Green's function so as to recover site-dependent acceleration time histories at the free-surface. Next, to focus on the dynamic behavior of a five storey R/C building, modeled and analyzed by the Finite Element Method (FEM). The nonlinear response of the building is computed for input base motions in the form of recorded earthquake signals at outcrop rock and the corresponding signals recovered at the free surface of the complex geological profile. All simulations reveal the importance of local site conditions on the ground motion at the free-surface and the ensuing structural damage. This aspect of seismicity has to be taken into account in both new construction and in retrofit activities of the existing building stock.

6.2.1 Seismic signal recovering methodology

Seismic waves propagating through complex geological profiles are modeled so as to produce ground motion records that account for local site conditions. The BEM is used to compute time history records in a laterally inhomogeneous geological profile situated in a half-plane with free-surface relief of arbitrary shape and material properties that vary with respect to depth. In particular, a BEM formulation based on the Green's function for a quadratically inhomogeneous (in terms of the depth coordinate) half-plane (Rangelov and Manolis, [40]) corresponding to embedded point sources or dipoles is used to reproduce transient seismic motions at the free surface. The non-conventional BEM employed here is developed and validated in Chapter 3 and for shake of completeness in what follows are presented the basic details of the problem's formulation for the examined cases.

Consider continuously inhomogeneous in depth half-plane with free-surface relief of arbitrary shape subjected to incident SH-wave. A Cartesian coordinate system Ox_1x_2 is introduced on a domain $G = R^2_-/V$, where $R^2_- = x_1, x_2, x_2 < 0$ and V is a canyon with boundary S_1, see Fig.6.1. Surface S_2 is denoted as that part of the line $x_2 = 0$ lying outside the canyon. Anti-plane wave motion is assumed in the plane Ox_1x_2. In this case the only nonzero field quantities are displacement $u_3(x, \omega)$ and stresses $\sigma_{i3}(x, \omega)$, i=1, 2.

The governing equation of motion in the absence of body forces and in frequency domain is:

$$\sigma_{i3,i} + \varrho(x_2)\omega^2 u_3 = 0 \tag{6.1}$$

and the constitutive equations are:

$$\sigma_{i3} = \mu(x_2)u_{3i}(x_2) \tag{6.2}$$

where $\mu(x_2)$ is the shear modulus and $\varrho(x_2)$ is the density.

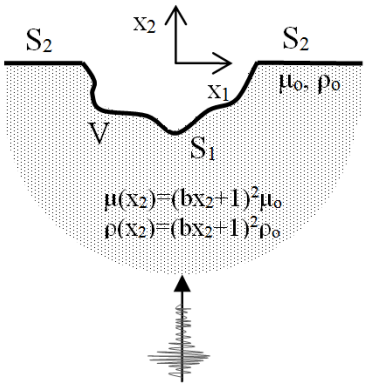

FIGURE 6.1: Inhomogeneous in depth half-plane with free-surface relief of arbitrary shape

The geological profile is presented with material characteristics modeled by continuous and smooth functions of depth:

$$\begin{array}{l} \mu(x_2) = \mu_o h(x_2) \qquad and \qquad \varrho(x_2) = \varrho_o h(x_2) \\ h(x_2) = (bx_2 + 1)^2, \quad b \leq 0, h \leq 0 \end{array} \tag{6.3}$$

where $h(x)$ is the inhomogeneity function of a quadratic type and b is the inhomogeneity coefficient, i.e., the inhomogeneity magnitude. A value $b = 0$ reflects the homogeneous case. Both parameters μ_0 and ϱ_o represent the reference constant values taken at the traction free surface of the half-plane. The wave propagating in the half-plane produces scattering wave when impinge on the free-surface relief. The total wave field is a superposition of the free-field motion (u_3^{ff}, u_3^{ff}) and wave scattered (t_3^{ff}, t_3^{ff}):

$$u_3 = u_3^{ff} + u_3^{sc}; \quad t_3 = t_3^{ff} + t_3^{sc} \tag{6.4}$$

In the above equation, $t_3 = \sigma_{13} n_1 + \sigma_{23} n_2$ is the traction and $n(n_1, n_2)$ is the vector of the outward normal to the boundary. Free field motion in the examined case is defined as SH-wave propagation in the elastic, inhomogeneous in depth half-plane, with a flat free surface and without any type of surface heterogeneities. This free-field motion in the quadratically inhomogeneous in depth half-plane is computed using the analytical solutions derived by Manolis et al. [92] given in Eqn.(3.4). The solution of the total wave field satisfies the following boundary condition along the surface $S = S_1 \cup S_2$:

$$t_3 \mid_{x_2=0} = 0 \tag{6.5}$$

The employed BEM is based on a closed form frequency-dependent Green's function for quadratically inhomogeneous in depth half-plane derived in Rangelov and Manolis [40]. The expression of the Green's function as well as a brief description of the derivation steps can be found in section 3.2.1. The boundary value problem in frequency domain presented by Eqn.(6.1), Eqn.(6.5) and Sommerfeld radiation

conditions can be reformulated and represented by boundary integral equations along the existing boundaries. Note that using the above mentioned closed form Green's function only the valley, surface S_1, needs discretization, excluding the flat part S_2 of the boundary along the free line $x_2 = 0$ (Fig.6.1). Following Brebbia and Dominguez [135], the previously defined boundary value problem is equivalent to the following displacement BIE along the canyon line S_1:

$$cu_3^{sc}(x) = -\int_{S_1} t_3^{g^*}(x,\xi)u_3^{sc}(\xi)dS_1 - \int_{S_1} g_3^*(x,\xi)t_3^{ff}(\xi)dS_1 \tag{6.6}$$

where $x = (x_1, x_2)$ and $\xi = (\xi_1, \xi_2)$ are the position vectors of the field and source points respectively and g_3^* is the Green's function for the displacement and $t_3^{g^*}$ presents its corresponding traction. Once the unknown scattered wave field $u_3^{sc}(x)$ is computed from Eqn.(6.6), the total wave field along the free-surface is obtained from Eqn.(6.4).

The generation of transient signals from the hitherto derived time-harmonic displacements is achieved through inverse Fourier transformation (IFFT).

$$u_3^{total}(x,t) = \Phi^{-1}[\hat{u}(x,\omega)S(\omega)] \tag{6.7}$$

Where $\hat{u}(x,\omega)$ is the BEM solution for the total displacement in frequency domain and $S(\omega)$ is the spectrum of the time function $f(t)$ of the transient incident wave. Note that for simplicity the same notations are used for field variables in frequency and time domain in equations above.

6.2.2 Geological profiles and ground motions

The methodology described in the previous section will be applied to four different geological profiles shown in Fig.6.2. The following key parameters are investigated: (a) the material inhomogeneity of soil and (b) the shape and size of surface relief. In particular, the site is represented by the following cases: (1) homogeneous half-plane without free-surface relief, Fig.6.2(a), (2) continuously inhomogeneous half-plane without free-surface relief, Fig.6.2(b), (3) homogeneous half-plane with semi-circle canyon, Fig.6.2(c) and (4) continuously inhomogeneous half-plane with semi-circle canyon, Fig.6.2(d). The soil material properties are: $\mu_o = 1.15625 \cdot 10^8 Pa$, $\varrho_o = 1850 kg/m^3$ and $V_{SH} = 250 m/sec$. The soil material inhomogeneity is equal to $b = -0.005$ with reference material properties μ_o and ϱ_o. The variation of shear modulus with depth is shown in Fig.6.3.

A suite of seven earthquake excitations (see Fig.6.4) recorded at the outcropping rock on site class A (according to FEMA [136] classification) from the PEER [137] strong motion database are considered as an input at the seismic bed of the

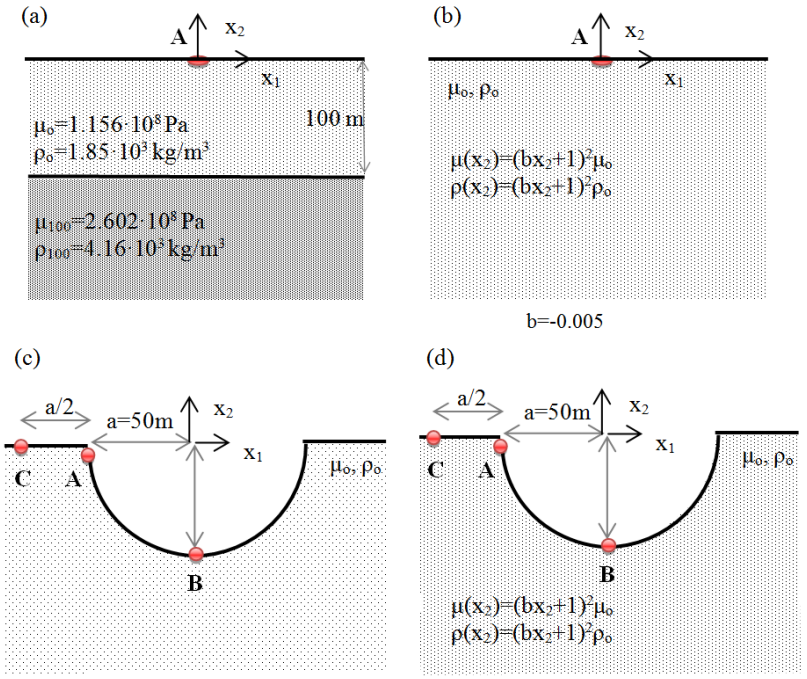

FIGURE 6.2: Investigated geological profiles with and without free-surface relief

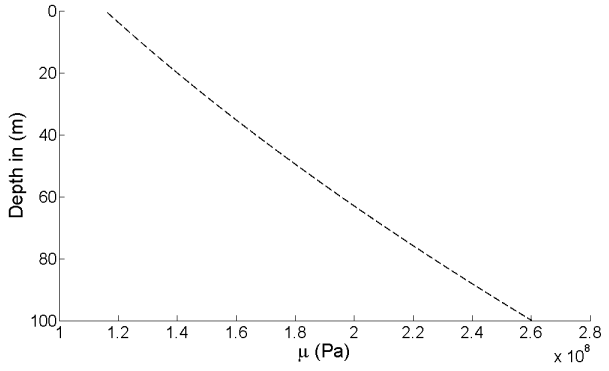

FIGURE 6.3: Variation of shear modulus (μ) with depth

above mentioned investigated geological profiles. Acceleration response spectra that correspond to these input excitations are shown in Fig.6.5. Next, acceleration time histories at the receiver points A, B and C (Fig.6.2) due to the seven earthquake excitations are recovered using the BEM technique described previously for the four investigated geological profiles. Fig.6.6 plots the acceleration time history recorded along the canyon situated in a continuously inhomogeneous half-plane under San Francisco excitation No.1. Observe that the seismic signal depends strongly on the canyon topographic effects. Free surface time histories are recorded at the geological profiles 1 and 2, see Fig.6.2(a) and Fig.6.2(b) respectively. In case of a canyon situated in a half-plane, time-histories are recorded at three receiver points along the free-surface: At the edge of the canyon (point A), at the bottom of the canyon (point B) and at a distance $s = a/2$ from the canyon (point C), see Fig.6.2(c) and Fig.6.2(d).

No	Date	Earthquake name	Magnitude (M)	Station name	Station number	Closest distance (Km)	Site Class	Component (deg)	PGA (g)
1	22.03.1922	San Francisco	5.3	Golden Gate Park	1117	8	A	100	0.112
2	17.01.1994	Northridge	6.7	Mt Wilson - CIT	24399	26.8	A	000	0.234
3	17.01.1994	Northridge	6.7	Littlerock Brainard Can	23595	46.9	A	090	0.072
4	17.01.1994	Northridge	6.7	Lake Hughes #9	127	28.9	A	090	0.217
5	18.10.1989	Loma Prieta	6.9	Monterey City hall	47377	44.8	A	000	0.073
6	10.01.1987	Whittier Narrows	6	Mt Wilson - CIT	24399	21.2	A	090	0.186
7	12.09.1970	Lytle Creek	5.4	Cedar Springs, Allen Ranch	111	20.6 (Hypocentral)	A	095	0.071

FIGURE 6.4: Ground motion records

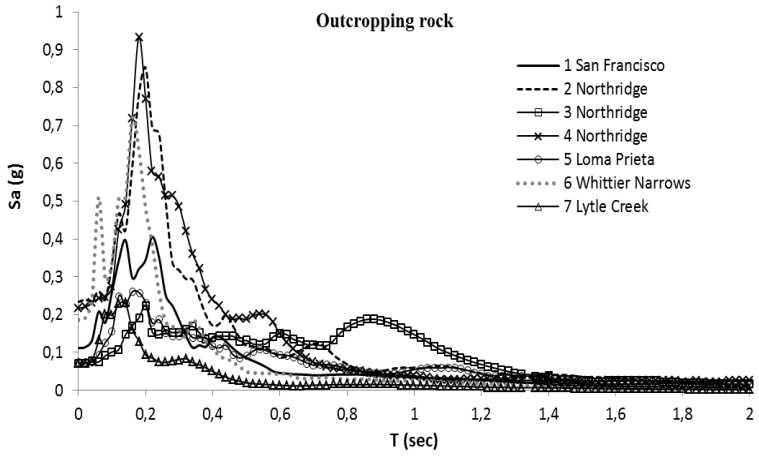

(a)

FIGURE 6.5: Acceleration response spectra recorded at the outcropping rock

The effect of local site conditions on the ground motions is demonstrated in Figs.6.7-6.8 where site-dependent response spectra of the examined ground motions are presented. Response spectra at the surface of the geological profiles 1 and 2 are illustrated in Fig.6.7(a) and Fig.6.7(b), respectively. As expected, the spectral values are twice in comparison with those recorded at the outcropping rock if we consider a single soil layer resting over infinite bedrock. Observe that the response spectrum is identical to that of the homogeneous medium when this special type of inhomogeneity is considered for $b = -0.005$, in which both stiffness and density variations are proportional.

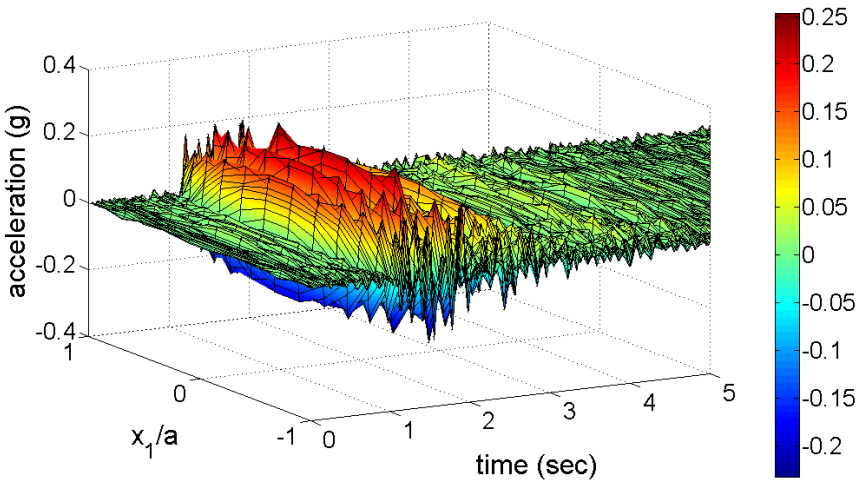

FIGURE 6.6: 3D figure of the acceleration time history recorded along the canyon situated in an inhomogeneous half-plane under San Francisco excitation No. 1

The influence of soil inhomogeneity in combination with the canyon topography on the ground motions can be seen in Fig.6.8, where response spectra recorded at the receiver points A, B and C for geological profile 3 are respectively shown. Comparing the spectral acceleration at the bottom (Point B) and at the edge (Point A and C) of the canyon, spectral accelerations are more pronounced for low values of period at the bottom of the canyon, while high values of the period lead to significant spectral accelerations at the edge of the canyon.

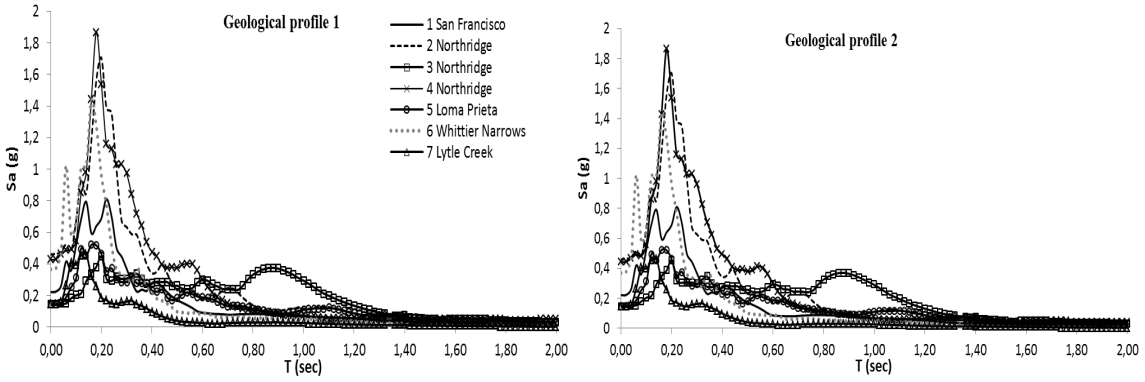

(a) (b)

FIGURE 6.7: Acceleration response spectra recorded at the free surface of geological profile 1(a) and 2(b)

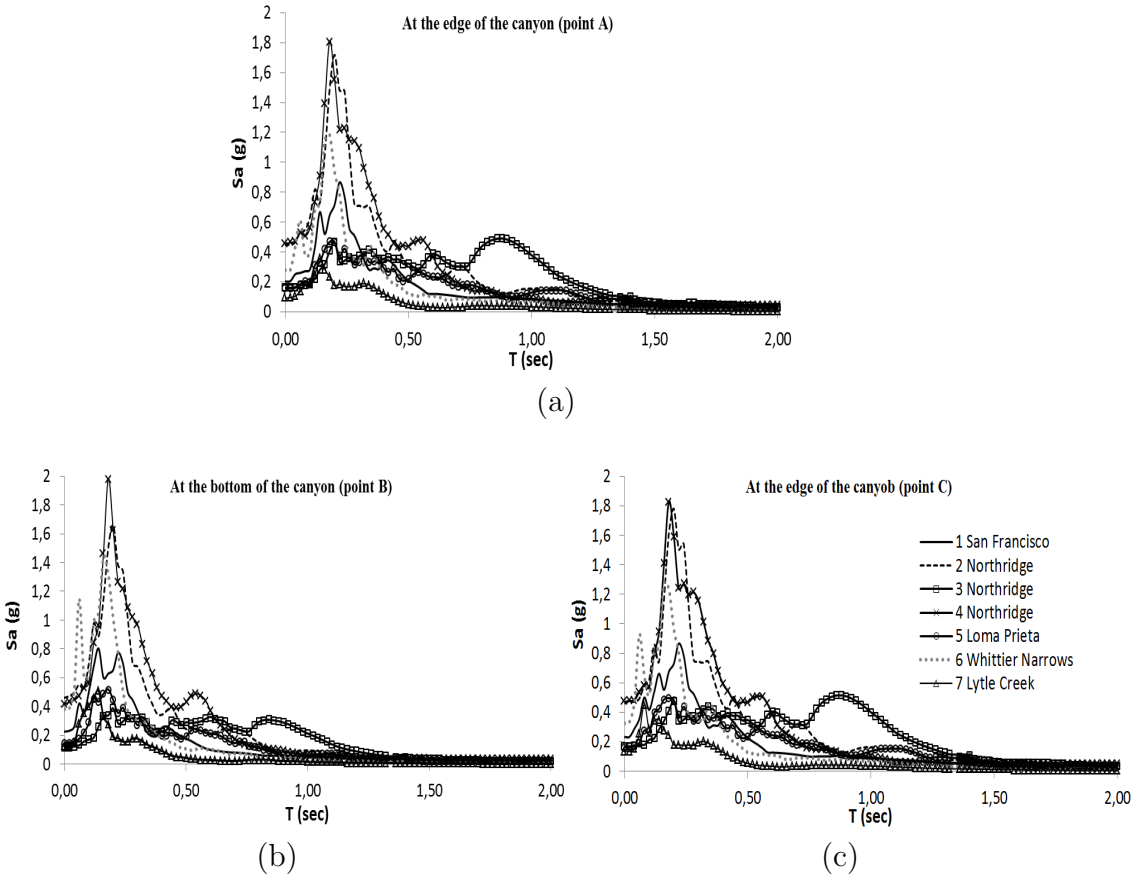

FIGURE 6.8: Acceleration response spectra recorded at receiver points (a) A, (b) B and (c) C for geological profile 3

6.2.3 Multi-storey building modeling

Next, we focus on the nonlinear response of a 3D, R/C building modeled using the FEM. A five storey building with a structural system that comprises beam elements in two perpendicular directions (along the x and y axes) is considered. Its plan view (see Fig.6.9) is doubly-symmetric with shear walls that receive more than 70% of the base shear along the x axis, and without shear walls along the y axis. The fundamental period of the building along x axis is T_x=0.67 sec and along y axis is T_y=1 sec.

The building was designed so as to behave as a medium ductility class building. For the numerical analysis and design, all basic recommendations of EC8 [120] were taken into consideration. The reinforced concrete structural elements were designed following the provisions of both EC2 [138] and EC8 [120]. Computer program RAF [139] was employed for the elastic analysis and design of the building.

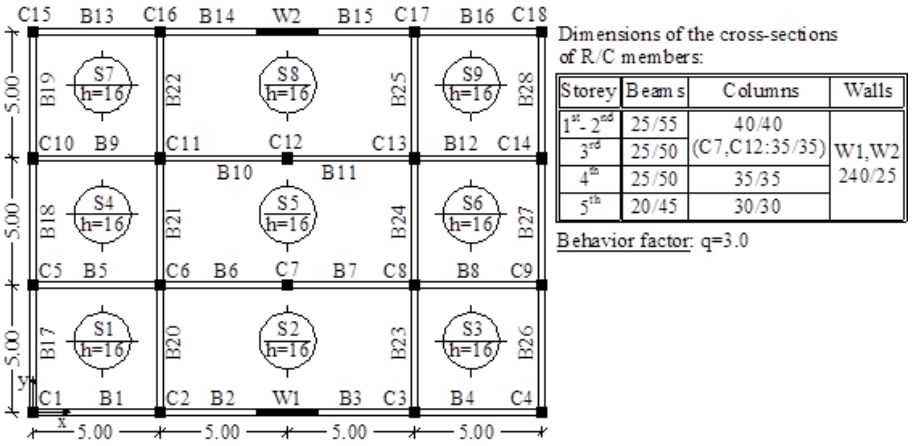

FIGURE 6.9: Plan view and design parameters of the building under investigation

6.2.4 Nonlinear dynamic response of the building

Next, a series of Nonlinear Time History Analyses were conducted using the aforementioned suite of ground motions recorded at rock outcrop, plus the same suite of ground motions as modified by the local site conditions and generated by the BEM at the free surface of the four geological profiles under investigation. In all cases, the records were scaled so that their spectral acceleration ($Sa(T_1)$) at the first mode of the structure match the elastic spectral acceleration given by EC8 for site class A. Analyses were carried out for two values of the seismic incident angle, namely $\theta = 0^o$ and $\theta = 90^o$ with respect to the principal axes x and y of the building (see Fig.6.9).

In the numerical modeling of the building's nonlinear behavior, potential plastic hinges were placed at the column-to-beam connections, as well as at the base of the shear walls. The material inelasticity of the structural members was modeled by means of the Modified Takeda hysteresis rule (Otani [140]). It is important to notice that the effects of axial force-biaxial bending moment (P-M1-M2) interaction at column and wall hinges were taken into consideration. The inelastic analyses of the building were conducted with the aid of the computer program Ruaumoko (Carr,[141]), [142].

For each ground motion the damage state of the five story building is determined. More specifically, the seismic response of the building is evaluated by using both the Maximum Inter-story Drift Ratio (MIDR) and the Overall Structural Damage Index (OSDI) (Park and Ang, [143]). In the present study, the modified Park and Ang damage index, given by Eqn.(6.8), has been used, i.e.,

$$DI = \frac{\phi_m - \phi_y}{\phi_u - \phi_y} + \frac{\beta}{M_y \phi_u} E_T \tag{6.8}$$

where DI is the local damage index, ϕ_m the maximum curvature attained during the load history, ϕ_u the ultimate curvature capacity of the section, ϕ_y the yield curvature, β a strength degrading parameter, M_y the yield moment of the section and E_T the dissipated hysteric energy. Eqn.(6.8) provides the local damage index (cross-section damage). This thesis addresses the overall structural damage index computed as the mean value of all local damage indices weighted by the local energy absorptions, see Eqn.(6.9).

$$OSDI = \frac{\sum[DI_{col.weighted}(E_{x,col} + E_{y,col})] + \sum[DI_{beam} E_{beam}]}{\sum[(E_{x,col} + E_{y,col})] + \sum[E_{beam}]} \tag{6.9}$$

In the above, $D.I._{\cdot col.weighted.,i}$ is the energy weighted average of the column damage indices, $D.I._{\cdot beam,i}$ the beam damage index, E the dissipated energy and n, m the number of columns and beams respectively. The following damage degrees are defined based on the values of $OSDI$: i) low for $OSDI < 0.11$, ii) medium for $0.11 < OSDI < 0.4$, iii) large for $0.4 < OSDI < 0.77$ and iv) total for $0.77 < OSDI$.

The effect of site conditions on the structural damage is demonstrated in Figs.6.10-6.13, where the overall structural damage index and the maximum inter-storey drift ratio of the examined building due to the site dependent ground motions and the ground motions recorded at rock outcrop are listed.

All site dependent ground motions produce greater values of OSDI and MIDR (double for some excitations) than the corresponding ground motions recorded at the rock outcrop. This result is expected given that the spectral values are twice in comparison with those recorded at the outcropping rock if we consider a single soil layer resting over infinite bedrock. Observe that the ground motions at the outcropping rock cause medium-level structural damage, while almost all corresponding site dependent ground motions cause a large extent of structural damage. It can also be seen that the presence of inhomogeneity on the soil profile 2 has minor effect on the structural damage.

The influence of the canyon topographic effects on the nonlinear response of the examined building is demonstrated in Fig.6.12 and Fig.6.13, where the $OSDI$ and $MIDR$ of the structure due to ground motions recovered at three receiver points A, B and C along the canyon are presented. As can be seen there, seismic signals recorded at the edge of the canyon have a more deleterious effect to the structure compared to those recorded at the bottom of the canyon. This finding is in line with what was stated above regarding the effects of the canyon topography

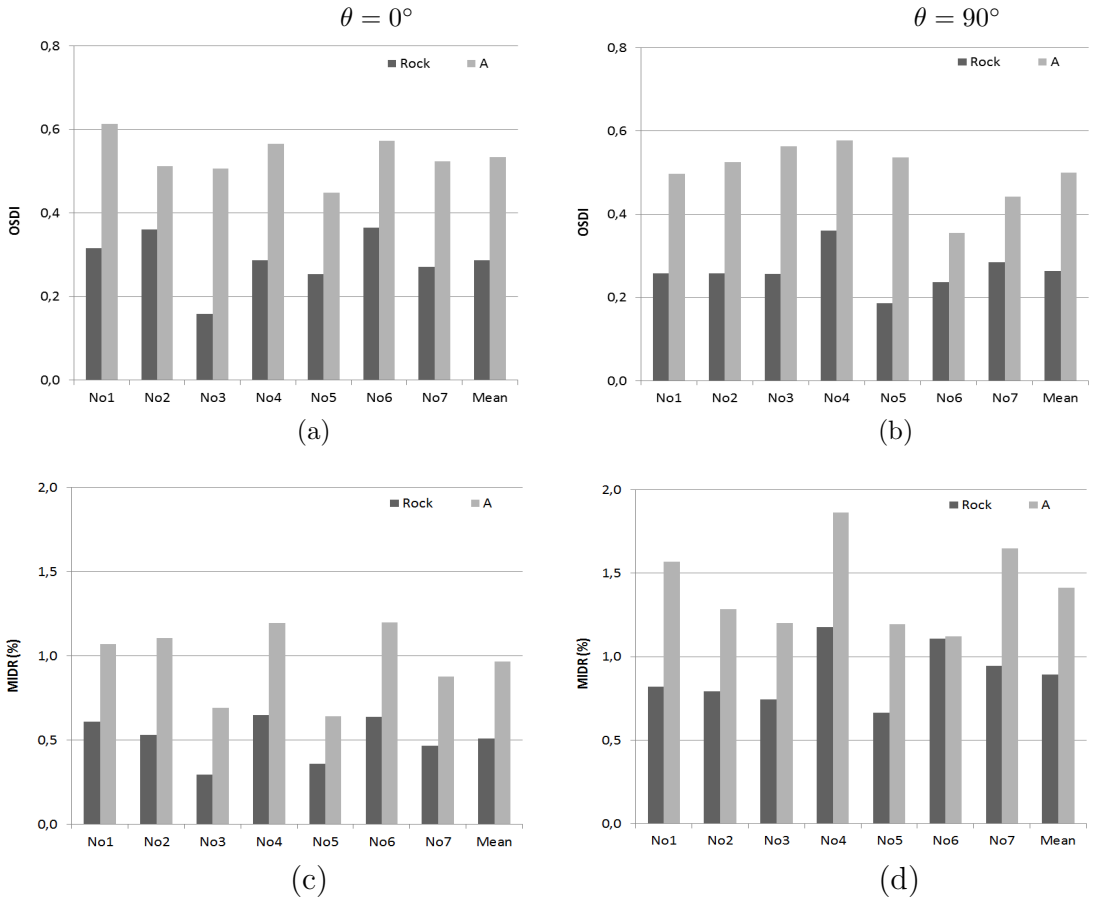

FIGURE 6.10: Overall structural damage index for incident angle (a) $\theta = 0^o$ and (b) $\theta = 90^o$ and maximum interstorey drift ratio for incident angle (c) $\theta = 0^o$ and (d) $\theta = 90^o$ for the geological profile 1

on the ground motions, given that the examined building has fundamental period $T_x = 0.67$ sec and $T_y = 1$ sec and taking into account the period elongation in the inelastic range (see Fig.6.8). Also observe that ground motions recovered at the edge of the canyon can cause different extent of structural damage compared to the same ground motions recovered at the bottom of the canyon.

Summarizing all the above numerical results, it is evidently demonstrated that the presence of local site conditions and canyon topography cannot be ignored since they influence the final damage state observed in a structure. Seismic signals recorded at different points along the canyon and correspond to the same ground motion recorded at the rock outcrop can cause different levels of structural damage. The ground motions and the ensuing structural damage are strongly affected by the canyon topography effects, and this effect is frequency dependent.

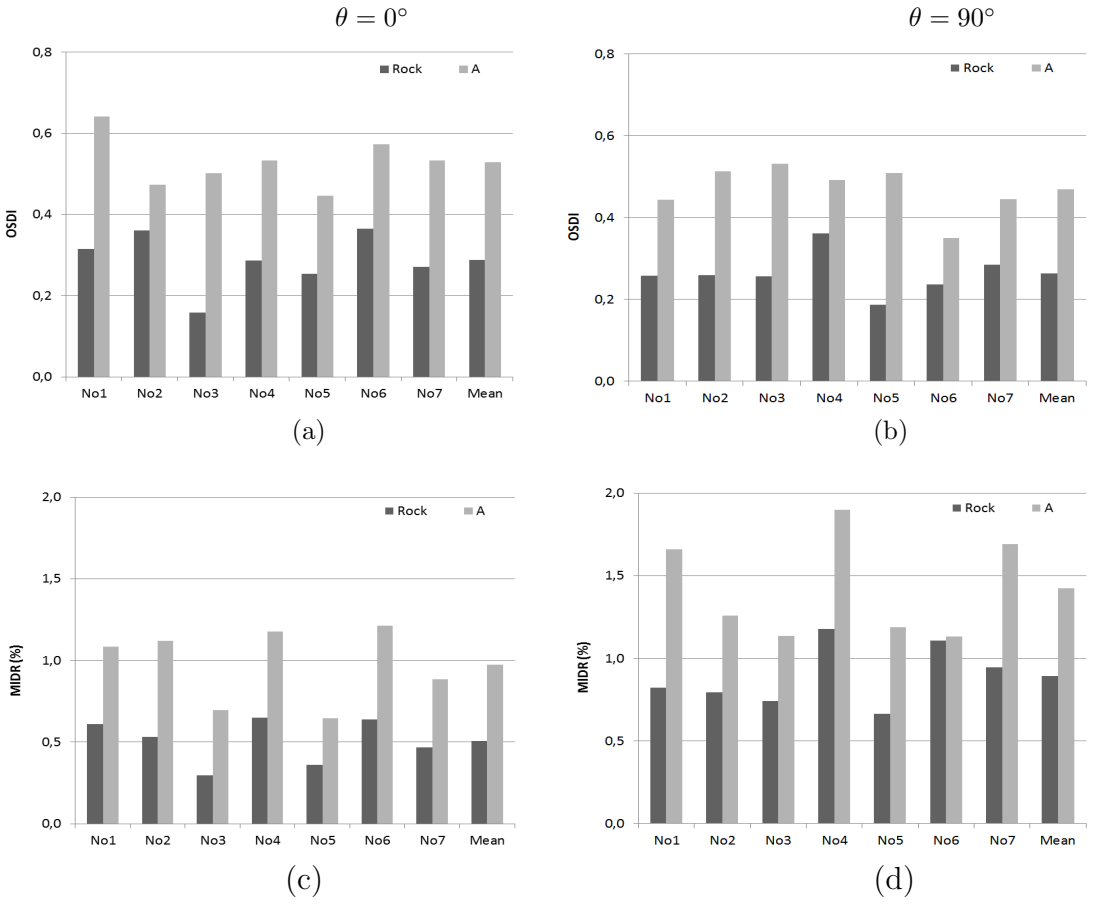

FIGURE 6.11: Overall structural damage index for incident angle (a) $\theta = 0^o$ and (b) $\theta = 90^o$ and maximum interstorey drift ratio for incident angle (c) $\theta = 0^o$ and (d) $\theta = 90^o$ for the geological profile 2

6.3 Effects of site conditions, canyon topography and SSI on reinforced concrete bridges

The present section investigates the influence of site effects, canyon topography and SSI phenomena on the inelastic dynamic analysis of bridge models, considering a 2D analysis of the soil profile via BEM based on special class of fundamental solution for geological media with variable velocity profile [144, 145]. First, seismic waves propagating through complex geological profiles are modeled, so as to recover ground motion records that account for local site conditions. To that purpose, the BEM is employed for computing time-history records for four different geological profiles considering (a) canyon topography, (b) soil layering and (c) material gradient effect. Then bridge support-dependent ground motions and equivalent dynamic impedance matrices at the soil-foundation interface are generated for each support point of a bridge along the canyon. More specifically, two configurations of an existing r/c bridge located in northern Greece are the reference cases, considering at the piers (i) seismic isolation and (ii) monolithic

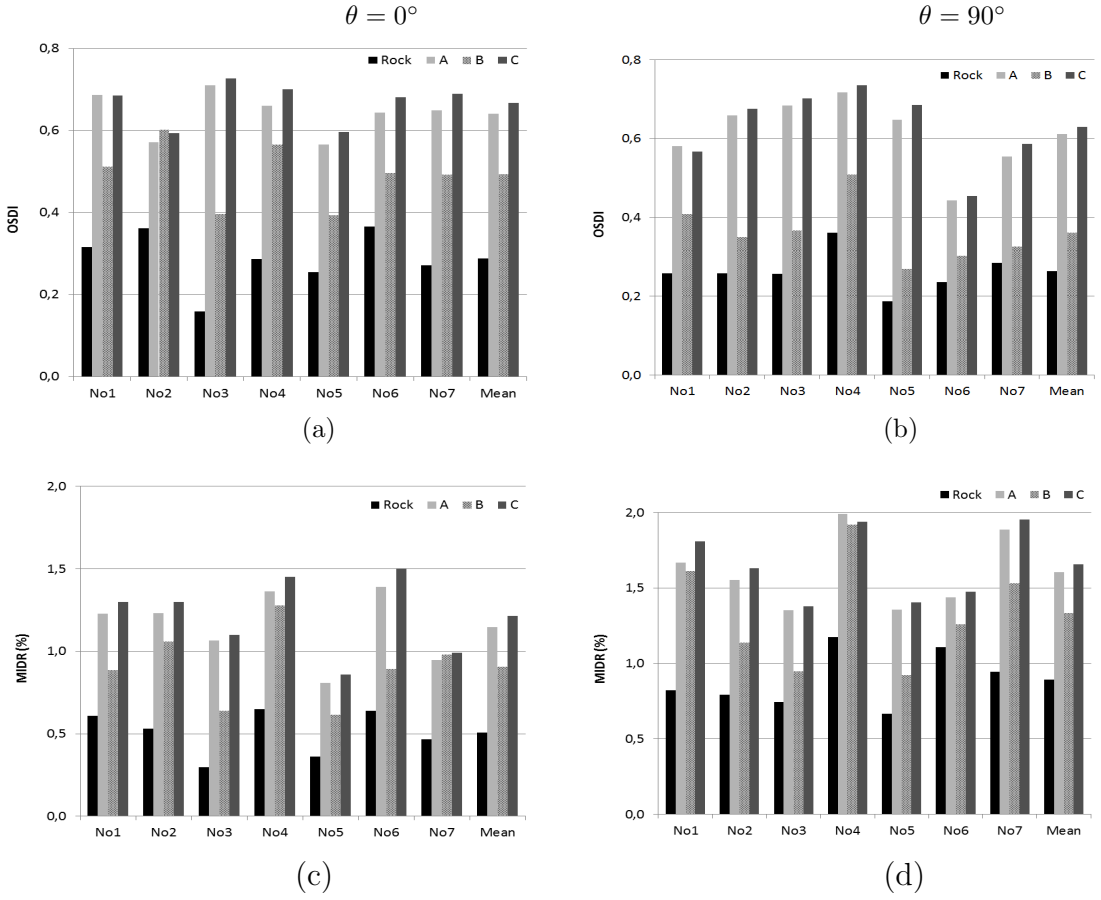

FIGURE 6.12: Overall structural damage index for incident angle (a) $\theta = 0^o$ and (b) $\theta = 90^o$ and maximum interstorey drift ratio for incident angle (c) $\theta = 0^o$ and (d) $\theta = 90^o$ for the geological profile 3

connection to the deck. Next, a series of time history analyses considering local nonlinearities is conducted for the bridge using the Finite Element Method (FEM) taking into account subsoil-structure-interaction phenomena.

6.3.1 Seismic signal recovering methodology

The BEM is used to model the seismic wave propagation through complex geological profiles so as to recover ground motion records that account for local site conditions. In particular, consider two dimensional wave propagation in viscoelastic, isotropic and inhomogeneous half-plane consisting of N parallel or non-parallel inhomogeneous layers Ω_N $(n = 0, 1, 2, N)$ with a free surface relief of arbitrary shape. The dynamic disturbance is provided by either an incident SH wave or by waves radiating from an embedded seismic source, see Fig.6.14. For this problem, a non-conventional BEM is applied which is based on a special class of analytically derived fundamental solution for continuously inhomogeneous media with variable wave velocity profiles [41, 42]. The employed here BEM is developed and validated

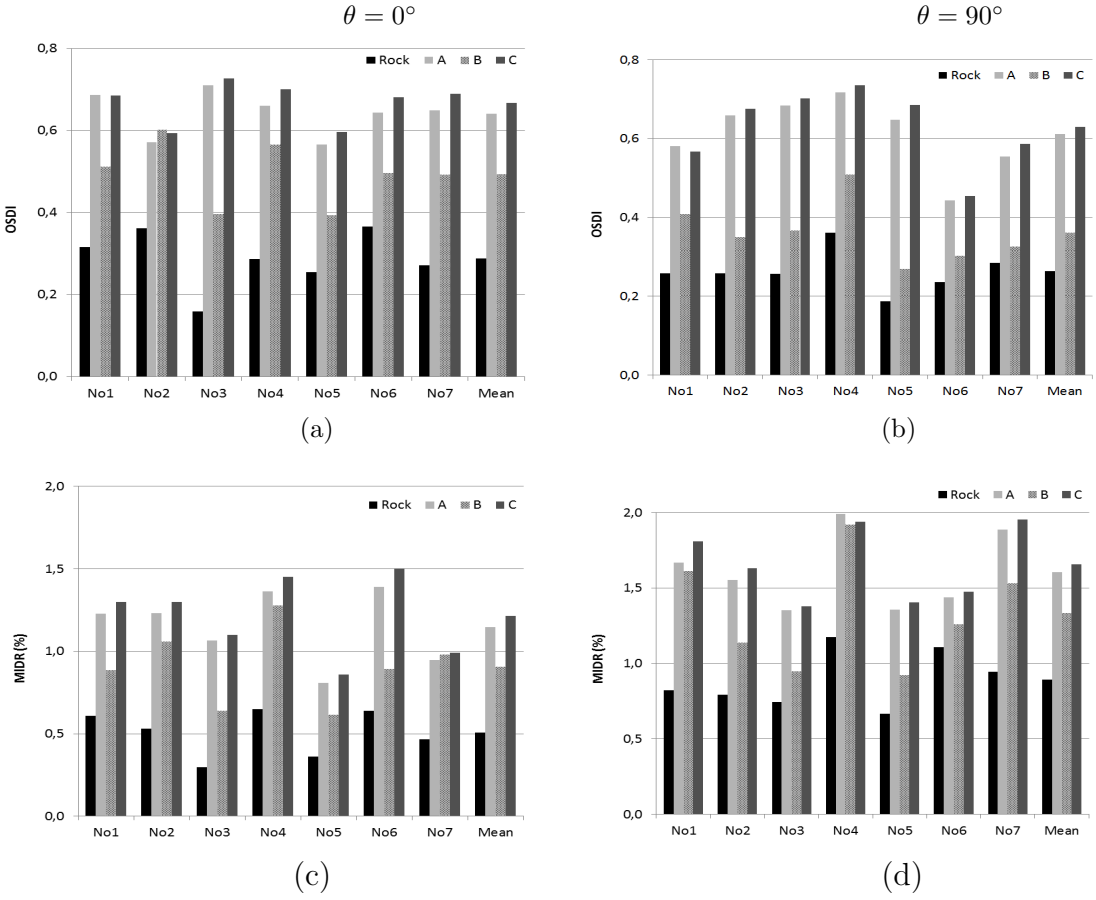

FIGURE 6.13: Overall structural damage index for incident angle (a) $\theta = 0^o$ and (b) $\theta = 90^o$ and maximum interstorey drift ratio for incident angle (c) $\theta = 0^o$ and (d) $\theta = 90^o$ for the geological profile 4

in Chapter 4 and for the shake of completeness in what follows are presented the basic details of the problem's formulation for the examined case.

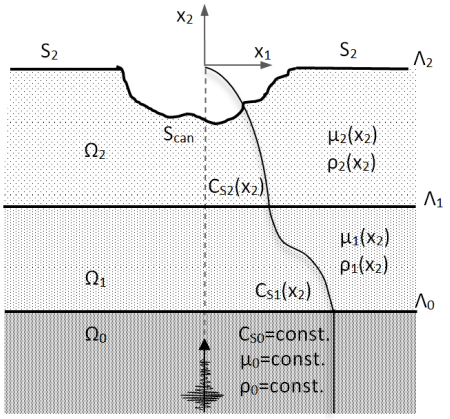

FIGURE 6.14: Inhomogeneous in depth half-plane with free-surface relief of arbitrary shape

More specifically, the material inhomogeneity is expressed by a position-dependent shear modulus and density of arbitrary variation in terms of depth coordinate. We define the inhomogeneity parameter $c_n = C^{bottom(\Lambda_{n-1})}/C^{top(\Lambda_n)}$ as the ratio of the wave velocity at the bottom to that at the top of any given layer. This model is also able to account for wave dispersion phenomena due to viscoelastic material behavior and to position-dependent material properties.

The BEM formulation in frequency domain based on the fundamental solutions for geological media with a velocity gradient [41, 42] is as follows:

$$cu_3^{(i)}(x,\omega) = \int_\Gamma U_3^*(x,y,\omega)t_3^{(i)}(y,\omega)d\Gamma - \int_\Gamma P_3^*(x,y,\omega)u_3^{(i)}(y,\omega)d\Gamma \qquad (6.10)$$
$$x \in \Gamma = \Lambda_0 \cup \Lambda_1 \cup \Lambda_2$$

In the above, x, y are source and field points, respectively, c is the jump term, U_3^* is the fundamental solution for geological media with variable velocity profile, and $P_3^*(x,y,\omega) = \mu(x_2)U_3^*(x,y,\omega)n_i(x)$ is the corresponding traction fundamental solution, where $i = 1, 2...N$ is the number of layers. The above equation is written in terms of total wave field and expresses the case of incident SH waves. Note that by using this closed form fundamental solution in the BEM technique, only the layer interfaces, as well as the free and sub-surface relief need to be discretized.

After discretization of all boundaries with constant (i.e., single node) boundary elements, the matrix equation system is formed below and displacements along the free surface can be computed:

$$[\mathbf{G}]\mathbf{t} - [\mathbf{H}]\mathbf{u} = \mathbf{0} \qquad (6.11)$$

The above system matrices $\mathbf{G}$ and $\mathbf{H}$ result from numerical integration using Gaussian quadrature of all surface integrals containing the products of fundamental solutions times interpolation functions used for representing the field variables. They are fully populated matrices of size NxN, where N is the total number of nodes used in the discretization of all surfaces and interfaces, while vectors u and t now contain the nodal values of displacements and tractions at all boundaries.

Finally, the generation of transient signals from the hitherto derived time-harmonic displacements is achieved through inverse Fourier transformation. Note here that both negative and positive values in the frequency, as well as in the time domain, are considered and both real and imaginary values for the response parameter are employed. The aforementioned BEM numerical implementation and production of the final seismic signal is programmed using the Matlab [94] software package.

6.3.2 Geological profiles

The methodology described in the previous section is now applied to four different hypothetical geological profiles of increasing complexity, on which the r/c bridge models in question are considered to be located, see Fig.6.15 below. The following key parameters are investigated: (i) canyon topography; (ii) layering; (iii) material gradient. In particular, the site is represented by the following geological profiles: (A) a homogeneous layer with flat-free surface producing a uniform excitation at all support points of the bridge; (B) a homogeneous layer with a valley in which the bridge is located; (C) a two-layer deposit as a damped soil column with a valley at the surface; (D) a two-layer damped soil column with the bridge valley at the surface, in which the top layer is continuously inhomogeneous with inhomogeneity parameter $c = 1.2$ expressing an otherwise arbitrary variation in the wave speed depth profile. The bottom layer is homogeneous and the interface between the first and the second layers is irregular. All geological profiles are overlying bedrock. The soil material properties of these subsoil geological configurations are shown in Fig.6.15 and Fig.6.16. Next, a suite of seven earthquake excitations given in

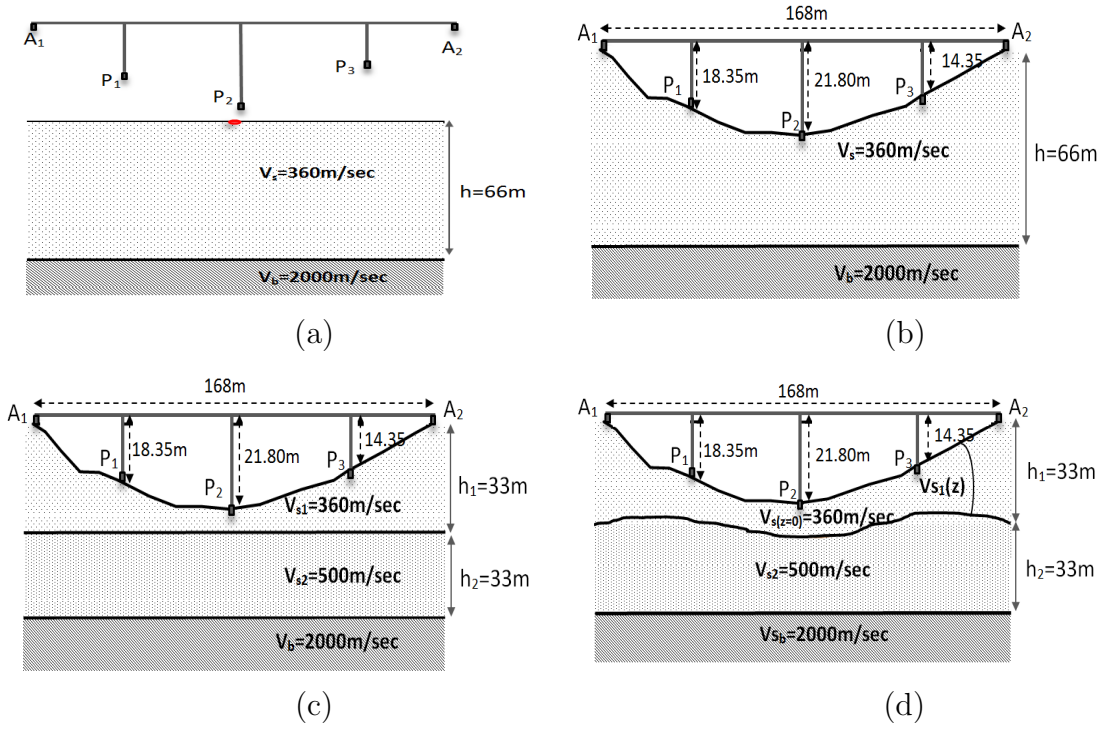

FIGURE 6.15: Four geological profiles, Types A-D, on which the R/C bridge is assumed to be located

Fig.6.4 are recorded at outcropping rock on a class A site according to FEMA [136] classification and are drawn from the PEER [137] strong motion database. These records are considered as an input at the seismic bed level for all geological profiles.

	Vs (m/sec)	μ (Pa)	ρ (N/m^2)
Layer 1	360	$233.28 \cdot 10^6$	1800
Layer 2	500	$450 \cdot 10^6$	1800
Bedrock	2000	$800 \cdot 10^7$	2000

FIGURE 6.16: Material properties of the basic geological structure

6.3.3 Ground motions

Next the influence of site effects on ground motions recorded along the free surface is investigated. The first geological profile comprising a single layer with a horizontal free surface that produces a uniform excitation pattern, considered as a reference case. Fig.6.17 plots the acceleration response spectra recorded at the surface of the Type B geological profile at the support points of the bridge along the canyon and for two different seismic motions. Observe that spectral values at the bridge support points are not the same and furthermore, they differ significantly at certain period values from those produced for the reference case of uniform excitation. Spectral accelerations are more pronounced for low values of period at the bottom of the canyon, while high period values lead to significant spectral acceleration at the edge of the canyon. Three dimensional time history recordings along the canyon are shown in Fig.6.18, where it is obvious that the seismic signal depends strongly on the canyon topography.

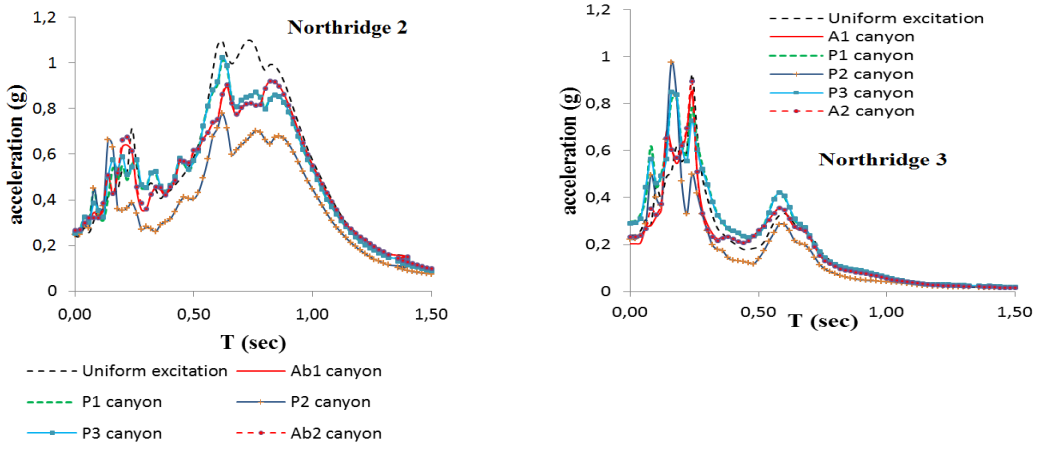

(a) (b)

FIGURE 6.17: Acceleration response spectra recorded at the free surface of Type B geological profile for (a) Northridge 2 and (b) Northridge 3 excitations

The influence of canyon topography and of the soil layering on ground motions is examined by comparing acceleration response spectra generated from the uniform excitation geological profile with those generated at the surface of the Type C geological profile that accounts for canyon topography and layering effect, see

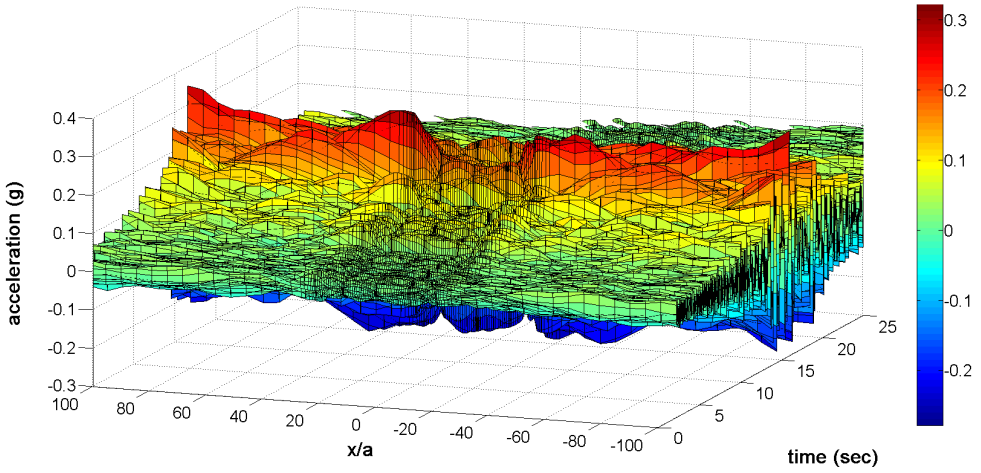

FIGURE 6.18: 3D figure of the acceleration time history recorded at the free surface of Type B geological profile for Northridge No2 excitation

Fig.6.19. It can be seen that the ground motions are strongly affected by the combined soil layering and canyon topography structure. The shape of the response spectra is now modified, while an expected shifting to the right (higher periods) due to the layering effect is clearly depicted. This is also evident from the 3D figure of time history recorded along the surface of the Type C geological profile shown in Fig.6.20. There, the acceleration peaks become smoother due to the increased stiffness of the bottom layer.

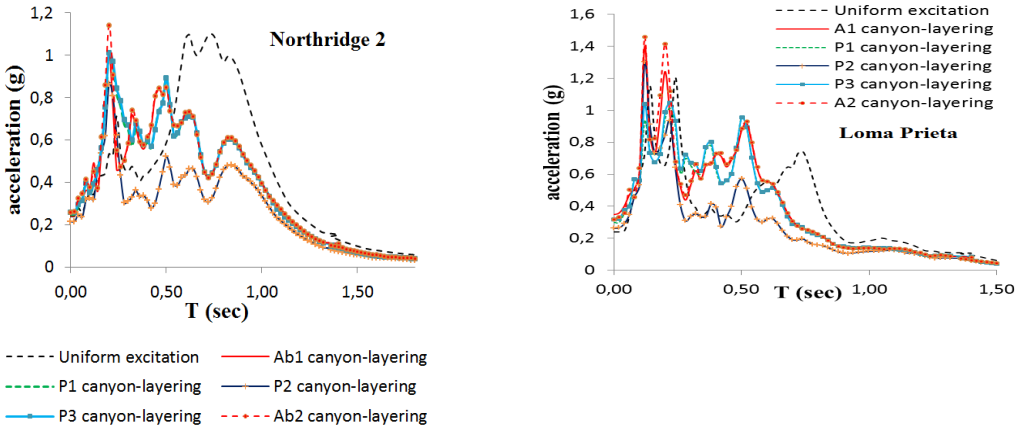

FIGURE 6.19: Acceleration response spectra recorded at the free surface of Type C geological profile for (a) Northridge 2 and (b) Loma Prieta excitations

The combined influence of canyon topography, layering and material gradient effect on the ground motions is now examined. As previously mentioned, in this case the top layer has a continuous variation of the wave speed with depth, avoiding this way the great wave speed contrast between the first and the second layer

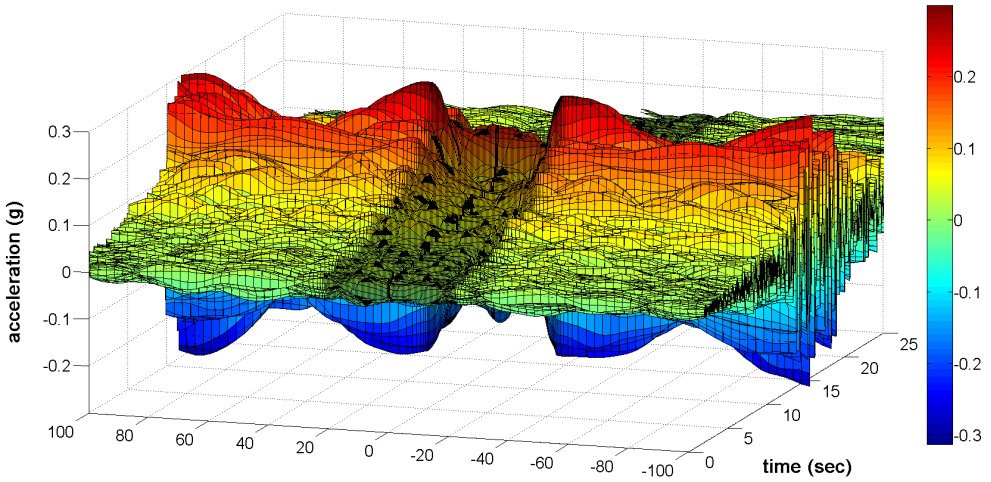

FIGURE 6.20: 3D figure of the acceleration time history recorded at the free surface of Type C geological profile for Northridge No2 excitation

of the previously examined case, as shown in Fig.6.21. In addition, it is also introduced here a spatial irregularity in the interface between the two soil layers. More specifically, in Fig.6.22 are compared the acceleration response spectra generated for the reference case of uniform excitation with those spectra generated at the surface of the Type D geological profile. It is clearly observed now how site effects significantly influence the seismic ground motions. The presence of material gradient increases the material stiffness gradually and the soil becomes stiffer. As a result, the spectral acceleration values are deamplified across the entire range of periods examined herein.

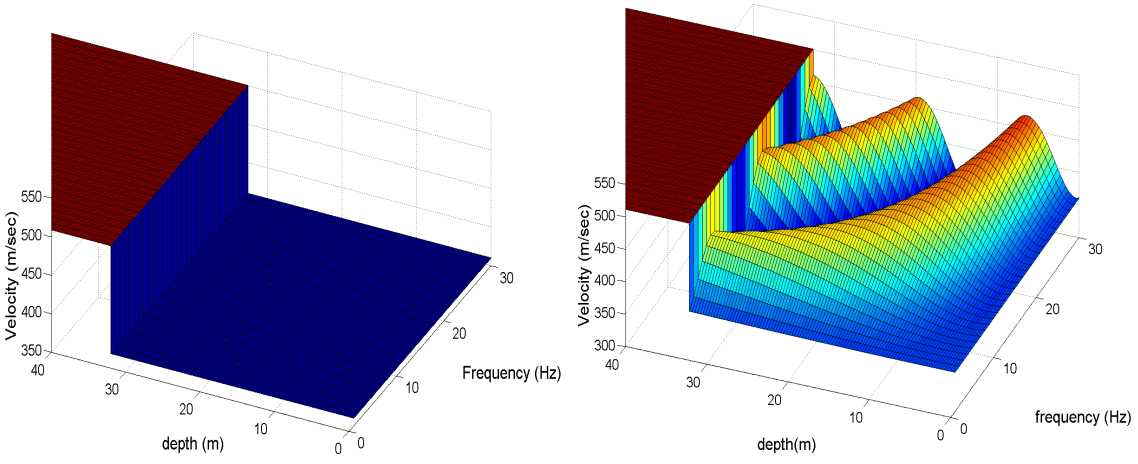

FIGURE 6.21: Velocity distribution of the subsoil structure: (a) Type C and (b) Type D geological profile

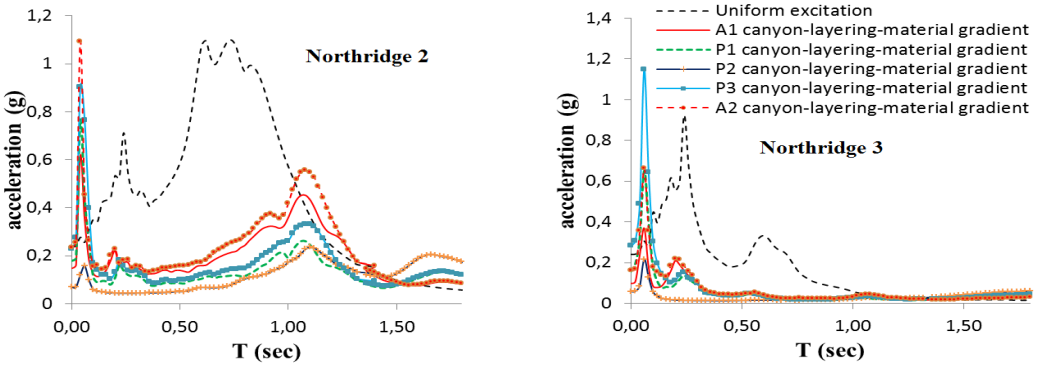

FIGURE 6.22: Acceleration response spectra recorded at the free surface of Type D geological profile for (a) Northridge 2 and (b) Northridge 3 excitations

6.3.4 Bridge modeling

Next we focus on the nonlinear response of an existing r/c bridge. In particular, it is considered a redesign scheme of the Greek Railway Organization (OSE) bridge located in Polycastro, Northern Greece (see [146]). Two different configurations of this bridge are investigated in terms of the piers-deck connections: (i) seismic isolation and (ii) monolithic connection. In both cases the bridge is straight with earthquake resistant abutments and has a total length of $168m$ supported on rectangular hollow piers of unequal height that varies from 14.35 to $21.8m$, as shown in Fig.6.23.

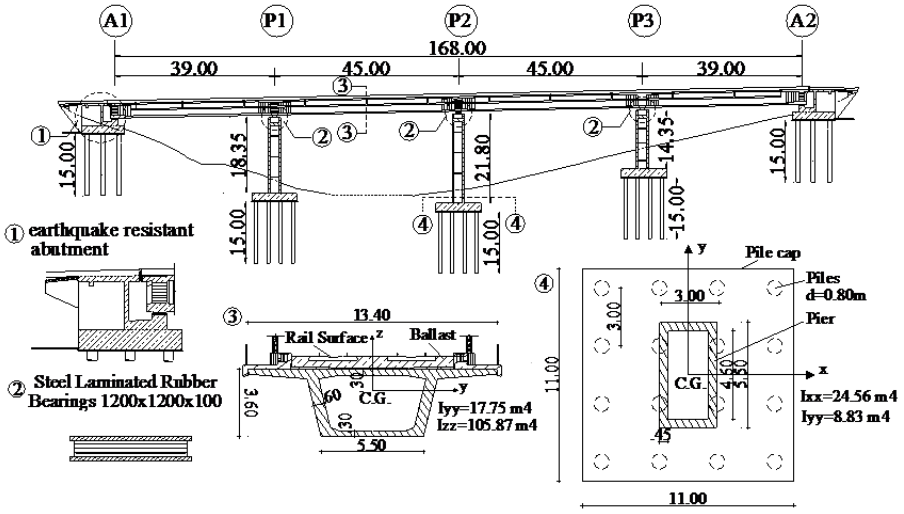

FIGURE 6.23: Section details along the bridge span: (1) Bridge abutment; (2) steel laminated rubber bearings; (3) deck cross-section; (4) plan view of the pier and its foundation

In terms of some additional details, the two end spans are $39m$ long, while the two intermediate spans have span lengths of $45m$ each. The concrete deck is a hollow box girder with a constant cross section along the length. For the design of the expansion joints, 40% of the seismic movements of the deck are considered according to Eurocode 8 [120], as well as serviceability-induced constrained movements of creep, shrinkage, pressing and 50% of the thermal movements of the deck. The cracked flexural stiffness of the piers is estimated as equal to 65% of the original cross-section.

The bridge is modeled using the FEM commercial program SAP2000 [147]. The bearings are modeled by a number of nonlinear-link elements, with bilinear behavior in order to simulate the translational and rotational stiffness of the bearings. Piers and deck are modeled by frame elements. Gap elements are used to model the $25mm$ opening at the expansion joints, which separate the backwall from the deck. Note here that the nonlinear response of the bridge in case of the monolithic model is localized and considered only by the geometrical nonlinearities of the gap elements as both the deck and the piers are designed to remain elastic under the design earthquake. In case of the seismic isolated bridge model, nonlinear response of the bridge is considered by nonlinearities of the gap elements as well as by the isolators.

The interaction of the foundation with the subsoil-structure and the bridge is considered by assigning six spring elements at the contact points, namely three translational and three rotational. For all support points of the bridge and for four different geological profiles, site dependent spring coefficients are computed from closed form equations. For the present case of pile group foundation, equations referring to a single pile [148, 149] are modified in order to account for the waves that are emitted from the piles and propagate towards the other members of the group. To that purpose, complex dynamic interaction factors α_{ij} are calculated from closed-form equations existing in the literature [150]. Soil-Structure-Interaction is strongly frequency dependent. Nevertheless, it is assumed that the dynamic impedance matrix is calculated based on the predominant frequency of the input motion. This assumption is rather common in the literature but it may not be accurate under certain conditions [151]. Hence a range of values between the predominant spectral period and the smoothed spectral predominant period of excitation is considered in the present study.

6.3.5 Dynamic response of the seismically isolated bridge model

For the case of seismically isolated bridge model [144], a series of nonlinear time history analyses are conducted under the following conditions: (i) a suite of ground

motions applied uniformly to all support points of the bridge and (ii) the same suite of site dependent ground motions, which are now different for each support point of the bridge. These motions also account for (a) canyon topography effect; (b) canyon plus soil layering effect and (c) canyon topography, layering with irregular interfaces and a material gradient effect. No SSI phenomena are taken into consideration in the seismically isolated bridge model. The fundamental period of the bridge with fixed base along the $X-axis$ is $T_x = 1.43$sec and along the $Y-axis$ is $T_y = 0.71$sec.

The influence of site effects on structural response of the seismically isolated r/c bridge is demonstrated in Figs.6.24-6.27 where input is ground motions at rock outcrop that have been filtered by the complex soil deposits of Fig.6.15 so as to account for (i) uniform excitation, (ii) canyon effect, (iii) canyon and layering effect and (iv) canyon, layering and material gradient effect.

More specifically, maximum displacements of the bridge deck are shown in Fig.6.24 for the middle point of the first joint (A1-P1) and for the second joint (P1-P2) along the bridge span for the four types of geological profiles. In most cases, the modified ground motions due to local site effects play an important role in modifying the kinematic response of the bridge in a way that is considered as beneficial. Moving on to the stress field that develops in the R/C bridge, Fig.6.25

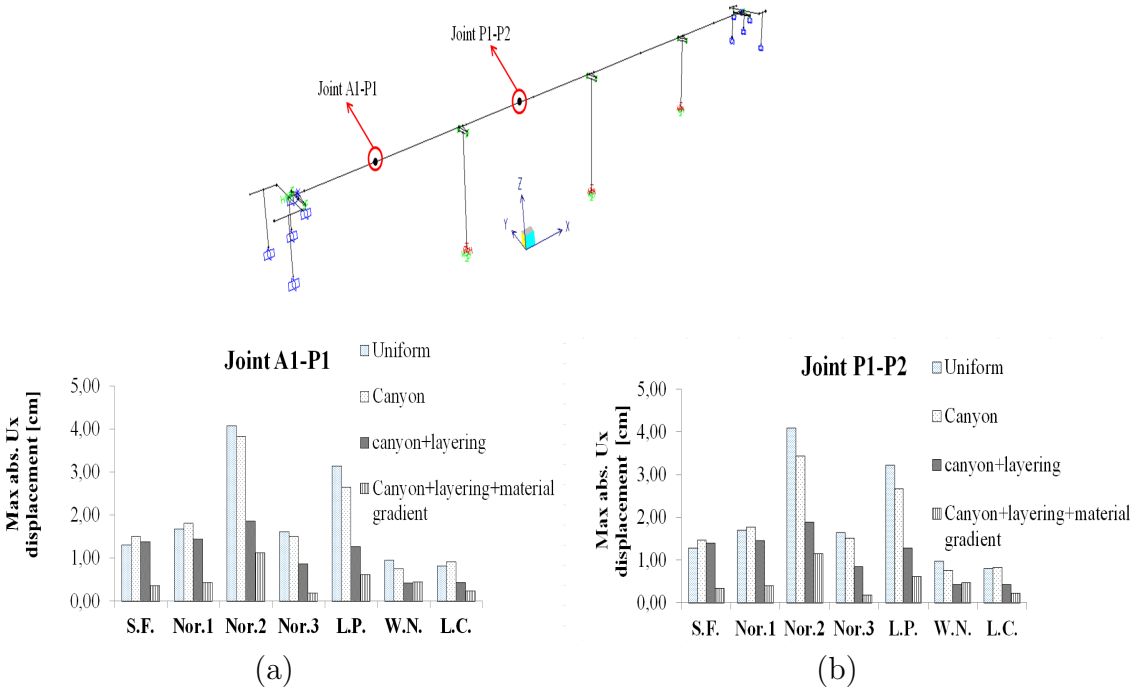

FIGURE 6.24: Maximum absolute deck displacements at joints (a) A1-P1; (b) P1-P2, due to ground motions recorded at the surface of the Types A-D geological profiles

gives the maximum absolute shear stresses at the bearings located at abutment $A1$ and at piers $P1$ and $P2$. Observe that for some seismic motions, local site conditions have a significant effect on the response of the bearings, while for other ground seismic motions local site conditions produce minor small differences in the bearing response as compared with the reference Type A soil deposit. For at least three ground motions histories, canyon topography results in motions that subsequently overstress the aforementioned supports. However, the input of identical motions as excitations at the bridge's supports will not always yield what is construed as a conservative response, indeed for the examined here case canyon topography effect can lead to 15% increase on the bearings response.

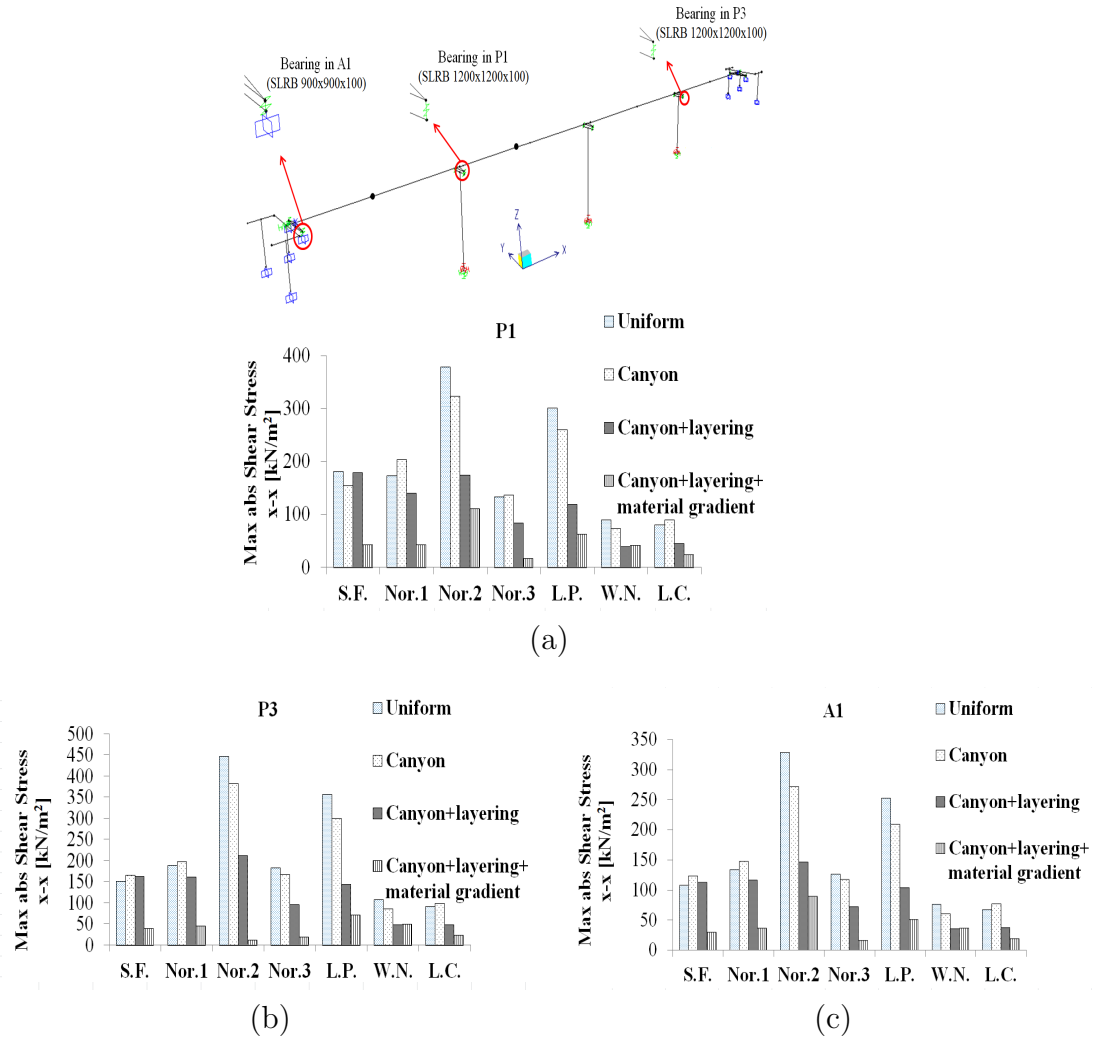

FIGURE 6.25: Maximum absolute bearing shear stresses at bearing (a) $P1$; (b) $P3$; (c) $A1$, due to ground motions recorded at the Types A-D geological profiles

Next, maximum absolute displacements at piers $P1$ and $P3$ are shown in Fig.6.26, where it is seen that pier $P1$ is the one most affected by the influence of local soil conditions. For all the cases examined here, ignoring site effects may introduce amplification effects reaching up to 70% in terms of the displacements.

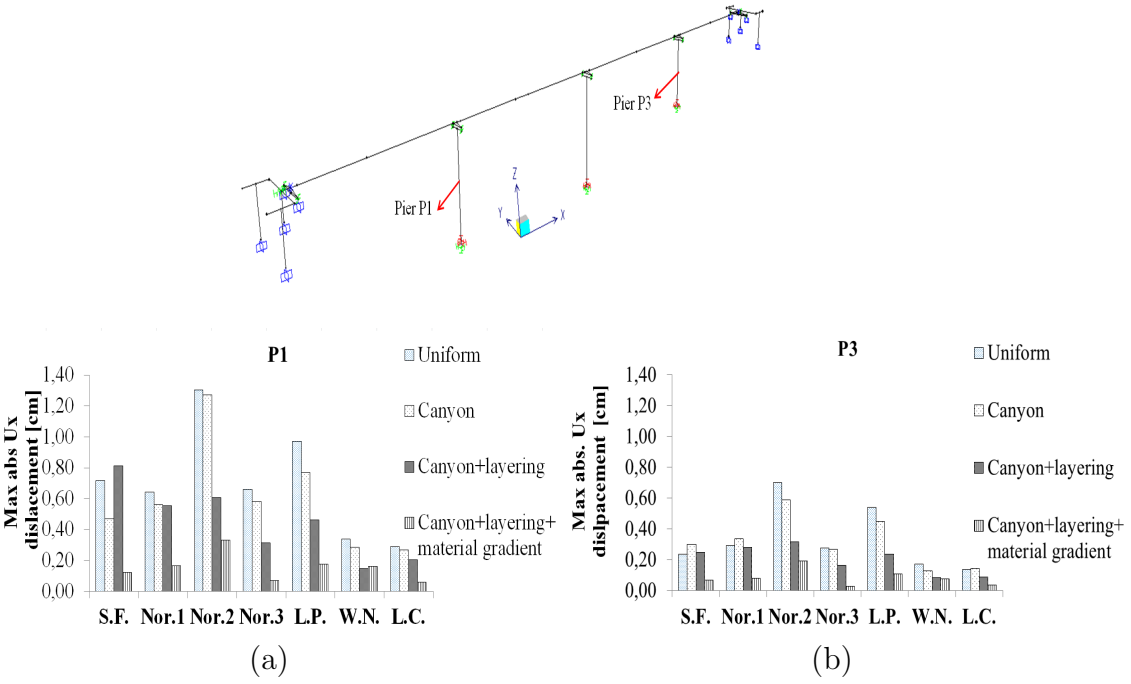

FIGURE 6.26: Maximum absolute pier displacements at joint (a) $P1$; (b) $P3$, due to ground motions recorded at the surface of the Types $A-D$ geological profiles

Displacement time histories of the bridge deck, and in particular of the middle point of the first span, are presented in Fig.6.27 for Loma Prieta ground motion (listed in Fig.6.4) due to uniform excitation case and to the ground motions that account for canyon, soil layering and material inhomogeneity. It is observed that canyon topography effect may either amplify or deamplify the displacement time history of the deck (the latter holds for the present case). When the canyon effect is combined with soil layering, the effect produces strong deamplification, due to the increase in stiffness of the soil system, plus a shifting of the peaks. The combination of canyon, layering and material gradient effect significantly modifies the displacement time history computed at the deck in terms of resonance frequencies and amplification levels.

6.3.6 Dynamic response of the monolithic bridge model

For the case of monolithic bridge model [145], a series of nonlinear time history analyses are conducted under the suite of seven ground motions considering SSI phenomena for the following two cases: (i) the same seismic record is applied to all support points of the bridge (uniform case) and (ii) site dependent ground motions (i.e. the records are different for each support point of the bridge). These ground motions and the corresponding spring coefficients account for (a) canyon

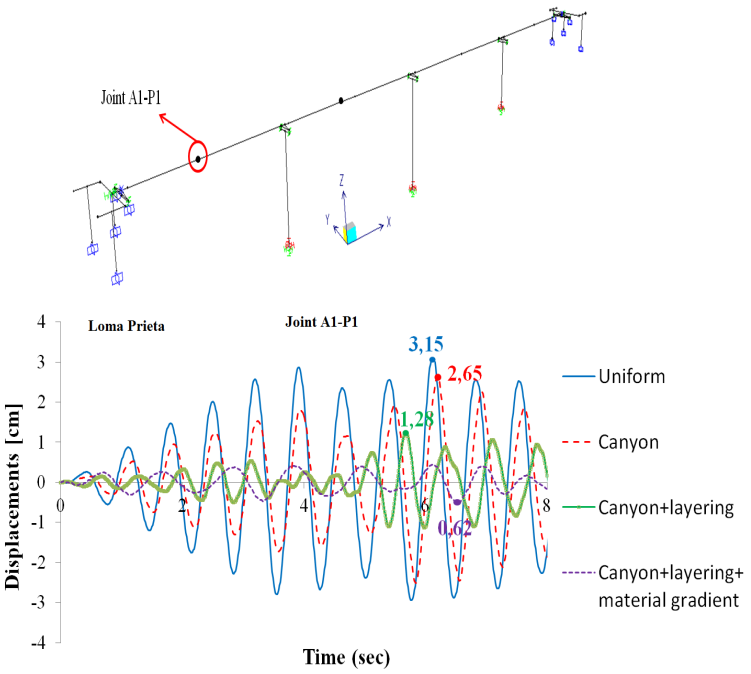

FIGURE 6.27: Displacement time history recorded at point $A1-P1$ on the deck due to ground motions recorded at the surface of the Types $A-D$ geological profiles

topography effect; (b) canyon plus soil layering effect and (c) canyon topography, layering with irregular interfaces and a material gradient effect.

In order to estimate the relative importance of the topographic effects and the subsequent multiple support excitation of the bridge two parametric sets of analyses are carried out. Namely, the following cases are considered: (1) "uniform" spring values where spring coefficients have the same values for all support points of the bridge for each ground motion and (2) multiple spring values where spring coefficients have different values for each support point of the bridge and for each ground motion based on 2D analysis of the subsoil structure.

Fig.6.28 shows the mean value of piers'dynamic lateral stiffness due to ground motions recorded at the surface of the Types $A-D$ geological profiles that account for i) uniform excitation, ii) canyon effect, iii) canyon and layering effect and iv) canyon, layering and material gradient effect. As can be seen, in terms of the foundation dynamic impedance matrix the presence of local site conditions has a beneficial effect to the bridge foundation stiffness for all here examined ground motions. The influence of (a) site effects, (b) spatial variability in terms of 2D analysis of wave propagation and (c) SSI on structural response of the r/c bridge is demonstrated in Figs.6.29-6.31. More specifically, maximum displacements of the bridge deck are shown in Fig.6.29 for the middle point of the first deck-span (joint A1-P1) and for the second deck-span (joint P1-P2) for the examined case

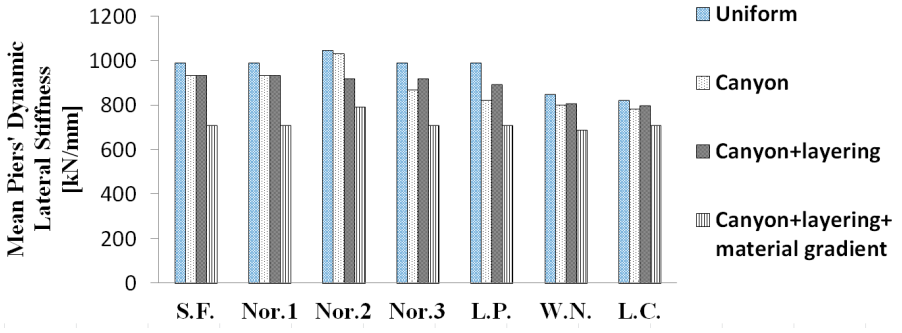

FIGURE 6.28: Mean value of piers'dynamic lateral stiffness due to ground motions recorded at the surface of the Types A-D geological profiles

of study. Observe that the presence of local site conditions can modify the kinematic response of the bridge either beneficially or detrimentally. For some ground motions, local site conditions have a significant effect on the response of the deck, while for other ground motions local site conditions produce a minor small difference in the displacement of the deck as compared with the reference type A soil deposit. The pronounce response of the bridge under excitation Northridge 2 and Whittier Narrows for the case of the uniform excitation compared to the other cases that account for site effects is reminiscent of dynamic resonance. In particular, the presence of a complex subsoil structure modifies the frequency of the propagating wave as well as the dynamic characteristics of the bridge through the change in the spring coefficients and the subsequent fundamental period of the structure. Furthermore, it can be seen that the effect of multiple spring values for the support points of the bridge produces minor small difference in the deck displacements comparing with the uniform spring values for all support points for each ground motion.

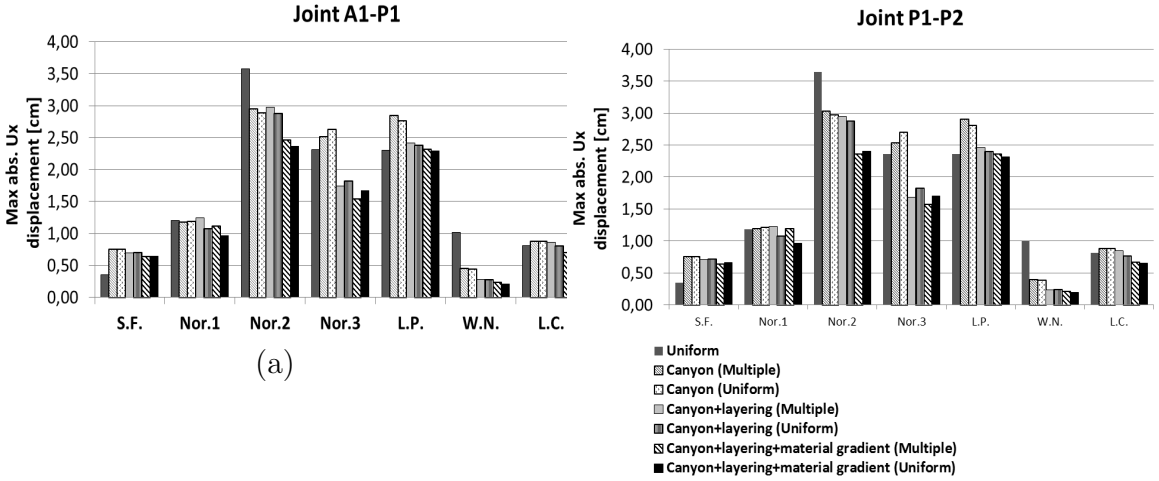

FIGURE 6.29: Maximum absolute deck displacements at joints (a) $A1 - P1$; (b) $P1 - P2$, due to ground motions recorded at the surface of the types $A - D$ geological profiles for (i) uniform spring values and (ii) multiple spring values

Next, maximum absolute displacements at piers $P1$ and $P3$ are shown in Fig.6.30, where it is observed that both piers respond similarly to all examined here cases. Ignoring site effects may introduce difference up to 50% in the bridge response in terms of the displacements for the considered here case of study.

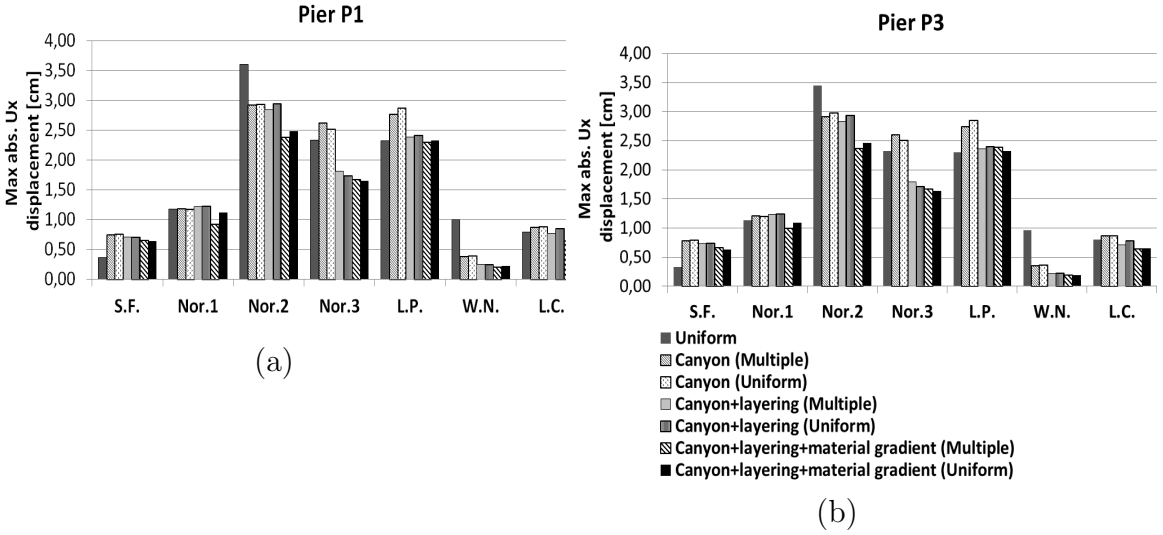

FIGURE 6.30: Maximum absolute pier displacements at joints(a) $P1$; (b) $P3$, due to ground motions recorded at the surface of the types a-d geological profiles for (i) uniform spring values and (ii) multiple spring values

Displacement time history of the bridge deck, and in particular of the middle point of the first span, is presented in Fig.6.31 for Northridge Nr3 ground motion (listed in Fig.6.4) due to uniform excitation case and to the ground motions that account for canyon, soil layering and material inhomogeneity for uniform or multiple values of spring coefficients. It is observed that canyon topography effect may amplify or deamplify slightly the displacement time history of the deck (the former holds for the present case). When the canyon effect is combined with soil layering, the effect produces strong deamplification, due to the increase in stiffness of the soil system, plus an obvious shifting of the peaks. The presence of material gradient additionally to canyon and layering effect does not change the shape of overall time history picture. However in case of multiple spring coefficient values the additional effect of the material gradient produce a small decrease in the amplification levels.

To sum up, from all the above numerical results is evidently demonstrated that the combination of local site conditions, spatial variability and SSI effects influence significantly the nonlinear response of extended structures like bridges. These effects cannot be neglected and should be modeled and implemented in as much as possible. It is not true from the cases examined herein that ignoring site effects, spatial variability and SSI phenomena leads to beneficial results for the r/c bridge.

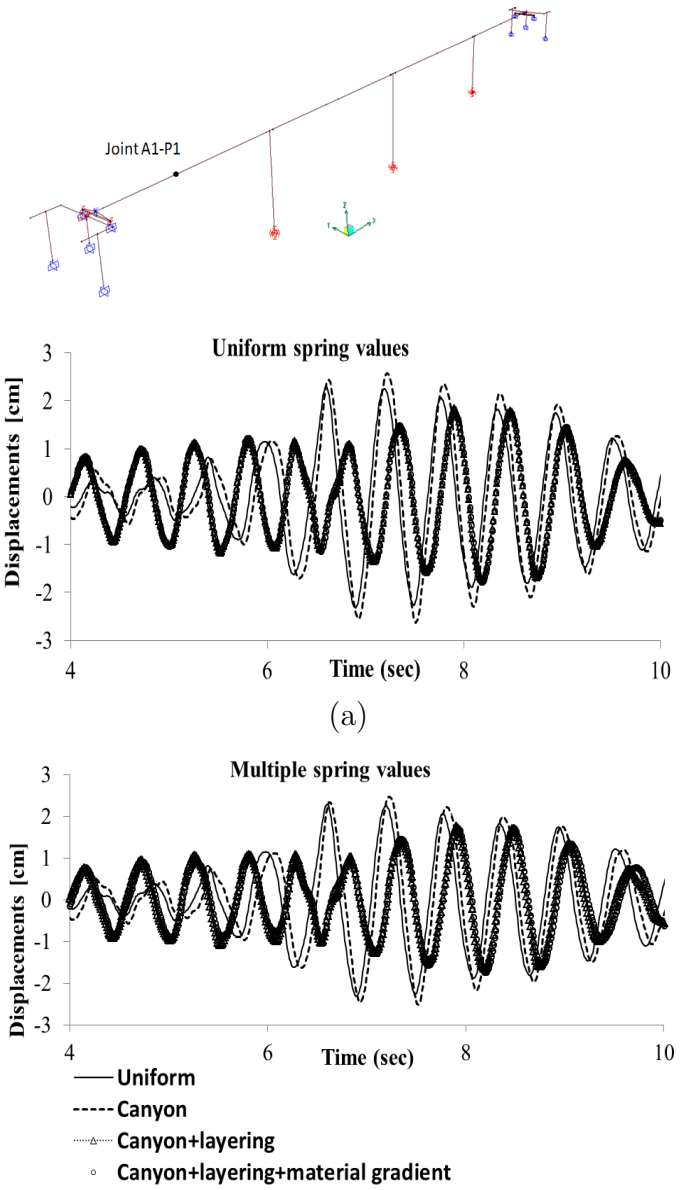

FIGURE 6.31: Displacement time history recorded at point $A1-P1$ on the deck due to ground motions recorded at the surface of the types $A-D$ geological profiles for (a) uniform spring values and (b) multiple spring values

Also, it cannot established a priory that these phenomena have beneficial influence on the seismic response of the bridge. Ignoring site effects via 2D analysis of the soil profile may introduce an error around 70% for the monolithic bridge model and 50% for the seismic isolated bridge model, in terms of kinematic field.

6.4 Conclusions

In the present chapter, the potential of the new developed BEM schemes to investigate the influence of site effects on structural damage is investigated. Bridge and building models are examined under site dependent ground motions computed at the surface of complex geological profiles considering 2D analysis of the soil profile. The complex geological profiles account for (a) canyon topography, (b) soil layering and (c) material gradient effect in terms of (i) quadratic variation of material properties (constant velocity) and (ii) variable velocity profile.

From the numerical simulation results the followings can be stated. Site dependent ground motions are generated efficiently by new-developed BEM that can represent wave propagation in complex geological media with material inhomogeneity, nonparallel layers, surface relief of arbitrary shape and buried cavities and tunnels. The ground motions and the subsequent structural response are strongly affected by the canyon topography, layering and material gradient effect and this effect is frequency-dependent. Local site conditions, spatial variability and SSI cannot be ignored since they influence the inelastic structural response, either beneficial or detrimental. The effect of site dependent ground motions on the seismic response of the building or bridge models considered here depends on the interplay between the dynamic characteristics of the aboveground construction, the heterogeneity and inhomogeneity in space of soil profile and the properties of the incoming wave field.

Chapter 7

General Conclusions and Outlook

7.1 Conclusions and main results

The present thesis focuses on the development of a non-conventional BEM numerical scheme for wave propagation in continuously or discrete inhomogeneous geological media with heterogeneities like homogeneous or graded layers, cavities, tunnels and valleys. In the BEM formulation are efficiently inserted special class of fundamental solutions and Green's functions that account for different types of material gradient. Limited number of studies exist in the literature that address wave propagation in continuously inhomogeneous media via BEM. However, they consider no heterogeneities or if they do, it is restricted to simple geometry like a single crack, a semi-circular alluvial valley or they turn to hybrid computational methods. Along this lines, the main objective of the present thesis is to develop, validate and use for simulations new BEM models and accompanied research software to deal with continuously inhomogeneous geological media with complex heterogeneities like homogeneous or graded layers, valleys, cavities, free and subsurface relief. Hence, the developed models are able to account for all three components of the seismic problem (source - wave path - subsurface geology) in one step in comparison with the hybrid two step techniques. When hybrid techniques are applied, the backscattering phenomena are not taken into consideration and this disadvantage of the hybrid approach is overcome by the proposed here non-conventional BEM models.

A brief introduction to the BEM formulation and an extensive literature review regarding wave propagation problems in continuously inhomogeneous geological media is presented. From this literature review one concludes first the potential of BEM to deal with high accuracy and minimal modeling effort unbounded complex geological media. Next, it is noted that there is a limited number of BEM models in

the literature able to investigate wave propagation in continuously inhomogeneous media containing complex multiple heterogeneities.

Novel BEM numerical schemes based on a library of fundamental solutions or Green's functions are developed validated and detailed presented for out-plane wave propagation problems. Different types of material gradient are expressed in the model through the implementation of appropriate fundamental solutions or Green's functions in the BEM frame. In particular, three types of material gradient are considered: (a) quadratic variation of material properties yielding to a macroscopically constant wave speed (Chapter 3); (b) arbitrary variation of material properties that yields to a variable velocity profile, both frequency and position dependent (Chapter 4); (c) position dependent shear modulus and constant density that yields to a linear velocity profile (Chapter 4 and 5). The inhomogeneous background following one of the aforementioned material gradient trends is combined with the presence of complex heterogeneities and the wave field picture is computed due to incident SH wave or wave radiating from embedded seismic source. A successful verification with existing solutions is given as well as a series of parametric studies considering different geological configurations and seismic scenarios.

Following the development of numerical tools and the supporting mechanical models the following points can be concluded. For the BEM based on Green's function for quadratically inhomogeneous half-plane the advantages are:

- direct modeling of inhomogeneity through the use of Green's function for quadratically inhomogeneous half-plane avoiding the discretization of all layer interfaces required in the discrete model. The inhomogeneity is expressed in terms of quadratic variation of material properties and macroscopically constant wave velocity;
- can take into consideration the backscattering phenomena in contrast to the hybrid two-steps methods;
- reduction of the problem dimensionality because the discretization is applied only along the existing boundaries (free- and sub-surface relief) without the need to discretize additionally the free-surface as in conventional BEM or the whole domain area as in FEM;
- the Green's function satisfies the Sommerfeld radiation condition and thus infinitely extended boundaries are automatically incorporated
- the mathematical form of the Green's function is not complex and can be inserted in the BEM software;
- the method is based on the Green's function for the half-plane and thus it can be considered as semi-analytical approach.

For the BEM based on a special family of fundamental solutions for continuously inhomogeneous media with variable or linear wave velocity profile the advantages are:

- direct modeling of inhomogeneity in terms of soil velocity variation avoiding the discretization of all layer interfaces required in the discrete model;
- it is one step technique, thus can take into consideration the backscattering phenomena in contrast to the hybrid two-steps methods;
- reduction of the problem dimensionality because the discretization is applied along the existing boundaries (free- and sub-surface relief) and the free surface as in conventional BEM for homogeneous full plane but additionally expressing an inherent continuous inhomogeneity. An equivalent mechanical model can be computed via FEM with the need to discretize the whole domain area;
- the model expressing variable velocity profile is able to account for wave dispersion phenomena due to viscoelastic behavior and to position-dependent material properties;
- the mathematical form of the fundamental solutions is not complex and it can be easily inserted in the BEM software. The displacement and the traction fundamental solutions exhibit the same singular behavior as this for the homogeneous case;
- the fundamental solutions satisfy the Sommerfeld radiation condition and thus infinitely extended boundaries are automatically incorporated.

Considering the investigated problem of SH-wave propagation in complex geological profiles the followings can be concluded. It is evidently demonstrated the potential of the developed numerical tools and accompanied research software to reveal the sensitivity of the seismic signal to the existence and type of the material gradient, to the type and properties of the seismic source and to the lateral inhomogeneity due to the free-surface and/or sub-surface relief peculiarities like layering, tunnels, cavities, valleys. Seismic signals in time domain are generated at the surface of complex geological profiles able to describe efficiently and with high accuracy all three components of the Earth system; seismic source, wave path and local geological region of interest.

Application of the developed BEM models in material modeling is demonstrated by reproducing wave motion phenomena in a continuous matrix with position dependent-material properties and containing any number and configuration of cavities for pure elastic and poroelastic geological media (Chapter 5). The presence, shape and spatial distribution of cavities is a key parameter in the development of the displacement wave field and of localization effects in the stress field.

Additionally the presence of inhomogeneity in the material matrix complicates further the wave field picture. The type and magnitude of the material inhomogeneity influence significantly the material response. Moreover, the parameter of poroelasticity of the soil material may greatly amplify its response for high values of porosity.

Applications of the developed BEM models in earthquake engineering are given by investigating the influence of site effects on the ground motions and the subsequent structural damage of aboveground structures considering 2D analysis of the soil profile (Chapter 6). Bridge and building models are examined under site dependent ground motions computed at the surface of complex geological profiles that account for canyon topography, soil layering and material gradient. It is demonstrated the potential of the new-developed BEM models to generate efficiently site dependent ground motions. It is shown that the effect of site dependent ground motions on the seismic response of aboveground constructions depends on the interplay among the dynamic characteristics of the aboveground construction, the heterogeneity and inhomogeneity in space of the soil profile and the inherent characteristics of the incoming wave field. Local site conditions, spatial variability and SSI phenomena cannot be ignored since they influence the inelastic structural response, either beneficial or detrimental.

7.2 Outlooks and future work

For extension of the present thesis, it is recommended to develop non-conventional BEM models for in-plane wave motion. Appropriate fundamental solutions or Green's functions for in-plane wave motion can be found in Manolis et al. [82] for exponential and quadratic variation of material properties and constant wave velocity and in Sanchez-Sesma et al. [71] for linear variation of wave velocity. With the extension to in-plane wave motion a complete numerical tool will be available for 2D analysis of wave propagation in complex geological media. However, the real wave field picture can be demonstrated only by 3D analysis of the soil profile. Hence, the development of 3D BEM models able to model unbounded media with complex geological morphology is of great and actual importance.

Another important venue for the present research work is to move to a stochastic BEM formulation, considering the many uncertainties in the soil formation properties and constitution. Given that the governing equation of motion is scalar and the availability of the fundamental solutions, the formulation of a stochastic BEM should be doable. All that is needed is the formation of covariance matrices based on the derivatives of the fundamental solutions with respect to the chosen material parameters that are uncertain (i.e., stochastic variables).

For further extension of the present thesis is proposed also the coupling of the existing BEM developments with FEM models. The FEM is appropriate to deal with non-homogeneity, anisotropy and non-linearity of materials while it is not able to deal successfully unbounded media. On the other hand, BEM represents an ideal approach for treating infinite and semi-infinite domains, easy-handling of data preparation also fields with stress concentration and moving loads. Therefore, an efficient coupling of FEM with BEM will overcome the limitations and strengthen the advantages of each model.

Application of the above mentioned numerical tools can be found in several engineering problems. 2D and 3D SSI problems taking into consideration the whole path: seismic source–unbounded wave path–finite local geological profile–foundation–structure, having in mind effects as poroelasticity, physical and geometrical nonlinearity, non-linear contact zone between the soil and structure. Moreover, they act as a base for further development of numerical tools for coupled hydro-mechanical or thermo-hydro-mechanical problems in inhomogeneous and heterogeneous geological continua. Finally, useful application can take place in inverse problem solution for identification and characterization of material profiles of geological media.

Bibliography

[1] *Site effects sketch.* Wikimedia at commons.wikimedia.org, 19 March 2011.

[2] E. Kausel and G.D. Manolis. *Wave motion in earthquake engineering.* WIT Press, Southampton, 2000.

[3] D.E. Beskos and S.A. Anagnostopoulos. *Computer analysis and design of earthquake resistant structures:handbook.* WIT Press, Southampton, 1997.

[4] M. D. Trifunac. Scattering of plane SH waves by semi–cylindrical canyon. *Earthq. Eng. Struct. Dyn.*, 1:267–281, 1973.

[5] H.L. Wong and M. D. Trifunac. Surface motion of semi–elliptical alluvial valley for incident plane SH-waves. *Bull. Seism. Soc. Am.*, 64:1389–1403, 1974.

[6] F.J. Sanchez-Sesma. Diffraction of elastic waves by three dimensional surface irregularities. *Bull. Seism. Soc. Am.*, 73:1621–1636, 1983.

[7] N. Moen-Vaziri and M. D. Trifunac. Scattering and diffraction of plane P- and SV-waves by two dimensional inhomogeneities: Part II. *Soil Dyn. Earthq. Eng.*, 7:189–200, 1988.

[8] V.W. Lee and X. Wu. Application of the weighted residual method to diffraction by 2–D canyons of arbitrary shape: II. incident P, SV, and Rayleigh waves. *Soil Dyn. Earthq. Eng.*, 13:365–375, 1994.

[9] V.M. Babich. *Ray methods for computation of the intensity of wavefronts.* Nauka Publications, Moscow, 1956.

[10] Y.H. Pao and R.R. Gajewski. The generalized Ray theory and transient responses of layered elastic solids. *Physical Acoustics*, 13:183–265, 1977.

[11] F. Schwab and L. Knopoff. Surface wave dispersion computations. *Bull. Seism. Soc. Am.*, 60:321–344, 1970.

[12] G.F. Panza. Synthetic seismograms: the Reyleigh waves modal summation. *Journal of Geophysics*, 58:125–145, 1985.

[13] I. Herrera. On a method to obtain a Green's function for a multilayered half–plane. *Bull. Seism. Soc. Am.*, 54:1087–1056, 1964.

[14] B.L.N. Kennett. *Seismic wave propagation in stratified media,* V*ol* I. Cambridge University Press, 1983.

[15] J.E. Luco and R.J. Apsel. On the Green's functions for layered half-space: Part I. *Bull. Seism. Soc. Am.*, 73:909–29, 1983.

[16] Y. Hisada. An efficient method for computing Green's functions for layered half–space with sources and receivers at close depths (Part1). *Bull. Seism. Soc. Am.*, 84 (5):1456–1472, 1994.

[17] Y. Hisada. An efficient method for computing Green's functions for layered half-space with sources and receivers at close depths (Part2). *Bull. Seism. Soc. Am.*, 85 (4):1080–1093, 1995.

[18] F. Wuttke. *Advanced site investigation by use of surface waves.* PhD thesis, Bauhaus University, Weimar, Germany, 2005.

[19] J. Lysmer and G. Waas. Shear waves in plane infinite structures. *ASCE journal of Engineering Mechanics*, 98:85–105, 1972.

[20] P. Moczo, J. Kristek, M. Galis, P. Pazak, and M. Balazovjech. The finite–difference and finite element modeling of seismic wave propagation and earthquake motion. *Acta Physica Slovaca*, 52 (2):177–406, 2007.

[21] D.M. Boore. Finite difference method for seismic wave propagation in heterogeneous materials, in D.M. Boore (ed.). *Methods in Computational Physics*, 11:1–37, 1972.

[22] G. D. Manolis and D. E. Beskos. B*oundary* E*lement* M*ethods in* E*lastodynamics.* Unwin and Allen, London, 1987.

[23] J. Dominguez. B*oundary* E*lements in* D*ynamics.* Computational Mechanics Publications, Southampton, 1993.

[24] D.J. Fah. *A hybrid technique for estimation of strong ground motion in sedimentary basins.* PhD thesis, Swiss Federal Institute of Technology, Zürich, Switzerland, 1992.

[25] F. Romanelli G.F. Panza and F. Vaccari. Seismic wave propagation in laterally heterogeneous inelastic media: theory and applications to seismic zonation. *Advances in Geophysics*, 43:1–95, 2000.

[26] T. Furumura, K. Koketsu, and K. Wen. Parallel PSM/FDM hybrid simulation of ground motions from the 1999 Chi-Chi Taiwan earthquake. *Pure and Applied Geophysics*, 159:2133–2146, 2002.

[27] F. Wuttke, P. Dineva, and T. Schanz. Seismic wave propagation in laterally inhomogeneous geological region via a new hybrid approach. *J. Sound Vibr.*, 330:664–684, 2011.

[28] P.S. Dineva, G.D. Manolis, and T.V. Rangelov. Transient seismic wave propagation in a multilayered cracked geological region. *J. Sound Vibr.*, 273:1–32, 2004.

[29] K.L. Leung, I.G. Vardoulakis, D.E. Beskos, and J.L. Tasoulas. Vibration isolations by trenches in continuously nonhomogeneous soil by the BEM. *Soil Dyn. Earthq. Eng.*, 10:172–179, 1991.

[30] J. Hisada. The BEM based on the Green's function of the layered half–space and the normal mode solution. In *Proceedings of Conference on Effects of Surface Geology*, Odawara, 1992.

[31] H. Fujiwara and H. Takenaka. Calculation of surface waves for a thin basin structure using a direct boundary element method with normal modes. *Geophysical Journal International*, 117:69–91, 1994.

[32] Z. Ge. Simulation of the seismic response of sedimentary basins with constant–gradient velocity along arbitrary direction using boundary element method: SH case. *Earthq. Sci.*, 23:149–155, 2010.

[33] G. Panza, I. Paskaleva, P. Dineva, and C. La Mura. Earthquake site effects modelling by hybrid MS–BIEM: The case study of Sofia Bulgaria. *Rend. Sci. Fis. Accad. Lin.*, 20:91–116, 2009.

[34] F. Chapel. Boundary element method applied to linear soil–structure interaction on a heterogeneous soil. *Earthquake Eng. Struct. Dyn*, 15:815–829, 1987.

[35] Y. Hisada, S. Yamamoto, and S. Tani. Analysis of strong ground motion of plain and basin being composed of soft soil by fault model and boundary element method. In *Ninth World Conference on Earthquake Engineering*, pages 185–189, August 2-9, Tokyo-Kyoto, Japan, 1988.

[36] P.S. Dineva, G.D. Manolis, and T.V. Rangelov. Site effects due to wave path inhomogeneity by BEM. *Engineering Analysis with Boundary Elements*, 32: 1025–1036, 2006.

[37] C. H. Daros. On modeling SH-waves in inhomogeneous anisotropic media via the Boundary Element Method. *ZAMM*, 90(2):113–121, 2010.

[38] F. Luzon, L. Ramirez, F.J. Sanchez-Sesma, and A. Posadas. Propagation of SH elastic waves in deep sedimentary basins with an oblique velocity gradient. *Wave Motion*, 38:11–23, 2003.

[39] F. Luzon, L. Ramirez, F.J. Sanchez-Sesma, and A. Posadas. Simulation of the seismic response of sedimentary basins with vertical constant–gradient of velocity. *Pure Applied Geoscience*, 12:1533–1547, 2004.

[40] T. Rangelov and G. Manolis. Point force and dipole solutions in the inhomogeneous half–plane under time-harmonic conditions. *Mech. Res. Commun.*, 56:90–97, 2014.

[41] G.D. Manolis and R.P. Shaw. Harmonic wave propagation through viscoelastic heterogeneous media exhibiting mild stochasticity-I.Fundamental solutions. *Soil Dyn. Earthq. Eng.*, 15:119–127, 1996.

[42] G.D. Manolis and R.P. Shaw. Harmonic wave propagation through viscoelastic heterogeneous media exhibiting mild stochasticity-I.Applications. *Soil Dyn. Earthq. Eng.*, 15:129–139, 1996.

[43] J. D. Achenbach. *Wave propagation in elastic solids*. North Holland, Amsterdam, 1973.

[44] W. J. Mansur. *A time–stepping technique to solve wave propagation problems using the boundary element method*. PhD thesis, University of Southampton, Southampton, U.K., 1983.

[45] W. J. Mansur and C. A. Brebbia. Formulation of the boundary element method for transient problems governed by the scalar wave equation. *Applied Mathematical Modelling*, 6:307–311, 1982.

[46] W. J. Mansur and C. A. Brebbia. Numerical implementation of the boundary element method for transient problems governed by the scalar wave equation. *Applied Mathematical Modelling*, 6:299–306, 1982.

[47] D. L. Karabalis and D. E. Beskos. Diffraction of pulses by cylindrical obstacles of arbitrary cross section. *Journal of Applied Mechanics*, 29(1):40–46, 1962.

[48] H. Antes. A boundary element procedure for transient wave propagation in two–dimensional isotropic elastic media. *Finite Elements Analysis and Design*, (1):313–322, 1985.

[49] P. K. Banerjee, S. Ahmad, and G.D. Manolis. Transient elastodynamic analysis of 3-D problems by boundary element method. *Earthquake Engineering and Structural Dynamics*, (14):933–949, 1986.

[50] D. E. Beskos. B*oundary* E*lement* M*ethods in* M*echanics*. Elsevier Science, Amsterdam, 1987a.

[51] D. E. Beskos. Boundary element methods in dynamic analysis. *Applied Mechanics Reviews*, 40(1):1–23, 1987.

[52] D. E. Beskos. Boundary element methods in dynamic analysis: Part II (1986-1996). *Applied Mechanics Reviews*, 50(3):149–197, 1997.

[53] M. B. Friedman and R. Shaw. Diffraction of pulses by cylindrical obstacles of arbitrary cross section. *Journal of Applied Mechanics*, 29(1):40–46, 1962.

[54] T. A. Cruse and F. J. Rizzo. A direct formulation and numerical solution of the general transient elastodynamic problem:I. *Journal of Mathematical Analysis and Applications*, (22):244–259, 1968.

[55] D. Nardini and C. A. Brebbia. *A new approach to free vibration analysis using boundary elements*. In Brebbia, C. A. (Ed): Boundary Element Methods, pp. 312-326, Springer-Verlag, Berlin, 1982.

[56] A.H.D. Cheng, D.L. Young, and C. C. Tsai. Solution of Poisson's equation by iterative DR-BEM using compactly supported positive definite radial basis functions. *Engineering Analysis with Boundary Elements*, (24):549–557, 2000.

[57] P. W. Patridge, C. A. Brebbia, and L. C. Wrobel. *The dual* R*eciprocity* B*oundary* E*lement* M*ethod*. Computational Mechanics Publications, Southampton, 1992.

[58] M. Schanz and H. Antes. Application of operational quadrature methods in time domain boundary element methods. *Meccanica*, 32:179–186, 1997.

[59] M. Schanz and H. Antes. A new visco- and elastodynamic time domain boundary element formulation. *Computational Mechanics*, 20:452–459, 1997.

[60] C. Lubich. Convolution quadrature and discretizes operational calculus I. *Numerische Mathematik*, 52:129–145, 1988.

[61] C. Lubich. Convolution quadrature and discretizes operational calculus II. *Numerische Mathematik*, 52:413–425, 1988.

[62] G. G. Stokes. On the dynamical theory of diffraction. *Trans. Camb. Phil. Soc.*, 9:1–62, 1849.

[63] E. Kausel. *Review of fundamental solutions in elastodynamics*. Cambridge University Press, Cambridge UK, 2006.

[64] L. Pan, F. Rizzo, and P.A. Martin. Some efficient boundary integral strategies for time-harmonic wave problems in an elastic halfspace. *Comp. Meth. Appl. Mechanics*, 128:449–461, 1894.

[65] K. Ito. E*ncyclopedic* D*ictionary of* M*athematics*. MIT Press, Kingsport, 2000.

[66] G.D. Manolis, P.S. Dineva, and T.V. Rangelov. Dynamic fracture analysis of a smoothly inhomogeneous plane containing defects by BEM. *Engineering Analysis with Boundary Elements*, 36:727–737, 2012.

[67] C. H. Daros. A fundamental solution for SH–waves in a class of inhomogeneous anisotropic media. *International Journal of Engineering Science*, 46: 809–817, 2008.

[68] K. Watanabe. Transient response of an inhomogeneous elastic solid to an impulsive SH-source. *Bulletin of the JSME*, 25(201):315–320, 1982.

[69] K. Watanabe and R. Payton. Green's function and its non-wave nature for SH-wave in inhomogeneous elastic solid. *International Journal of Engineering Science*, 42:2087–2106, 2004.

[70] C. H. Daros. Green's function for SH-waves in inhomogeneous anisotropic elastic solid with power-function velocity variation. *Wave Motion*, 50:101–110, 2013.

[71] F.J. Sanchez-Sesma, R. Madariaga, and K. Irikura. An approximate elastic 2-D Green's function for a constant–gradient medium. *Geophys. J. Int.*, 146: 237–248, 2001.

[72] C. Z. Karakostas and G. D. Manolis. Transient signal simulation due to explosion in heterogeneous soil media. *The international journal of BEM Communications.*, 8:160–167, 1997.

[73] R. J. Apsel. *Dynamic Green's functions for layered media and applications to boundary–value problems.* PhD thesis, University of California, San Diego, 1979.

[74] R. Apsel and E. J. Luco. The Green's functions for a layered half-space. Part I. *Bull. Seismol. Soc. Am*, 73(4):909–929, 1983.

[75] R. Apsel and E. J. Luco. The Green's functions for a layered half-space. Part II. *Bull. Seismol. Soc. Am*, 73(4):931–951, 1983.

[76] E. Kausel and R. Peek. Dynamic load in the interior of a layered stratum: An explicit solution. *Bull. Seismol. Soc. Am.*, 72:1459–1481, 1982.

[77] S. Hull and E. Kausel. Dynamic loads an layered halfspaces. In A. P. Boresi and K. P. Chong, editors, *Engineering mechanics in civil engineering*, pages 185–189, New York: ASCE, 1992.

[78] T. Kundu and A. K. Mal. Elastic waves in a multi-layered solid due to a dislocation source. *Wave Motion*, 7:459–471, 1985.

[79] F. Chapel and C. Tsakalidids. Computation of the Green's functions of elastodynamics for a layered half–space through a Hankel transformation. Applications to foundation vibration and seismology. In T. Kawamoto and Y. Ichikawa, editors, *Numerical methods in geomechanics*, pages 1311–1318, Nagoya, Rotterdam: A.A. Balkena, 1985.

[80] Y. Hisada, S. Yamamoto, and S. Tani. The BEM based on the Green's function of the layered half–space and the normal mode solution. In *International Symposium on the effects of surface geology on seismic motion*, pages 185–189, Odawara, Japan, 1992.

[81] F. Luzon, F.J. Sanchez-Sesma, A. Perez-Ruiz, L. Ramirez, and A. Pech. In–plane seismic response of inhomogeneous alluvial valleys with vertical gradients of velocities and constant Poisson ratio. *Soil Dyn. Earthq. Eng.*, 29:994–1004, 2009.

[82] G.D. Manolis, P.S. Dineva, and T.V. Rangelov. Wave scattering by cracks in inhomogeneous continua using BIEM. *International Journal of Soilds and Structures*, 41(14):3905–3927, 2004.

[83] P.S. Dineva, G.D. Manolis, and T.V. Rangelov. Sub-surface crack in inhomogeneous half-plane: wave scattering phenomena by BEM. *Engineering Analysis with Boundary Elements*, 30(5):350–362, 2006.

[84] T.V. Rangelov, G.D. Manolis, and P.S. Dineva. Elastodynamic fundamental solutions for certain families of 2D inhomogeneous anisotropic domains: basic derivations. *European Journal of Mechanics: A/Solids*, 24:820–836, 2005.

[85] C. H. Daros. A time–harmonic fundamental solution for a class of inhomogeneous transversely isotropic media. *Wave Motion*, 46:269–279, 2009.

[86] P.S. Dineva, T.V. Rangelov, and G.D. Manolis. Elastic wave propagation in a class of cracked functionally graded materials by BIEM. *Computational Mechanics*, 39(3):293–308, 2007.

[87] J. F. Hook. Green's function for axially symmetric elastic waves in unbounded inhomogeneous media having constant velocity gradients. *J. Appl. Mech. ASMEE*, 29:293–298, 1962.

[88] K. Watanabe and T. Takeuchi. Green's function for two dimensional waves in a radially inhomogeneous elastic solid. In K. Watanabe and F. Ziegler, editors, *Proceedings of IUTAM Symposium on Dynamics of Advanced Materials and Smart Structures*, pages 459–468, Yonezawa, Japan. Berlin Springer, 2002.

[89] P.C. Xu and A. K. Mal. Calculation of the in–plane Green's functions for a layered viscoelastic solid. *Bull. Seismol. Soc. Am.*, 77:1823–1837, 1987.

[90] S. Chaillat, M. Bonnet, and J. F. Semblat. A new fast multi-domain BEM to model seismic wave propagation and amplification in 3-D geological structures. *Geophys. J. Int.*, 177:509–531, 2009.

[91] T.V. Rangelov and P.S. Dineva. Steady-state plane wave propagation in inhomogeneous 3D media. *J. Theor. Appl. Mech.*, 35:17–38, 2005.

[92] G.D. Manolis, T.V. Rangelov, and P.S. Dineva. Free-field wave solutions in a half-plane exhibiting a special–type of continuous inhomogeneity. *Wave Motion*, 44:304–321, 2007.

[93] S. Kobayashi. Some problems of the boundary integral equation method in elastodynamics. In T. Futagami C. A. Brebbia and M. Tanaka, editors, *Boundary Elments V*, pages 775–784, Springer-Verlag, Berlin, 1983.

[94] MATLAB (2008). *The language of* T*echnical* C*omputing,* V*ersion 7.7.* The math-works, Inc., Natick, Massachusetts.

[95] F. Wuttke, I-K. Fontara, P. Dineva, and T. Rangelov. SH–wave propagation in a continuously inhomogeneous half-plane with free–surface relief by BIEM. *ZAMM, Z. Angew. Math. Mech.*, DOI 10.1002/zamm.201300198: 1–16, 2014.

[96] H. Hirai. Analysis of transient response of SH–wave scattering in a half–plane by the boundary element method. *Eng. Anal.*, 5:189–194, 1988.

[97] F.J. Sanchez-Sesma and E. Rosenblueth. Ground motion at a canyon of arbitrary shape under incident SH waves. *Earth. Engin. Struct. Dynamics*, 7:441–450, 1979.

[98] A. H. Shah, K. C. Wong, and S. K. Datta. Diffraction of SH waves in a half-space. *Earthq. Eng. Struct. Dyn.*, 10:519–528, 1982.

[99] M. Ohtsu and S. Uesugi. Analysis of SH wave scattering in a half-space and its applications to seismic responses of geological structures. *Eng. Anal.*, 2 (4):198–204, 1985.

[100] I-K. Fontara, S. Parvanova, P. Dineva, and F. Wuttke. Wave propagation due to an embedded seismic source in a graded half-plane with relief peculiarities. Part I: mechanical model and computational technique. *Journal of Theoretical and Applied Mechanics*, 45(1):87–98, 2015.

[101] H. Lamb. On the propagation of tremors over the surface of an elastic solid. *Phil. Trans. R. Soc.*, Series A203, 1904.

[102] C.S. Yeh, T. J. Teng, and Wi Liao. On evaluation of lamb's integrals for waves in a two-domain elastic half–space. *The Chinese Journal of Mechanics*, 16(2):109–124, 2000.

[103] I.-K. Fontara, F. Wuttke, T. Rangelov, and P. Dineva. A non–conventional BEM for seismic wave propagation in continuously inhomogeneous half-plane. In *8th European Conference on Numerical Methods in Geotechnical Engineering, NUMGE*, pages Hicks, Brinkgreve and Rohe (Eds), Taylor and Francis Group, London, ISBN 978–1–138–00146–6, pages 367–372, Delft, The Netherlands, 2014.

[104] I.-K. Fontara, S. Parvanova, P. Dineva, T. Rangelov, and F. Wuttke. Seismic signals synthesis for laterally inhomogeneous geological media via BIEM. In *37th International Conference on Boundary Elements and other Mesh Reduction Methods*, pages edited by Carlos Brebbia Wessex Institute of Technology, WIT press, Southampton, Boston, ISBN: 978–1–84564–896–1, ISSN: (print) 1746–4064, pages 265–278, The New Forest, UK, 2014.

[105] R.A. Flinn and P.K. Trojan. E*ngineering* M*aterials and their* A*pplications, 4th Edition*. Wiley, Somerset, New Jersey, 1991.

[106] M.F. Ashby and D.R.H. Jones. E*ngineering* M*aterials* II*, 4th* E*dition*. Elsevier Science, Amsterdam, 2012.

[107] G.H. Paulino, Z.H. Jin, and R.H. Dodds. *Failure of functionally graded materials. In: Encyclopedia of Comprehensive Structural Integrity, Volume* II. edited by Karihaloo BL et al., Elsevier, pp.607–644, Amsterdam, 2003.

[108] C. Zhang and D. Gross. *On wave propagation in elastic solids with cracks.* Computational Mechanics Publications, Southampton, 1998.

[109] C. Hellier. *Handbook of non-destructive evaluation, 2nd Edition.* McGraw-Hill, New York, 2012.

[110] X.W. Gao, Ch. Zhang, J. Sladek, and V. Sladek. Fracture analysis of functionally graded materials by a BEM. *Composites Science and Technology*, 68(5):1209–1215, 2008.

[111] C.-E. Rousseau and H.V. Tippur. Influence of elastic gradient profiles on dynamically loaded functionally graded materials: cracks along the gradient. *International Journal of Solids and Structures*, 38:7839–7856, 2001.

[112] S. Momennia and A. H. Akbarzadeh. Proceedings of ICCS 16th International Conference on Composite Structures. pages 775–784, FEUP, Porto, 2011.

[113] J.E. Luco and C.P. Barros. Dynamic displacements and stresses in the vicinity of a cylindrical cavity embedded in a half–space. *Earthquake Engineering and Structural Dynamics*, 23:321–340, 1994.

[114] Y.H. Pao and C.C. Mow. *Diffraction of elastic waves and dynamic stress concentration.* New York: Crane Russak, 1971.

[115] I.-K. Fontara, P. Dineva, G. Manolis, and F. Wuttke. BEM modeling of elastic waves in a graded half-plane with position-dependent velocity containing cavities. In *EUROMECH-Colloquia: Micromechanics of Metal Ceramic Composites*, Stuttgart, Germany, 2015.

[116] F. Wuttke, I.-K. Fontara, and P. Dineva. Study of tunnel response in underground geomaterials with poroelastic structure by BEM modelling. In *2nd International Conference on Continuous Media with Microstructure*, Lagow, Poland, 2015.

[117] J.P. Bardet. A viscoelastic model for the dynamic behavior of saturated poroelastic soils. *Transaction of the ASME*, 59:128–135, 1992.

[118] M. Biot. Theory of propagation of elastic waves in a fluid–saturated porous solid. *Journal of Acoustical Society of America*, 4:168–191, 1956.

[119] C.H. Lin, V.W. Lee, and M.D. Trifunac. The reflection of plane waves in a poroelastic half–space saturated with inviscid fluid. *Soil Dynamics and Earthquake Engineering*, 25:205–223, 2005.

[120] Eurocode 8. *Design of Structures for Earthquake Resistance.* European Committee for Standardization, Brussels, 2003.

[121] T. Ohmachi and Y. Nakamura. Local site effects detected by microtremors measurements on the damage due to the 1990 Philippine earthquake. In *Proceedings of the 10th World Conference on Earthquake Engineering*, Rotterdam, 1990.

[122] D. Jongmans and M. Campillo. The 1983 Liege earthquake: Damage distribution and site effects. *Earthquake Spectra*, 6(4):713–728, 1990.

[123] H. Arai, H. Hibino, M. Okuma, Y. Matsuoka, T. Kubo, and F. Yamazaki. Estimation of ground motion characteristics and damage distribution in Golcuk, Turkey, based on microtremor measurements. In *Proceedings of the 6th International Conference on Seismic Zonation*, Earthquake Engineering Research Institute (EERI), Palm Springs/CA, 2000.

[124] M. Navaro, T. Enomoto, T. Yamamoto, A. Garcia-Jerez, F. Vidal, and M. Breton. Analysis of site effects and their correlation with damage distribution observed during the Colima (Mexico) earthquake of January 21, 2003. In *Proceedings of the 14th World Conference on Earthquake Engineering*, 12-17 October, Beijing, China, 2008.

[125] D.H. Lang. *Damage potential of seismic ground motion considering local site effects*. PhD thesis, Bauhaus University, Weimar, Germany, 2004.

[126] G.D. Manolis and A.M. Athanatopoulou. Structural response to complex synthetic ground motions. In NATO Science for Peace and Security Series C: Environmental Security 2009, editors, *Coupled site and soil-structure interaction effects with application to seismic risk mitigation*, pages 209–223, 2005.

[127] A. Sextos, K. Pitilakis, and A. Kappos. Inelastic dynamic analysis of RC bridges accounting for spatial variability of ground motion, site effects and soil-structure interaction phenomena. Part 1: Methodology and analytical tools. *Earthquake Engineering and Structural Dynamics*, 32:607–627, 2003.

[128] A. Sextos, K. Pitilakis, and A. Kappos. Inelastic dynamic analysis of rc bridges accounting for spatial variability of ground motion, site effects and soil-structure interaction phenomena. Part 2: Parametric study. *Earthquake Engineering and Structural Dynamics*, 32:629–652, 2003.

[129] B. Jeremic, G. Jie, M. Preisig, and N. Tafazzoli. Time domain simulation of soil-foundation-structure interaction in non–uniform soils. *Earthquake Engineering and Structural Dynamics*, 38(5):699–718, 2009.

[130] K. Bi, H. Hao, and N. Chouw. Influence of ground motion spatial variation, site condition and SSI on the required separation distances of bridge structures to avoid seismic pounding. *Earthquake Engineering and Structural Dynamics*, 40(9):1027–1043, 2011.

[131] K. Soyluk and E.A. Sicacik. Soil-structure interaction analysis of cable-stayed bridges for multiple-support excitations. In *Proceedings of the 8th International Conference on Structural Dynamics, EURODYN*, pages MS03–499, 547–554, 4-6 July, Leuven, Belgium, 2011.

[132] J.A. Esquivel and F.J. Sanchez-Sesma. Effects of canyon topography on dynamic soil–bridge interaction for incident plane SH waves. In *Proceedings of the 7th World Conference on Earthquake Engineering*, pages 153–160, Istanbul, Turkey, 1980.

[133] G. Zhou, X. Li, and X. Qi. Seismic response analysis of continuous rigid frame bridge considering canyon topography effects under SV waves. *Earthquake Science*, 23:53–61, 2010.

[134] I.-K. Fontara, K. Kostinakis, F. Wuttke, A. Athanatopoulou, and G. Manolis. Effects of site conditions on ground motion and ensuing structural damage. In *2nd European Conference on Earthquake Engineering and Seismology*, Istanbul, Turkey, 2014.

[135] C.A. Brebbia and J. Dominguez. B*oundary* E*lements: an* I*ntroductory* C*ourse*. CMP, Southampton, 1992.

[136] FEMA 356. *Pre-standard and* C*ommentary for the* S*eismic* R*ehabilitation of* B*uildings*. Federal Emergency Management Agency, Washington, DC, 2000.

[137] PEER. P*acific* E*arthquake* E*ngineering* R*esearch* C*enter*. Strong Motion Database available at http://peer.berkeley.edu/smcat/, Berkeley, 2003.

[138] Eurocode 2. D*esign of* C*oncrete* S*tructures*. European Committee for Standardization, Brussels, 2004.

[139] RAF. V*ersion 3.3:* S*tructural* A*nalysis and* D*esign* S*oftware*. TOL-Engineering Software House, Iraklion, Creta, Greece, 2012.

[140] A. Otani. Inelastic analysis of r/c frame structures. *Journal of Structural Division (ASCE)*, 100(7):1433–1449, 1974.

[141] A. J. Carr. *Ruaumoko–a program for inelastic time-history analysis,* P*rogram manual*. PhD thesis, Department of Civil Engineering, University of Canterbury, New Zealand, 2004.

[142] I-K. M. Fontara, K. Kostinakis, G. Manoukas, and A. Athanatopoulou. Parameters affecting the seismic response of buildings under bi–directional excitation. *Structural Engineering and Mechanics*, 53(5):957–979, 2015.

[143] Y.J. Park and AH.-S. Ang. Mechanistic seismic damage model for reinforced-concrete. *Journal of Structural Engineering (ASCE)*, 111(4):722–739, 1985.

[144] I.-K. Fontara, M. Titirla, F. Wuttke, A. Athanatopoulou, G. Manolis, and P. Dineva. Effects of local site conditions on the inelastic dynamic analysis of r/c bridges. In *Workshop on Dynamic Analysis, Testing and Design of Infrastructure funded by DAAD*, Thessaloniki, Greece, 2014.

[145] I.-K. Fontara, M. Titirla, F. Wuttke, A. Athanatopoulou, G. Manolis, and A. Sextos. Multiple support excitation of a bridge based on BEM analysis of the sub–soil structure-interaction phenomenon. In *5th International Conference on Computational Methods in Structural Dynamics and Earthquake Engineering (COMPDYN)*, Creta Island, Greece, 2015.

[146] S.A. Mitoulis, M.D. Titirla, and I.A. Tegos. Design of bridges utilizing a novel earthquake resistant abutment with high capacity wing walls. *Engineering Structures*, 66:35–44, 2014.

[147] User's Reference Manual SAP 2000 Nonlinear Version 14. *Computer and Structures*. Inc., Berkley, California, 2007.

[148] M.J. Pender. Aseismic pile foundation design analysis. *Bulletin of the New Zealand National Society on Earthquake Engineering*, 26(1):49–161, 1993.

[149] M. Kavadas and G. Gazetas. Kinematic seismic response and bending of free–head piles in layering soil. *Geotechnique*, 43:207–222, 1993.

[150] G. Gazetas, K. Fan, A. Kaynia, and E. Kausel. *Dynamic interaction factors for floating pile groups,* V*ol.* I. NCEER-90-0021. National Center of Earthquake Engineering Research, Baffalo, NY, 1990.

[151] N. Makris and G. Gazetas. Dynamic pile–soil–pile interaction. Part II: lateral and seismic response. *Earthquake Engineering and Structural Dynamics*, 21(2):145–162, 1992.